Preklinische SPECT-beeldvorming gebaseerd op compacte collimatoren en hogeresolutiescintillatiedetectoren

Preclinical SPECT Imaging Based on Compact Collimators and High Resolution Scintillation Detectors

Karel Deprez

Promotoren: prof. dr. S. Vandenberghe, prof. dr. R. Van Holen
Proefschrift ingediend tot het behalen van de graad van
Doctor in de Ingenieurswetenschappen

Vakgroep Elektronica en Informatiesystemen
Voorzitter: prof. dr. ir. J. Van Campenhout
Faculteit Ingenieurswetenschappen en Architectuur
Academiejaar 2013 - 2014

ISBN 978-90-8578-672-6
NUR 954, 959
Wettelijk depot: D/2014/10.500/18

Department of Electronics and Information Systems
Medical Image and Signal Processing (MEDISIP)
Faculty of Engineering and Architecture
Ghent University

MEDISIP
IBiTech
Campus Heymans, Blok B
De Pintelaan 185
9000 Ghent
Belgium

Promotors
Prof. dr. Stefaan Vandenberghe
Prof. dr. Roel Van Holen

Board of examiners
Prof. dr. ir. Patrick De Baets, Ghent University, chairman
Dr. Michael Tytgat, Ghent University / CERN, secretary
Prof. dr. Luc Van Hoorebeke, Ghent University
Prof. dr. Dennis Schaart, Delft University of Technology, The Netherlands
Prof. dr. Carlo Fiorini, Politecnico di Milano, Italy
Dr. Samuel España Palomares, Advanced Imaging Unit, Centro Nacional de Investigaciones Cardiovasculares (CNIC), Spain
Dr. Peter Bruyndonckx, Bruker MicroCT, Belgium

This work was supported by the 7th Framework Programme (FP7) of the European Union through the SUBLIMA project (Grant Agreement No 241711)

Acknowledgements

The work presented in this dissertation started in 2008, shortly after the birth of my daughter, and was finished in early 2014. Before I started at the university I had been working for several years as a electronics design engineer at Barco and Gemidis. The first thing that struck me when I started at the university was the content of my work. My new job involved a lot of different aspects, from that time on I would, besides designing electronics, also design mechanics, collimators, software and a lot of other things (such as adapting the architectural plans of the lab and mounting pegs in the corridor). This diversity was refreshing for me and it surely has boosted my creativity.

This work would not have been possible without the help of a lot of people. First, I would like to thank prof. dr. Stefaan Vandenberghe, prof. dr. Roel Van Holen and prof. dr. ir. Steven Staelens. When I started at MEDISIP I was the first hardware designer; at that time most researchers at MEDISIP were performing simulation and image reconstruction studies. In order to develop innovative imaging hardware, one has to do substantial investments because the measurement devices and hardware components are very expensive. Stefaan, Roel and Steven made funding available to buy these components and gave me the freedom and time to develop MEDISIP's first hardware. Additionally, they allowed me to present my research at numerous conferences abroad. I have to thank Stefaan for guiding me and for helping me to focus on the most innovative parts of my research. Roel convinced me at the start of my employment that I was doing innovative research by inviting me to Harry Barrett's laboratory at the university of Arizona. It is Roel who, especially during the last two years, indicated how my research should evolve. Steven was a professor at the MEDISIP department during the first years of my employment. I want to thank him for the confidence he had in me.

I want to thank prof. dr. Christian Vanhove for the fruitful discussions

and for allowing me to develop hardware in the Infinity lab.
The people of the nuclear medicine division of the university hospital Ghent have helped me a lot by providing me ^{99m}Tc to perform measurements. I would especially like to thank Ingeborg Goethals, Lieselotte Moerman, Michel Ravier, Tamara Blanken and Carine Wartel.
I would like to thank prof. dr. Romain Lefebvre for allowing me to use the tools in the mechanical workshop. Tom Vanthuyne, Sam Tshitengé and Diego De Baere have helped me a lot by learning me how to operate the various tools in the workshop. Also Bart Blanckaert and Cyriel Mabilde helped me a lot with practical machining issues during the first years of my employment.
In this dissertation I developed an electronics board to perform the readout of a photodetector. This board is rather complex and I would not have been able to layout it without the help of Lieven Degrendele (CMST, Ghent university).
Additive manufacturing is presented here as a new production method for tungsten collimators. Layerwise is the first company in the world that was able to produce these tungsten parts. I would like to thank Tom De Bruyne and Jonas Van Vaerenbergh for the successful collaboration.
The first lofthole collimators were machined by VASKON. I especially would like to thank Patrick D'Haeyer for the swift service.
I am grateful to Prof dr. Pieter Dorenbos for explaining the spectra obtained with the LYSO detector.
The production and processing of scintillators can be considered as some sort of artform; a lot of parameters determine the quality of a scintillator. I owe many thanks to Paul Schotanus (Scionix) and Jim Telfer (Hilger Crystals) to provide us with scintillators and to share knowledge with us.
I would like to thank Vicky Van Ooteghem and Gerwin Raes for proofreading the Dutch parts of this dissertation.
Ewout Vansteenkiste and Kris Bonnarens were very supportive for the patent applications and valorization issues. I especially have to thank Ewout for his extensive knowledge and advice on the different possibilities to obtain funding for research and valorization.
I also want to express my gratitude to my colleagues at MEDISIP. Bert never hesitated to (re-)explain image reconstruction algorithms to me, to bring a sandwich for lunch and to help me solving software issues. Karen is always keen on a SPECT-related discussion. I will never forget our legendary Everglades kayaking trip and I would like to thank her for convincing me to go running during lunch break. Lara has developed

the lofthole sensitivity formulas that are presented in this book. Besides that, she has great knowledge on mathematics and she was always willing to help me with math problems. Carmen has helped me when I encountered a physics related problem, thanks for that. Gregor is an EEG-researcher and a great DJ, thanks for the good vibes on several parties. I have to thank Saskia, Inge, Anne-Marie and Ayfer for generating all those order forms, for handling loads of administrative issues and for a talk once in a while. I would like to thank Vincent for his medical insights. Thanks to Pieter (Van Mierlo) and Pieter (Mollet) for the many interesting discussions during lunch break and for helping me with PhD related things (dissertation, defense and parties). Many thanks to Nathalie and Shandra for promoting kayaking at MEDISIP. Willeke recently started and is MEDISIP's youngest researcher, I'm sure that she will perform great research and I thank her for being such a nice person. Faruk frequently helped me with simulations, thanks for your expertise! Victoria and Hendrik were two of MEDISIP's most remarkable persons, thanks for being around. I also have to thank Benedicte, Scharon, Philippe and Steven (Deleye) for helping me with practical issues in the lab. Radek is building an innovative PET system, I thank him for sharing the lab with me and I hope that we can collaborate in the future. Also thanks to Roma, Aaike, Erwann, Sinem, Enrico and Long. Thanks to Tom Ghekiere for helping me to solve C++ pointer problems and to Hans Hallez for explaining me math-related things.

Ik wens ook mijn ouders te bedanken voor de steun die ze mij steeds gegeven hebben. Zonder het doorzettingsvermogen dat ik van mijn moeder geërfd heb en de technische handigheid die ik van mijn vader geërfd heb zou dit doctoraat er niet gekomen zijn. Via deze weg wil ik hen ook het beste voor de toekomst wensen.

Mijn vriendin Leen wil ik bedanken voor de liefde, de kinderen, de interesse in mijn onderzoek, de flexibiliteit, het begrip, het nalezen en nog heel wat andere zaken.

Mijn schoonouders, Marie-Anne en Guido, dank ik voor de interesse en voor het helpen met de kinderen.

Finaal wens ik ook mijn kinderen, Sky en Andreas, te danken voor hun jeugdige enthousiasme en om mij te leren om met een andere blik naar de wereld te kijken.

Karel, 20 maart 2014

"I do not seek. I find."
Pablo Picasso

Table of Contents

Table of Contents i

List of Figures vii

List of Tables xxiii

List of acronyms xxvi

English summary xxxi

Nederlandstalige samenvatting xxxv

1 Introduction 1
- 1.1 Medical imaging . . . 1
- 1.2 Single photon emission computed tomography . . . 4
- 1.3 Outline . . . 5

2 Single photon emission computed tomography 7
- 2.1 Introduction . . . 7
- 2.2 Radioisotopes and tracers for SPECT . . . 10
- 2.3 SPECT physics - interactions of gamma rays . . . 11
  - 2.3.1 Photoelectric absorption . . . 11
  - 2.3.2 Compton scatter . . . 12
  - 2.3.3 Attenuation . . . 13
- 2.4 Collimators . . . 17
  - 2.4.1 Introduction . . . 17
  - 2.4.2 The parallel hole collimator . . . 19
    - 2.4.2.1 Introduction . . . 19
    - 2.4.2.2 Sensitivity and resolution . . . 20
  - 2.4.3 The pinhole collimator . . . 21
    - 2.4.3.1 Introduction . . . 21

2.4.3.2 Sensitivity . . . 22
2.4.3.3 Resolution . . . 25
2.4.3.4 Resolution-sensitivity trade-off . . . 27
2.4.3.5 Non-ideal pinholes . . . 27
2.4.3.6 Other pinhole geometries . . . 28
2.4.3.7 Multi-pinhole collimators . . . 28
2.4.4 Fanbeam and conebeam collimators . . . 30
2.4.4.1 Introduction . . . 30
2.4.4.2 Sensitivity and resolution . . . 32
2.4.5 Collimator materials and collimator production techniques . . . 33
2.5 Gamma-ray detectors for SPECT . . . 34
2.5.1 Introduction . . . 34
2.5.1.1 Spatial resolution . . . 35
2.5.1.2 Energy resolution . . . 36
2.5.1.3 Detection Efficiency . . . 38
2.5.1.4 Count rate performance . . . 38
2.5.2 Scintillation detectors . . . 40
2.5.2.1 Introduction . . . 40
2.5.2.2 Scintillation mechanism . . . 41
2.5.2.3 Examples . . . 44
2.5.2.4 Detector sensitivity . . . 46
2.5.2.5 Light emission: spectrum, time course and light yield . . . 46
2.5.2.6 Photodetectors . . . 48
2.5.2.6.1 Introduction . . . 48
2.5.2.6.2 Vacuum tube photodetectors . . . 49
The photomultiplier tube (PMT) . . . 49
The position sensitive PMT (PSPMT) . . . 53
2.5.2.6.3 Semiconductor photodetectors . . . 55
PN photodiode . . . 55
PIN photodiode . . . 55
Avalanche photodiode (APD) . . . 56
Silicon photomultiplier (SiPM) . . . 57
dSiPM . . . 59
Silicon drift detector (SDD) . . . 61
Electron-multiplying charge-coupled device (EMCCD) . . . 61
2.5.2.7 Event positioning . . . 62
2.5.2.7.1 Introduction . . . 62

2.5.2.7.2 Center of gravity (COG) 63
2.5.2.7.3 Maximum likelihood Estimation (MLE) 64
Calibration 64
Event positioning 65
2.5.2.7.4 k-nearest neighbor (k-NN) 68
Calibration 68
Event positioning 68
2.5.3 Semiconductor detectors 70
2.5.3.1 Introduction 70
2.5.3.2 Silicon 72
2.5.3.3 High-purity germanium (HPGe) 73
2.5.3.4 CdTe and CdZnTe (CZT) 73
2.6 SPECT image reconstruction 74
2.6.1 Introduction 74
2.6.2 Algorithm 74
2.6.3 System matrix 78
2.7 Summary 79

3 A compact high-resolution detector based on a NaI(Tl) scintillator 81
3.1 Introduction 81
3.2 Scintillator and PSPMT 83
3.3 Readout electronics 84
3.3.1 Pre-amplifier 84
3.3.2 Analog to digital conversion 87
3.3.3 Digital processing 87
3.4 Event positioning software 90
3.4.1 Calibration 90
3.4.2 Event positioning algorithm and energy windowing . 92
3.5 Spatial resolution and bias measurements 92
3.6 Energy resolution measurements 96
3.7 Detector count rate measurements 96
3.8 Discussion 99
3.9 Summary and original contributions 102

4 The lofthole: a novel shaped pinhole geometry for optimal detector usage 103
4.1 Introduction 103
4.2 The lofthole 105

4.3 Characterization of sensitivity . . . 106
4.3.1 The umbra and the penumbra . . . 106
4.3.2 Analytical sensitivity formulas . . . 107
4.4 Validation of the sensitivity formulas with simulations . . . 114
4.5 Comparison of a lofthole and a pinhole collimator . . . 118
4.5.1 Flood map comparison . . . 119
4.5.2 Penetration comparison . . . 119
4.6 Discussion . . . 125
4.7 Summary and original contributions . . . 126

5 FlexiSPECT: A compact SPECT system consisting of a high resolution NaI(Tl) detector and a lofthole collimator 129
5.1 Introduction . . . 129
5.2 Mechanical setup . . . 130
5.3 Geometric system calibration . . . 130
5.4 Image reconstruction . . . 134
5.4.1 MLEM reconstruction . . . 134
5.4.2 Sensitivity correction . . . 134
5.5 SPECT system measurements (Rat Setup) . . . 136
5.5.1 Geometric calibration . . . 136
5.5.2 Flood source calibration . . . 137
5.5.3 Rat-size hot rod phantom . . . 137
5.5.4 Rat-size uniform phantom . . . 139
5.6 SPECT system measurements (Mouse Setup) . . . 141
5.6.1 Geometric calibration . . . 141
5.6.2 Flood source calibration . . . 141
5.6.3 Mouse-size hot rod phantom . . . 142
5.6.4 Mouse-size uniform phantom . . . 142
5.7 Discussion . . . 143
5.8 Summary and original contributions . . . 145

6 A high resolution LYSO-based SPECT detector 147
6.1 Introduction . . . 147
6.2 Previous work . . . 148
6.3 Detector . . . 149
6.3.1 Scintillators, PSPMT and readout electronics . . . 149
6.3.2 MNN calibration . . . 151
6.3.3 Event positioning . . . 154
6.3.3.1 Coarse energy windowing . . . 154

6.3.3.2 Mean nearest-neighbor event positioning (MNN) . . . 155
6.3.3.3 Fine energy windowing . . . 155
6.3.3.4 Distance thresholding . . . 156
6.4 Evaluation of detector performance . . . 156
6.4.1 Mean light spread . . . 156
6.4.2 Energy resolution . . . 157
6.4.3 Intrinsic radioactivity . . . 160
6.4.4 Spatial resolution measurements . . . 161
6.4.4.1 Beam source measurement . . . 161
6.4.4.2 Tungsten resolution collimator measurement 163
6.5 Discussion . . . 163
6.6 Summary and original contributions . . . 169

7 Rapid additive manufacturing of collimators with selective laser melting of tungsten powder 171
7.1 Introduction . . . 171
7.2 Collimator design . . . 172
7.2.1 First-generation collimator . . . 172
7.2.2 Second-generation collimator . . . 174
7.3 Collimator production . . . 174
7.4 Measurements on printed sample pieces . . . 177
7.4.1 Density . . . 177
7.4.2 Attenuation . . . 178
7.5 Collimator measurements (first-generation collimator) . . . 180
7.5.1 Density . . . 180
7.5.2 Production accuracy . . . 180
7.5.3 Sensitivity measurement . . . 182
7.6 Collimator measurements (second-generation collimator) . . . 189
7.6.1 Density . . . 189
7.6.2 Production accuracy . . . 189
7.7 Discussion . . . 192
7.8 Summary and original contributions . . . 193

8 A multi-lofthole collimator based SPECT system 195
8.1 Introduction . . . 195
8.2 SPECT system calibration . . . 200
8.2.1 System matrix calculation . . . 200
8.2.1.1 Flood map acquisitions and derivation of the lofthole borders . . . 203

8.2.1.2 Point source acquisitions 205
8.2.1.3 Geometric calibration 207
8.2.1.4 Sensitivity and resolution of measured grid 212
8.2.1.5 Sensitivity and resolution modeling 213
8.2.1.6 System matrix calculation 214
8.2.2 Center of rotation in image space (COR_{Im}) 215
8.3 Image reconstruction 217
8.4 Measurements 217
8.4.1 Derenzo phantom 218
8.4.1.1 Scan 1: one bed position, five angles . . . 218
8.4.1.2 Scan 2: one bed position, fifty angles . . . 219
8.4.1.3 Scan 3: ten bed positions, five angles . . . 222
8.4.1.4 Scan 4: ten bed positions, fifty angles . . . 222
8.4.2 Uniform phantom 225
8.4.2.1 Scan 5: one bed position, five angles . . . 225
8.4.2.2 Scan 6: one bed position, fifty angles . . . 225
8.4.2.3 Scan 7: ten bed positions, five angles . . . 227
8.4.2.4 Scan 8: ten bed positions, fifty angles . . . 229
8.5 Discussion 229
8.6 Summary and original contributions 234

9 General conclusions **235**
9.1 Summary 235
9.2 Final conclusion 238

References **241**

List of Publications **259**

List of Figures

1.1 (a) A radiograph of the wrist, (b) an MRI image of the brain and (c) an ultrasound image of a fetus 2
1.2 A brain SPECT study showing the cerebral blood perfusion. 2
1.3 (a) The MILabs U-SPECT-II/CT is a SPECT/CT system for mice and rats. (b) The Bruker Pharmascan is an MR scanner for small animals. 3

2.1 An Inter Medical Prism 3000 SPECT scanner. The three gamma cameras rotate around the patient and projections are obtained at a multitude of angles. 8
2.2 A schematic view of the system depicted in Fig. 2.1 for a gantry angle of 0° (a), 10° (b) and 20° (c). The gantry rotates from 0 to 120° for this triple-head SPECT system. . 8
2.3 A gamma camera consists of a parallel hole collimator, a NaI(Tl) scintillator, a lightguide, PMTs and readout electronics. 9
2.4 (a) The gamma photon and the electron before Compton scattering occurred. (b) The gamma photon has deflected and part of its energy has been transferred to the electron after Compton scattering. 13
2.5 The probability of a certain type of interaction depends on the material and the energy of the gamma photon. The red curve is where photoelectric interactions and Compton scatter interactions are equally probable. Typical collimator materials are lead (Z=82) and tungsten (Z=74). The dominant type of interaction for these materials (for energies below 511 keV) is the photoelectric interaction. 14
2.6 The probability of interactions in water 15
2.7 The probability of interactions in tungsten 16

2.8 This narrow beam setup allows to measure the total attenuation coefficient (μ) of a material. 16
2.9 Some examples of the total attenuation of tungsten, lead, NaI(Tl) and water. Tungsten and lead are used for collimators, NaI(Tl) is used for SPECT detectors, and, a large fraction of the body is water. 17
2.10 (a) A parallel hole gamma camera and (b) a fanbeam gamma camera are fixed to a gantry (red circle); the green lines depict the collimator FOV. The system FOV (blue circle) can be derived by rotating the gantry (only 6 angles are shown here) and is the intersection of all collimator FOVs. . 18
2.11 An ideal parallel hole collimator only allows perpendicularly incident gamma photons to reach the detector. 19
2.12 Illustration of the symbols used for the resolution and sensitivity formulas of the parallel hole collimator. 21
2.13 (a) A high resolution parallel hole collimator and (b) a low resolution collimator with larger diameter holes. The acceptance angle (hatched area) of the low resolution collimator is larger, which results in more uncertainty on the origin of the gamma photon ($R_1 < R_2$). Additionally, the resolution degrades at larger collimator-source distance ($R_1 > R_3$). . . 22
2.14 (a) Top and side view of a pinhole collimator. (b) Ideally, only the gamma rays that pass through the pinhole's aperture reach the detector. The other gamma rays are absorbed in the collimator material. 23
2.15 Top and side view of a the shape of a pinhole. The exit opening is oriented towards the detector, the entrance opening is oriented towards the subject. 23
2.16 Pinholes scale the object on the detector. (a) Magnification and (b) minification. 24
2.17 The sensitivity of a pinhole collimator depends on d (the aperture diameter), θ (the angle of incidence) and h (the height of the source above the aperture plane) 25
2.18 The resolution of the pinhole collimator (R_{Coll}) depends on d (aperture diameter), f (the detector-collimator distance) and h (the height of the source above the collimator). 26
2.19 Ideally only the gamma rays passing through the aperture can reach the detector (e.g. path 2). In reality, also other paths are possible (e.g. paths 1,3,4). 27

2.20 (a) a knife-edge pinhole, (b) a keel-edge pinhole and (c) a clustered pinhole. The latter two are beneficial to image higher-energy isotopes. 29
2.21 (a) A 2-pinhole SPECT collimator that has a significant amount of multiplexing and (b) the same collimator with a slat to prevent overlapping projections. 29
2.22 The holes of the fanbeam collimator are focused to a line. . 31
2.23 The holes of the conebeam collimator are focused to a point. 31
2.24 A sectional view of a conebeam or fanbeam collimator. . . . 32
2.25 The energy spectrum of a 140 keV gamma ray source. Detector 1 (6.7%) has a better energy resolution than detector 2 (21.2%). 37
2.26 The behavior of paralyzable and nonparalyzable detectors. The paralyzable detector detects events 1, 2, 3 and 6. The nonparalyzable detector detects events 1, 2, 3, 5 and 6. . . . 39
2.27 Ideally the output count rate of a detector increases linearly with the event rate. In reality this is not the case, a paralyzable detector's output count rate will drop to zero and a nonparalyzable detector's output count rate saturates when the event rate is too high. 39
2.28 A hygroscopic scintillator such as NaI(Tl) needs a hermetically sealed package. 40
2.29 (a) A monolithic scintillator and (b) a pixelated scintillator. The light spread of the pixelated detector is more focused on the photodetectors. 42
2.30 A monolithic and a pixelated LYSO scintillator. The monolithic block is wrapped in a reflector during assembly. 42
2.31 A scintillation detector consists of the scintillator, a light guide and an array of photodetectors. A multitude of light photons are emitted isotropically at the point of interaction. The top and side surfaces of the scintillator are reflective to guide the light photons to the photodetectors. The number of light photons emitted is related to the energy of the detected gamma photon. The position of the interaction can be estimated based on the measured light spread. 43
2.32 The addition of activators leads to a modified band structure. 43
2.33 The QE of a PMT (ET Enterprises 9107B) and the emission spectrum of NaI(Tl) (Saint-Gobain Crystals). 47

2.34 The output of a PMT that is coupled to a NaI(Tl) scintillator, measured with an oscilloscope in infinite persistence mode. A source of ^{99m}Tc is positioned in front of the scintillator. 47
2.35 A Hamamatsu PMT that was once operational in a large clinical SPECT gamma camera. Its round package has a diameter of 7.5 cm. 50
2.36 The major parts of the PMT: the photocathode (PC), the focusing electrodes (F), the dynodes (Dy) and the anode (A). 50
2.37 The QE of a PMT is a function of the wavelength of the incident light photons. The graph shown is for the Hamamatsu R11102 PMT. Image courtesy of Electron Tube Division, Hamamatsu Photonics K.K. 52
2.38 A Hamamatsu H8500 PSPMT has 8x8 anodes. Image courtesy of Electron Tube Division, Hamamatsu Photonics K.K. . 53
2.39 The metal channel dynodes multiply the electrons with minimum spatial spread. By doing so, most electrons will hit the anode underneath the interaction position of the light photon. 54
2.40 The photo-sensitive part of a photodiode is the depletion region. 56
2.41 A Geiger-mode APD needs quenching. The simplest method is to use passive quenching by putting a resistor in series with the APD. 57
2.42 A SensL SiPm array; the pixel size is 3 mm x 3mm (image courtesy of SensL). 58
2.43 A SiPM consists of an array of thousands of Geiger-mode APDs, all placed in parallel. 59
2.44 An 8x8 array of dSiPMs. The pixels size is 3.2 mm x 3.8 mm. 60
2.45 The Hamamatsu ImagEM EM-CCD camera uses a 512 x 512 EMCCD sensor and has a frame rate of 70 frames/s. The sensor is cooled to -65° C. Image courtesy of System Division, Hamamatsu Photonics K.K. 62
2.46 (a) COG algorithm without linearity correction and (b)COG algorithm with linearity correction 64
2.47 (a) A robot stage is used to acquire calibration data. (b) The beam source used to scan the detector consists of a narrow collimated beam. 65

2.48 A histogram of the charge of a photodetector channel for a certain calibration grid position. The histogram is fit with a Gaussian function. 66
2.49 The mean value of an anode of a small gamma camera for different event positions. The measured and interpolated values are shown. 66
2.50 The lightspread measured by an 8x8 array of photodetectors for an event in the center of the detector. 68
2.51 The estimate of the point of interaction is set to the detector pixel with the maximum log-likelihood (see formula 2.46). . 69
2.52 (a) A pixelated detector and (b) a double-sided strip detector (DSSD). The advantage of the DSSD is the reduced number of channels. 72
2.53 Iterative image reconstruction algorithms differ in the way the calculated and measured projections are compared, and, in the way the image estimate is update. 76
2.54 The iterative MLEM image reconstruction algorithm. 77
2.55 Reconstructions of a Derenzo phantom at 10, 50 and 100 iterations. 78

3.1 The NaI(Tl) scintillator. Dimensions are in mm. 83
3.2 Four boards are used to do the readout of the PSPMT. The PSPMT and scintillator are in the aluminum block on the right. 84
3.3 The PCB has the following circuitry (from left to right): pre-amplifiers, ADCs, FPGA and Ethernet circuitry. 85
3.4 The pre-amplifier converts the anode current to a differential voltage which is suitable to be digitized by the ADC. Voffset and Vcm are bias voltages. 86
3.5 A SPICE simulation of the pre-amplifier. V(Outlp+) is the positive pulse, V(Outlp-) is the negative pulse. Both output voltages have a positive DC offset, this is caused by the positive Voffset voltage in the first stage of the pre-amplifier circuit. The offset is required to bring the differential voltage within the input range of the ADC. 86
3.6 FPGA block diagram. 87
3.7 Flowchart of the integrator of channel 1. 88
3.8 Histogram of the ADC Data. 89
3.9 Flowchart of the baseline searching algorithm. 89

3.10 The beam source which was used for the calibration and measurements. The hole length of the collimator is 10 mm, the hole diameter is 355 μm . This collimator is made of MT-17C (Midwest Tungsten, USA, see section 2.3 for more information). The ^{99m}Tc container is typically filled with a total activity of about 370 MBq. 91

3.11 All the energy-filtered events of one calibration position are positioned using the COG algorithm (green dots in the graph). The mean position is calculated (red dot in the graph). Events whose position is more than 1 mm away from this mean are not used for the calibration. The black circle depicts this 1 mm border. 91

3.12 Detector view of the 5.5 mm grid scan (9 x 9 positions). The usable detector area is 44 mm x 44 mm. 94

3.13 Profile of Fig. 3.12 at X=21.5 mm. The peaks have a (beam diameter corrected) FWHM of 2.2 mm, 1.4 mm, 1.3 mm, 1.3 mm, 1.0 mm, 1.0 mm, 1.1 mm, 1.7 mm and 2.0 mm (from left to right). 94

3.14 Profile of Fig. 3.12 at Y=21.5 mm. The peaks have a (beam diameter corrected) FWHM of 2.1 mm, 1.4 mm, 1.3 mm, 1.1 mm, 1.0 mm, 1.0 mm, 1.1 mm, 1.4 mm and 2.1 mm (from left to right). 95

3.15 COG Event positioning (a) and linearity corrected COG event positioning (b). Only the central 5x5 beam positions can be distinguished. The mean spatial resolution of the central 5x5 beam positions is 1.95 mm. 95

3.16 Energy spectrum of a ^{99m}Tc beam pointed to the center of the detector (solid line) and Gaussian fit (dotted line). The energy resolution is 9.3% in the center of the detector. . . . 97

3.17 The energy resolution changes over the detector surface. The energy resolution degrades close to the edges and corners of the crystal. 98

3.18 (a) Total count rate and (b) energy windowed count rate of a decaying ^{99m}Tc source. 99

3.19 The real count rate and the measured count rate. 100

3.20 Energy spectrum at time 0h, 5h, 10h and 40h (all spectra have been scaled and include the same number of events, a log scale is used on the ordinate axis). 101

4.1 (a) A 6-pinhole SPECT collimator and (b) the same collimator with one top plate removed revealing the shielding used to separate the different projections. 104
4.2 (a) Top and side view of a knife-edge pinhole and (b) a lofthole with a square entrance and exit opening. The aperture of both collimating holes is circular. The cross section of this lofthole gradually change from a circle to a square. . . . 105
4.3 6 Pinholes and a rectangular detector (410 mm x 250 mm). (a) 6 Pinholes without overlap; 71.8% of the detector area is used. (b) 6 Pinholes using the complete detector; 32.9% overlap. (c) 6 Loftholes, the setup with the loftholes uses the whole detector and has no overlap. 106
4.4 The high-sensitive (*HiSens*), low-sensitive (*Penumbra*) and insensitive (*Umbra*) areas on the detector and in the image space. 107
4.5 Top: Schematic representation of the pinhole and its parameters. Bottom: Intersection of the pinhole aperture circle with the exit circle projected from the point source onto the aperture plane. 109
4.6 The derived sensitivity formulas can also be used for this geometry. The FOV and the sensitivity of the aperture are only limited by the exit opening and not by the entrance opening. 109
4.7 Top: Schematic representation of the lofthole and its settings. Bottom: Intersection of the lofthole aperture circle with the exit square projected from the point source onto the aperture plane. 110
4.8 A top view on the aperture plane. The reference frame used in the pinhole formulas is centered on the center of the aperture. The x-axis is aligned with the perpendicular projection of the point source *Src* on the aperture plane. . . 111
4.9 A top view on the aperture plane. The reference frame used in the lofthole formulas is centered on the center of the aperture. The axes are aligned with the sides of the exit opening for the lofthole. The coordinates of an arbitrary point source on the aperture plane are (x_{Src}, y_{Src}) at angle ϕ. 113
4.10 A side and top view of the simulated pinhole collimator. Not all simulated point source positions are displayed for clarity reasons. 115

4.11 A side and top view of the simulated lofthole collimator. The setup is identical to Fig. 4.10 except for the exit opening, the lofthole has a square exit opening. The side length of this square exit opening is equal to the diameter of the pinhole's exit opening. The point sources are located on a line that has a $45\,^{\circ}$ angle and on a line that has a $30\,^{\circ}$ angle to the square exit opening. 116

4.12 There is good agreement between the outcome of the simulations and the outcome of the corrected sensitivity formula. The red traces are the outcome of the pinhole setup, The green traces are for the first lofthole setup ($\phi = 45\,^{\circ}$) and the blue traces are for the second lofthole setup ($\phi = 30\,^{\circ}$). (a) The sensitivity calculated with the basic sensitivity formula, the simulated sensitivity and the sensitivity calculated with the corrected formula. The *Basic* traces in the graphs are based on the basic sensitivity formula (4.1); the *Sim* traces are results from simulations and the *Corr* traces are based on the corrected sensitivity formulas ((4.2), (4.3), (4.9) for the pinhole and (4.2), (4.3), (4.15) for the lofthole). (b) The deviation from the calculated sensitivity (based on corrected sensitivity formula) to the simulated sensitivity. (c) The deviation from the calculated sensitivity (based on basic sensitivity formula) to the simulated sensitivity. 117

4.13 (a) The lofthole collimator and (b) the pinhole collimators used for the measurements. 118

4.14 The setup used to measure the flood maps. A vial filled with ^{99m}Tc is positioned on top of the aperture. A clinical NaI(Tl) gamma camera was used as detector. Dimensions are in mm. 119

4.15 (a) Flood maps for the lofthole , (b) pinhole 1 and (c) pinhole 2. These maps were acquired with the setup depicted in Fig. 4.14. The flood map of pinhole 1 is the circumscribed circle of the flood map of the lofthole. The flood map of pinhole 2 is the inscribed circle of the flood map of the lofthole. . . 120

4.16 The setup used to measure penetration. This setup has a high magnification factor and allows to investigate penetration. Dimensions are in mm. 121

4.17 The four extreme rays originating from the point source (drawn to scale, according to the dimensions of Fig. 4.16). . 122

4.18 The four extreme rays have divided the irradiated detector area in two zones (drawn to scale, according to the dimensions of Fig. 4.16). 122
4.19 Pinhole projection on the detector. Profiles through the vertical, horizontal and diagonal lines are shown in Fig. 4.20. . 123
4.20 (a) A vertical, (b) a horizontal and (c) a diagonal profile (log scale) of the pinhole projection (see Fig. 4.19). The half maximum and the tenth maximum are shown as horizontal lines in each profile graph. The lofthole has less penetration than a knife-edge pinhole that irradiates the same rectangular detector area with full coverage. The abscissa *Event Position* is the distance from the center of the projection. . 124
4.21 Examples of different possible lofthole geometries and the irradiated detector area. The 4-sided lofthole has a square projection on the detector. This geometry is well-suited for use with rectangular detectors. The pentagonal and hexagonal geometries can be useful when curved detectors are used. 126

5.1 The SPECT setup. 131
5.2 The lofthole collimator used for the flexiSPECT setup. This figure shows the exit opening of the collimator. The other side is flat and only contains the circular aperture. 131
5.3 (a) The rat-size SPECT system and (b) the mouse size SPECT system. Dimensions are in mm. The circle represents the system FOV. 132
5.4 (a) The rat-size calibration phantom and (b) the mouse-size calibration phantom. The red circles represent the holes that contain the ^{99m}Tc. Dimensions are in mm. 133
5.5 The three rotating point sources (blue) project through the aperture (green) onto the detector (red). 133
5.6 Flood source measurement (drawn to scale). 135
5.7 The projection of the flood Source on the detector. 137
5.8 Profile through the flood source projection and the corrected flood source projection on the line indicated in Fig. 5.7. . . . 138
5.9 The rat-size hot rod phantom. 138
5.10 Reconstructed rat-size hot rod phantom. 139
5.11 (a) Transverse view and (b) coronal view of the reconstructed rat-size uniform phantom 140
5.12 Profile view at the line indicated in Fig. 5.11(a). 140
5.13 The mouse-size hot rod phantom. 142

5.14 Reconstructed mouse-size hot rod phantom. 143

5.15 (a) Transverse and (b) coronal view of the reconstructed mouse-size uniform phantom. 144

5.16 Profile view at the line indicated in Fig. 5.15(a). 144

6.1 The NaI(Tl) and LYSO scintillators (drawn to scale, dimensions are in mm). The light guide cannot easily be omitted because NaI(Tl) is hygroscopic and hermetic sealing is required. 150

6.2 The beam source used for detector calibration and resolution measurements (dimensions are in mm). The capillary tube is filled with approximately 370 MBq ^{99m}Tc at the start of the calibration. 151

6.3 A histogram of the charge of a PSPMT channel for a measurement grid position. The histogram is fit with a Gaussian function. 152

6.4 The mean value of a PSPMT anode. The measured and interpolated values are shown. 153

6.5 The processing steps performed for each detected event. Each event has to be accepted by a coarse energy window before it is positioned. Afterwards a fine energy window and a distance threshold are applied. 154

6.6 The mean light spread of events interacting in the center of the scintillator (measured on an 8x8 channel H8500 PSPMT). (a) The NaI(Tl) measurement and (b) the LYSO measurement. 157

6.7 The energy resolution measured with the beam source positioned on a Cartesian grid. (a) The NaI(Tl) measurement and (b) the LYSO measurement. 158

6.8 The energy spectrum measured with a beam source pointing to the center of the detector (NaI(Tl)). 158

6.9 The energy spectrum measured with a beam source pointing to the center of the detector (LYSO). Note the X-ray escape peak at 86 KeV; this peak is caused by $K\alpha_1$ X-ray escape of lutetium. The high-energy tail in the LYSO spectrum is caused by the LYSO intrinsic radioactivity. 159

6.10 This LYSO background image was obtained during a 531 min acquisition without external activity. Image (a) shows the positioned intrinsic activity when no distance thresholding is used. Image (b) is obtained by using distance thresholding. The use of distance thresholding results in a lower LYSO background (7.4% less, see table 6.4) and in a more uniform background image. The intrinsic count rate is low (0.024 cps/mm^3, see table 6.4). 161
6.11 The decay scheme of ^{176}Lu 162
6.12 Result of the beam source measurement on (a) the NaI(Tl) detector and (b) the LYSO detector. The grid spacing is 5.5 mm. Profiles on the dotted lines are depicted in Fig. 6.13 . 163
6.13 (a) Horizontal and (b) vertical profile view of the beam source measurement on the NaI(Tl) detector. The FWHM of the central beam position is 1.18 mm. (c) Horizontal and (d) vertical profile view of the beam source measurement on the LYSO detector. The FWHM of the central beam position is 750 μm. The pixel size is 250 μm. 164
6.14 The resolution collimator is a 2 mm thick tungsten plate and contains groups of parallel holes of different diameters. . . . 165
6.15 The setup used to obtain a projection of the resolution collimator (not drawn to scale) 166
6.16 The image acquired using the resolution collimator on (a) the NaI(Tl) detector and (b) the LYSO detector (only the detector area uncovered by the collimator holes is shown). The 0.8 mm holes can be resolved on the NaI(Tl) detector, the 0.6 mm holes can be resolved on the LYSO detector. . . 167
6.17 The LYSO background image, processed with (a) COG, (b) MNN and (c) MLE event positioning. No distance thresholding or likelihood thresholding has been used. 168

7.1 The first-generation collimator (CAD rendering). (a) The top side of the collimator. The top of the plate contains 20 apertures, the loftholes do not have an entrance opening. (b) The bottom side of the collimator. This view depicts the exit openings of the loftholes. (c) A side view of the collimator. (d) A profile view shows the sharp edges between the different loftholes. 173
7.2 (a) A CAD rendering of the second-generation collimator and (b) a profile view. 174

7.3 Illustration of the production process: (a) laser source, (b) scanner system, (c) collimator, (d,f) powder delivery system, (e) object piston and (g) powder. 175
7.4 Bottom view of the produced first-generation multi-lofthole collimator (16 mm thick and 70 mm x 52 mm transverse size) 176
7.5 The manufactured second-generation collimator 176
7.6 Some details of the second-generation collimator. (a) A microscopic view of the entrance openings and apertures. (b) The resolution of the manufacturing process allows for fine details such as text. 179
7.7 The setup used to measure attenuation. Three sample plates were made (250 μm, 500 μm and 750 μm thick). The detected events were energy and position filtered to obtain a narrow beam measurement that excludes scatter. 179
7.8 (a)(b)(c) Transmission scan of the three plates (GE eXplore Locus SP micro-CT). (d)(e)(f) Profiles of the transmission images on the dashed lines, the profiles show the uniform attenuation of the plates. 181
7.9 The deviation between the first-generation collimator and the CAD design (positive deviations in red, negative deviations in blue). The top figure shows the bottom side of the collimator; this is the surface that contains the exit opening of the loftholes. The bottom figure shows the top side of the collimator, this surface contains the apertures. The used measurement technique did not allow us to measure the apertures, the deepest parts of the loftholes and the sharp edges that separate the different loftholes. 183
7.10 A magnified view of the collimator depicting the largest deviations. The biggest deviations are found in the same lofthole. 184
7.11 A histogram of the deviations across the whole collimator (unit is mm) 184
7.12 A microscopic image of the aperture at row 1, column 1 (first-generation collimator). 185
7.13 The setup used to measure sensitivity. A small point source was positioned in front of the center of the collimator. The point source was moved from a height of 5 mm to a height of 34 mm above the aperture plane. This was done in steps of 1 mm. 186

7.14 Measurement of a point source at a height of 34 mm above the aperture plane, the point source is seen by all the apertures. 187

7.15 Measured and expected number of counts. The expected number of counts was calculated using the ideal pinhole diameters (500 μm) and using the measured pinhole diameters (see table 7.5). 187

7.16 The deviation between the second-generation collimator and its CAD design (positive deviations in red, negative deviations in blue). The top figure shows the top side of the collimator; this is the surface that contains the entrance opening of the loftholes. The bottom figure shows the bottom side of the collimator, this surface contains the exit openings. . . 190

7.17 A microscopic view of the entrance openings and apertures of the second-generation collimator 191

7.18 (a) A casted lead parallel hole collimator and (b) a tungsten parallel hole collimator made by additive manufacturing. The tungsten collimator allows the usage of smaller holes and thinner septa. The tungsten collimator has a hole size of 525 μm and the septal thickness is 150 μm, the hole length is 25 mm. 192

8.1 The design procedure for cylindrical SPECT geometries . . . 196

8.2 The optimal sensitivity for different values of detector distance L and pinhole distance l. The optimal system is the system that has the largest optimal sensitivity and is marked by a red asterisk in this scatter plot. 197

8.3 A CAD rendering of the system 198

8.4 A cross-sectional view of a gamma camera (section made in a plane that is perpendicular to the aperture plane and that intersects with the apertures of lofthole row 3). 198

8.5 The collimator subdivides the detector in 20 sub-detectors. (a) The gamma camera, (b) the gamma camera with a cross-sectional view of the collimator at a height of 5 mm above the scintillator plane and (c) the gamma camera with a cross-sectional view of the collimator at a height of 1 mm above the scintillator plane. Each collimator consists of 20 loftholes and irradiates the central 48 mm x 48 mm of a detector. . . 199

8.6 The prototype system consists of one detector and one second-generation collimator. A rotation stage is used to rotate phantoms. 200

8.7 A cross-section of the gamma camera. The path of two possible gamma-rays is drawn in black; these gamma-rays illustrate that there is a small amount of overlap due to the non-zero DOI. 202

8.8 The different calibration steps that are done before the calculation of the system matrix. The calculations are based on the acquisition of a flood map of each lofthole and on point source measurements. 202

8.9 The setup used to measure the flood maps. The flood source and the tungsten alloy plate with the 5 mm diameter hole are attached to a robotic stage. By doing so, we can sequentially irradiate the lofthole apertures. 204

8.10 (a) A flood image of a lofthole and (b) the median filtered flood image 204

8.11 (a) A flood image of a lofthole, (b) the column sum and (c) the row sum. The sub-detector borders are marked with red lines in (a) and with green circles in (b) and (c). 205

8.12 The sum of all the median filtered flood images reveals the overlap under the lofthole edges. The rectangles represent the derived sub-detector delineation. 206

8.13 A small point source is fixed to a robotic stage and positioned in the system FOV. 207

8.14 The point source is moved to several positions in the system FOV. These positions are marked with blue dots in the drawing, the front of the collimator is marked with a red rectangle ((a) side view and (b) top view). 208

8.15 (a) The PSF acquired when the point source is in the center of the measurement grid (253.8 mm, 138.5 mm, 73.5 mm). (b) The detector mask used for geometric calibration. 209

8.16 The detector coordinate system (ξ, η) and the voxel coordinate system (x, y, z). 210

8.17 An optimization algorithm searches the geometric parameters that result in the best fit between the measured interaction position and the calculated interaction position. The result of this optimization is shown for the lofthole at row 3 an column 2 (see Fig. 7.13 for the lofthole indexing). The measured and calculated centroid positions show good agreement. 212

8.18 (a) A single-aperture collimator. A point source rotates to multiple angles (red dots) and this results in a projection on the detector (red line). We are not able to resolve the COR_{lm} because multiple circular point source paths (green circles) can be found that agree with the backprojected detector data. (b) A multi-aperture collimator. A point source rotates to multiple angles (red dots) and this results in two projections on the detector (red lines). Only one circular point source path (green circle) exists that agrees with the backprojected detector data. 216

8.19 (a) The Derenzo insert is positioned in (b) the recipient, (c) depicts the complete phantom. The recipient has an inner diameter of 24 mm; the inner diameter widens to 26 mm at a height of 6 mm, this is marked with an arrow in (b) and (c). 218

8.20 The reconstructed Derenzo phantom (acquisition for 5 angles, 1 bed position) after (a) 100 iterations, (b) 300 iterations and (c) 500 iterations. The transaxial and coronal view are depicted. 220

8.21 The reconstructed Derenzo phantom (acquisition for 50 angles, 1 bed position) after (a) 100 iterations, (b) 300 iterations and (c) 500 iterations. The transaxial and coronal view are depicted. 221

8.22 The reconstructed Derenzo phantom (acquisition for 5 angles, 10 bed positions) after (a) 100 iterations, (b) 300 iterations and (c) 500 iterations. The transaxial and coronal view are depicted. 223

8.23 The reconstructed Derenzo phantom (acquisition for 50 angles, 10 bed positions) after (a) 100 iterations, (b) 300 iterations and (c) 500 iterations. The transaxial and coronal view are depicted. 224

8.24 The reconstructed uniform phantom (acquisition for 5 angles) after (a) 100 iterations, (b) 300 iterations and (c) 500 iterations. The transaxial and coronal view are depicted. Profiles are shown in Fig. 8.25 226
8.25 Profile views of the reconstructed uniform phantom (acquisition for 5 angles, 1 bed position) depicted in Fig. 8.24 for 100, 300 and 500 iterations. 227
8.26 The reconstructed uniform phantom (acquisition for 50 angles, 1 bed position) after (a) 100 iterations, (b) 300 iterations and (c) 500 iterations. The transaxial and coronal view are depicted. Profiles are shown in Fig. 8.27. 228
8.27 Profiles of the reconstructed uniform phantom (acquisition for 50 angles, 1 bed position) depicted in Fig. 8.26 for 100, 300 and 500 iterations. 229
8.28 The reconstructed uniform phantom (acquisition for 5 angles, 10 bed positions) after (a) 100 iterations, (b) 300 iterations and (c) 500 iterations. The transaxial and coronal view are depicted. 230
8.29 Profiles of the reconstructed uniform phantom (acquisition for 5 angles, 10 bed positions) depicted in Fig. 8.28 for 100, 300 and 500 iterations. 231
8.30 The reconstructed uniform phantom (acquisition for 50 angles, 10 bed positions) after (a) 100 iterations, (b) 300 iterations and (c) 500 iterations. The transaxial and coronal view are depicted. 232
8.31 Profiles of the reconstructed uniform phantom (acquisition for 50 angles, 10 bed positions) depicted in Fig. 8.28 for 100, 300 and 500 iterations. 233

List of Tables

2.1 Radioisotopes for SPECT imaging 10
2.2 Radioisotopes for radionuclide therapy that can be imaged with SPECT 10
2.3 Collimator materials 34
2.4 Inorganic scintillators - main properties 44
2.5 Detection efficiency 46
2.6 Semiconductors for gamma-ray detection 71

3.1 Spatial resolution 96

4.1 FWHM of the profiles shown in Fig. 4.20 122
4.2 FWTM of the profiles shown in Fig. 4.20 122
4.3 Calculated sensitivity of an ideal collimator (without penetration) and measured sensitivities of the three collimators. The standard deviation of the number of detections is based on Poisson statistics. 124

5.1 Outcome of the geometric calibration (rat-size setup) 136
5.2 Geometric parameters (not calibrated) 136
5.3 Derived geometric parameters 136
5.4 Outcome of the geometric calibration (mouse-size setup) . . 141
5.5 Geometric parameters (not calibrated) 141
5.6 Derived parameters 141

6.1 A comparison of NaI(Tl) and LYSO 148
6.2 Details of the NaI(Tl) setup and the LYSO setup 150
6.3 The minimum, maximum and mean energy resolution 159
6.4 Intrinsic LYSO events 160
6.5 Spatial resolution 162
6.6 Spatial resolution 169

7.1 Dimensions of the three tungsten plates 177
7.2 Densities of the three tungsten plates 177
7.3 Expected attenuation and measured attenuation for 140 keV gamma ray photons. The expected attenuation uses the dimensions and densities from tables 7.1 and 7.2. 178
7.4 The attenuation factors of pure tungsten plates (density 19.25 g/cm^3, μ_m 1.88 cm^2/g) and pure lead plates (density 11.34 g/cm^3, μ_m 2.39 cm^2/g) for the thickness of the three plates are given for comparison. 180
7.5 Measured diameters of the pinholes. See Fig. 7.13 for the nomenclature. 182

8.1 Parameters of the simulated pentagonal system 199
8.2 Acquisitions of the Derenzo phantom 219
8.3 Acquisitions of the uniform phantom 225

List of acronyms

A

AC	Alternate Current
ADC	Analog to Digital Converter
APD	Avalanche Photodiode

C

CFOV	Central Point of the Field of View
CNC	Computer Numerical Control
COG	Center of Gravity
CT	Computed Tomography
CZT	Cadmium Zinc Telluride
CNC	Computer Numerical Control

D

DOI	Depth of Interaction
dSiPM	Digital Silicon Photomultiplier
DSSD	Double-Sided Strip Detector

E

EDM	Electric Discharge Machining
EMCCD	Electron-Multiplying Charge-Coupled Device

F

FDG	Fluorodeoxyglucose
FIFO	First In First Out
FOV	Field of View
FPGA	Field Programmable Gate Array
FWHM	Full Width at Half Maximum
FBP	Filtered Back Projection

G

GPU	Graphics Processing Unit

H

HEP	High Energy Physics
HPGe	High-purity germanium

K

k-NN	k-Nearest Neighbor

L

LVDS	Low Voltage Differential Signaling
LYSO	Lutetium Yttrium Orthosilicate

M

MDP	Methylene Diphosphonate
MRI	Magnetic Resonance Imaging
MLE	Maximum likelihood Estimation
MLEM	Maximum Likelihood Expectation Maximization
MNN	Mean Nearest-Neighbor

P

PaHo	Parallel Hole
PCB	Printed Circuit Board
PDE	Photon Detection Efficiency
PE	Photoelectric
PET	Positron Emission Tomography
PMMA	Polymethyl Methacrylate
PMT	Photomultiplier Tube
PSPMT	Position Sensitive Photomultiplier Tube
PSF	Point spread function

Q

QE	Quantum Efficiency

S

SBA	Super Bialkali
SiPM	Silicon Photmultiplier
SLM	Selective Laser Melting
SPECT	Singe Photon Emission Computed Tomography
SDD	Silicon Drift Detector

T

TOF	Time of Flight
TOF-PET	Time of Flight Positron Emission Tomography

U

US	Ultrasound imaging

W

WEDM	Wire Electric Discharge Machining

English summary

Nederlandstalige samenvatting

English summary

Single photon emission computed tomography (SPECT) is a medical imaging modality that visualizes the 3D distribution of a radio-active labeled compound (the tracer) in the body. The composition of the tracer is chosen such that it takes part in a certain physiological process (e.g. ^{99m}Tc-MAA tracer for blood perfusion, ^{99m}Tc-MDP tracer for osteogenesis). The SPECT camera detects a fraction of the gamma radiation that is emitted by the tracer and uses the acquired data to generate projection images. These projection images are then used by the image reconstruction algorithm to derive a 3D image of the tracer distribution.

By imaging the tracer, SPECT provides images of functional processes in the body. Functional imaging leads for example to an early detection of certain diseases because disease symptoms can be visualized before an anatomical change has taken place.

The main components of the SPECT camera are the collimator and the detector. The collimator is a slab of a dense material (mostly lead or tungsten) with one or more holes in it. An ideal collimator only allows gamma photons to reach the detector if their path passes through a collimator hole; photons whose path intersects with collimator material are absorbed. The detector outputs a detection coordinate for each detected gamma photon. The combination of detection coordinate and knowledge of the collimator's hole positions allows us to estimate the path of the detected gamma photons.

Several types of collimators and detectors exist. The most used ones are the parallel hole collimator (frequently used for the imaging of humans) and the multi-pinhole collimator (often used for the imaging of mice and rats). These collimators are typically used in combination with a NaI(Tl)/PMT-based scintillation detector. An overview of different collimators and detectors and an introduction to iterative image reconstruction are given in the second chapter of this dissertation.

Multi-pinhole collimators are frequently used for small-animal SPECT systems. Such a collimator provides a high sensitivity and a high resolution close to the pinhole. In most cases, the pinhole collimator employs magnification to overcome a mediocre detector resolution. The drawback of magnification is that it results in large systems that often require a dedicated laboratory room. In this dissertation we present SPECT detector and SPECT collimator technology that enables us to use small magnification or even minification and, as such, enables us to build compact high-performance small-animal SPECT systems.

In a first step, we have developed a high-resolution scintillation detector. This is presented in chapter 3. The detector uses, similar to typical clinical cameras, a monolithic NaI(Tl) scintillator. A position sensitive photomultiplier tube (PSPMT) is used to measure the light spread that is generated when a gamma photon interacts in the scintillator. Dedicated electronics have been developed that digitize all PSPMT channels and transmit all the data to a computer. A GPU accelerated maximum likelihood (MLE) event positioning algorithm is then used to estimate the position of interaction in the scintillator. Mainly due to the PSPMT and the MLE algorithm, this detector has a spatial resolution that is more than twice as good as the resolution of a typical clinical detector.

In chapter 4 we introduce a new pinhole geometry called the lofthole. The lofthole has, similar to the pinhole, a circular aperture but employs a shaped entrance and/or exit opening. The shapes of the entrance and exit opening are reflected in the shape of the irradiated detector area. A multi-lofthole collimator allows to use the detector area more efficiently than a multi-pinhole collimator. One can for instance use a square entrance and exit opening, such a lofthole has a square irradiation area on the detector, the tiling of a multi-lofthole collimator's square projections results in a larger fill fraction than the tiling of a multi-pinhole collimator's circular projections.

In chapter 4 we present sensitivity formulas for pinholes and loftholes that take the penumbra and umbra regions of the collimator into account. Measurements on a prototype lofthole that has a square exit opening have been done. These measurements indicate that the irradiated detector area takes the same square shape as the exit opening, and, that a lofthole has less penetrating photons than a pinhole that irradiates the same square detector area.

A single lofthole collimator has been used in conjunction with our NaI(Tl) detector (chapter 3) to build a simple compact pre-clinical SPECT system (chapter 5). Maximum-likelihood expectation-maximization (MLEM) was

employed to reconstruct the images. The resolution and sensitivity of this demonstrator system are low compared to the state-of-the-art pre-clinical SPECT scanners, this is mainly due to the fact that the collimator consists of only one lofthole. To improve on this, a two-stage approach was used. In a first stage, the detector resolution was further improved; in a second stage, a new multi-lofthole collimator was developed.

In chapter 6, we try to improve our first detector's spatial resolution by using a different scintillator, the relatively thick NaI(Tl) scintillator is exchanged for a thinner LYSO scintillator. LYSO is denser than NaI(Tl) and a 2 mm thick LYSO scintillator has approximately the same detection efficiency as a 5 mm thick NaI(Tl) scintillator. The LYSO detector was evaluated and compared with the NaI(Tl) detector. Measurements prove that the LYSO detector has a better spatial resolution than the NaI(Tl) detector. This is however achieved at the expense of energy resolution.

A new multi-lofthole collimator was designed especially for the LYSO-based detector by Van Holen et al. [1]. This collimator has a complex geometry and it would have been very expensive or even impossible to produce the collimator using traditional machining techniques. We have used a new 3D-printing related technique called additive manufacturing to produce the collimator in pure tungsten (chapter 7). Collimator measurements illustrate that the density is close to solid tungsten and that the production accuracy is sufficient for the production of our multi-lofthole collimator. The major advantage of this new technique is the possibility for novel collimator geometries that could not be produced with the conventional machining techniques.

An additional compact SPECT system was built, it employs the LYSO detector in combination with the multi-lofthole collimator. The system setup, calibration and image reconstruction are presented in chapter 8. Simulations of this setup indicate that it should be possible to reconstruct (without artifacts) projection data that is acquired for five angles. According to our measurements of a Derenzo and a uniform phantom, more angles and bed positions are needed. This is probably due to inaccuracies in the system matrix. We are able to reconstruct the phantoms with few artifacts using 50 angles and 10 bed positions.

This research was performed in the MEDical Image and SIgnal Processing research group (MEDISIP). MEDISIP is a research group of the ELIS department of the faculty of engineering of the Ghent University. The work that is presented in this dissertation has resulted in 2 patent applications [2, 3], 5 A1 journal publications as first author [4–8], 3 A1 journal publications as

co-author [1, 9, 10] and 15 conference contributions [11–25].

Nederlandstalige samenvatting

Single Photon Emission Computed Tomography (SPECT) is een medische beeldvormingstechniek die de 3D-distributie van een radioactief gemerkte stof (de speurstof) in het lichaam in beeld brengt. De samenstelling van de speurstof is zodanig dat deze deelneemt aan een bepaald fysiologisch proces (bvb. ^{99m}Tc-MAA speurstof voor bloed perfusie, ^{99m}Tc-MDP speurstof voor osteogenese). De SPECT-camera detecteert een deel van de gammastraling die uitgezonden wordt door de speurstof en gebruikt deze data om projectiebeelden te genereren. Deze projectiebeelden worden gebruikt door het beeldreconstructiealgoritme om een 3D-beeld van de speurstofverdeling in het lichaam te berekenen.

Door gebruik te maken van een speurstof maakt een SPECT-scanner beelden van functionele processen in het lichaam. Functionele beeldvorming leidt tot een vroege detectie van bepaalde ziektes doordat de beeldvorming van symptomen kan gebeuren voordat er anatomische veranderingen waarneembaar zijn.

De belangrijkste componenten van een SPECT-camera zijn de collimator en de detector. De collimator is een plaat van een materiaal met hoge dichtheid (meestal wordt lood of wolfraam gebruikt) met één of meerdere gaten erin. Een ideale collimator laat enkel toe dat een gammafoton de detector bereikt indien zijn pad door een collimatorgat gaat. Indien het pad van het gammafoton collimatormateriaal kruist dan wordt het foton geabsorbeerd in de collimator. De detector geeft een interactiecoördinaat voor elke detectie. De combinatie van interactiecoördinaat en kennis van de positie van de collimatorgaten laat toe om het pad van de gedetecteerde fotonen te schatten.

Er bestaan verschillende types van collimatoren en detectoren. De meest gebruikte zijn de parallellegatencollimator (de standaard collimator voor

humane beeldvorming) en de multipinholecollimator (vaak toegepast voor beeldvorming van kleine proefdieren zoals muizen en ratten); deze collimatoren worden meestal gebruikt in combinatie met een NaI(Tl)/PMT-gebaseerde scintillatiedetector. Een overzicht van de verschillende collimatoren en detectoren en een inleiding tot iteratieve beeldreconstructie worden gegeven in het tweede hoofstuk van dit proefschrift.

Multipinholecollimatoren worden vaak ingezet voor SPECT-beeldvorming van kleine proefdieren zoals muizen en ratten. De reden hiervoor is dat een dergelijke collimator een hoge sensitiviteit en een hoge resolutie heeft dicht bij de pinhole. Deze collimator wordt doorgaans gebruikt met magnificatie, dit laat toe om een hoge systeemresolutie te behalen ondanks het gebruik van lageresolutiedetectoren. Het nadeel van magnificatie is dat het leidt tot grote systemen die vaak een eigen lokaal vereisen. In dit proefschrift stellen we SPECT-detector- en SPECT-collimatortechnologie voor die ons toelaat om beperkte magnificatie of zelfs minificatie te gebruiken en op deze manier compacte hoog-performante SPECT-systemen voor kleine proefdieren te bouwen.

Als eerste hebben we een hogeresolutiescintillatiedetector ontwikkeld (hoofdstuk 3). Deze detector gebruikt, net als de traditionele klinische detectoren, een monolithische NaI(Tl)-scintillator. Een *Position Sensitive Photomultiplier Tube* (PSPMT) wordt gebruikt om de lichtspreiding op te meten die gegenereerd wordt wanneer een gammafoton een interactie ondergaat met de scintillator. Er werd uitleeselektronica ontwikkeld die alle PSPMT-kanalen digitaliseert en deze data naar een computer doorstuurt. Een maximaal waarschijnlijkheidsalgoritme wordt dan gebruikt om de interactiepositie in de scintillator te schatten. Voornamelijk door het gebruik van een PSPMT en het maximale waarschijnlijkheid algoritme, heeft deze detector een spatiale resolutie die meer dan tweemaal hoger is dan de resolutie van een typische klinische detector.

In hoofdstuk 4 introduceren we de lofthole, een nieuwe pinholegeometrie. De lofthole heeft, net zoals de pinhole, een ronde opening maar gebruikt een niet-circulaire ingangs- en/of uitgangsopening. De vorm van deze ingangsopening en uitgangsopening wordt gereflecteerd in de vorm van de bestraalde detectoroppervlakte. Een multiloftholecollimator maakt efficiënter gebruik van de detectoroppervlakte. Men kan bijvoorbeeld een vierkante uitgangsopening gebruiken, dit resulteert dan in een vierkant bestraald detectoroppervlak. De optimale plaatsing van de verschillende vierkante projecties van een multiloftholecollimator resulteert in een groter bestraald detectoroppervlak in vergelijking met het plaatsen van de cirkelvormige pro-

jecties van een multipinholecollimator. In hoofdstuk 4 stellen we pinhole en lofthole sensitiviteitsformules voor die de penumbra en umbra zones in rekening brengen. Metingen op een prototype loftholecollimator met een vierkante uitgangsopening tonen dat het bestraald detectoroppervlak ook vierkant is en dat een lofthole minder penetrerende gammafotonen heeft dan een pinhole die dezelfde vierkante detectoroppervlakte bestraald.

Een loftholecollimator werd gebouwd en is gebruikt in combinatie met de NaI(Tl)-detector om een eenvoudig compact pre-klinisch SPECT-systeem te bouwen (hoofdstuk 5). Het iteratieve MLEM-algoritme is gebruikt voor beeldreconstructie. De resolutie en de sensitiviteit van dit systeem zijn matig in vergelijking met de performantie van recente pre-klinische SPECT-scanners, de voornaamste reden hiervoor is dat de gebruikte collimator slechts 1 lofthole bevat. Om dit te verbeteren kiezen we voor een tweeledige aanpak. In een eerste stap verbeteren we de detectorresolutie, in een tweede stap ontwikkelen we een nieuwe multiloftholecollimator.

Onze tweede detector (hoofdstuk 6) gebruikt dezelfde PSPMT en uitleeselektronica. De relatief dikke NaI(Tl)-scintillator is vervangen door een dunnere LYSO-scintillator. LYSO heeft een hogere dichtheid dan NaI(Tl) en een 2 mm dikke LYSO-scintillator heeft ongeveer dezelfde detectie-efficiëntie als een 5 mm dikke NaI(Tl)-scintillator. De performantie van de LYSO-detector is opgemeten en werd vergeleken met de NaI(Tl)-detector. De metingen tonen aan dat de LYSO-detector een beduidend betere spatiale resolutie heeft, dit gaat echter gepaard met een slechtere energieresolutie.

Van Holen et al. [1] hebben een nieuwe multiloftholecollimator ontworpen die specifiek voor de LYSO-detector is ontwikkeld. Deze collimator heeft een complexe geometrie en het zou zeer duur of zelfs onmogelijk zijn om deze te produceren met de traditionele metaalbewerkingstechnieken. Wij hebben *additive manufacturing*, een techniek die gerelateerd is aan het 3D-printen, gebruikt om de collimator in puur wolfraam te vervaardigen (hoofdstuk 7). Metingen tonen aan dat de dichtheid van het geprinte wolfraam ongeveer gelijk is aan de dichtheid van massief wolfraam en dat de productienauwkeurigheid voldoende is voor de productie van onze multiloftholecollimator. Het belangrijkste voordeel van deze nieuwe techniek is de mogelijkheid om nieuwe collimatorgeometrieën te produceren die niet kunnen gemaakt worden met de traditionele bewerkingstechnieken.

Door de LYSO-detector te combineren met de 3D-geprinte multiloftholecollimator hebben we een tweede SPECT-systeem gebouwd (hoofdstuk 8). Simulaties van dit systeem tonen aan dat het mogelijk zou moeten zijn om artefactvrije beelden te reconstrueren gebaseerd op projectiedata van

slechts 5 acquisitiehoeken en 1 axiale bedpositie. Onze metingen van een resolutiefantoom en een uniformiteitsfantoom tonen aan dat meer hoeken en axiale bedposities nodig zijn. Dit is waarschijnlijk te wijten aan afwijkingen in de systeemmatrix die gebruikt wordt voor beeldreconstructie. We zijn in staat om de fantomen met weinig artefacten te reconstrueren wanneer projectiedata opgenomen zijn voor 50 hoeken en 10 axiale bedposities.

Dit onderzoek is uitgevoerd in de *MEDical Image and SIgnal Processing* onderzoeksgroep (MEDISIP). MEDISIP is een onderzoeksgroep van de ELIS afdeling van de faculteit van de ingenieurswetenschappen en architectuur aan de Universiteit Gent. Het werk dat voorgesteld wordt in dit proefschrift heeft geresulteerd in 2 patentaanvragen [2, 3], 5 A1 publicaties als eerste auteur [4–8], 3 A1 publicaties als co-auteur [1, 9, 10] en 15 conferentiebijdrages [11–25].

Chapter 1

Introduction

1.1 Medical imaging

Medical imaging techniques are used to create images of the inside of the human body for diagnostic, interventional, therapeutic or research purposes. Diagnostic images can be essential to accurately identify a disease or disorder. Interventional imaging is employed when a medical doctor inserts instruments (e.g. a catheter with a stent) in the body of a patient. Therapeutic imaging is performed to define a treatment plan (e.g. a radiotherapy plan for a patient having cancer). Besides this, medical imaging is also frequently used for research purposes. This is done, for example, to obtain more knowledge on the functioning of the brain or to obtain a better understanding on the functioning of a drug.

Several medical imaging modalities exist and are frequently used in medical practice. The best known modalities are X-ray radiography, X-ray computed tomography (CT), magnetic resonance imaging (MRI), ultrasound (US), positron emission tomography (PET) and single photon emission computed tomography (SPECT). These modalities can be subdivided in two imaging classes: structural (or anatomical) imaging and functional imaging.

Structural imaging visualizes the anatomy of the patient. Examples of this are the imaging of the wrist using radiography (Fig. 1.1(a)), structural brain imaging using an MR scanner (Fig. 1.1(b)) and a sonograph of a fetus in the mother's womb using ultrasound (Fig. 1.1(c)). CT, MR and ultrasound are mostly used for structural imaging, and have limited functional imaging potential.

SPECT and PET are imaging modalities that are used to perform func-

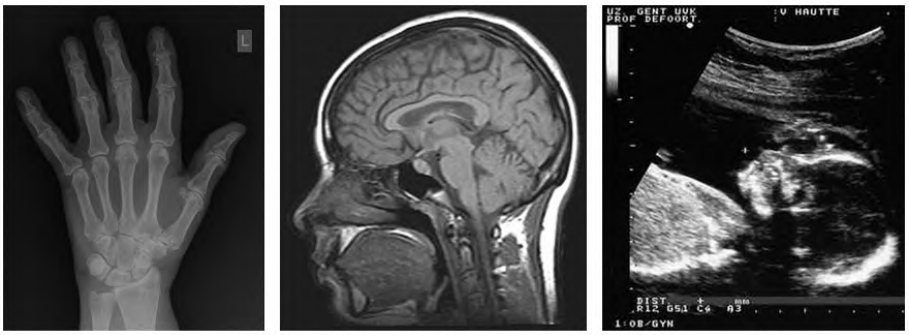

Figure 1.1: (a) A radiograph of the wrist, (b) an MRI image of the brain and (c) an ultrasound image of a fetus

tional and molecular imaging, these modalities derive the 3D distribution of a radio-active compound (the tracer) in the body. As the name suggests, functional imaging is used to image functional processes in the body. An example of functional imaging is a pulmonary perfusion scan using a ^{99m}Tc-MAA tracer; this scan images the blood supply through the lungs. Molecular imaging is functional imaging at the molecular and cellular level, it visualizes a molecular process in a human or animal body. An example is a bone scan using the ^{99m}Tc-MDP tracer, which allows imaging of areas of abnormal osteogenesis. Molecular and functional imaging lead to an early detection of certain diseases because visualization can be done before an anatomical change has taken place in the body. An example of a brain SPECT study is shown in Fig. 1.2, this example shows the cerebral perfusion.

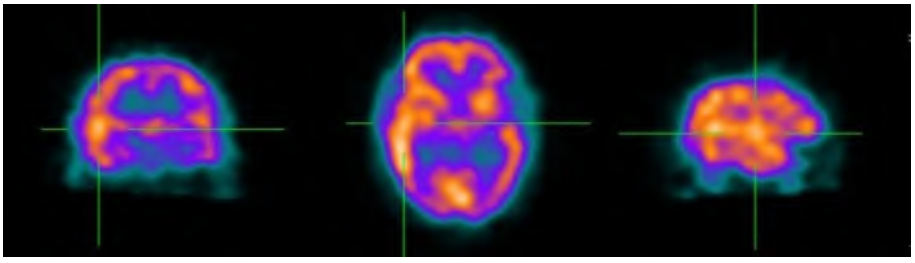

Figure 1.2: A brain SPECT study showing the cerebral blood perfusion.

More recently, multi-modality systems became commercially available.

The combination of SPECT/CT, PET/CT, PET/MR and SPECT/MR (the latter is only available in a research setting) provides fused images that show both functional (PET or SPECT) and structural (CT or MR) images. An additional advantage is that the anatomical information of the CT image or MR image can be used to derive the attenuation coefficient, which is used to correct for the attenuation of gamma-rays in the body [26, 27] in PET and SPECT.

Imaging of humans is known as clinical imaging. Besides this, small animals are often imaged for research purposes; this is known as preclinical imaging. Mostly small animals (mice and rats) are used for this purpose. Preclinical imaging is for example used for drug development, oncology research and neuroscience studies. Special high-resolution imaging systems have been developed for this purpose because of the small organs and body size associated with these animals (Fig. 1.3). Preclinical in-vivo and non-invasive imaging is important because it allows to study the change over time within the same individual (i.e. longitudinal imaging). Before the availability of these in-vivo imaging instruments, one had to sacrifice animals at different time points and study each sacrificed animal using an in-vitro technique (such as histology). To have sufficient statistical power, multiple animals were sacrificed at one point in time. New developments (e.g. PET/MR and SPECT/MR) often become available first for pre-clinical use because the size, the cost and the technical difficulties associated to the pre-clinical systems is lower than for the clinical systems.

(a) (b)

Figure 1.3: (a) The MILabs U-SPECT-II/CT is a SPECT/CT system for mice and rats. (b) The Bruker Pharmascan is an MR scanner for small animals.

1.2 Single photon emission computed tomography

This dissertation focuses on preclinical single photon emission computed tomography (SPECT) imaging. A SPECT scanner images the 3-D distribution of a radioactive tracer in the body, in-vivo. A tracer is a chemical compound in which one or more atoms have been replaced by a radioisotope; in most cases, it is administered intravenously to the patient. A small fraction of the gamma photons, emitted by the tracer, is detected by the SPECT instrument.

The two main hardware components of a SPECT scanner are the gamma-ray detector and the collimator.

The gamma-ray detector detects gamma-rays and derives the spatial coordinates and the energy of the detected events. Traditional clinical SPECT systems use a NaI(Tl) scintillation detector, detectors with an intrinsic resolution of typically 3 mm.

The collimator is made of a dense material to efficiently stop the high energy gamma photons. Lead and tungsten are frequently used, gold and platinum have been used in some prototypes. The collimator can be described as a solid plate with one or more holes. Gamma-ray photons can only reach the detector by passing through a collimator hole. The purpose of the collimator is to mechanically limit the direction of incidence of the photons to the detector. When a photon is detected on the detector, one can derive information on its origin, which is approximately positioned along a line that connects the point of detection on the detector and the center of the collimator hole. Most clinical SPECT exams are performed using a parallel hole collimator, an array of long and narrow parallel holes in a slab of lead. Due to this, only gamma-ray photons that have a perpendicular incidence can reach the detector. SPECT systems have a relatively low sensitivity due to this collimator since the majority of the gamma-ray photons are not directed towards the gamma camera or, are absorbed in the collimator material and are thus not able to reach the detector.

The collimator is typically mounted on the detector, such an assembly is called a gamma camera. In most cases, multiple planar acquisitions (or projections) are made by rotating the gamma camera around the patient. Image reconstruction derives the three dimensional tracer distribution in the patient from these projections.

The spatial resolution of a SPECT system depends on the geometrical parameters of the collimator and on the spatial resolution of the detector. Typically, high spatial resolution systems have a low sensitivity and

low spatial resolution systems have a high sensitivity, this is the so-called resolution-sensitivity trade-off. Most clinical SPECT scanners use low energy high resolution (LEHR) parallel hole collimators. In these scanners the system resolution is mainly determined by the collimator so the detector's intrinsic spatial resolution has a minor contribution to the system resolution. The relation between intrinsic detector resolution and total system resolution is more complex when multi-pinhole collimators are used. In the latter case, a high-resolution detector can lead to a significant improvement in system resolution and system sensitivity [23, 28, 29].

In this dissertation we introduce new collimator and detector technology and use this new technology to build two compact demonstrator preclinical SPECT systems.

1.3 Outline

Chapter 2 provides an introduction to the SPECT imaging technique. First, the different possible interactions of gamma photons with matter, which are relevant for SPECT are discussed. Hereafter an overview of the different collimators is given: parallel hole, pinhole, conebeam and fanbeam collimators are briefly described. The next section focuses on SPECT detectors, these can be subdivided in two classes: scintillator based detectors and semiconductor based detectors. Due to their cost-effectiveness, the scintillator based detectors are the most frequently used.

A scintillation detector is an indirect conversion detector: a gamma photon is converted in a multitude of light photons. By measuring these light photons with an array of photodetectors, one can estimate the energy of the detected gamma photon and the position of interaction. Semiconductor detectors are direct conversion detectors, here the gamma photon is converted in a multitude of electron-hole pairs. These electrons and holes are attracted by an electric field and as such induce a current. By measuring the current, one can estimate the energy and the position of the detected gamma photon. The final section of the introduction chapter handles on image reconstruction; the foundations of iterative image reconstruction are presented here.

A compact high-resolution NaI(Tl) detector has been designed and characterized; measurements on this detector are presented in chapter 3. An overview of the components (read-out electronics, PSPMT and scintillator) is given and measurements of spatial and energy resolution are presented.

Chapter 4 introduces the lofthole, a new collimator geometry. The lofthole makes optimal use of the detector area by dividing the detector in rectangular areas. An additional advantage of the lofthole is that penetration of a rectangular lofthole is lower than an equivalent knife-edge pinhole that irradiates the same rectangular detector area with full coverage.

The NaI(Tl) detector and the lofthole collimator are then used to build a compact demonstrator SPECT system. Acquisitions of a hot rod and uniform phantom have been done. The design of the system and results obtained with this system are presented in chapter 5.

In order to further improve this first SPECT system, the detector is updated to obtain a higher spatial resolution. This is accomplished by replacing the 5 mm thick NaI(Tl) scintillator with a 2 mm thick LYSO scintillator. LYSO is a dense material and the 2 mm thick LYSO scintillator has a detection efficiency that is comparable to the detection efficiency of 5 mm thick NaI(Tl). The light spread of the thin LYSO scintillator is smaller than the light spread of the thicker NaI(Tl) scintillator and results in an improved spatial resolution. The disadvantage of LYSO is its poor energy resolution. Chapter 6 described the materials and methods used and presents a performance comparison of the LYSO and NaI(Tl) based detectors.

A very good collimator material is tungsten, it has a very high density and a high stopping power for gamma ray photons. The drawback of tungsten is that it is a very hard and brittle material. Due to this, it is very challenging to manufacture collimators that have a complex geometry. In chapter 7, we introduce additive manufacturing (a 3D-printing technique) as a new method for tungsten collimator production. The major advantage of this method is the possibility to produce collimator geometries that can not be produced with the conventional techniques. We used this new technique to produce a multi-lofthole collimator that was optimized for the LYSO detector.

The multi-lofthole collimator is mounted on the LYSO detector and the resulting gamma camera is used for SPECT imaging. A Derenzo and a uniform phantom were measured using several different scan protocols. The system calibration and the reconstructed images are presented in chapter 8.

The final chapter contains a general conclusion of this dissertation.

Chapter 2

Single photon emission computed tomography

2.1 Introduction

A SPECT scanner images the distribution of a radio-active labeled compound (the tracer) in the body. SPECT uses gamma-ray emitting tracers. The energy of the emitted gamma-rays is dependent on the radioisotope used to label the tracer (an overview of the different radioisotopes used for SPECT imaging is given in section 2.2). A frequently used SPECT tracer is for example ^{99m}Tc labeled methylene diphosphonate (MDP) which is used to image bone metastases; the energy of the gamma photons emitted by ^{99m}Tc is 140 keV.

The tracer is usually injected into the bloodstream of the patient and distributes over the different body parts. After a while a the tracer distribution stabilizes and this is typically the time point when the patient undergoes the scan.

A typical clinical SPECT system is depicted in Fig. 2.1. The patient is positioned on the bed; three gamma cameras are attached to a gantry and rotate around the patient. Projections are acquired for 120 angles, meaning that the gantry rotates to 40 different angles because this is a triple-head system (see Fig. 2.2). The gamma cameras can be positioned at different radial positions. In most cases, the gamma camera is positioned radially as close as possible to the patient to obtain the optimal sensitivity and resolution.

Each gamma camera consists of a detector (see Fig. 2.3) and a parallel

Figure 2.1: An Inter Medical Prism 3000 SPECT scanner. The three gamma cameras rotate around the patient and projections are obtained at a multitude of angles.

hole collimator; this collimator ideally only allows perpendicular incident gamma photons to reach the detector (path 1 in Fig. 2.3). Photons with another angle of incidence are absorbed in the collimator material (path 2 in Fig. 2.3) or are not directed towards the gamma camera (path 3 in Fig. 2.3). Section 2.4 provides a detailed overview of the different types of collimators.

Fig. 2.3 also depicts the inside of a NaI(Tl) scintillation detector. Light photons are emitted isotropically at the interaction position when a gamma photon interacts in the scintillator. This light is measured by an array of photomultiplier tubes (PMTs): very sensitive light sensors that generate a

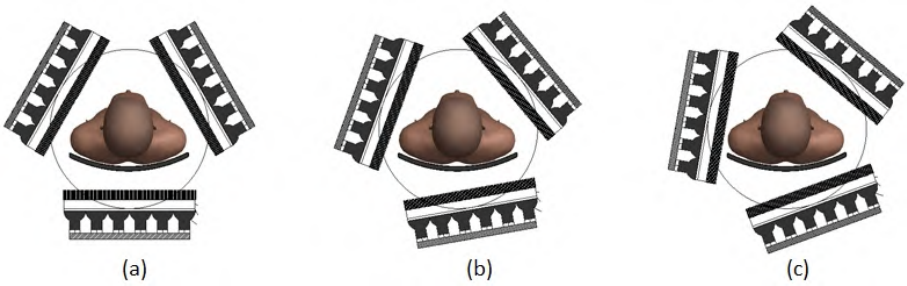

Figure 2.2: A schematic view of the system depicted in Fig. 2.1 for a gantry angle of 0° (a), 10° (b) and 20° (c). The gantry rotates from 0 to 120° for this triple-head SPECT system.

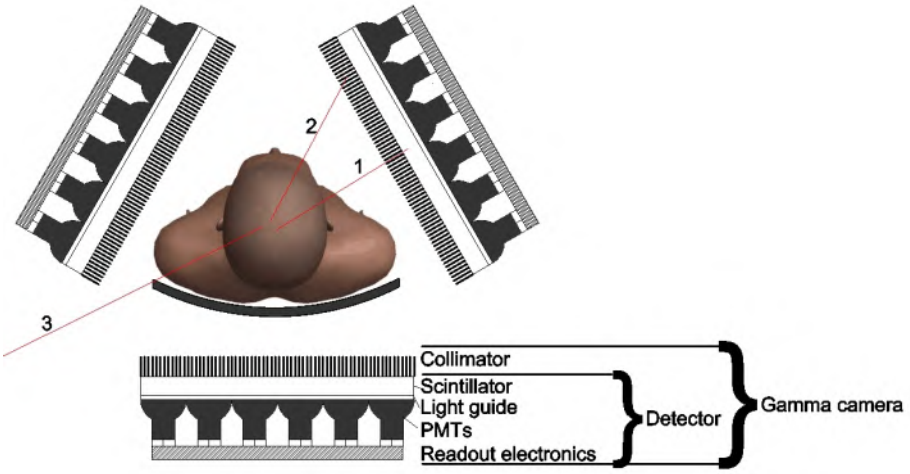

Figure 2.3: A gamma camera consists of a parallel hole collimator, a NaI(Tl) scintillator, a lightguide, PMTs and readout electronics.

current which is proportional to the amount of measured light photons per unit of time. An array of PMTs is used and, as such, the light generated in the scintillator and transmitted through the glass lightguide is measured. An overview of the different types of SPECT detectors is given in section 2.5.

The readout electronics process the PMT signals, the charge generated at the anode of a PMT is proportional to the amount of light photons detected. Based on the PMT charges, the interaction position and energy of the detected photon are estimated. An energy window is applied to remove Compton scattered photons: an event is accepted when its energy is in an energy window (e.g. a 20% window centered at 140 keV when ^{99m}Tc is used), otherwise it is rejected. The projection pixel, which has the same position as the accepted event's estimated position, is incremented.

Finally, all the projection data are sent to a computer and used by the image reconstruction software to derive the three dimensional tracer distribution in the body. Typically, for SPECT imaging the iterative maximum likelihood expectation maximization (MLEM) algorithm is used for image reconstruction. Section 2.6 focuses on iterative image reconstruction.

Table 2.1: Radioisotopes for SPECT imaging

Name	Half-life	γ-Energy	Prod.	Application example
^{99m}Tc	6.02 h	141 keV (89%)	Reactor	Bone scan
^{111}In	2.80 d	171 keV (91%) 245 keV (94%)	Cyclotron	Neuroendocrine tumor imaging
^{67}Ga	3.26 d	93 keV (39%) 185 keV (21%) 300 keV (17%) 394 keV (5%)	Cyclotron	Inflamation imaging
^{123}I	13.22 h	159 keV (83%)	Cyclotron	Thyroid imaging

2.2 Radioisotopes and tracers for SPECT

Table 2.1 lists some radioisotopes that are used for SPECT imaging. Besides this, SPECT can also be used to image the radioisotopes (see table 2.2) that are used for radionuclide therapy.

A tracer consists of a radioisotope bound to a biomolecule. The biomolecule can for example be an antibody (a protein) or a peptide [30].

^{99m}Tc is the most widely applied SPECT isotope because of its convenient 6 h half-life and because it can easily be eluted from a generator. The production of ^{99m}Tc involves several steps. In a first step, ^{99}Mo is produced by bombarding an uranium target with neutrons in a reactor. This leads to fission of the uranium and one of the isotopes that is produced during this process is ^{99}Mo. A technetium generator is then made by adsorption of $^{99}MoO_4^{2-}$ on aluminum oxide. This generator is then transported to the hospital because of the relatively long decay time of ^{99}Mo (66 h). $^{99}MoO_4^{2-}$ decays to $^{99m}TcO_4^-$ through β^- decay. Finally, $^{99m}TcO_4^-$ is extracted from the generator by drawing a saline solution through the generator.

The production of ^{99}Mo is only done at a small number of reactor facilities. This leads to a shortage of ^{99m}Tc when one of these reactors is shut

Table 2.2: Radioisotopes for radionuclide therapy that can be imaged with SPECT

Name	Half-life	β^--Energy$_{Avg}$	γ-Energy
^{177}Lu	6.65 h	134 keV (100%)	113 keV (10%), 208 keV (10%)
^{67}Cu	2.58 d	141 keV (100%)	185 keV (49%)
^{125}I	59.4 d	n/a	35 keV (7%)
^{131}I	8.03 d	182 keV (100%)	365 keV (82%)

down for maintenance. Because of this, the usage of a cyclotron has been proposed for ^{99m}Tc production [31].

Other isotopes are produced by bombarding a target material with protons in a cyclotron. An example of such an isotope is ^{111}In, which is produced by proton irradiation of a ^{112}Cd target.

2.3 SPECT physics - interactions of gamma rays

The gamma photons emitted by the tracer have to be collimated (by the collimator) and detected (by the gamma-ray detector).

Collimation is based on absorption, ideally only the gamma photons which are directed towards the gamma camera and which do not interact in the collimator can be detected. Once a gamma photon has traveled through the collimator, it still has to be detected. In order to detect a gamma photon, it needs to interact in the detector.

There are four possible types of interaction processes that can occur for gamma photons: photoelectric absorption, Compton (or incoherent) scattering, pair production and Rayleigh (or coherent) scatter. Pair production only appears when the energy of the gamma-rays exceeds 1.02 MeV (the energy of SPECT and PET isotopes is lower than or equal to 511 KeV). Photons that undergo Rayleigh scatter do not loose energy and as such they cannot be distinguished from non-scattered photons by the detector. Because Compton scatter is the dominant scattering process at typical SPECT energies and because the deflection angle of Rayleigh scatter is small [32, 33], Rayleigh scatter is in most cases ignored.

The remaining two important interaction mechanisms are briefly discussed in the following sections. Finally, attenuation of gamma rays is introduced because this is a direct consequence of these interaction processes.

2.3.1 Photoelectric absorption

A photoelectric interaction is the desired type of interaction in collimators and detectors because the photon completely disappears and deposits all of its energy at a single location.

Photoelectric absorption occurs when a photon interacts with an atom. An electron (the photoelectron) absorbs the energy of the gamma photon, a part of the absorbed energy is used to eject the electron from its shell, the residual energy contributes to the electron's kinetic energy. In this case, the

gamma photon completely disappears. The photoelectron has an energy that is given by equation 2.1; the photoelectron's energy depends on the energy of the photon (E_γ) and the binding energy of the electron (E_b).

$$E_{e^-} = E_\gamma - E_b \tag{2.1}$$

The vacant electron position in the atom is filled by capture of a free electron or by capture of electrons from other shells. This re-arrangement results, in most cases, in the emission of characteristic X-rays. Alternatively, an Auger electron can be ejected. The sum of the energies of the photo-electron and the characteristic X-rays (or Auger electron) equals the energy of the gamma photon.

The probability per unit pathlength (τ) of a photoelectric interaction increases for materials with a high atomic number (or proton number Z) and density (e.g. lead and tungsten), and for low energy gamma photons (E_γ).

Photoelectric interactions are preferred in the detector because the energy is deposited at a single location and this leads to an increase in detector resolution. Additionally, photoelectric interactions are also preferred in the patient and in the collimator because it results in less detected scattered photons.

2.3.2 Compton scatter

Compton scattering occurs when a photon interacts with an outer shell electron and when the incident photon does not completely disappear. In that case, only a part of the energy of the incident photon is transferred to the electron (the recoil electron). The energy of the emerging gamma photon (E'_γ) depends on the scatter angle θ and the energy of the incident gamma photon (E_γ) and is defined by formula 2.2. The Compton scattering effect is schematically depicted in Fig. 2.4.

$$E'_\gamma = \frac{E_\gamma}{1 + \frac{E_\gamma}{m_0 c^2}(1 - \cos\theta)} \tag{2.2}$$

Here, $m_0 c^2$ is the rest-mass energy of an electron (511 KeV) and θ is the photon scatter angle.

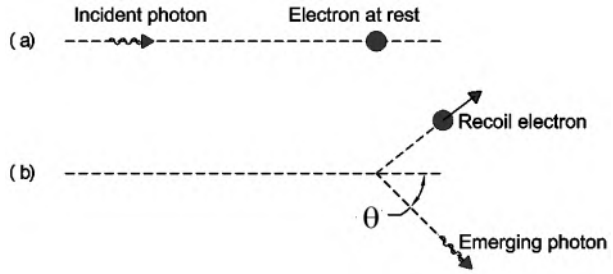

Figure 2.4: (a) The gamma photon and the electron before Compton scattering occurred. (b) The gamma photon has deflected and part of its energy has been transferred to the electron after Compton scattering.

A Compton scattered photon is not useful for SPECT imaging because it no longer carries directional information. This is the reason why a SPECT detector measures the energy of the gamma photons; a gamma photon is labeled as *scattered* when the energy is not equal to the expected photon energy of the used isotope (e.g. 140 keV for ^{99m}Tc). By doing so, the scattered events can be removed from the dataset. The energy resolution of a detector is however not perfect and due to this an energy window is used. Detected photons having an energy inside a window (e.g. a 126 to 154 keV window for ^{99m}Tc) are accepted, events outside this window are rejected.

A photon can also experience Compton scatter in the detector. The scattered photon can escape the detector material or it can experience another photoelectric or Compton interaction in the detector material. When the photon deposits its full energy in the detector in multiple interactions (e.g. a Compton interaction followed by a photoelectric interaction) then the detector is not able to correctly position the event, resulting in a degradation of spatial resolution. Additionally, the detector is not able to reject this event by energy windowing.

2.3.3 Attenuation

When a bundle of gamma rays travels through a medium, then the intensity of this bundle is attenuated. Attenuation is a direct consequence of the different possible interactions, for SPECT mainly photoelectric absorption and Compton scattering. Fig. 2.5 shows the dominant types of interaction for different energies and materials. Fig. 2.6 and fig. 2.7 depict the probability

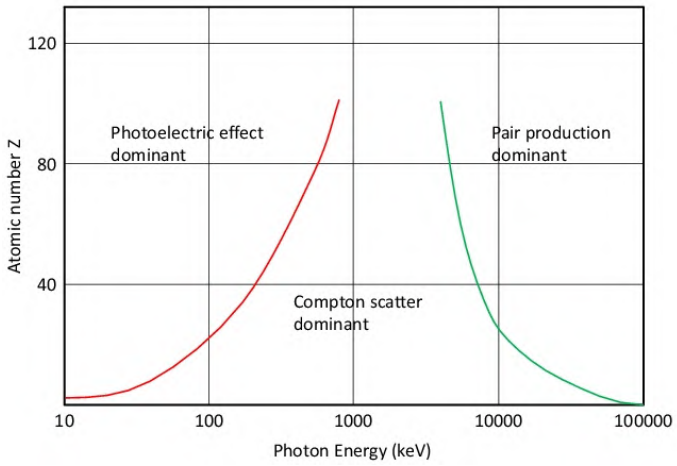

Figure 2.5: The probability of a certain type of interaction depends on the material and the energy of the gamma photon. The red curve is where photoelectric interactions and Compton scatter interactions are equally probable. Typical collimator materials are lead (Z=82) and tungsten (Z=74). The dominant type of interaction for these materials (for energies below 511 keV) is the photoelectric interaction.

of an interaction for water and for tungsten; water is shown because it is a good representative of soft tissue and tungsten because it is a frequently used collimator material.

The probability of interaction per unit pathlength of a gamma photon in a material (μ) is a combination of τ and σ, respectively the probability for photoelectric interaction and Compton scatter, and, is defined by equation 2.3. The attenuation of gamma photons in a material is exponentially related to the thickness T of the material as shown in equation 2.4; this equation is known as the *Beer-Lambert law*.

$$\mu = \tau + \sigma \tag{2.3}$$

$$I_{out} = I_{in}\ e^{-\mu T} \tag{2.4}$$

With I_{out} the intensity of the outgoing gamma ray bundle, I_{in} the intensity

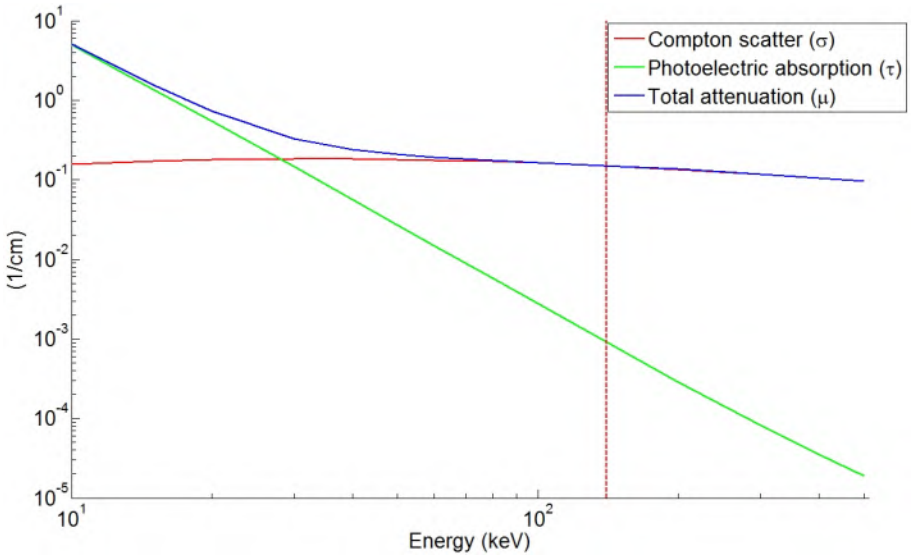

Figure 2.6: The probability of interactions in water [34]. Compton scatter dominates for energies higher than 30 keV. The vertical red dotted line marks 140 keV (^{99m}Tc).

of the incident gamma ray bundle. The constants μ, τ and σ depend on the material, the density and the energy of the gamma photons.

Fig. 2.8 shows how the total attenuation coefficient of a material with thickness T can be measured. A collimated source is used to generate a narrow beam of gamma photons. Some of these photons will undergo a photoelectric interaction in the material and will not be detected by the detector. Other photons might undergo Compton scatter; in that case they will be deflected and will thus not be detected by the small detector. Finally, some photons will not experience any interaction in the material and will probably be detected. The attenuation measurement is performed first without the plate to measure I_{in} and then with the attenuating plate to measure I_{out}, equation 2.4 can then be used to determine μ.

The attenuation for 140 keV gamma ray photons of some frequently used SPECT materials is shown in Fig. 2.9. Tungsten and lead are used to build collimators, NaI(Tl) is a material that is often employed in SPECT detectors. Finally, water is shown because a large percentage of the body is water and because it is used to fill SPECT quality control phantoms.

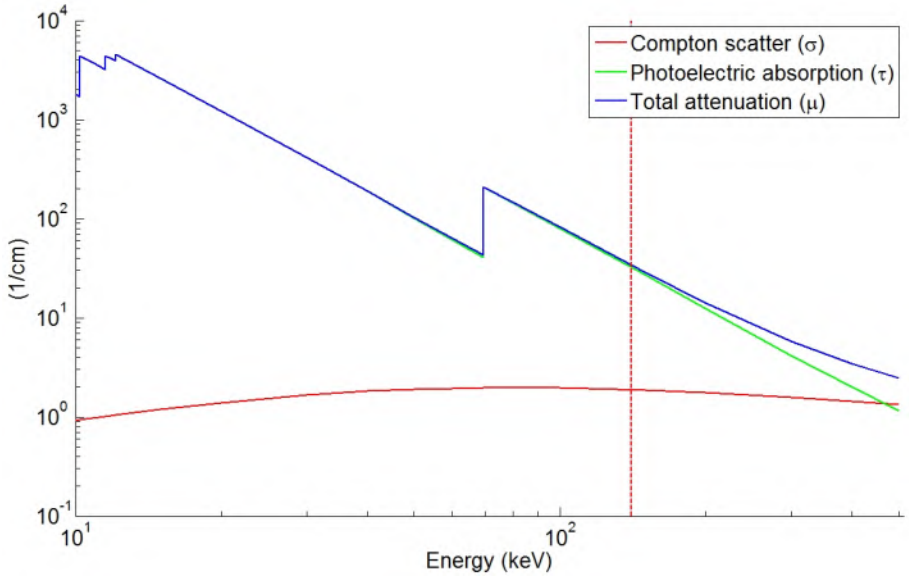

Figure 2.7: The probability of interactions in tungsten [34]. The photoelectric interaction is the dominant type of interaction and the probability for such an interaction is high, this explains why tungsten is frequently used for collimators. The vertical red dotted line marks 140 keV (^{99m}Tc).

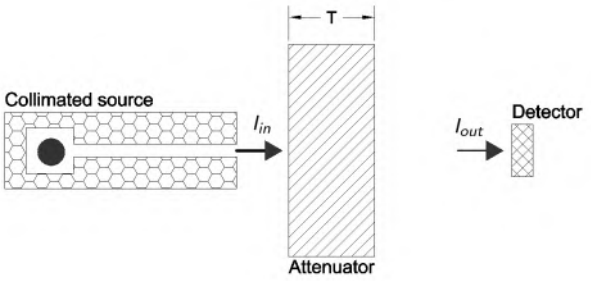

Figure 2.8: This narrow beam setup allows to measure the total attenuation coefficient (μ) of a material.

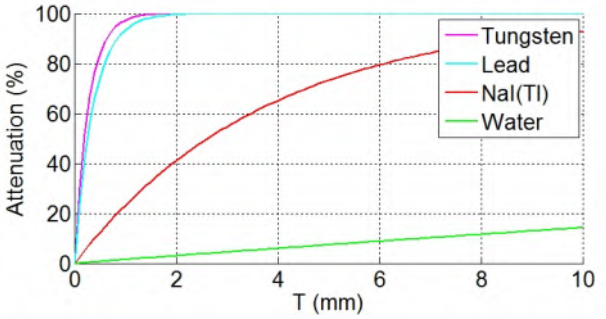

Figure 2.9: Some examples of the total attenuation of tungsten, lead, NaI(Tl) and water. Tungsten and lead are used for collimators, NaI(Tl) is used for SPECT detectors, and, a large fraction of the body is water.

2.4 Collimators

2.4.1 Introduction

It is not possible to deflect gamma-rays in a manner similar to the bending of light photons by using lenses because the index of refraction for gamma rays is almost equal to one. Due to this, SPECT imaging is based on the principle of absorption collimation [35]. With a collimator, the direction of incidence of the photons on the detector is mechanically limited. Photons that are not traveling in the collimator's allowed direction of incidence are absorbed in the collimator material (by photoelectric and Compton interactions). For this reason dense collimator materials are used to obtain a high stopping power for gamma rays (e.g. lead and tungsten). By using the information on the hole position and the coordinates on the detector, an estimate of the angle of incidence can be derived for each detected photon.

Several types of collimators exist; the choice for a certain collimator depends upon the target object size and the desired balance between resolution and sensitivity.

Fig. 2.10 depicts a gamma camera with a parallel hole collimator (a) and a gamma camera equipped with a fanbeam collimator (b). The holes of a fanbeam collimator are all focused on a line. The gamma cameras are fixed to a gantry (red circle); the green lines depict the collimator FOV. The system FOV (blue circle) can be derived by rotating the gantry (only 6 angles are shown) and is the intersection of all collimator FOVs. It is clear from the drawing that the fanbeam system has a smaller system FOV

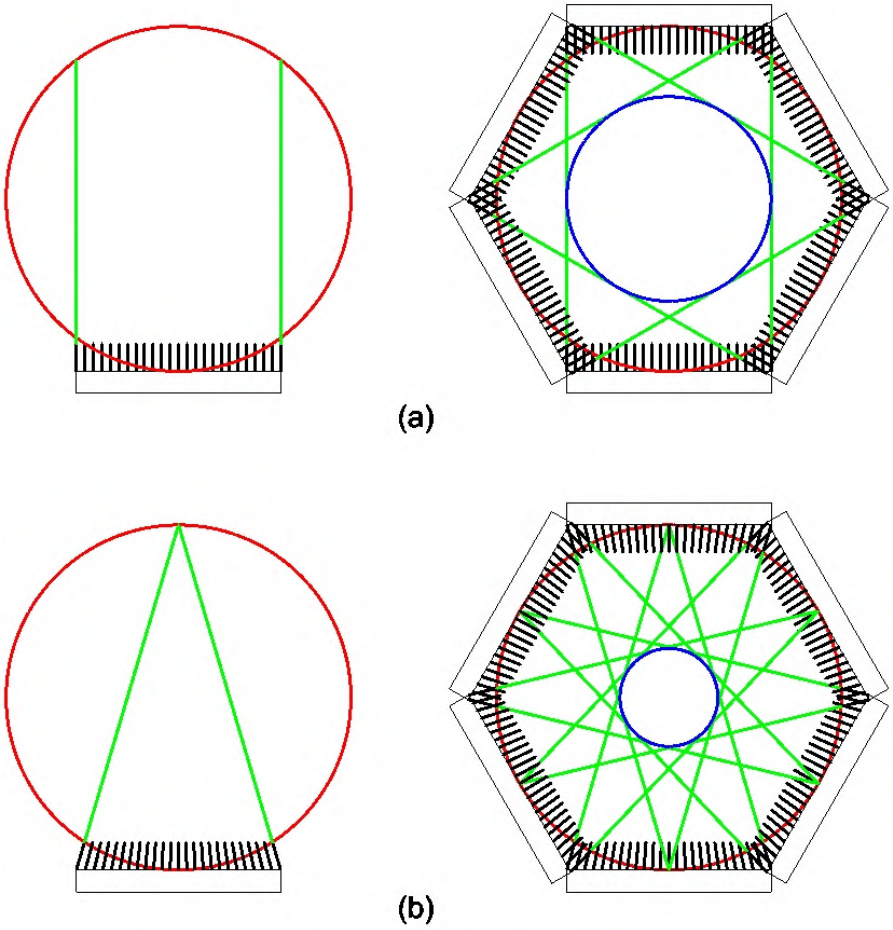

Figure 2.10: (a) A parallel hole gamma camera and (b) a fanbeam gamma camera are fixed to a gantry (red circle); the green lines depict the collimator FOV. The system FOV (blue circle) can be derived by rotating the gantry (only 6 angles are shown here) and is the intersection of all collimator FOVs.

than the parallel hole system. The target object size should be smaller than the system FOV to allow artifact-free image reconstruction. The resolution and sensitivity are key performance parameters of a SPECT system and depend heavily on the collimator geometry (parallel hole, pinhole, fanbeam or conebeam); they are discussed in the next sections.

The parallel hole collimator, the conebeam collimator and the fanbeam collimator are only briefly described. A detailed overview of the pinhole

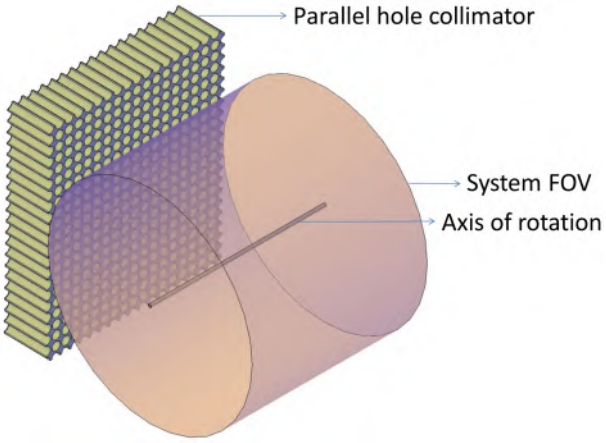

Figure 2.11: An ideal parallel hole collimator only allows perpendicularly incident gamma photons to reach the detector.

collimator is presented, this collimator is closely related to the lofthole collimator, which will be used for our SPECT systems. The first section handles on the parallel hole collimator because this collimator is the workhorse for clinical imaging.

2.4.2 The parallel hole collimator

2.4.2.1 Introduction

Fig. 2.11 shows a parallel hole collimator. Ideally such a collimator only allows gamma photons with a perpendicular angle of incidence to reach the detector.

Most clinical SPECT systems are equipped with an LEHR (low-energy, high-resolution), LEAP (low-energy, all-purpose), MEAP (medium-energy, all-purpose) and a HEAP (high-energy, all-purpose) parallel hole collimator. Each collimator has a different geometrical design (hole diameter, septal thickness, hole length, ...) and each one is dedicated to certain acquisitions (need for high energy, high resolution or high sensitivity). The low-energy collimators are used for e.g. ^{99m}Tc (140 keV) scans, the medium-energy collimators are used for e.g. ^{111}In (172 keV, 247 keV) scans and the high-energy collimators are used for e.g. ^{131}I (284 keV, 364 keV) scans. The high-energy collimators have thicker septa (collimator walls) to prevent penetration. The high-resolution and all-purpose labels give a rough indication on the chosen

balance of sensitivity versus resolution.

2.4.2.2 Sensitivity and resolution

The sensitivity of a SPECT system is an important performance parameter. A SPECT system with a low sensitivity requires long scan times to obtain an acceptable level of noise in the reconstructed images. Long scan times are problematic for the patient (a typical scan time is 20 minutes) and decrease the scanner throughput.

The sensitivity of a point source for a SPECT system (S_{Sys}) is defined as:

$$S_{Sys} = \frac{Number\ of\ detected\ gamma\ photons}{Number\ of\ emitted\ gamma\ photons}. \tag{2.5}$$

Both the collimator sensitivity (S_{Coll}) and the detector sensitivity (S_{Det}) define the SPECT system sensitivity:

$$S_{Sys} = S_{Det} \times S_{Coll}. \tag{2.6}$$

The sensitivity of an ideal parallel hole collimator is formulated as:

$$S_{PaHo} = \frac{d^2}{4\pi h_c^2}, \tag{2.7}$$

where d is the diameter of the holes and h_c is the height of the collimator holes (see Fig. 2.12).

The sensitivity increases when short, large diameter holes are used. Indeed, a wider range of incidence angles is accepted by the collimator when the holes are shorter and have a larger diameter. One would expect that the sensitivity would, due to the smaller solid angle formed by the collimator hole, drop when the source is positioned further away from the collimator. This is not the case and is due to the fact that more collimator holes *see* the source when h increases.

The resolution of a SPECT system is another key performance parameter. A high resolution system allows for the visualization of fine structures. The parallel hole collimator resolution is formulated as:

$$R_{PaHo} = d\frac{h + h_c}{h_c}, \tag{2.8}$$

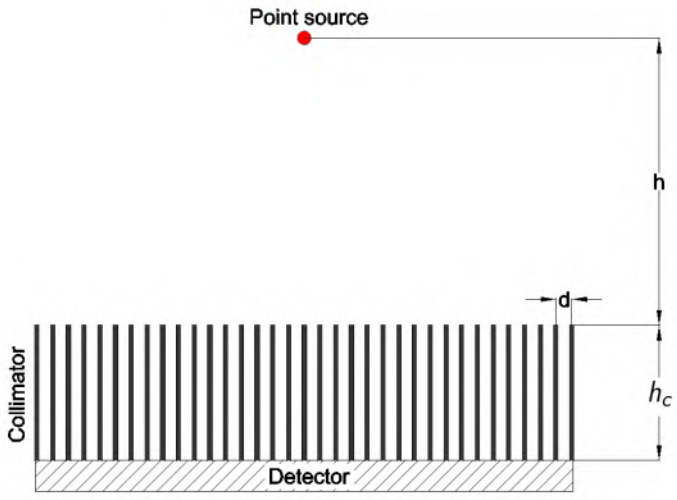

Figure 2.12: Illustration of the symbols used for the resolution and sensitivity formulas of the parallel hole collimator.

where h is the height of the source above the collimator. The resolution becomes worse when short and/or large diameter holes are used because the acceptance angle of such a collimator is larger, which results in more uncertainty on the origin of the gamma photon. Resolution also degrades at larger source-collimator distances. Both effects are visualized in Fig. 2.13.

The SPECT system resolution, when a parallel hole collimator is used, is defined by:

$$R_{Sys} = \sqrt{R_{PaHo}^2 + R_i^2}, \tag{2.9}$$

where R_i is the intrinsic spatial resolution of the detector.

2.4.3 The pinhole collimator

2.4.3.1 Introduction

A pinhole collimator is a collimator that consists of a single hole through which gamma photons can reach the detector (see fig. 2.14). The collimator hole is depicted in fig. 2.15 and has an hourglass shape. The aperture is located at the pinhole's smallest cross section; the sharp edge at the aperture is known as the knife-edge of the pinhole. The entrance opening is the

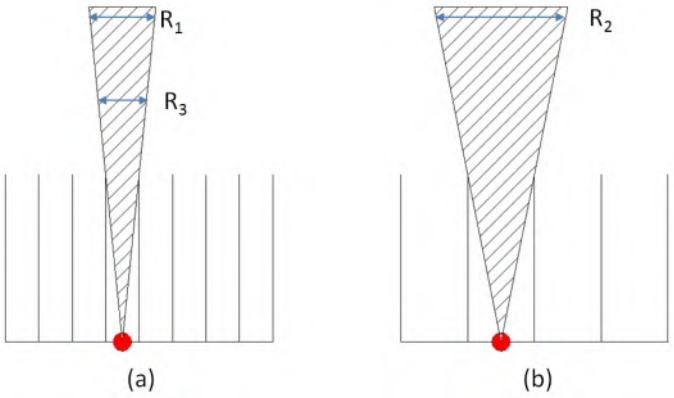

Figure 2.13: (a) A high resolution parallel hole collimator and (b) a low resolution collimator with larger diameter holes. The acceptance angle (hatched area) of the low resolution collimator is larger, which results in more uncertainty on the origin of the gamma photon ($R_1 < R_2$). Additionally, the resolution degrades at larger collimator-source distance ($R_1 > R_3$).

hole opening oriented towards the patient, the exit opening is the opening oriented towards the detector. The entrance opening in combination with the aperture and exit opening define the opening angle (or acceptance angle) of the pinhole, and as such, defines the collimator FOV.

The pinhole collimator is merely used for the imaging of small animals (e.g. rats and mice) and small organs (e.g. thyroid imaging). This is due to the fact that sensitivity and resolution of a pinhole collimator increase close to the pinhole's aperture.

This collimator scales an object on the detector (see Fig. 2.16). Magnification can be used to overcome a mediocre detector resolution (see section 2.4.3.3). Minification can be used to improve the sensitivity of multi-pinhole SPECT systems when high-resolution detectors are used [1, 28, 29].

2.4.3.2 Sensitivity

The derivation of the sensitivity of the pinhole collimator for a point source is basically a solid angle calculation:

$$S_{Pin} = \frac{A_{aperture}}{A_{sphere}}. \tag{2.10}$$

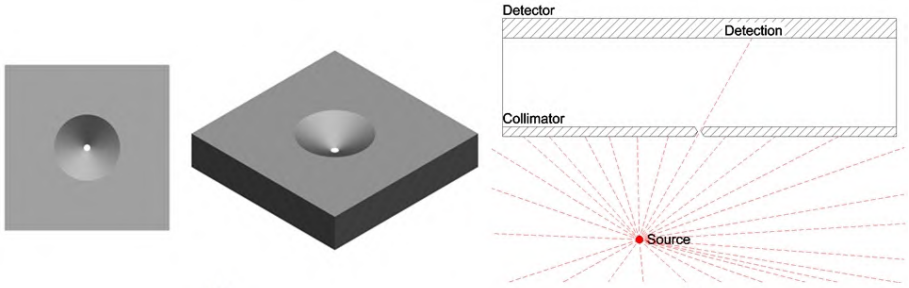

Figure 2.14: (a) Top and side view of a pinhole collimator. (b) Ideally, only the gamma rays that pass through the pinhole's aperture reach the detector. The other gamma rays are absorbed in the collimator material.

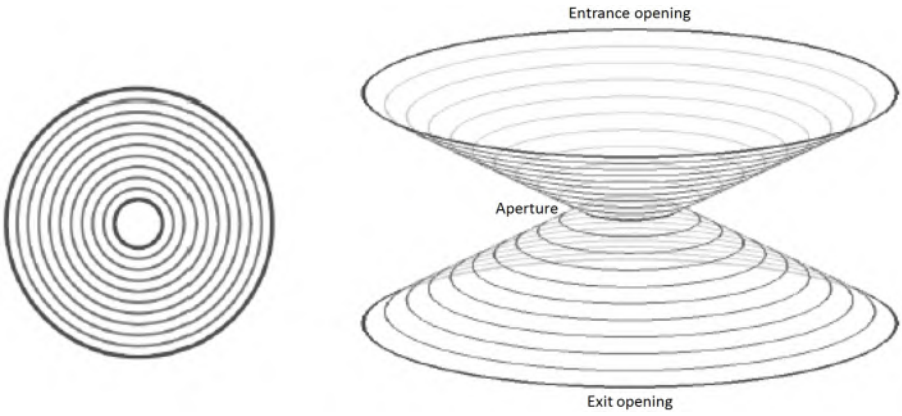

Figure 2.15: Top and side view of a the shape of a pinhole. The exit opening is oriented towards the detector, the entrance opening is oriented towards the subject.

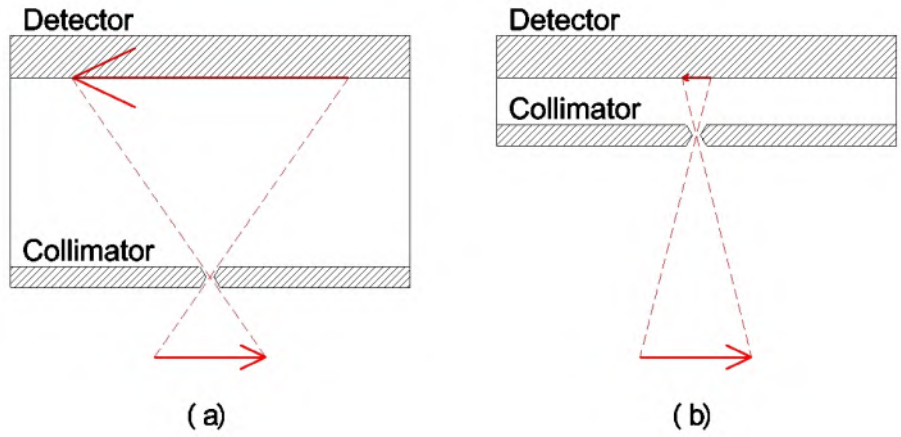

Figure 2.16: Pinholes scale the object on the detector. (a) Magnification and (b) minification.

Here $A_{aperture}$ is the area of the aperture as seen by the point source, a section through this area is marked by the blue solid line in Fig. 2.17. A_{sphere} is the area of the sphere with as center the point source and a radius equal to the source-aperture distance. A section through this sphere is marked as the red dotted line in Fig. 2.17. These areas can be approximated by:

$$A_{aperture} = \frac{\pi d^2 \sin\theta}{4} \tag{2.11}$$

and

$$A_{sphere} = \frac{4\pi h^2}{\sin^2\theta}. \tag{2.12}$$

See Fig. 2.17 for the symbols. Formula 2.10 can now be simplified and this results in the final sensitivity formula:

$$S_{Pin} = \frac{d^2 \sin^3\theta}{16h^2}. \tag{2.13}$$

Formula 2.13 illustrates that the sensitivity drops quadratically with the perpendicular distance from aperture to the point source. The sensitivity of the pinhole becomes very high close to the pinhole. This formula is an approximation and is valid for sources that are positioned *far* from the

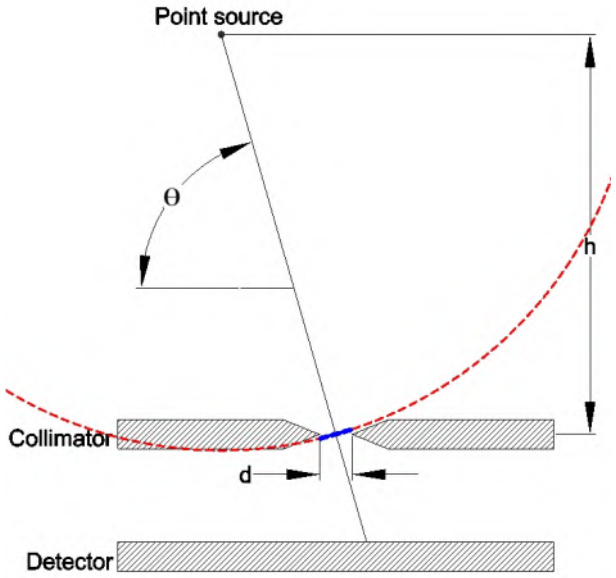

Figure 2.17: The sensitivity of a pinhole collimator depends on d (the aperture diameter), θ (the angle of incidence) and h (the height of the source above the aperture plane)

aperture; as a rule of thumb one can state that the formula is a good approximation when $h > 2d$.

2.4.3.3 Resolution

The resolution of a SPECT system (R_{Sys}), when a pinhole collimator is used, is determined by the collimator resolution (R_{Coll}) and the intrinsic detector resolution (R_i). The relation between them depends upon the magnification factor (m), which is defined as

$$m = f/h \tag{2.14}$$

for a pinhole collimator, where f is the detector-collimator distance (see Fig. 2.18).

$$R_{Sys} = \sqrt{R_{Pin}^2 + (R_i/m)^2}. \tag{2.15}$$

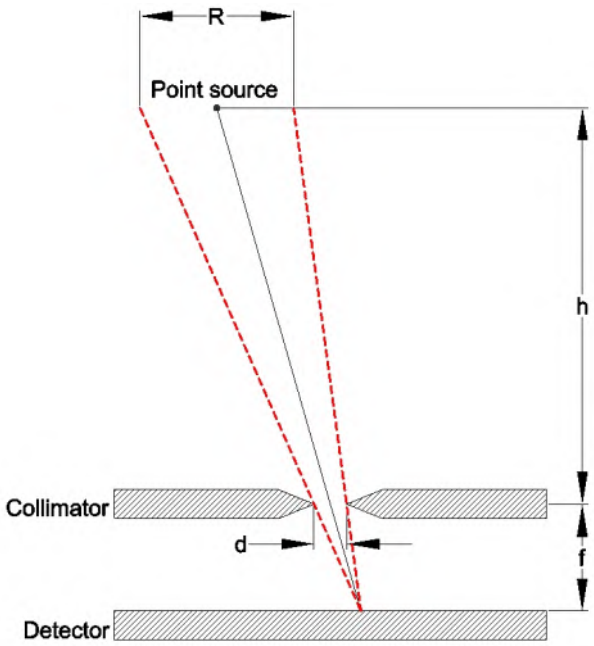

Figure 2.18: The resolution of the pinhole collimator (R_{Coll}) depends on d (aperture diameter), f (the detector-collimator distance) and h (the height of the source above the collimator).

Formula 2.15 explains how the magnification can be used to overcome a mediocre detector resolution by positioning the detector far away from the collimator. The FOV becomes smaller (for equal detector area) but the resolution R_{Sys} improves by using a larger magnification.

The collimator resolution at a distance h can be derived by analyzing the width of the FOV at that distance for a single point on the detector [36]; this is shown graphically in Fig. 2.18.

By making use of congruent triangles we can formulate the collimator resolution as

$$R_{Pin} = \frac{d(h+f)}{f}. \tag{2.16}$$

Note that the resolution is independent of the angle of incidence.

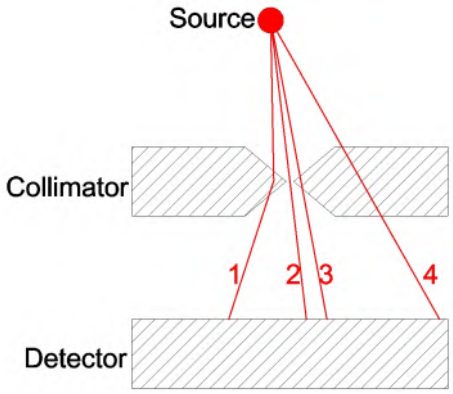

Figure 2.19: Ideally only the gamma rays passing through the aperture can reach the detector (e.g. path 2). In reality, also other paths are possible (e.g. paths 1,3,4).

2.4.3.4 Resolution-sensitivity trade-off

By combining formulas 2.13 and 2.16, and eliminating d we achieve a relation between resolution and sensitivity:

$$S_{Pin} = R_{Pin}^2 \times \frac{f^2 \sin^3 \theta}{16(h+f)^2 h^2}. \tag{2.17}$$

This illustrates the resolution-sensitivity trade-off for pinhole collimators: a high resolution collimator (R_{Pin} small) is a collimator with a low sensitivity (S_{Pin} small).

2.4.3.5 Non-ideal pinholes

Ideally only the gamma rays passing through the aperture can reach the detector (e.g. path 2 in Fig. 2.19). These rays are classified as geometrical photons. In reality, also other paths are possible (paths 1,3,4 in Fig. 2.19). Path 1 is a gamma photon that undergoes Compton scatter in the knife-edge of the pinhole; this photon loses energy due to this interaction and the detector rejects this photon if its energy is not in the energy window. Some photons will travel through the collimator material without interacting, this effect is known as penetration. This will mainly happen in the knife-edge of the pinhole, where the collimator wall is thin (path 3). The probability

that penetration occurs through the thicker pinhole plate (path 4) is much lower.

Sensitivity and resolution formulas have been developed for knife-edge pinholes that include the effect of photon penetration [37–40].

2.4.3.6 Other pinhole geometries

Imaging of high-energy isotopes is problematic with knife-edge pinholes due to the high amount of penetration in the knife-edge of the pinhole. For this reason, other pinhole geometries besides the knife-edge pinhole (Fig. 2.20(a)) have been developed.

A keel-edge pinhole [41] has a channeled aperture and has a higher attenuation near the aperture to prevent penetrating gamma photons (see Fig. 2.20(b)). However, a drawback of the keel-edge pinhole is that the sensitivity is lower than for a knife-edge pinhole with the same aperture diameter. Goorden et al. [42] used clustered pinholes to image the high energy (511 keV) gamma photons of a PET tracer (see Fig. 2.20(c)). A cluster consists of four knife-edge pinholes that each have a smaller opening angle than an equivalent knife-edge pinhole; therefore the amount of penetration is lower.

Others have proposed a square pinhole with a square aperture, square entrance opening and square exit opening. Such pinholes have anisotropic resolution. The choice for square pinholes was made for ease of machining [43, 44], to optimize the used detector area and to increase detection efficiency of an X-ray fluorescence system [45] and to make a pinhole with an adjustable aperture size [46].

In chapter 4 we introduce a new pinhole geometry with a round aperture and a square entrance and exit opening. This was done to optimize the detector area and to lower the amount of penetration while preserving an isotropic resolution.

2.4.3.7 Multi-pinhole collimators

The sensitivity can be increased by making use of multiple pinholes, a multi-pinhole collimator has a sensitivity equal to:

$$S_{MPColl} = \sum_{i=1}^{n} S_i. \tag{2.18}$$

Where n defines the number of pinholes that *see* the source.

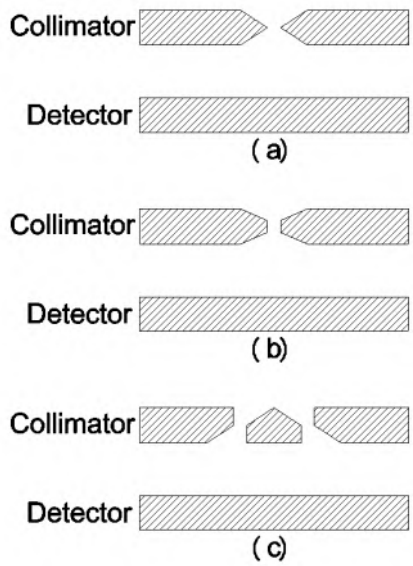

Figure 2.20: (a) a knife-edge pinhole, (b) a keel-edge pinhole and (c) a clustered pinhole. The latter two are beneficial to image higher-energy isotopes.

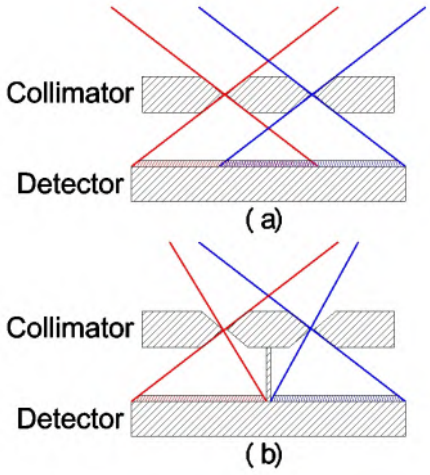

Figure 2.21: (a) A 2-pinhole SPECT collimator that has a significant amount of multiplexing and (b) the same collimator with a slat to prevent overlapping projections.

In some multi-pinhole collimator designs there is a certain amount of overlap of the projections on the detector (see Fig. 2.21) [47–49]. Those systems use multiplexing to increase the collimator sensitivity. The problem with multiplexing is that one can not define exactly what the path of the detected photon was because it can come from different pinholes; consider for example Fig. 2.21(a); a photon that was detected in the overlapping region of the detector might have gone through both pinholes. This lowers the amount of information a photon carries. Due to this, uncareful use of multiplexing can lead to image artifacts.

Quite some research has been done on multiplexing. Ideally, multiplexing could be used to significantly increase the sensitivity of a SPECT scanner with no or low additional costs. Vunckx et al. have studied multiplexing and conclude that the sensitivity gained with a multiplexing design only compensates for the decrease in information due to overlap [50]. Mok et al. found that the gains in improved detection efficiency and resolution by increased multiplexing are offset by increased image degradations [51] and that multiplexing can help for sparse objects but leads to image degradation in non-sparse objects [52]. More recently, Lin [53] and Van Audenhaege et al. [54] have defined conditions to design artifact-free multiplexing pinhole systems. The simulations of [53] indicate that, under the stated conditions, the usage of multiplexing can be exploited to increase image quality.

2.4.4 Fanbeam and conebeam collimators

2.4.4.1 Introduction

Fanbeam and conebeam collimators are converging beam collimators; these collimators use a combination of parallel hole geometry and magnification. Fig. 2.22 shows a fanbeam collimator. With such a collimator all the holes are focused on a line. The consequence is that the subject will be magnified in the trans-axial direction onto the detector. The axial direction is not magnified. Fig. 2.23 depicts a conebeam collimator. Here, all the holes are focused on a point. The subject is thus magnified (in both axial and trans-axial) direction on the detector. The magnification can, similar to the pinhole collimator, be used to overcome a mediocre detector resolution.

These collimators are used to image small organs or animals because the magnification improves the resolution, and, the focused holes provide a larger sensitivity. Fanbeam collimators are for example frequently used for imaging of the heart.

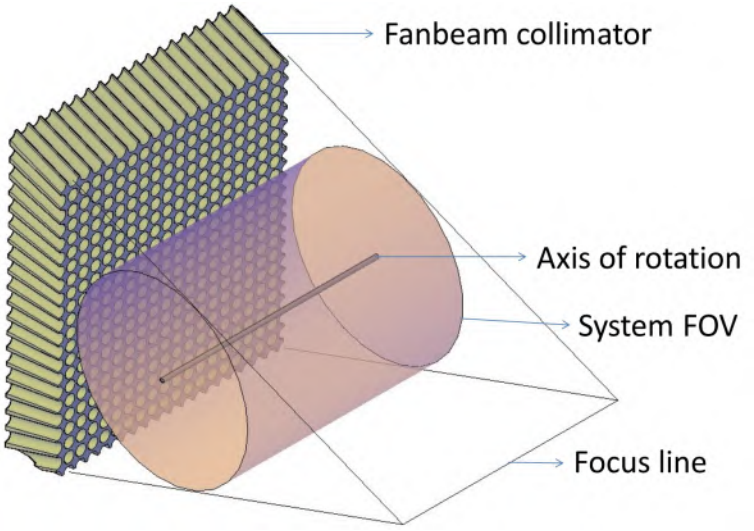

Figure 2.22: The holes of the fanbeam collimator are focused to a line.

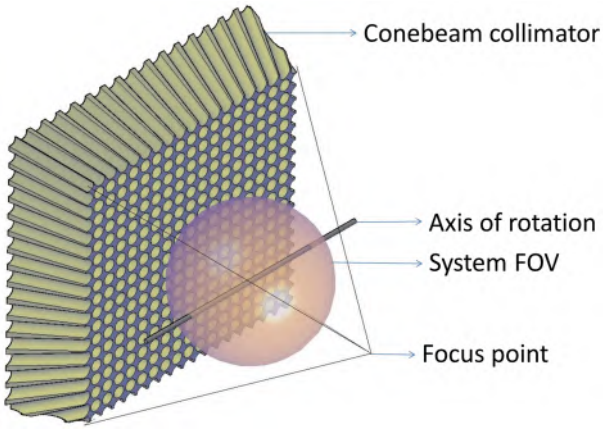

Figure 2.23: The holes of the conebeam collimator are focused to a point.

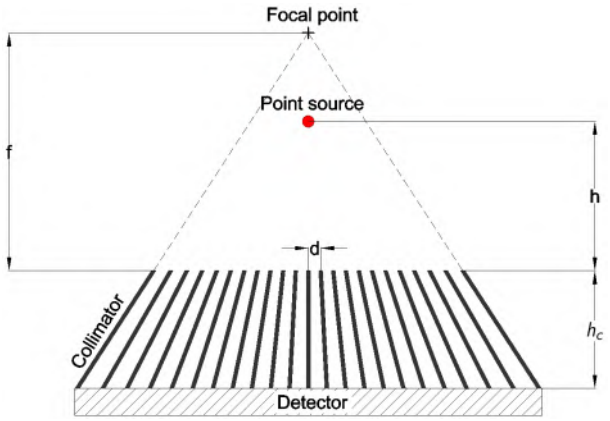

Figure 2.24: A sectional view of a conebeam or fanbeam collimator.

2.4.4.2 Sensitivity and resolution

The sensitivity of these collimators is given by:

$$S_{Conv} = \frac{d^2}{4\pi h_c^2} \left(\frac{f}{f-h} \right)^n . \tag{2.19}$$

Where n is a constant which is set to 1 for a fanbeam collimator and 2 for a conebeam collimator. The used symbols are depicted in Fig. 2.24.

The resolution of these collimators is formulated by:

$$R_{Conv} = d \left(\frac{h_c + h}{h_c} \right) \left(\frac{f}{f + h_c} \right) . \tag{2.20}$$

The magnification factor m equals to

$$m = \frac{f + h_c}{|f - h|} . \tag{2.21}$$

The system resolution is equal to:

$$R_{Sys} = \sqrt{R_{Conv}^2 + (R_i/m)^2} . \tag{2.22}$$

Note the similarity with the sensitivity and resolution of the parallel hole collimator. Indeed, in the limit case where f is infinite (as for a parallel

hole collimator), then the sensitivity formula (formula 2.19) equals the sensitivity formula of the parallel hole collimator (formula 2.7). In that case the resolution formula (formula 2.20) equals the resolution formula of the parallel hole collimator (formula 2.8). Additionally the magnification factor m becomes 1 and the system resolution (formula 2.22) simplifies to the formula used for the parallel hole collimator (formula 2.9).

2.4.5 Collimator materials and collimator production techniques

Collimators are composed of materials that have a high probability for gamma ray interactions. A high stopping power is obtained by using materials with a high number of electrons (typically in the range of $Z = 72 - 82$) and a high density (typically in the range of 9-24 g/cm^3). The choice of collimation material is determined by its attenuation, cost, required rigidity and machining complexity. An overview of some possible collimator materials is given in table 2.3.

Traditionally, parallel hole, fan beam or cone beam collimators are fabricated by sheets of lead foil, folded in half-hexagonal holes. Several stacked sheets then form a honeycomb structure. Also cast collimators based on precise molding techniques exist. The latter type of collimator is more precise and can be fabricated with a smaller septal thickness but is more expensive. These two production techniques can only be used for lead because it is a soft and flexible material and because it has a low melting point (327° C).

Pinhole and multi-pinhole collimators can, similar to parallel hole collimators, be made by casting lead in a mold. Alternatively, one can introduce pinholes (by drilling, milling or electric discharge machining) in solid plates or cylinders from high density materials. The latter techniques can be used for lead and tungsten alloys; an example of a tungsten alloy is MT-17C (table 2.3). Tungsten alloys can in some cases be preferable over lead because of their higher stopping power (see table 2.3) and their mechanical rigidity. Tungsten alloys are used because the alloys are easier to machine than pure tungsten (drills and mills have a tungsten carbide layer to improve their strength).

Lead and tungsten alloys are by far the most frequently used collimator materials. In some cases gold [55] or depleted uranium [56, 57] have been used for a small part of the collimator.

For very oblique pinholes or pinholes with a very small opening angle the current production techniques are not optimal and certain geometries are

Table 2.3: Collimator materials

Name	Pb	W	MT-17C	Au	Pt	U
Composition			90% W 6% Ni 4% Cu			
Dens. (g/cm^3)	11.34	19.25	17	19.3	21.45	19.1
Tot. att. (0.1 mm, 140 keV)	23.7%	30.4%	25.3%	34.7%	36.9%	42.8%
Tot. att. (1 mm, 140 keV)	93.3%	97.3%	94.6%	98.6%	99%	99.6%

not possible to produce. Novel production techniques like cold casting with tungsten epoxy and lost-wax casting with platinum have been described recently [58]. For the production of animal beds, phantoms and parts of the gantry, 3D additive manufacturing has also become an important tool. This technique is also used for collimator fabrication: in a first step a mould is constructed by additive manufacturing and in a second step the collimator is produced using tungsten epoxy and the mold. However, all these production processes for collimators are still indirect as an intermediate step is needed. The resulting density of tungsten epoxy is also lower than lead based collimators and, platinum is a very expensive material.

In chapter 7 we introduce a new method to produce pure tungsten collimators, based on additive manufacturing of pure tungsten powder.

2.5 Gamma-ray detectors for SPECT

2.5.1 Introduction

The two key parts of a SPECT scanner are the collimator and the detector. The collimator was discussed in section 2.4; in this section we focus on the detector.

Most of today's SPECT detectors are still based on Anger's first gamma camera [59]. Such detectors consist of a large and thick monolithic NaI(Tl) scintillator plate, coupled to an array of photomultiplier tubes (PMTs). A center of gravity algorithm is implemented in hardware to estimate the position of interaction of an event based on the lightspread measured by the PMTs.

A detector determines two coordinates (X and Y) and an energy for each

detected gamma photon. The accuracy of the event coordinates is defined by the spatial resolution of the detector (or intrinsic detector resolution R_i), the accuracy of the event energy is defined by the energy resolution of the detector.

The four main performance parameters of a gamma-ray detector are its spatial resolution, energy resolution, detection sensitivity (S_{Det}) and count rate performance. These are explained in the following sections.

Hereafter we give an overview of the different detector types. There are two main classes of detectors: scintillation detectors and semiconductor detectors. Scintillation detectors are described in depth because this type of detector is also used in this work. Scintillation detectors are indirect conversion detectors, the gamma photon is converted into light photons in the scintillator; a current is generated by the photodetector when light photons are detected. The semiconductor detectors are direct conversion detectors. Here the gamma photons are directly converted into a current when they interact with the biased semiconductor material.

2.5.1.1 Spatial resolution

The spatial resolution of a detector (or the intrinsic detector resolution R_i) has an impact on the system resolution (see formulas 2.15, 2.9 and 2.22); a better intrinsic detector resolution results in a better system resolution. However, the improvement will be small if the collimator resolution is much larger than the intrinsic detector resolution. This is the case for the standard clinical systems; a typical parallel hole collimator has a resolution of 8 mm at a height of 10 cm and the detector resolution is typically 3 mm. Consider that one is able to improve the detector resolution by 50 %, then the system resolution would drop from 8.5 mm to 8.1 mm, which has a marginal impact on the image quality of the system. The gain in system resolution would be more pronounced if the collimator was also optimized for a better resolution but this has the drawback of a lower collimator sensitivity.

Several research detectors have been produced that have a better intrinsic detector resolution than the standard detectors used for clinical systems, but, the improvement in spatial resolution is, in most cases, accompanied by a deterioration of another detector characteristic. A resolution down to 65 μm has been measured using a thin dense $Lu_2O_3(Eu)$ scintillator coupled to an electron-multiplying charge-coupled device (EMCCD) (section 2.5.2, [60]), however, this detector has a detection efficiency of only 66 % for 140 keV gamma photons and a poor energy resolution of 84 %.

2.5.1.2 Energy resolution

Energy resolution of a detector is important because it enables us to reject gamma ray photons that have undergone Compton scatter in the body, and, to perform multi-isotope SPECT studies [48].

The scattered photons are removed from the measured data because they have deflected and, as such, do not carry information on their origin.

Multi-isotope studies are investigations where two (or more) tracers are injected; this can be interesting when more than one functionality of the subject is studied simultaneously. The two tracers can be reconstructed separately if they emit gamma photons of different energies.

An energy spectrum is a histogram of the measured event energies. Fig. 2.25 shows a possible energy spectrum obtained from a ^{99m}Tc source (140 keV) measured with two different detectors. The energy resolution of a detector is defined as:

$$E_{Res} = \frac{\Delta_E}{E}. \tag{2.23}$$

The energy resolution depends on the abscissa of the photopeak E and the FWHM of the photopeak Δ_E in the energy spectrum (Fig. 2.25).

Detector 1 has a better energy resolution than detector 2 (6.7% vs. 21.2%). Scattered photons are removed from the detector data by using energy windowing; this means that events whose energy is not in a window (e.g. a 28 keV window around the photopeak) are rejected. The energy window width is related to the energy resolution of the detector, a typical energy window width equals twice the detector's energy resolution. By doing so, the windowed events of detector 1 will contain less scattered photons than the windowed events of detector 2. This illustrates the importance of energy resolution.

An estimate of the detector's energy resolution can be made by considering that the creation of a charge carrier in a detector is a Poisson process. An average of N charge carriers will have a standard deviation of $\sqrt{N}$. When there are amplifiers in the readout chain, then the mean becomes AN and the standard deviation $A\sqrt{N}$ with A being the amplification factor. The

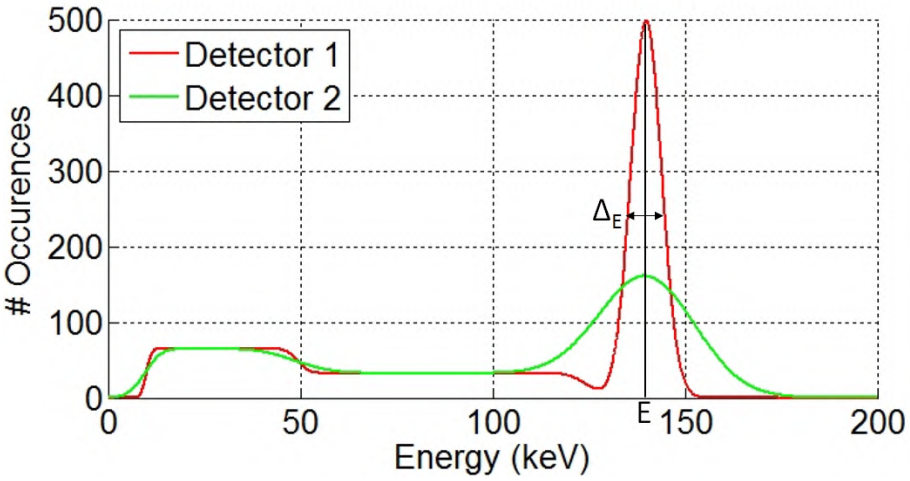

Figure 2.25: The energy spectrum of a 140 keV gamma ray source. Detector 1 (6.7%) has a better energy resolution than detector 2 (21.2%).

energy resolution can then be written as:

$$\begin{aligned} R_{Det} &= \frac{FWHM_{Photopeak}}{Photopeak} \\ &= \frac{2.35\sigma}{Photopeak} \\ &= \frac{2.35A\sqrt{N}}{AN} \\ &= 2.35/\sqrt{N}. \end{aligned} \tag{2.24}$$

Note that the detector's energy resolution is independent from the amplification factor.

The detectors used in clinical systems (NaI(Tl) scintillator and PMTs) typically have an energy resolution of 10% for 140 keV gamma photons. The energy resolution improves when the energy of the gamma photons increases. In that case, more light is generated in the scintillator and, as a consequence, more charge carriers are generated at the cathode of the PMT.

Measurements have indicated that some detectors deviate from Poisson

statistics. Therefore the Fano-factor has been defined as:

$$F = \frac{R_{Det,observed}}{R_{Det,predicted}} \tag{2.25}$$

Where $R_{Det,predicted}$ is the energy resolution as predicted by 2.24.

The best energy resolution is obtained by making use of semiconductor detectors (see section 2.5.2.6.3). A germanium detector with an energy resolution of 0.96% was used for SPECT imaging by Johnson et al. [61].

The energy resolution of a scintillation detector is above all defined by the light yield of the scintillator and by the quantum efficiency of the photodetector. This is explained in sections 2.5.2.5 and 2.5.2.6.

2.5.1.3 Detection Efficiency

The detector efficiency is defined by:

$$S_{Det} = \frac{Nbr\ of\ detected\ gamma\ photons}{Nbr\ of\ gamma\ photons\ incident\ on\ the\ detector}. \tag{2.26}$$

S_{Det} depends on the energy of the gamma photons, the detector material and the thickness of the detector. The detection efficiency has a major impact on the system sensitivity because:

$$S_{Sys} = S_{Coll} \times S_{Det}. \tag{2.27}$$

S_{Coll} is the collimator sensitivity and includes the geometrical sensitivity.

The detection efficiency of a detector can be estimated by using the Beer-Lambert law (see section 2.3.3).

2.5.1.4 Count rate performance

Ideally the output count rate of a detector increases linearly with the event rate, in reality this is not the case. Radiation detectors can be classified based on their count rate behavior: *paralyzable* and *nonparalyzable* detectors [33].

A detector is *dead* for a certain time (the dead time τ) when an event is detected. Events which are detected while the detector is dead are lost.

Events that occur during the dead time of a nonparalyzable detector have no influence on the detector's behavior. This is different for the paralyzable

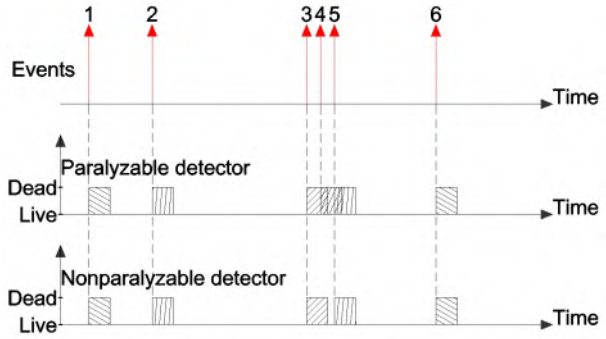

Figure 2.26: The behavior of paralyzable and nonparalyzable detectors. The paralyzable detector detects events 1, 2, 3 and 6. The nonparalyzable detector detects events 1, 2, 3, 5 and 6.

detector. Events that occur during the dead time of a paralyzable detector enlarge the dead time by τ. Because of this, a nonparalyzable detector detects more events than a paralyzable detector at high count rate. This is illustrated in Fig. 2.26.

Eventually, at a certain event rate, a paralyzable detector's count rate will drop to zero and a non-paralyzable detector's count rate will saturate. This is illustrated in Fig. 2.27.

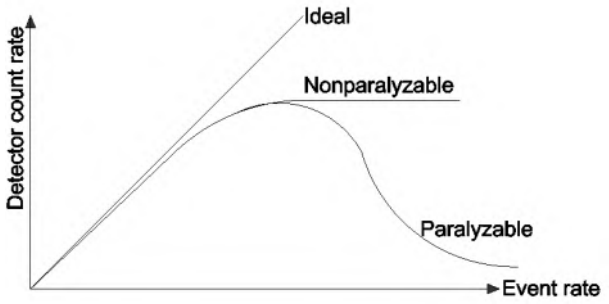

Figure 2.27: Ideally the output count rate of a detector increases linearly with the event rate. In reality this is not the case, a paralyzable detector's output count rate will drop to zero and a nonparalyzable detector's output count rate saturates when the event rate is too high.

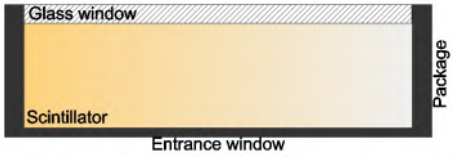

Figure 2.28: A hygroscopic scintillator such as NaI(Tl) needs a hermetically sealed package.

2.5.2 Scintillation detectors

2.5.2.1 Introduction

A typical scintillation detector consists of the scintillator, which is optically coupled to a light guide and this light guide is then optically coupled to an array of sensitive photodetectors (see Fig. 2.31); the optical coupling is done with optical grease. In some cases the light guide is omitted; the scintillator is then directly coupled to the photodetectors.

The scintillator emits light photons when a gamma photon loses energy by interacting with the scintillator material. The amount of light photons emitted is a statistical process, and, is proportional to the energy deposited in the scintillator by the gamma photon. By measuring the amount of light and the light spread, one can identify the energy and the position of the interaction in the scintillator. The majority of today's SPECT detectors makes use of a NaI(Tl) scintillator coupled to an array of PMTs.

Some scintillators are hygroscopic and need to be handled in low humidity environments. Such scintillators require a hermetically sealed package once they leave this environment. The package is typically made out of aluminum. This aluminum housing contains the scintillator; a glass window is present in the package to optically couple the photodetectors to the scintillator. Care should be taken to minimize the thickness of the entrance window (the side of the package which the gamma photons have to penetrate to reach the scintillator). A substantial fraction of the gamma photons might be lost by absorption in this entrance window. To enhance this, one might also consider the usage of a beryllium entrance window. Beryllium is, due to its low density, nearly transparent for gamma photons.

Two distinct scintillator geometries are commonly used: continuous (monolithic) scintillators and pixelated scintillators (see Fig. 2.29 and 2.30). A monolithic scintillator is one continuous block of scintillator material. To optimize the collection of light photons, the top and sides of the scintillator

are covered with a reflector. A pixelated scintillator consists of an array of small blocks of scintillator material; the top and sides of each small block is wrapped in a reflector. These pixelated detectors have found widespread use as PET detectors. The scintillator of a PET scanner is typically made thick (22 mm) to have sufficient detection efficiency for 511 keV gamma ray photons. The light spread of a 22 mm thick monolithic scintillator is large and there would be a lot of positioning artifacts at the edges of the scintillator when standard event positioning algorithms (COG) are used. This is where the pixelated detectors become interesting: the small *pixels* channel the light towards the photodetectors, thereby reducing the light spread. Another advantage is the improvement in detector count rate. The smaller light spread results in fewer PMTs detecting light photons. The consequence of this is that the probability for pulse pile-up at high count rates decreases (this is important for PET imaging where the count rate is much higher than for SPECT systems). There are however some disadvantages to pixelated detectors. These detectors tend to be more expensive than the monolithic detectors: a lot of labor is required to cut the scintillator into pixels, to add the reflectors and to glue it all back together. The light photons experience a lot of reflections, this leads to a considerable amount of photon absorption, and, results in a worse energy resolution. Additionally, the sensitivity of the detector drops due to the gaps (filled with reflector) in between the pixels. A common pixel size for a pixelated PET detector is 4 mm x 4 mm (22 mm long), but smaller sizes (down to 0.5 mm x 0.5 mm, [62]) have been produced as well.

2.5.2.2 Scintillation mechanism

Based on the scintillation mechanism, the scintillators can be subdivided in two classes.

The first class are the *organic scintillators*, these scintillators have a low stopping power for gamma ray photons and are, due to this, not used for SPECT detectors. The organic scintillators are mainly used for the detection of fast electrons and alpha particles. This type of scintillator is not further discussed here.

The second class are the inorganic scintillators. They are widely used as SPECT detector. H.O. Anger used a NaI(Tl) scintillator for the first gamma camera [63][59]; to date NaI(Tl) is still the the most frequently used scintillator for SPECT detectors. The scintillation mechanism of inorganic scintillators is based on activators that are added to the crystal (e.g. the addition of Tl to a NaI crystal to produce a NaI(Tl) scintillator).

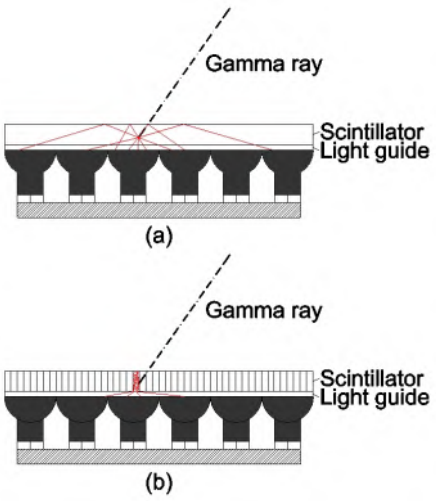

Figure 2.29: (a) A monolithic scintillator and (b) a pixelated scintillator. The light spread of the pixelated detector is more focused on the photodetectors.

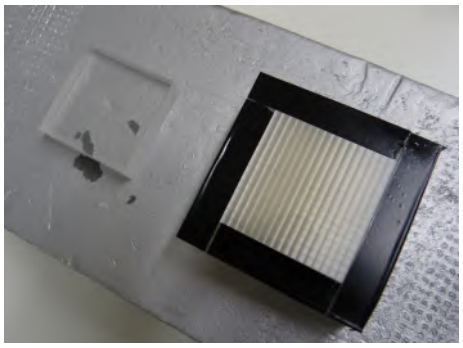

Figure 2.30: A monolithic and a pixelated LYSO scintillator. The monolithic block is wrapped in a reflector during assembly.

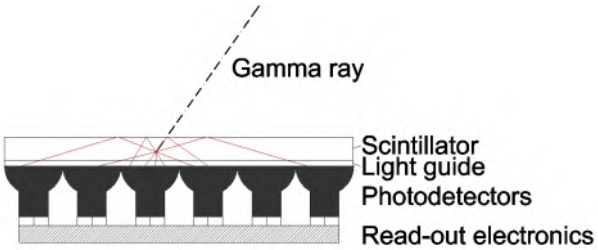

Figure 2.31: A scintillation detector consists of the scintillator, a light guide and an array of photodetectors. A multitude of light photons are emitted isotropically at the point of interaction. The top and side surfaces of the scintillator are reflective to guide the light photons to the photodetectors. The number of light photons emitted is related to the energy of the detected gamma photon. The position of the interaction can be estimated based on the measured light spread.

The electrons in an insulator can only be in some discrete energy bands. The valence band contains the bound electrons, these are bound at lattice sites; the conduction band contains the loose electrons. In between the valence band and the conduction band there is a band gap zone. Electrons can not be present in this band gap zone.

An electron can move from the valence band to the conduction band by absorbing energy, it loses energy when it de-excites and returns from the conduction band to the valence band. This energy can be released as photons or as phonons (heat) [64]. The return of the electron from the conduction band to the valence band by photon emission is not efficient in the pure lattice, and, due to the large band gap, the energy of these light photons is too high to be in the visible range.

Because of this, a small amount of activators (impurities) is added to the lattice. These activators create sites in the lattice where the band gap

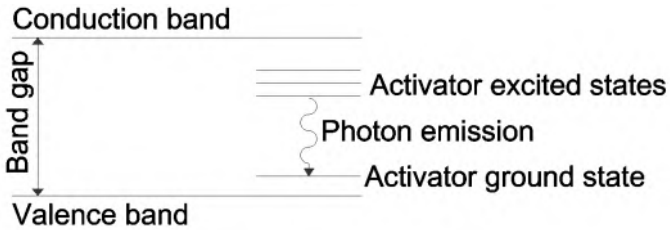

Figure 2.32: The addition of activators leads to a modified band structure.

Table 2.4: Inorganic scintillators - main properties

Name	Density (g/cm^3)	τ 140 keV (cm^{-1})	Wavelength (nm)	Decay time (μs)
NaI(Tl)	3.67	2.05	415	0.23
CsI(Tl)	4.51	3.14	540	0.68, 3.34
CsI(Na)	4.51	3.14	420	0.63
LYSO	7.1	8.2	428	0.04
$LaBr_3(Ce)$	5.08	2.11	380	0.026

Name	Required energy per light photon (eV)	Hygroscopic	Usage	Ref.
NaI(Tl)	26.3	yes	SPECT	[63]
CsI(Tl)	18.5	slightly	HEP[0], Space	[65]
CsI(Na)	24.4	yes	Space	[65]
LYSO	40	no	PET	[66]
$LaBr_3(Ce)$	15.9	yes	PET	[67]

structure is modified (see Fig. 2.32). Additional energy states are present in the band gap zone at these activator sites. The electron can de-excite, using those new energy states, to the valence band. The energy levels at such a site are narrower than the band gap and the energy of the emitted photons will be smaller than the band gap. By doing so, the emission spectrum shifts away from the absorption spectrum of the crystal (this prevents re-absorption of the light photons), and, the emitted photons are in the visible range.

A photo-electron or a recoil electron, resulting from a photoelectric or Compton interaction of the gamma photon with the scintillator, which is losing energy will form a large number of electron-hole pairs by exciting electrons from the valence to the conduction band. The holes migrate to an activator site and ionize the activator because the ionization energy of an activator site is less than the ionization energy of a pure lattice site. The electron moves through the crystal until it encounters such an ionized activator site. Here, it de-excites, using the modified band structure (Fig. 2.32) and by doing so, the probability is high that a visible light photon is emitted [33].

2.5.2.3 Examples

[0]HEP: High energy physics

The most important characteristics of some frequently used scintillators are listed in table 2.4, these and other characteristics are discussed in the following sections.

NaI(Tl) is used for the majority of SPECT systems because it has a high light output, its wavelength of maximum emission suits well with PMTs (Fig. 2.33) and it can be grown to large sizes (a typical clinical detector measures 30 cm x 40 cm and is 9.5 mm thick). NaI(Tl) is a brittle material that is hygroscopic, and therefore, requires encapsulation.

CsI(Tl) is bright scintillator but its emission spectrum does not match well with the efficiency spectrum of a bialkali PMT. A better performance can be obtained by coupling CsI(Tl) to photodiodes whose efficiency spectrum matches well with this scintillator's emission spectrum. A pixelated CsI(Tl) scintillator that is coupled to photodiodes is used in Digirad's Cardius SPECT system. This material is only slightly hygroscopic and is quite rugged, which makes it well-suited for space research. It can be used for particle discrimination (e.g. protons and α-particles) by comparing the ratio between the two decay times, due to this it is frequently used in high energy physics (HEP) experiments [65].

CsI(Na) is well suited for usage with a bialkali PMT. It is more hygroscopic than CsI(Tl) but less than NaI(Tl), and, it is quite rugged and is therefore also used for space research. Pixelated CsI(Na) coupled to a PSPMT was used for the LinoView small-animal SPECT system [68].

The majority of recent PET systems make use of LYSO because it has a high density (essential to detect the 511 keV gamma rays) and because it is a fast scintillator (necessary for TOF-PET[1]), an example is the Philips Gemini TF system. We present an LYSO-based SPECT detector in chapter 6.

$LaBr_3$(Ce) is a new scintillators material with promising characteristics: it is faster than LYSO and it emits more light than NaI(Tl), its stopping power is however lower than the stopping power of LYSO. To date it is still very expensive and, it is very sensitive to moisture. A full-body TOF-PET system that consists of pixelated $LaBr_3$(Ce) crystals and PMTs was constructed by Daube-Witherspoon et al. [69].

[1]TOF-PET: time of flight PET. The time difference between two coincident detections is used to estimate the emission position more accurately. This approach results in PET images with lower noise.

Table 2.5: Detection efficiency

	T (mm)	NaI(Tl)	LYSO
S_{PE} (%)	2	31.9	73.5
	5	57	85.7
	10	72	86.5

2.5.2.4 Detector sensitivity

The probability for a photoelectric interaction per unit pathlength (τ) defines, together with the scintillator's thickness (T), the sensitivity of the scintillator for photoelectric interactions. Using the Lambert-Beer law (eq. 2.4) we can formulate the sensitivity (S) for a photoelectric interaction in the scintillator as:

$$S_{PE} = \frac{\tau}{\mu}(1 - e^{-\mu T}). \tag{2.28}$$

Note that this formula is only valid for perpendicular incident gamma rays. Some examples are given in table 2.5.

2.5.2.5 Light emission: spectrum, time course and light yield

The spectrum of the light generated by the scintillator is continuous (see Fig. 2.33) and should be matched to the efficiency spectrum of the photodetector. Table 2.4 lists the wavelength of maximum emission of some scintillators.

For most scintillators, the time course of the light emission can, to good approximation, be modeled by an exponential function:

$$I = I_0 e^{-t/\tau}. \tag{2.29}$$

Some scintillators have two decay times (e.g. CsI(Tl)):

$$I = I_0 e^{-t/\tau_0} + I_1 e^{-t/\tau_1}. \tag{2.30}$$

With τ being the decay time constants as listed in table 2.4. The rise time is much smaller than the decay time and because of this, the rise time is often considered as being infinite. Fig. 2.34 depicts an oscilloscope measurement of a PMT coupled to a NaI(Tl) scintillator.

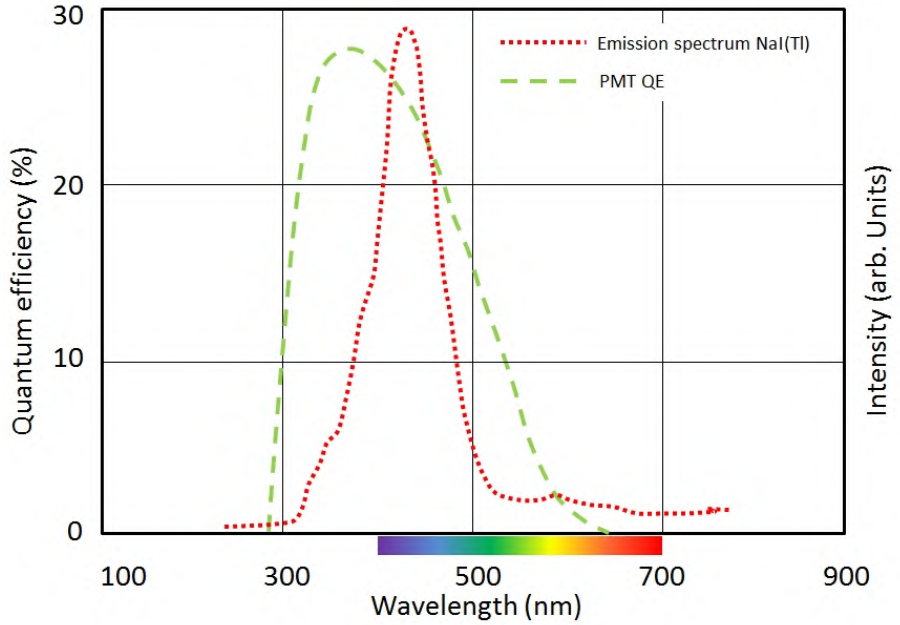

Figure 2.33: The QE of a PMT (ET Enterprises 9107B) and the emission spectrum of NaI(Tl) (Saint-Gobain Crystals).

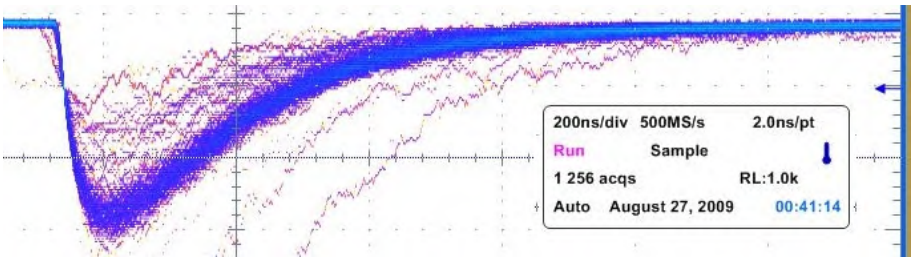

Figure 2.34: The output of a PMT that is coupled to a NaI(Tl) scintillator, measured with an oscilloscope in infinite persistence mode. A source of ^{99m}Tc is positioned in front of the scintillator.

The emission time is important, mainly for PET, because it has an impact on the maximum count rate and on the accuracy of the event's timestamp (fast and bright scintillators provide a more accurate timestamp). This timestamp is used to group the coincidences and for time-of-flight PET (TOF-PET). Schaart et al. have used a $LaBr_3$(Ce) scintillator coupled to a SiPM to achieve a TOF-PET coincidence resolving time of 100 ps [70].

The more light a scintillator generates, the better. It has a large impact on the energy resolution (see section 2.5.1.2), on spatial resolution and on timing resolution (for PET and TOF-PET).

2.5.2.6 Photodetectors

2.5.2.6.1 Introduction In this section photodetectors for scintillator read-out are introduced.

Such photodetectors have several desirable properties. They need to be efficient in converting light photons into photoelectrons because the amount of photo-electrons has a large impact on energy resolution (see section 2.5.1.2) and spatial resolution of the detector. This conversion efficiency is characterized by the quantum efficiency (QE):

$$QE = \frac{Nbr\ of\ collected\ photoelectrons}{Nbr\ of\ light\ photons\ incident\ on\ sensor}. \tag{2.31}$$

The QE is a function of wavelength (see Fig. 2.33). Generally, one tries to match the scintillator's wavelength of maximum emission with a sensor that has a similar wavelength of maximum QE.

Most gamma-ray detectors employ an array of photodetectors (e.g. 10x10 PMTs). The gaps between these sensors should be as small as possible to avoid loss of light photons. The size of these gaps is related to the shape of the sensors (e.g. square, round and hexagonal photodetectors exist). Sometimes a reflector or a special light guide is used to minimize light loss caused by these gaps. The active light sensitive area of a photodetector is always less than the package size. This is characterized by the fill factor:

$$Fill\ Factor = \frac{Sensor\ active\ area}{Sensor\ total\ area}. \tag{2.32}$$

In most cases, each photodetector has a dedicated amplifier and sometimes also a dedicated analog to digital converter (ADC). As such, the size of the readout electronics scales up with the amount of photodetectors.

Using a lot of small sensors coupled to a relatively thick scintillator (with a large lightspread) will require large and expensive readout electronics and will only result in a marginal gain in spatial resolution.

Finally, the performance of the detector in magnetic fields is an important property for the design of multi-modal PET-MR and SPECT-MR scanners. These sensors have to operate flawlessly in a magnetic field of up to 9T (the earth's magnetic field is approximately 45 μT).

The photodetectors can be subdivided into two classes: those based on vacuum tube technology and those based on semiconductor technology.

2.5.2.6.2 Vacuum tube photodetectors The vacuum tube photodetectors rely on the concept of electron multiplication to measure light photons. By doing so, they provide a large signal that can easily be post-processed. The main drawbacks of these tubes is the amount of hand labor involved in producing them, their large size and their sensitivity to magnetic fields.

The photomultiplier tube (PMT) An array of photomultiplier tubes was used by H.O. Anger for the first gamma camera [59] (see Fig. 2.35). To date it is still the photodetector of choice for the majority of clinical SPECT and PET detectors. The main reason for this being the fact that their price-to-surface ratio outperforms that of the other sensors. Note however that quite some hand labor is required and that only a small amount of suppliers is available for this type of photodetector (Hamamatsu, ET Enterprises, ADIT).

A PMT consists of a vacuum glass tube. Its major parts are the photocathode, the focusing electrodes, the dynodes and the anode (see Fig. 2.36).

When a light photon strikes a photocathode, then a photoelectron can be released (by the photoelectric effect). To accomplish this, an electron from the cathode has to absorb the energy from a light photon.

This energy should be sufficient to let the electron migrate towards the cathode surface ($E_{migrate}$) and, to let it escape from the cathode (the work function W).

This means that there is a minimum frequency (or a maximum wavelength) which still allows to let a photoelectron escape from the cathode: $hf_{photon} > E_{migrate} + W$. This long wavelength threshold is associated with the colors red/infrared.

Figure 2.35: A Hamamatsu PMT that was once operational in a large clinical SPECT gamma camera. Its round package has a diameter of 7.5 cm.

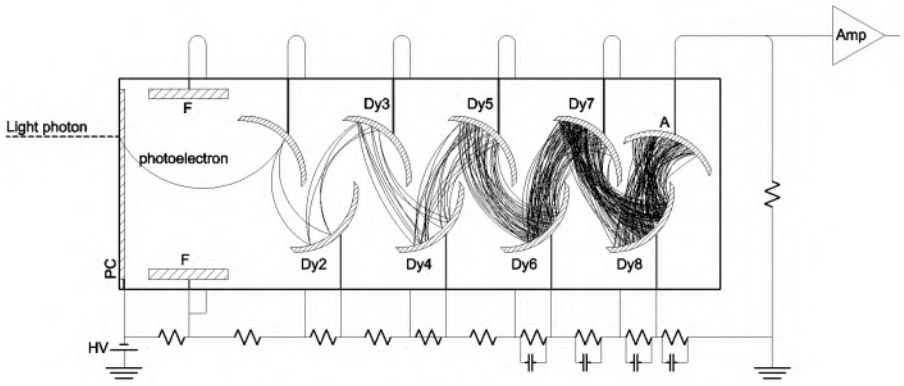

Figure 2.36: The major parts of the PMT: the photocathode (PC), the focusing electrodes (F), the dynodes (Dy) and the anode (A).

Besides this threshold, there is also a short wavelength cut-off, defined by the entrance glass window. This cut-off is at 350 nm for glass (associated with the color violet).

Thin cathodes are used to enlarge the probability that a photoelectron escapes the cathode. The thin cathode is semitransparent so only a fraction of the incident light photons will interact in the cathode. As such, the photocathode has a major impact on the spectrum and magnitude of the QE. Typically the peak QE of a PMT is in a range from 25% to 30%. The QE plot of a Hamamatsu R11102 PMT is shown in Fig. 2.37. A commonly used photocathode is the *bialkali* photocathode which consists of antimony (Sb), potassium (K) and cesium (Cs). The spectral response of these bialkali photocathodes shows good overlap with the emission spectrum of the NaI(Tl) scintillator (see Fig. 2.33).

The photoelectrons that have escaped the cathode are attracted by the first dynode because the dynode is at a higher voltage than the cathode. The photo-electrons are thus accelerated and gain energy while traveling from the cathode to the first dynode. Focusing electrodes are used to focus the photoelectrons on the first dynode.

When the photoelectron strikes the first dynode then secondary emission occurs; the energy of the accelerated photoelectron gives rise to the emission of multiple electrons. The multiplication factor of a dynode is defined by:

$$\delta = \frac{\textit{Nbr of emitted electrons}}{\textit{Nbr of incident electrons}}. \tag{2.33}$$

The total multiplication structure consists of multiple dynodes. Different dynode geometries exist, all having their own advantages and disadvantages. The total amplification equals:

$$A_{\textit{Total}} = \alpha\delta^{N}, \tag{2.34}$$

where α is the fraction of collected photoelectrons and N is the number of dynodes. A typical tube has an $A_{\textit{Total}}$ of 10^7 ($\delta \approx 5$, $\alpha \approx 1$, $N = 10$).

Finally, the electrons are collected by the anode. Readout electronics are then used to amplify and shape the PMT current. The dynode structure acts as a very good amplifier, the magnitude of the anode signal is relatively large and as such, off-the-shelf electronics can be used to post-process the PMT signal.

For proper operation each PMT stage should be at a higher voltage than its preceding stage (e.g. $V_{\textit{Anode}} > V_{\textit{Last dynode}}$). This is commonly done

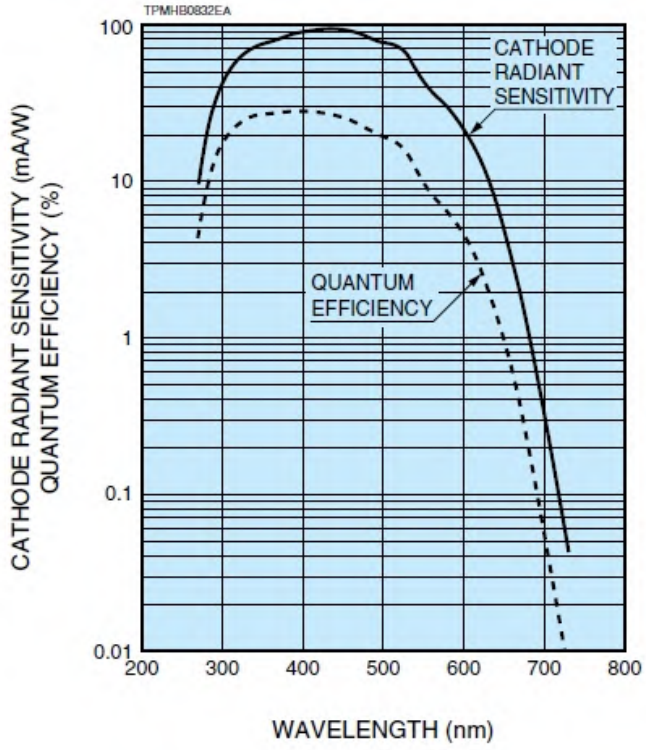

Figure 2.37: The QE of a PMT is a function of the wavelength of the incident light photons. The graph shown is for the Hamamatsu R11102 PMT. Image courtesy of Electron Tube Division, Hamamatsu Photonics K.K.

using a resistor divider (depicted in Fig. 2.36) where capacitors are added to the last dynode stages to improve the voltage ripple caused by the relatively large currents which are drawn from these dynodes. A typical high voltage of a PMT is 1000V. This high voltage can be used in two ways: the cathode can be connected to a negative high voltage while the anode is grounded (the *anode grounded* configuration, as shown in Fig. 2.36) or the cathode can be grounded while the anode is connected to a positive high voltage (the *cathode grounded* configuration).

The path of the electrons in a PMT is very sensitive to magnetic forces and because of this, PMTs do not function well in magnetic fields.

PMTs are available in a wide variety of sizes (from 10 mm up to 50 cm in diameter) and shapes (circular, hexagonal, square). Typical gamma

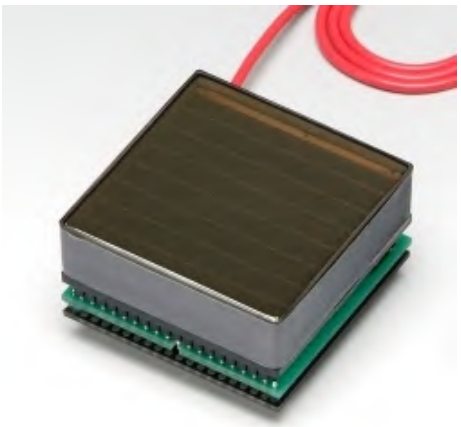

Figure 2.38: A Hamamatsu H8500 PSPMT has 8x8 anodes. Image courtesy of Electron Tube Division, Hamamatsu Photonics K.K.

cameras for clinical SPECT systems use large diameter (5 cm) circular or hexagonal PMTs.

PMTs are used in most clinical SPECT systems (e.g. Philips BrightView, Siemens Symbia) and in some pre-clinical systems. PMTs do not allow to obtain a high intrinsic detector resolution and, to compensate for this, a multi-pinhole collimator with a large magnification factor has to be used in those PMT-based pre-clinical systems (eq. 2.15). The large magnification and the spacious detectors result in large systems. Examples of pre-clinical system that uses PMT-based detectors are the MiLabs U-SPECT-II system [55] and Bioscan's NanoSPECT [47].

The position sensitive PMT (PSPMT) The conventional PMTs do not allow to measure small light spreads or to build compact gamma-ray detectors. The smallest PMTs (e.g. Hamamatsu R1635) have a circular package with a 10 mm diameter; the active area is circular with a diameter of only 8 mm. Using an array of these small PMTs would result in a low fill factor, resulting in a mediocre energy resolution and spatial resolution. This is solved by the introduction of the position sensitive PMT and can be considered as a PMT with multiple anodes. The most recent devices (Hamamatsu H8500, H9500, H12700) have a large fill factor.

By measuring multiple anodes, one can get an idea on the lightspread detected by the photocathode. State-of-the-art PSPMTs are for example

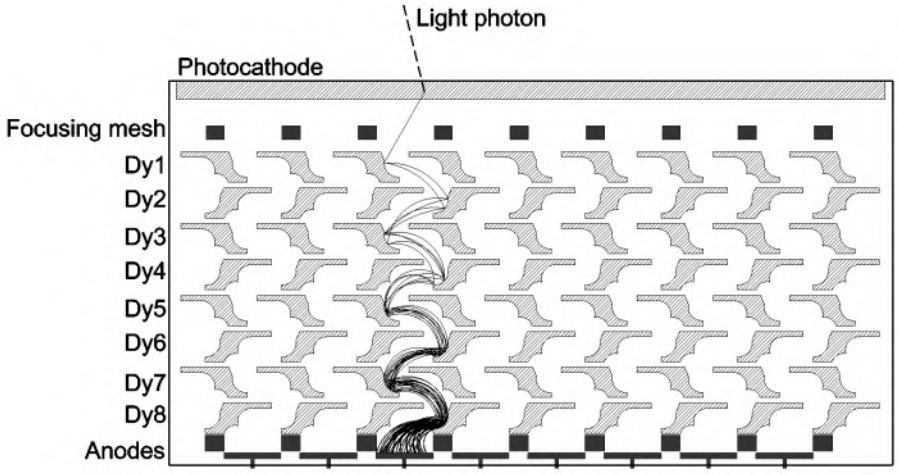

Figure 2.39: The metal channel dynodes multiply the electrons with minimum spatial spread. By doing so, most electrons will hit the anode underneath the interaction position of the light photon.

the Hamamatsu H8500 and H9500. The H8500 has an 8x8 anode matrix (anode size 6 mm x 6 mm); the H9500 has a 16x16 anode matrix (anode size 3 mm x 3 mm). These tubes employ metal channel dynodes [71] (see Fig. 2.39). With such a dynode structure, the electrons are multiplied with minimal spatial spread and the electrons are guided towards the anode that is underneath the interaction position of the light photon. The size of such a PSPMT is small compared to a PMT. The H8500 measures (BxWxH) 52 mm x 52 mm x 14.4 mm; the active area is 49 mm x 49 mm. This results in a high fill factor of 88.8%, additionally, the square shape makes them easily tileable. The small depth is possible due to the dynodes which are thin and placed close to each other.

PSPMTs are used for compact high-resolution gamma detectors (e.g. [72], [73], [74]). One of the problems associated with these devices is the large inter-anode gain variation (max. 1:4 for the Hamamatsu H8500). They are more tolerant to magnetic fields than standard PMTs due to the shorter electron path; usage inside an MR bore is however not possible.

The Bruker Albira pre-clinical PET/SPECT/CT system uses two SPECT detectors that consist of an H8500 PSPMT and a continuous CsI(Na) scintillator [75].

2.5.2.6.3 Semiconductor photodetectors The research to performant semiconductor photodetectors has been largely driven by the need for compact detectors that can operate in the magnetic field of an MR scanner.

Drawbacks of the semiconductor detectors are their sensitivity to temperature and bias voltage changes. Additionally, they often need dedicated cooling to lower the amount of dark counts, which are thermally generated charge carriers.

PN photodiode PN photodiodes have not been used for scintillator read-out; they are mentioned here because the PIN photodiode is based on the PN photodiode.

The resistivity of the depletion region, which is formed by reverse biasing a PN junction is very high. Because of this, the majority of the voltage and the electric field are present across this region (see Fig. 2.40). Electron-hole pairs are generated when a photon is absorbed in the semiconductor. These electrons and holes will experience a strong electromotive force in the depletion region where there is a large electric field. The electromotive force in the depletion region will move the electrons to the cathode and the holes to the anode. This charge movement then leads to an induced current [76][77] which can be sensed by the read-out electronics.

The measured current (A in Fig. 2.40) is the sum of a leakage current (or the dark current) and the photo-current.

A strong reverse bias is used; this has the advantage of a thicker photo-sensitive region, a faster electron-hole collection (the electron and hole velocity increases with the strength of the electric field) and a lower junction capacitance. A lower junction capacitance results in a smaller amplification of the pre-amplifier's voltage noise. Noise on the photodetector's signal will degrade the energy and spatial resolution of the detector.

PIN photodiode A PIN diode is a PN diode with a high-resistivity intrinsic semiconductor ($n = p$) layer between the P and the N regions. By doing this, the depletion region extends and as such, the sensitive volume of the diode increases and the capacitance decreases.

The QE of a PIN diode is much higher than that of a PMT, typical values are 70%-80%. The problem is that, unlike with a PMT, the diodes do not have an internal gain mechanism. Because of this, low-noise electronics are needed to amplify and filter (or shape) the photo-current. The energy resolution of these detectors is mainly defined by electronic noise and not

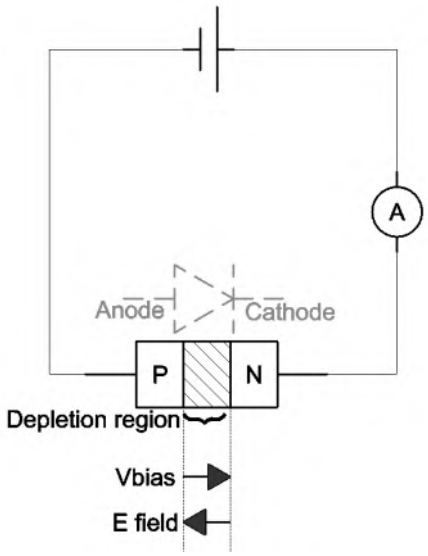

Figure 2.40: The photo-sensitive part of a photodiode is the depletion region.

by photo-electron statistics.

PIN photodiodes have been used as photodetector in PET and SPECT detectors. An advantage of the PIN photodiodes compared to the PMTs and PSPMTs is that a photodiode can be used at both sides of the scintillator. A silicon photodiode is thin compared to a bulky PMT and can be employed on the scintillator's front side. Reading out a scintillator at both sides can be used to estimate the DOI [78, 79].

Gruber et al. [80] have built a SPECT detector for breast cancer imaging that consists of a pixelated CsI(Tl) scintillator and PIN silicon photodiodes. Each scintillator pixel is individually read out by a photodiode (one-to-one coupling). The photodiodes' quantum efficiency spectrum matches well with the emission spectrum of CsI(Tl) resulting in an energy resolution of 10.7% for 140 keV gamma rays. This detector is very compact and event positioning is drastically simplified by making use of one-to-one coupling.

Avalanche photodiode (APD) Avalanche photodiodes (APD) do have an internal gain mechanism in contrast to PN and PIN photodiodes. The special geometry and bias voltage allow for avalanche multiplication. Normally, the bias voltage is set below the APD's breakdown voltage. When a photon is absorbed and electron-hole pairs have been formed, then the elec-

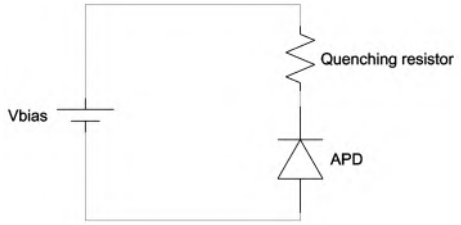

Figure 2.41: A Geiger-mode APD needs quenching. The simplest method is to use passive quenching by putting a resistor in series with the APD.

trons are accelerated by a high electric field. By doing so they gain energy and, if their energy is large enough, they can generate new electron-hole pairs by impact ionization. Because of this, the APD signal has a gain. The output is thus amplified and relates to the amount of light photons detected. The gain is typically in a range from 100 to 1000 and is sensitive to the bias voltage and to the temperature; a stable bias and temperature are mandatory for good operation.

One can also operate an APD above its breakdown voltage (Geiger-mode APD). In that case, the avalanche is self-preserving (Geiger discharge) and the APD's current has to be limited by quenching; otherwise the device can become defective. Quenching can be done by using active components or by using passive components. An example of passive quenching is shown in Fig. 2.41. When a light photon is detected then a large current is created by the Geiger discharge. This current causes a voltage drop on the quenching resistor. Because of this, the APD's bias voltage drops and the Geiger multiplication stops. The APD current is again low when the APD has recovered. After recovery, the APD is ready for a new detection. At first sight, this might not be an interesting operation mode because in this mode the APD's current is not related to the amount of detected light-photons. The Geiger-mode APD is the key component of the silicon photomultiplier (SiPM), which is described in the next section.

APDs have been used to build detectors for PET and SPECT (e.g. [81][82]). The LabPET scanner is an APD based PET scanner for imaging of small animals [83]; the Siemens whole body simultaneous PET-MR scanner makes use of APDs [84].

Silicon photomultiplier (SiPM) The silicon photomultiplier [85] (SiPMs, or multi-pixel photon counter (MPPC)) is currently being con-

Figure 2.42: A SensL SiPm array; the pixel size is 3 mm x 3mm (image courtesy of SensL).

sidered as being the best candidate for replacing the PMT in PET(-MR) scanners.

These compact photodetectors are available in a wide variety of sizes, they provide a large gain, offer a fast response, are insensitive to magnetic fields and are available from several manufacturers (Hamamatsu, FBK-AdvanSiD, SensL, RMD, ...).

A SiPM basically is an array of thousands of Geiger-mode APDs, all connected in parallel. Each combination of an APD and its associated quenching is called a *microcell* (a typical size of a microcell is $50\mu m \times 50\mu m$). The probability, with low light-levels, that multiple light photons hit the same microcell is low, thus each microcell functions as a binary, digital device (light is detected *or* light is not detected). The sum of all the microcells is calculated analog (all the microcells are placed in parallel) and provides a measure for the amount of detected light photons. Saturation can occur at higher light-levels, when the probability of multiple photons incident on one microcell is no longer negligible. The typical gain of a SiPM is 10^6, similar to a PMT.

The detection efficiency of a SiPM is lower than the QE of a Geiger-mode APD due to the geometric efficiency of the microcell array [86]:

$$\epsilon_{Geo} = \frac{A_{sensitive}}{A_{total}}, \tag{2.35}$$

where $A_{sensitive}$ is the sum of all the microcell sensitive areas and A_{total} is

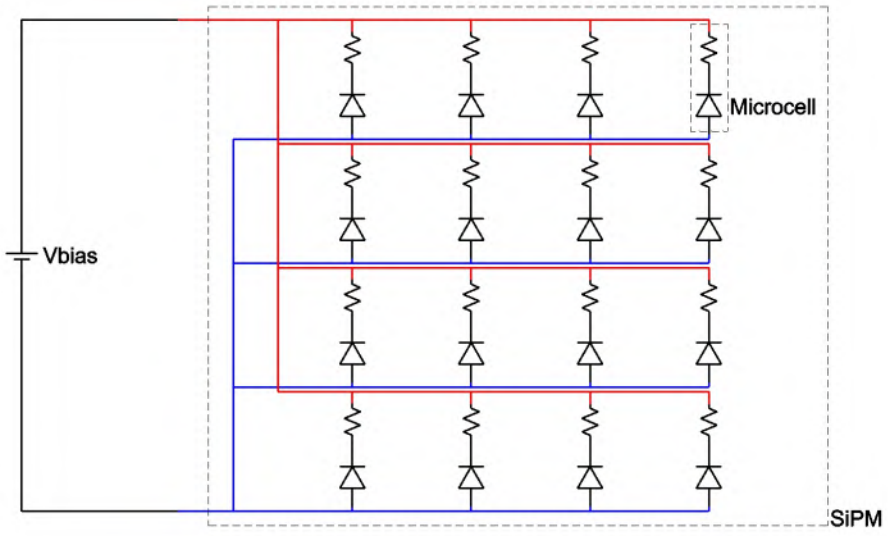

Figure 2.43: A SiPM consists of an array of thousands of Geiger-mode APDs, all placed in parallel.

the total area of the SiPM. The photon detection efficiency (PDE) is equal to:

$$PDE = QE_{Microcell} \times \epsilon_{Geo} \times \epsilon_{Geiger}, \tag{2.36}$$

where ϵ_{Geiger} is the probability that a Geiger discharge is triggered.

Typical values for the fill factor are in a range of 20-80%, ϵ_{Geiger} is typically in a 0.5-1 range, and, the QE is typically larger than 80% for visible light [87].

SiPMs have been used for a variety of PET detectors, mostly for use in the magnetic field of an MR scanner (e.g. [88][89]). Similar to the photodiodes, SiPMs are thin, and allow for front-side readout. Schaart et al have used this to obtain a higher spatial resolution [88]; for optimal spatial resolution it is beneficial to couple the photodetector close to the interaction position and the majority of interactions occur at the front side of the scintillator.

dSiPM The digital SiPM (dSiPM) was introduced by Philips Digital Photon Counting [90] in 2009. Here, the binary nature of the microcell is fully exploited by changing the readout from analog (SiPM) to digital

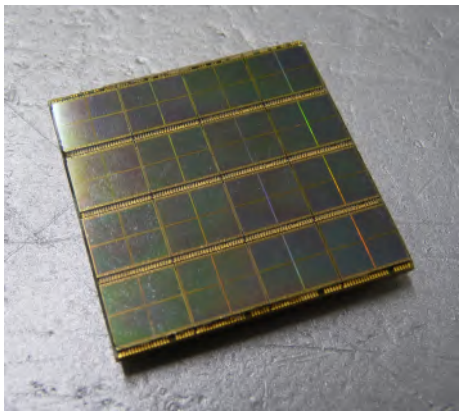

Figure 2.44: An 8x8 array of dSiPMs. The pixels size is 3.2 mm x 3.8 mm.

(dSiPM). This device uses active quenching, by doing so the microcells can be recharged in a controlled manner. The number of triggered microcells are counted and transmitted by the on-chip digital electronics. The device is recharged when a time counter exceeds a programmable value. The time counter is reset at the start of the scintillation event.

The dSiPM also incorporates a time-to-digital converter that can be used for accurate event time-stamping (for TOF-PET).

This approach leads to a new detector architecture. With traditional analog PMTs, PSPMTs, diodes or APDs one has to post-process the analog outputs. In most cases this involves amplification, filtering and digitization. A gamma-camera might involve hundreds of channels and because of this the post-processing electronics is often implemented in an application specific integrated circuit (ASIC). The required electronics are power-hungry and this leads to large power requirements and heat dissipation. Basically, the design of a SPECT or PET detector becomes increasingly difficult when so many channels have to be processed. With the digital dSiPM this is different. Here, the sensor itself has a digital output. The main difficulty now becomes a digital bandwidth problem because all the sensor data has to be transmitted to a digital processing board. This reduction of read-out electronics is a large advantage for PET-MR systems where space restrictions and heat dissipation are of major concern.

To date, the usage of this promising technology is not yet widespread, this is mainly due to the fact that the devices are only available from a single supplier (Philips Digital Photon Counting). Seifert et al. [91] have

coupled a monolithic 24 x 24 x 10 mm^3 LSO(Ce) scintillator to a dSiPM and obtained an average spatial resolution of 1 mm FWHM for 511 keV gamma photons. A dSiPM based SPECT detector was built by Bouckaert et al. [92]. They coupled a 32 x 32 x 2 mm^3 monolithic LYSO scintillator to a dSiPM and obtained a resolution of 486 μm.

Recently, Philips Medical Systems has announced the Vereos time-of-flight PET/CT scanner that uses dSiPMs one-to-one coupled to a pixelated scintillator.

Silicon drift detector (SDD) A silicon drift detector (SDD) employs a series of electrode rings to generate an electric field that is parallel to the detector's surface. Due to this transversal field, the electrons that are generated when a photon is absorbed, drift towards a small collection anode that is positioned in the center of these rings. The collection anode has a low capacitance that is independent of the SDD's active area, this allows to build photodetectors with a large active area and with very low noise. SDDs are typically cooled to approximately -5$^\circ C$.

The advantages of the SDD-based detectors are that they are compact and offer a high quantum efficiency (70 % at 565 nm). Their active area can be in a range from a few mm^2 to some cm^2 [93]. SDDs remain functional but show a reduction in signal amplitude when operated in a large magnetic field [94].

Fiorini et al. have designed and evaluated several SDD based scintillation detectors.

An intrinsic spatial resolution better than 200 μm and an energy resolution of 14% for 122 keV gamma photons was measured with a monolithic array of 19 hexagonal SDDs (total sensitive area 95 mm^2) and a 3 mm thick monolithic CsI(Tl) crystal [95]. Each SDD is hexagonal and has an area of 5 mm^2 and an inner diameter of 2.4 mm.

Another SDD-based detector is the HICAM gamma camera [96]. This camera has a 12 x 10 cm^2 FOV and employs 100 SDDs (active area 1 cm^2) coupled to a 10 mm thick monolithic CsI(Tl) scintillator. Using this detector, an intrinsic resolution of 0.8 mm and an energy resolution of 20% were obtained.

Electron-multiplying charge-coupled device (EMCCD) An electron-multiplying charge-coupled device (EMCCD) is a CCD which has an internal gain mechanism; this gain mechanism is based on impact

Figure 2.45: The Hamamatsu ImagEM EM-CCD camera uses a 512 x 512 EMCCD sensor and has a frame rate of 70 frames/s. The sensor is cooled to -65° C. Image courtesy of System Division, Hamamatsu Photonics K.K.

ionization. An EMCCD is cooled to reduce the dark counts.

CCD-based sensors require a special event discrimination and energy calculation algorithm because they are read out at a certain frame-rate while a PMT/SiPM/APD based system is read out when an event is detected.

EMCCD's are expensive and are only available for small sensitive surfaces. Lenses or optical tapers can be used to demagnify a large scintillator on an EMCCD [97]. An example of an EMCCD is shown in Fig. 2.45.

These photodetectors have been used to build very high spatial resolution detectors (an R_i of 65 μm has been reported) [60], the energy resolution is worse than the energy resolution of PMT based detectors (E_{Res} worse than 50%) [98, 99].

2.5.2.7 Event positioning

2.5.2.7.1 Introduction Scintillation detectors are indirect conversion detectors. The scintillator emits light photons where the gamma photon interacts. This results in a lightspread which is measured by the photodetectors. Then, a positioning algorithm is used, which uses the measured lightspread, to estimate the position of interaction. SPECT detectors output an X and a Y coordinate and do not provide depth of interaction (DOI) information.

An ideal positioning algorithm is accurate (accurate positioning leads to a better detector resolution), does not require additional hardware (to limit cost and power requirements of the detector), does not require a lengthy calibration and is fast (the positioning should not lead to a substantial longer processing time).

In this section we present three positioning methods: center of gravity, maximum likelihood and k-nearest neighbor.

2.5.2.7.2 Center of gravity (COG) The center of gravity (COG) method was developed by H.O. Anger [59]; it is also known as *Anger logic*.

The need for sufficient sensitivity at large distance in clinical SPECT results in low resolution collimators with large holes (e.g. 7 mm collimator resolution at a height of 10 cm). The detectors of such a SPECT system typically have a 3 mm intrinsic detector resolution. Due to this an improved detector resolution will only result in a marginal increase in system resolution (see formula 2.9).

The COG event positioning algorithm is traditionally used for those clinical detectors. It does not result in the optimal spatial resolution but it is easily implemented in hardware and it only needs limited calibration.

The energy of an event is calculated as the sum of all photodetector signals ($Charge_k$):

$$Energy = \sum_{k=1}^{K} Charge_k, \tag{2.37}$$

where K is the total number of photodetectors.

The coordinates of interaction are calculated as follows:

$$X_i = \frac{\sum_{k=1}^{K}(PhotoDetXCoord_k \times Charge_k)}{Energy} \tag{2.38}$$

$$Y_i = \frac{\sum_{k=1}^{K}(PhotoDetYCoord_k \times Charge_k)}{Energy} \tag{2.39}$$

$PhotoDetXCoord_k$ and $PhotoDetYCoord_k$ are related to the planar position of the photodetector with reference to the center of the photodetector array. The major advantage of this method is that it can be implemented using analog electronics. The disadvantage is that it results in severe bias

at the edges and in a suboptimal spatial resolution. The algorithm requires a linearity correction to improve the distortions at the edges. Figure 2.46 shows the COG result of a measurement on a 49 mm x 49 mm x 5 mm NaI(Tl) based detector [4]. A beam source is positioned on a 5 mm orthogonal grid. The first image (Fig. 2.46(a)) is the result of uncorrected COG (by using formulas 2.37, 2.38 and 2.39). The points close to the edges of the detector are warped towards the center of the detector. The measured data improves when a linearity correction is used (Fig. 2.46(b)).

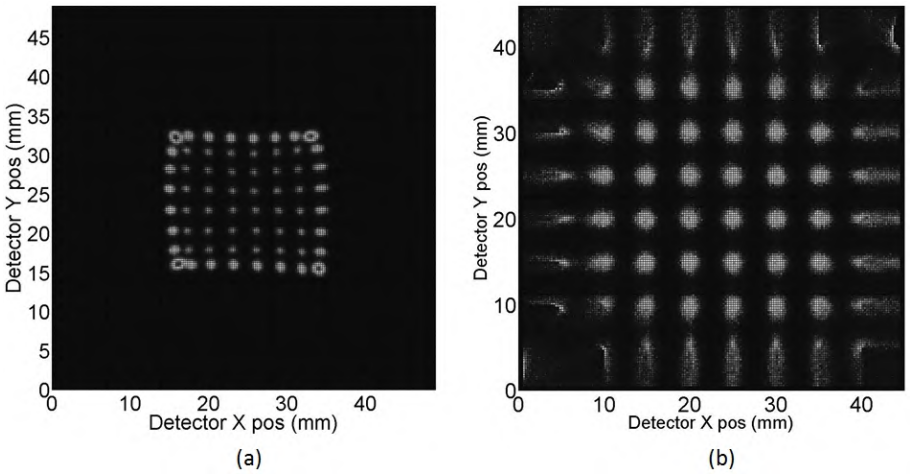

Figure 2.46: (a) COG algorithm without linearity correction and (b)COG algorithm with linearity correction

2.5.2.7.3 Maximum likelihood Estimation (MLE) Maximum likelihood estimation (MLE, [100, 101]) is a technique which requires a more extensive calibration based on an orthogonal grid scan with a beam source. The likelihood that an unclassified event occurred at a certain detector pixel is calculated for all detector pixels. The position assigned to the unclassified event is the detector pixel which has the largest likelihood.

Calibration and event positioning are explained in detail in the following paragraphs.

Calibration Calibration data are acquired by scanning an orthogonal grid with a beam source and acquiring events at each grid position (see Fig. 2.47). The data is energy-windowed so that the majority of the remaining

calibration events are photoelectric events. After this, the event data is scaled to make it independent of energy:

$$ScaledCharge_k = \frac{Charge_k}{\sum_{l=1}^{K}(Charge_l)}, \tag{2.40}$$

where k and l are photodetector channel indexes.

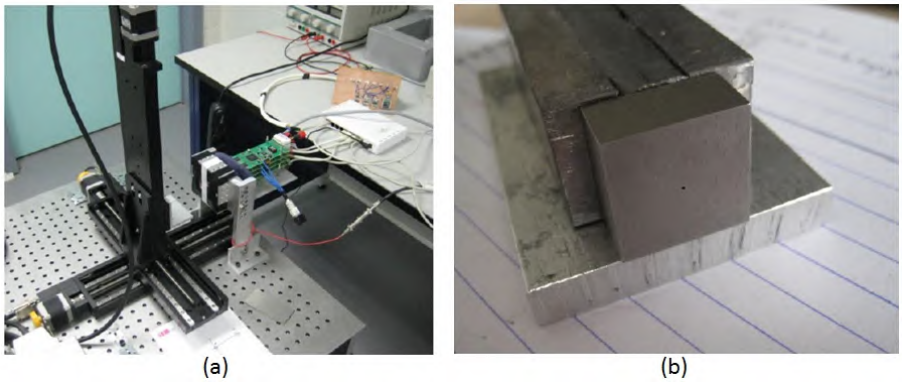

Figure 2.47: (a) A robot stage is used to acquire calibration data. (b) The beam source used to scan the detector consists of a narrow collimated beam.

One can now generate a histogram for each photodetector channel for each calibration position. A Gaussian function is fit to each histogram ([101], others have used a Poisson distribution [100]). This is shown in Fig. 2.48. This results in a mean (μ) and a standard deviation (σ) for each calibration position and for each channel k.

Filtering and interpolation are used to obtain values of μ and σ for a denser grid (see Fig. 2.49). Fig. 2.49 shows the mean value of an anode of a small gamma camera for different event positions, both measured and interpolated values are shown.

Finally, this results in two matrices; one that contains the mean values and one that contains the standard deviations. The number of elements in these matrices equals the number of detector positions (or pixels) multiplied by the number of photodetector channels.

Event positioning An unclassified event is represented by its photodetector values. First, the event data is scaled to make it independent of its energy, similar to the scaling performed on the calibration data (see equation

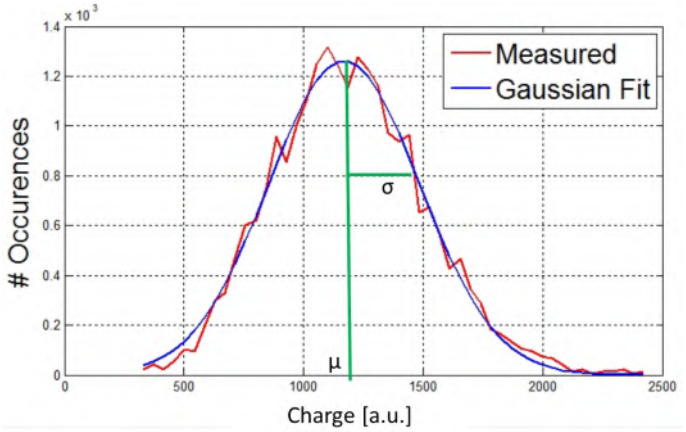

Figure 2.48: A histogram of the charge of a photodetector channel for a certain calibration grid position. The histogram is fit with a Gaussian function.

2.40).

The likelihood that an unclassified event i occurred at detector pixel j is

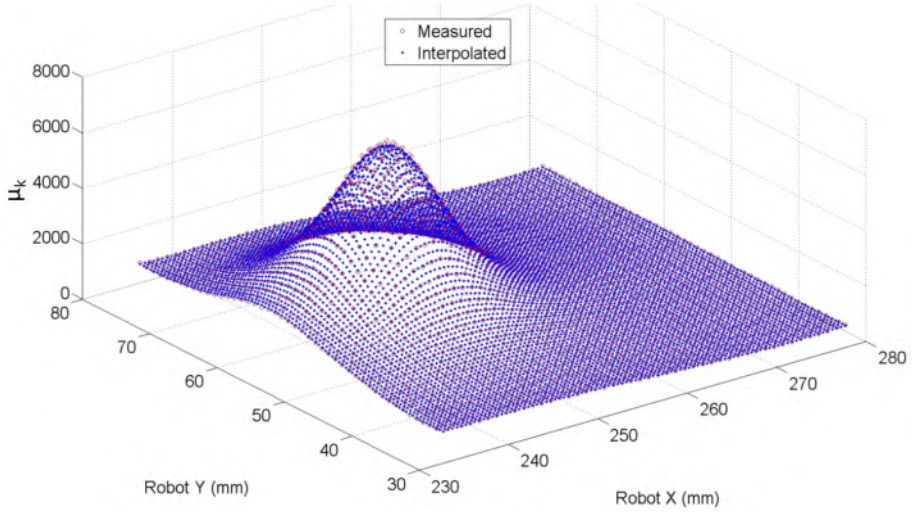

Figure 2.49: The mean value of an anode of a small gamma camera for different event positions. The measured and interpolated values are shown.

calculated as:

$$L_{i,j} = \Pi_{k=1}^{k=K} P_{i,j,k} \tag{2.41}$$

and,

$$P_{i,j,k} = \frac{1}{\sigma_{j,k}\sqrt{2\pi}} \exp\left(-\frac{ScaledCharge_{i,k} - \mu_{j,k}}{2\sigma_{j,k}^2}\right); \tag{2.42}$$

where $P_{i,j,k}$ is the probability that photodetector channel k has a value $ScaledCharge_{i,k}$ when the event would have taken place at the position of detector pixel j. $ScaledCharge_{i,k}$ is the scaled value of photodetector channel k for the measured event i (eq. 2.40). The values $\mu_{j,k}$ and $\sigma_{j,k}$ have been derived from the calibration data (see previous section).

The estimated position of the event i is then set to:

$$Pos_i = \arg\max_j(L_{i,j}). \tag{2.43}$$

The log likelihood is often used because of its ease of calculation:

$$\ln(L_{i,j}) = \Sigma_{k=1}^{k=K} \ln(P_{i,j,k}) \tag{2.44}$$

with

$$\ln(P_{i,j,k}) = -\ln\sqrt{2\pi} - \ln\sigma_{j,k} - \frac{(ScaledCharge_{i,k} - \mu_{j,k})}{2\sigma_{j,k}^2}. \tag{2.45}$$

When log-likelihood is used, then the estimated position of the event is set to:

$$Pos_i = \arg\max_j(\ln L_{i,j}). \tag{2.46}$$

Consider for example an event on a detector with 8 x 8 photodetectors; this event has a measured lightspread as shown in Fig. 2.50. The log-likelihood can now be calculated for each detector pixel, this is shown in Fig. 2.51. The estimate of the point of interaction is then set to the detector pixel with the maximum log-likelihood.

This basic MLE algorithm does an exhaustive search and calculates the likelihood for every detector pixel. One can also use the contracting grid MLE algorithm [102] which starts by searching the best position on a coarse

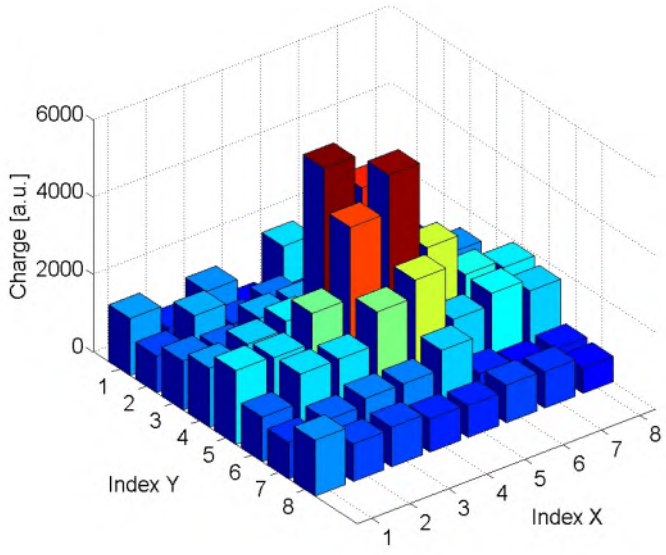

Figure 2.50: The lightspread measured by an 8x8 array of photodetectors for an event in the center of the detector.

grid and gradually makes this grid finer and smaller. The contracting grid algorithm is faster than the exhaustive search because fewer likelihood calculations have to be done.

2.5.2.7.4 k-nearest neighbor (k-NN) k-NN is another event positioning method which also needs an extensive calibration. This method is based on the Euclidean distance between an unclassified event and the events from the calibration data.

It was implemented for positioning scintillator events in a PET detector by Maas et al. [82].

Calibration The calibration data is acquired by performing measurements on a 2D orthogonal grid (similar to the MLE calibration). The data is energy filtered and scaled (eq. 2.40); no further processing is done.

Event positioning The Euclidean distances from the lightspread of the unclassified event i to the lightspreads of all the calibration events j is

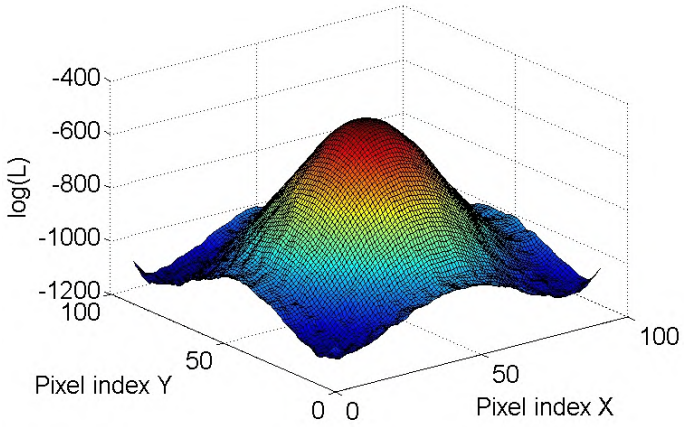

Figure 2.51: The estimate of the point of interaction is set to the detector pixel with the maximum log-likelihood (see formula 2.46).

calculated.

$$Dist_{i,j} = \sqrt{\sum_{k=1}^{K} (ScaledCharge_{i,k} - CalibScaledCharge_{j,k})^2} \qquad (2.47)$$

$ScaledCharge_{i,k}$ is the scaled charge of photodetector channel k for event i. $CalibScaledCharge_{j,k}$ is the scaled charge of photodetector channel k for calibration event j.

A nearest neighbor list of m events is computed which contains the m calibration events with the smallest Euclidean distance and their corresponding calibration position, m is a constant and is typically set to 200 [82]. The position of interaction is now estimated as the calibration position that has most entries in this list.

This method is computationally very demanding, a typical calibration set can contain for example 10^7 events. For one unclassified event, the distance has to be calculated to all the calibration events and after each distance calculation, the nearest neighbor list has to be updated.

Some improvements in accuracy and processing speed of this method are presented in [103]. By making use of the full nearest neighbor list (in stead of only the most occurring calibration position in the nearest neighbor list) they were able to further improve the spatial resolution by approximately 10% to 25%. Processing and calibration speed was improved by using less

calibration events. Additionally, they investigated the usage of a line source in stead of a beam source for calibration; such a line source allows for faster calibration whithout loss of spatial resolution.

2.5.3 Semiconductor detectors

2.5.3.1 Introduction

As opposed to the indirect conversion detectors (scintillation detectors) there are also direct conversion detectors, based on semiconductors. The most frequently used semiconductors for gamma-ray detection are listed in table 2.6.

Semiconductor detectors for gamma photons show a lot of similarities to the photodiodes used to detect light photons. The semiconductor detector is also a diode which is reverse biased and, also here, the depletion region is the only sensitive part of the detector. An incident gamma photon gives rise to one or multiple energetic electrons, these lose energy by ionization and this results in the creation of electron-hole pairs. The electrons and holes drift to opposite sides due to the electric field which is strongly present in the depletion region. This charge movement then leads to an induced current [76][77] which can be sensed by read-out electronics.

The reverse bias voltage should be high to enable efficient charge collection and to obtain a thick and low-capacitive depletion region. This high voltage will result in a leakage current which is inherently noisy. Careful design and adequate cooling should make sure that the noisy leakage current does not mask the small current caused by gamma-radiation.

One of the main drawbacks of scintillation detectors is their moderate energy resolution which is mainly due to the indirect conversion and Poisson statistics. Consider for example a NaI(Tl) scintillator where 26 eV is required to generate a light photon (see table 2.4). However, the photodetector QE should also be considered (typically 35% for a PMT). This means that in fact 74 eV is required to create one photo-electron at the PMT's cathode.

This is different for a semiconductor detector. Here, the amount of collected electron-hole pairs determine the statistics. The energy required to create an electron-hole pair in a semiconductor is much lower than the energy required to create a photoelectron at the photocathode of a PMT-based scintillation camera (see table 2.6). A 140 KeV gamma photon creates about 1892 photo-electrons at the cathode of a typical PMT (considering ideal photon collection) for a NaI-PMT system; the same gamma photon

Table 2.6: Semiconductors for gamma-ray detection [105][106]

Name	Density (g/cm^3)	Att. at 140 keV (cm^{-1})	Required energy per e-h pair (eV)	Band gap (eV)
Si	2.33	0.02	3.61	1.11
Ge	5.32	0.72	2.98	0.66
CdTe	5.85	3.22	4.43	1.44
CdZnTe (CZT)	5.82	3.07	$\sim$5	2.2

creates 28000 electron-hole pairs in a CZT detector. Additionally, the Fano factor of semiconductor detectors is much smaller than 1 (e.g. a value of 0.143 has been reported for silicon [104]). Because of this, the energy resolution of a semiconductor detector is not limited by Poisson statistics but by other noise sources such as the leakage current and the electrode capacitance.

The energy resolution of a CZT detector is approximately 5% for 140 keV gamma photons, while a NaI(Tl) scintillation detector's energy resolution is typically 10%.

Semiconductor detectors are generally more compact than scintillator based detectors and are only minimally affected by the magnetic field of an MR scanner [107].

Two geometries are commonly used for semiconductor detectors: the pixel detector and the double-sided strips detector (DSSD). Pixel detectors use a pixel pattern on one side of the crystal (typically the anode side), see Fig. 2.52(a); the other side (typically the cathode) is a plane. The DSSD, see 2.52(b), uses strips on anode and cathode side. The interaction position has to be estimated by combining the two strips which gave a simultaneous signal. The advantage of the DSSD is the reduction in read-out channels. The drawbacks are that both anode (referred to ground) and cathode (referred to a large bias voltage) have to be read and that the electrode capacitance is larger.

Different semiconductor detectors exist, here we discuss silicon detectors, germanium detectors and CZT detectors. Semiconductor detectors are not frequently used for SPECT systems because of their high price tag. CZT is by far the most frequently used semiconductor detector for SPECT systems [48, 108, 109].

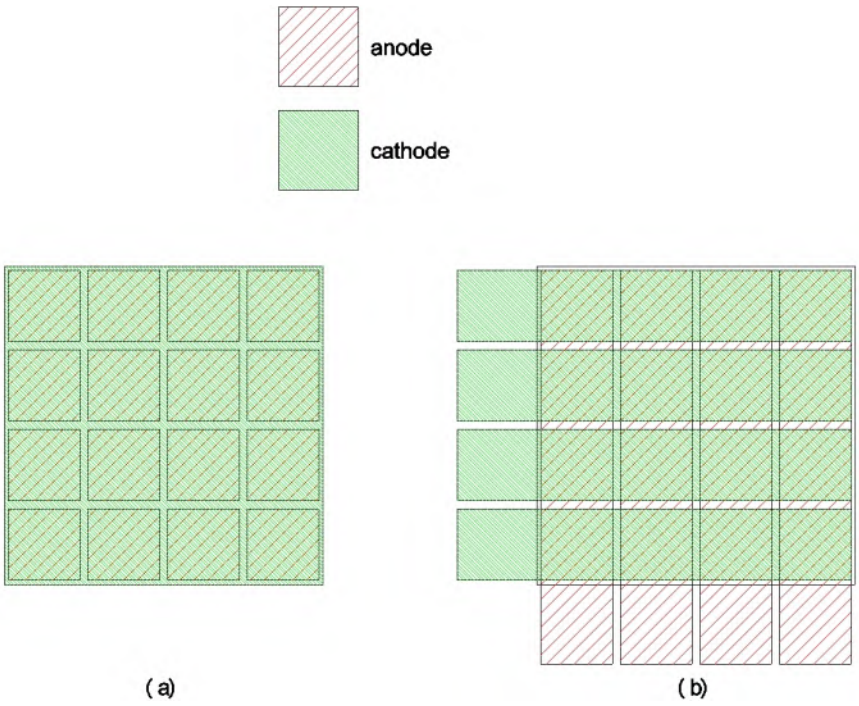

Figure 2.52: (a) A pixelated detector and (b) a double-sided strip detector (DSSD). The advantage of the DSSD is the reduced number of channels.

2.5.3.2 Silicon

Silicon finds wide usage for the production of integrated circuits. Because of this, purified silicon is widely available and a lot of experience in processing silicon is present. Silicon shows good energy resolution and, due to its relatively high band gap, it can be used at room temperature.

The drawback of silicon detectors is their low detection efficiency. The sensitive volume of a semiconductor detector is limited to the depletion region. This region can be enlarged by increasing the voltage; the voltage should however always be less than the diode's breakdown voltage. At fixed voltage, the depletion depth can be further increased by reducing the amount of impurities [33]. Silicon crystals can not be produced with sufficient purity to build thick detectors with high detection efficiency for gamma rays, the maximum thickness of a silicon detector is limited to 2 mm [110]. Several detectors can be stacked to further increase the detection efficiency.

Silicon has been used to image low-energy x-rays and gamma-rays. Shokouhi et al. [111] used a 1 mm thick 60.4 mm x 60.4 mm Silicon DSSD to image ^{125}I; their detector has a detection efficiency of 39% at 30 keV and a spatial resolution of 59 μm.

2.5.3.3 High-purity germanium (HPGe)

Germanium has a good stopping power for gamma rays. In contrast to silicon, high purity germanium is available and this makes it possible to build thick HPGe detectors. HPGe shows an outstanding energy resolution (1% at 140 keV) but the detector needs cryogenic cooling due to the small band gap. Johnson et al. [61] used a HPGe DSSD detector (90 mm diameter, 10 mm thick, cooled to 60 K, 600 V bias voltage) for SPECT imaging. This detector has an energy resolution of 0.96% at 140 keV. The spatial resolution is better than the strip width because the neigboring strips are also used to estimate the position. By doing so a spatial resolution of 1.5 mm is obtained. The detection efficiency is low (43.3%) due to the inter-strip gaps (19% of the detector area) and due to Compton scattered events that distribute their energy across multiple strips.

2.5.3.4 CdTe and CdZnTe (CZT)

CdTe and CdZnTe are semiconductor materials that have found relatively widespread use in SPECT imaging [48, 108, 109, 112–114]. They have a good stopping power for gamma rays (see table 2.6) and they can operate at room temperature. Poor hole-mobility in these semiconductors leads to a depth-dependent signal that results in a low-energy tail in energy spectra. This can also be used advantageously, the DOI can be estimated based on the ratio of the signals from the cathode and the anode [115].

GMI's Triumph triple-modality system [48] uses CZT detectors for the SPECT scanner. These gamma camera's have a surface of 12.7 cm x 12.7 cm; they consist of 5 x 5 CZT tiles. Each tile is a 16 x 16 pixel module; the pixel pitch is 1.6 mm. Different CZT modules are tiled because CZT is not available in large sizes.

2.6 SPECT image reconstruction

2.6.1 Introduction

The first part of this introductory chapter has focused on SPECT instrumentation. The instrumentation allows to acquire projection data which are acquired for a multitude of angles. Image reconstruction is used to derive from this projection data a three-dimensional image of the tracer distribution.

There are two classes of image reconstruction algorithms: analytical reconstruction algorithms (e.g. filtered back projection) and iterative reconstruction algorithms (e.g. maximum likelihood expectation maximization).

Filtered back projection (FBP) is an analytical reconstruction algorithm and is still commonly used for CT scanners. These scanners use large projection data (high-resolution detectors are used and data are acquired for numerous angles) that have to be reconstructed in a reasonable amount of time, and, due to this, FBP is used. Additionally, the line integrals used by the FBP algorithm are a good approximation of the CT acquisition geometry. Finally, data are high-count which means that extensive noise-modeling is not necessary.

The situation is different for SPECT imaging [116], where the projection data are smaller, and, the reconstruction speed is less of an issue. Here, iterative methods are mostly used because they allow for better modeling of the imaging chain (collimator resolution, detector resolution, scattered gamma photons, attenuation in the patient) which results in higher resolution and less noisy images. Due to this, iterative reconstruction methods generally provide better image quality than the analytical methods.

In the next section we describe the general iterative approach and the maximum likelihood expectation maximization (MLEM) algorithm. MLEM is currently the most frequently used algorithm for SPECT and PET image reconstruction.

2.6.2 Algorithm

The projection data acquired by the gamma camera can be modeled as:

$$p_i = \int_{FOV} f(x, y, z) h_i(x, y, z) dxdydz. \tag{2.48}$$

Where p_i represents the value of detector pixel for a certain acquisition

angle ($i \in [1 \quad I]$, with $I = A \times D$, where A is the number of angles and D the number of detector pixels), the total set p contains all detector pixels at all projection angles. The $h_i(x, y, z)$ kernel represents the probability that a photon originating at position (x, y, z) is detected by pixel/angle i; this kernel is a mathematical description of the system. It includes physical effects like sensitivity, resolution and collimator penetration. The tracer distribution is represented by $f(x, y, z)$. The task of image reconstruction is to find back f based on the projection data $\mathbf{p}$ and a derived system description h.

The tracer distribution f is described here as a continuous function. In practice, f is discretized to voxels. The equation then becomes:

$$p_i = \Sigma_{k=1}^{K} f_k h_{ik}. \tag{2.49}$$

Here, f_k represents the tracer concentration in voxel k; K is the total number of voxels. The system is now described by a matrix: h_{ik} is the probability that a photon originating in voxel k is detected by detector pixel/angle i. The matrix $\mathbf{H}$, which contains the elements h_{ik} with $i \in [1 \quad I]$ and $k \in [1 \quad K]$ is called the system matrix.

Equation 2.49 can now be rewritten as a matrix multiplication:

$$\mathbf{p} = \mathbf{H}\mathbf{f}. \tag{2.50}$$

The better $\mathbf{H}$ describes the SPECT system, the more accurate the reconstructed image $\hat{\mathbf{f}}$ will be. The problem, to estimate $\hat{\mathbf{f}}$ from $\mathbf{p}$ and $\mathbf{H}$, is solved by making use of iterative methods that search a solution by successive estimates.

The basic iterative reconstruction scheme is shown in Fig. 2.53. The first image estimate is typically a uniform image. This image is forward projected to derive the estimated projections, these are then compared with the measured projections. This comparison results in a projection error, which is backprojected to obtain an error in image space. The image error is used to update the image estimate. This loop is executed several (typically 30-500) times to obtain the final image estimate.

The iterative algorithms differ in the way that the projections are compared and the image estimate is updated.

Maximum likelihood expectation maximization (MLEM) [117] takes Poisson noise on the projection data into account; MLEM calculates the 3D image that has the highest likelihood to produce the measured projections

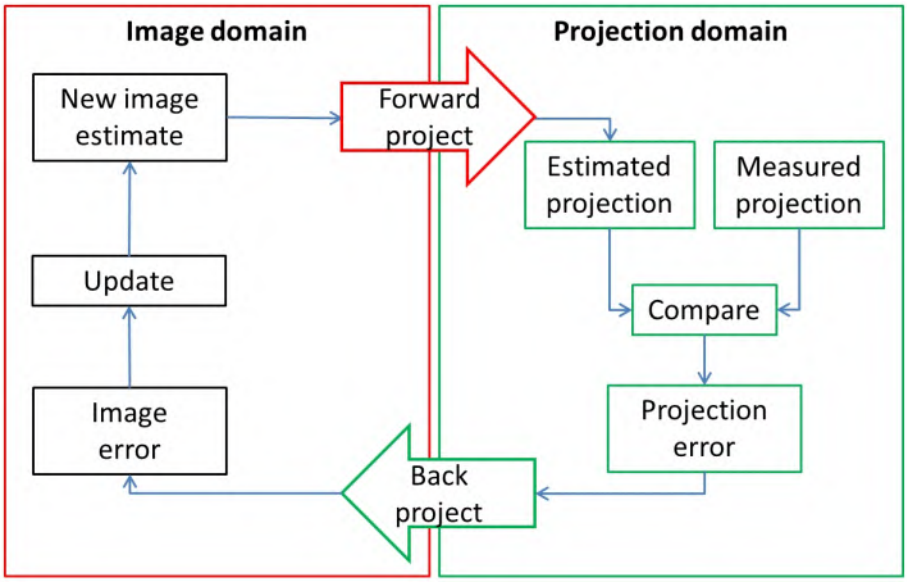

Figure 2.53: Iterative image reconstruction algorithms differ in the way the calculated and measured projections are compared, and, in the way the image estimate is update.

$\mathbf{p}$. Here, the comparison step is a division of the estimated projections by the measured projections, the update step is a multiplication by the image error. This is depicted in 2.54.

MLEM can be mathematically described as:

$$f_k^{t+1} = \frac{f_k^t}{\Sigma_{i=1}^{I} h_{ik}} \Sigma_{i=1}^{I} h_{ik} \frac{p_i}{\Sigma_{k=1}^{K} h_{ik} f_k^t}, \tag{2.51}$$

where t is the loop index.

The start image f^0 for this iterative algorithm is typically set to a uniform non-zero image. The MLEM algorithm can be subdivided into several steps.

In a first step, image estimate f^t is forward projected:

$$FWProj = \Sigma_{k=1}^{K} h_{ik} f_k^t \tag{2.52}$$

The forward projected estimate is then compared to the measured pro-

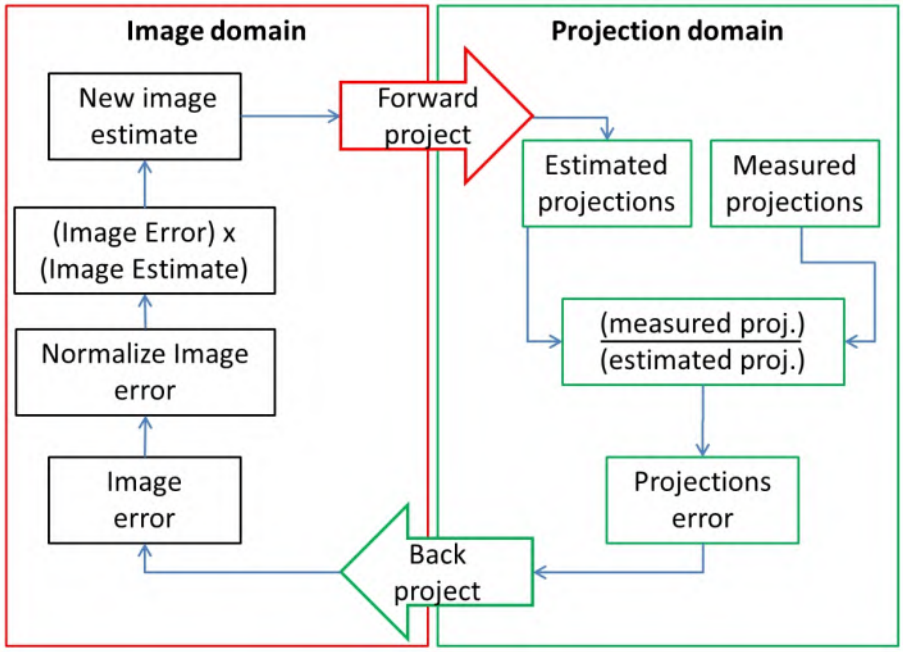

Figure 2.54: The iterative MLEM image reconstruction algorithm.

jections by taking the ratio:

$$Comp_i = \frac{p_i}{FWProj_i}. \tag{2.53}$$

This comparison is backprojected into image space:

$$BackProj_k = \Sigma_{i=1}^{I} h_{ik} Comp_i. \tag{2.54}$$

The new image estimate is then calculated as the backprojected data, normalized and multiplied by the current image estimate:

$$f_k^{t+1} = \frac{f_k^t}{\Sigma_{i=1}^{I} h_{ik}} BackProj_k \tag{2.55}$$

Fig. 2.55 depicts a reconstructed Derenzo phantom at 10, 50 and 100 iterations. Increasing the number of iterations results in improved resolution but also in a noisier image.

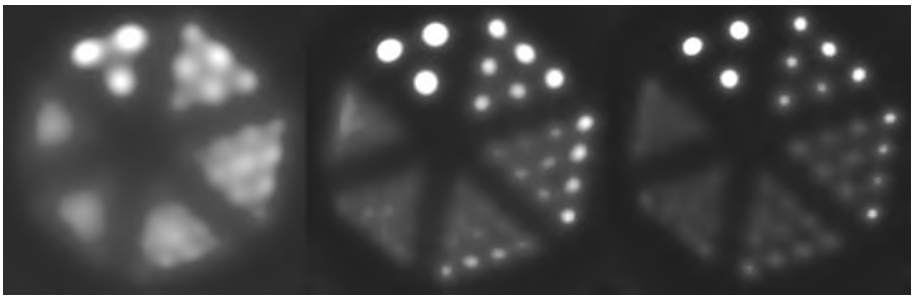

Figure 2.55: Reconstructions of a Derenzo phantom at 10, 50 and 100 iterations.

2.6.3 System matrix

In the previous section we have introduced the concept of iterative image reconstruction. Image reconstruction makes use of forward projection from image to projection domain, and, of back projection from projection domain to image domain. These steps are described by eq. 2.52 (forward projection) and by eq. 2.54 (back projection). Both equations make use of the system matrix $\mathbf{H}$. This matrix is a description of the SPECT system, it contains the detector response (or point-spread function) of each voxel.

In practice, the forward and back projection operators can be implemented in two ways.

A first method does not store the full system matrix but calculates its elements on the fly. Forward projection is implemented by ray-tracing from each voxel, through the collimator hole(s) onto the detector. Back projection is implemented by tracing a ray from each detector pixel through the collimator hole(s) and through the image space. Resolution modeling can be done by using, for example, several rays for a collimator hole [118]. The advantage of this approach is that it is easier to incorporate patient dependent effects (such as patient attenuation).

The second method uses a full system matrix which has been calculated in advance (before performing actual reconstructions). This computation can take a substantial amount of time and has to be repeated when the geometry changes. The system matrix is large and is stored as a sparse matrix to reduce computation time and computer memory. System matrix calculation can be (partially) based on measurements of the system matrix. Such measurements include stepping a small point source through the image space by making use of a 3D robot stage. By using measurements the whole instrumentation chain is taken into account and, one can accurately define

the system matrix, which can result in an additional gain in system resolution [119].

2.7 Summary

In this introductory chapter we have introduced the complete SPECT imaging chain.

The most frequently used collimators have been presented and we have introduced the two main collimator performance parameters: sensitivity and resolution. The collimator geometry that will be presented in chapter 4 is derived from the pinhole collimator.

We have also introduced the different detector types. In the next chapter and in chapter 6 we present two compact scintillator-based high-resolution detectors. We have also introduced three event-positioning algorithms; an additional new algorithm will be introduced in chapter 6.

Two pre-clinical SPECT systems have been built that use these components; these are presented in chapters 5 and 8. Image quality phantoms have been measured on both systems and the images have been reconstructed using MLEM, this image reconstruction method was introduced here in section 2.6.

Chapter 3

A compact high-resolution detector based on a NaI(Tl) scintillator

3.1 Introduction

This chapter focuses on a high-resolution gamma ray detector. In the introduction we will first present some existing detector designs, then the advantages of high-resolution detectors will be discussed. Finally, we will introduce the concepts of our detector.

Other researchers have presented high-resolution detectors before. Some of these detectors offer an impressive intrinsic resolution but have the drawback of a mediocre energy resolution and/or detection sensitivity. In most cases, a high spatial resolution scintillation detector is obtained by minimizing the lightspread on the photodetectors which can be done by using a thin scintillator. However, the drawback of this is a lower detection sensitivity. Additionally, reflectors on the scintillator are sometimes avoided and this has as consequence a worse energy resolution. Miller et al. [120] developed a high-resolution detector for the FastSPECT III system that consists of a thin columnar CsI(Tl) scintillator, an image intensifier and a fast-frame-rate charge-coupled device (CCD). The intrinsic resolution of this detector is 100 μm. Others used an EMCCD in combination with thin columnar CsI(Tl) scintillators [99]. A drawback of these detectors is their low sensitivity due to the thin scintillator. SiPMs and an EMCDD were coupled to a 3 mm thick CsI(Tl) scintillator by Heemskerk et al. [98]. Such a detector has a

better detection efficiency (66%) due to the thicker scintillator; a spatial resolution of 160 μm and an energy resolution of 49% was obtained for 140 keV gamma rays. Pani et al. compared several scintillators [121] and achieved an energy resolution of 9% and an intrinsic resolution of 0.9 mm with a 5 mm thick $LaBr_3(Ce)$ scintillator coupled to a PSPMT. Drawbacks of this scintillator material are its high cost and the fact that $LaBr_3(Ce)$ is more hygroscopic than $NaI(Tl)$. Finally, Meng et al. [114] have build a semiconductor gamma-ray detector, based on 1 mm thick CdTe with a pixel pitch of 350 μm. Drawbacks of this detector are the low detection efficiency (due to the thickness of the detector), the complexity of the read-out system and the high cost. On the other hand, solid state detectors like this have an outstanding energy resolution (3% FWHM at 140 KeV).

All SPECT systems suffer from the resolution-sensitivity trade-off. Rogulski et al. [28], Nillius et al. [36], Goorden et al. [29] and Van Holen et al. [1] have studied this in detail and have shown the benefits of high-resolution detectors for pinhole SPECT systems. A high-resolution detector could for example lead to a higher sensitivity [1, 28, 29] or to a more compact SPECT system [1, 36]. Van Holen et al. [1] have developed a design procedure for SPECT systems that use cylindrical detectors and collimators; this procedure derives the system having the highest system sensitivity, based on a certain target system resolution. One of the input parameters of this procedure is the intrinsic detector resolution R_i. When a higher-resolution detector is used then less magnification is required and the detector can be positioned closer to the pinhole. By doing so, more pinholes and detectors can be positioned and, the system sensitivity increases. A fact that is often overlooked is that the mechanical design of a SPECT system becomes less complicated (especially when it is a non-stationary system) if several compact high-resolution detectors are used instead of bulky low-resolution detectors that require a large magnification.

The standard clinical detectors use a thick (9.5 mm) and large NaI(Tl) scintillator coupled to an array of PMTs. The COG-algorithm is used for event positioning. Such detectors typically have a spatial resolution of 3 mm and an energy resolution of 10 %. Several design decisions were made for our detector to improve the spatial resolution. First, we replaced the thick NaI(Tl) scintillator by a 5 mm thick NaI(Tl) scintillator, this will make the light spread smaller. The readout of this scintillator is not done by PMTs but by a PSPMT, this allows to sample the light spread with a higher resolution. Finally, an MLE algorithm is used to position the events.

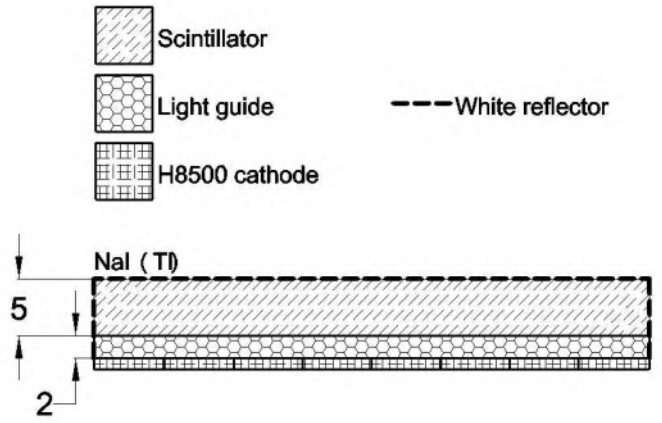

Figure 3.1: The NaI(Tl) scintillator. Dimensions are in mm.

3.2 Scintillator and PSPMT

A NaI(Tl) scintillator is used for our detector. NaI(Tl) is frequently used for SPECT detectors and due to this it can be obtained from several vendors at an acceptable price. Besides this, it also has a high light output. The main drawback of NaI(Tl) is that it is hygroscopic and requires packaging. Our NaI(Tl) scintillator has a 49 mm x 49 mm surface and is 5 mm thick. The scintillator has reflecting edges and top surface to improve the amount of detected light photons, which results in an improved energy resolution (eq. 2.24). The scintillator is depicted in Fig. 3.1.

The Hamamatsu H8500 PSPMT is optically coupled to this scintillator. This PSPMT has 8x8 anodes and an active area of 49 mm x 49 mm. We also considered the Hamamatsu H9500 PSPMT; this PSPMT has 16x16 anodes. It is however an expensive device and it is not possible to implement the readout of this PSPMT using commercial off-the-shelf parts on a compact printed circuit board (PCB). SiPMs were not considered for this design because these devices were not yet widespread and still very expensive at the time of development. The high-voltage of the PSPMT is set to 900V. The voltage was decreased from 1000V to 900V after observing saturation effects at high count rates. These effects are probably caused by the increase in anode current when the count rate is high.

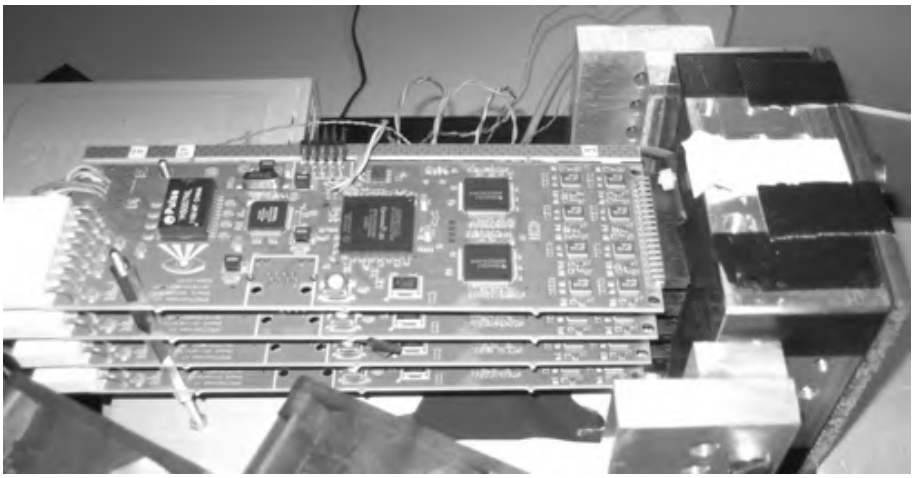

Figure 3.2: Four boards are used to do the readout of the PSPMT. The PSPMT and scintillator are in the aluminum block on the right.

3.3 Readout electronics

The Hamamatsu H8500 PSPMT has 64 anodes, these are connected to 4 output connectors, those connectors all have a similar pin out. Because of this, four identical boards are used for readout of the whole PSPMT. The nickname *SPECTatress readout* was given to these boards. Fig. 3.2 shows the complete detector.

Such a readout board digitizes and processes 16 channels. A 1 Gbit Ethernet switch is used to connect the 4 boards to a PC. Fig. 3.3 shows the different parts of the readout printed circuit board (PCB). The PCB has 10 layers, this was necessary for several reasons: some of the traces are impedance controlled traces and require a reference plane, digital and analog traces have to be separated to avoid crosstalk issues and finally, a large amount of power supplies are used and each power supply requires a local plane.

3.3.1 Pre-amplifier

Traditional pre-amplifiers for a PMT consist of an integrating amplifier (with active or passive reset) and a pulse-shaper. The output of the pulse-shaper is then digitized by an analog to digital converter (ADC). These circuits often have AC-coupling and require an analog baseline correction circuit.

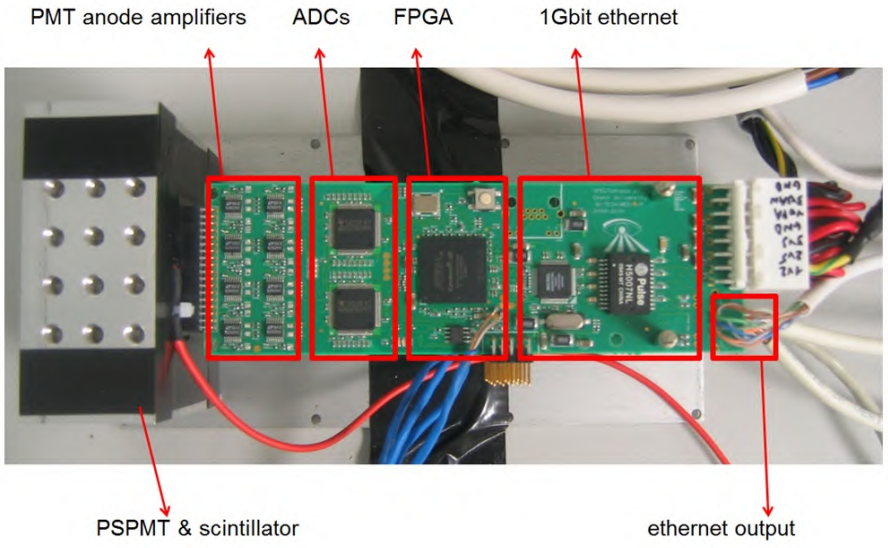

Figure 3.3: The PCB has the following circuitry (from left to right): pre-amplifiers, ADCs, FPGA and Ethernet circuitry.

The footprint of the total circuit when implemented with off-the-shelf components is rather large.

For this reason a different approach was used for the readout electronics of our detector. A compact low-pass filtering current to differential voltage amplifier has been designed (Fig. 3.4). In contrast to traditional pre-amplifiers, where the PMT current is integrated using analog electronics, the amplifier output is digitized and the integral is calculated as a discrete sum in the field-programmable gate array (FPGA). An FPGA is used to process the data because FPGAs can be reprogrammed and are much less expensive (for small batches) than application specific integrated circuits (ASIC).

Fig. 3.5 shows a simulation of a current pulse from a PMT anode (I(PMTAnode)) and the output of the pre-amplifier (V(Outlp+) and V(Outlp-)); the 99% settling time is 2.1 μs. The integral of the differential output voltage (V(Outlp+) - V(Outlp-)) over the length of one pulse (3 μs in Fig. 3.5) is proportional to the integral of the current (I(PMTAnode)) over the length of one pulse, and, is thus also proportional to the amount of electrons collected by one of the anodes of the PSPMT.

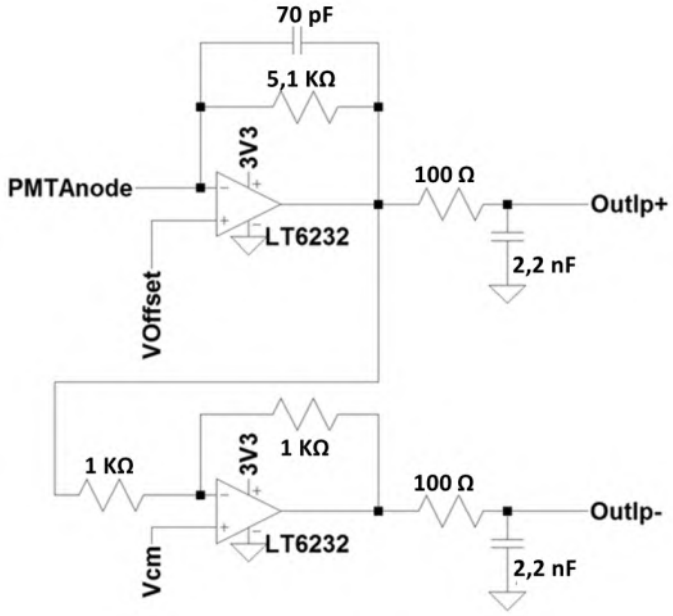

Figure 3.4: The pre-amplifier converts the anode current to a differential voltage which is suitable to be digitized by the ADC. Voffset and Vcm are bias voltages.

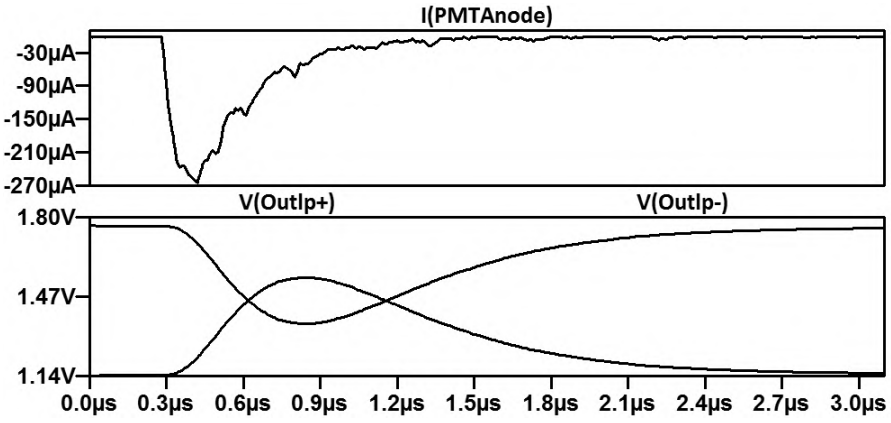

Figure 3.5: A SPICE simulation of the pre-amplifier. V(Outlp+) is the positive pulse, V(Outlp-) is the negative pulse. Both output voltages have a positive DC offset, this is caused by the positive Voffset voltage in the first stage of the pre-amplifier circuit. The offset is required to bring the differential voltage within the input range of the ADC.

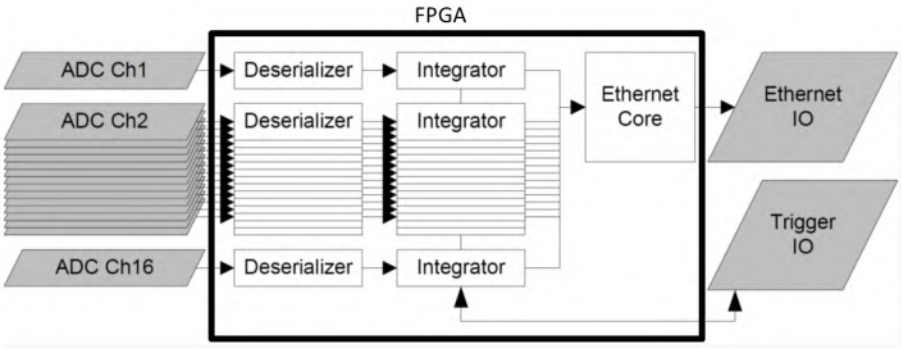

Figure 3.6: FPGA block diagram.

3.3.2 Analog to digital conversion

Each analog channel is digitized using one channel of an eight-channel ADC (ADS5270). The main reason for selecting this ADC is that it provides 8 channels in a small package; additionally, the serialized LVDS (low voltage differential signaling) outputs make PCB routing easier (only 10 digital differential signals are required for 8 analog inputs) and only require a small amount of FPGA pins. The ADC's maximal sampling frequency is 40 MHz and it has a 12 bit resolution, in this design the ADC uses a sampling frequency of 20 MHz (40 MHz would probably not improve performance and it has the drawbacks of a higher power consumption and more stringent FPGA input/output constraints).

3.3.3 Digital processing

A block schematic of the FPGA is depicted in Fig. 3.6. The main blocks are the deserializers, the integrators and the Ethernet core. The deserializers convert the high-speed serial data streams from the ADCs to low-speed parallel data streams. These parallel streams can then easily be processed in the FPGA.

The integrators integrate the voltage pulses from the preamplifier. A flowchart of an integrator is shown in Fig. 3.7.

When an incoming ADC sample exceeds the baseline by a certain threshold, then a trigger is launched which triggers the other 15 channels and the other three boards of the detector. This trigger starts the integration; during a time period c_{PD} (pulse duration constant) all samples are accumu-

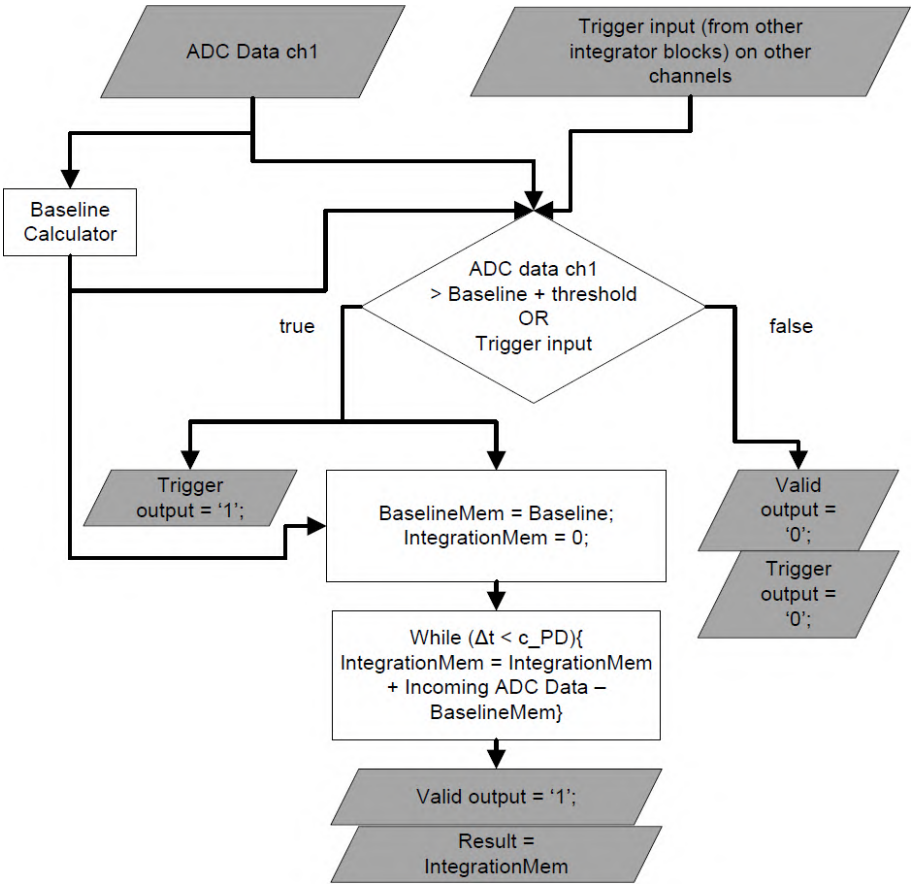

Figure 3.7: Flowchart of the integrator of channel 1.

lated while the baseline is subtracted (c_{PD} is 2.5 μs, related to the settling time of the input amplifier, 50 samples are used to calculate the integral result).

The histogram of the incoming ADC data (Fig. 3.8) during a fixed period will show a peak at the ADC code of the baseline (provided that the amount of pulse pile-up still allows the signal to settle to the baseline). The baseline searching algorithm (Fig. 3.9) searches for the peak in the histogram in a sequential way. The first step counts the number of occurrences of a certain ADC value (this variable is called V). The second step updates the baseline variable with V if it occurred more than the baseline occurred. The third step updates V; V sweeps through a range from c_L to c_U. The baseline of a

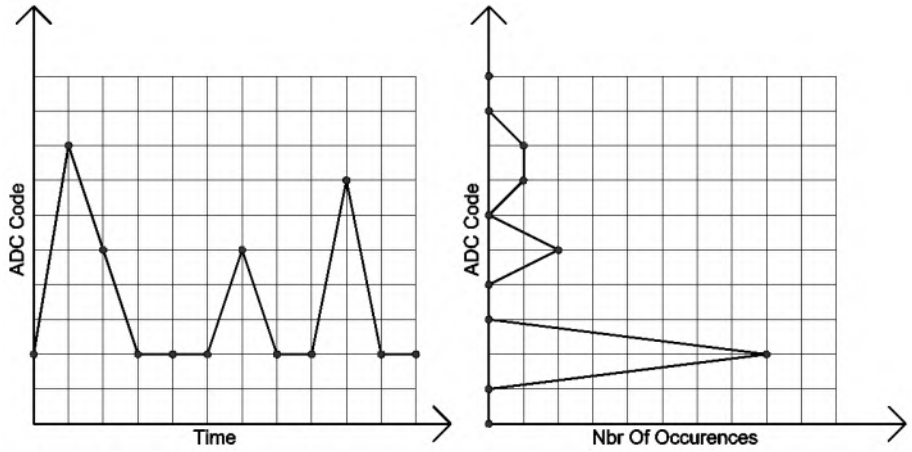

Figure 3.8: Histogram of the ADC Data.

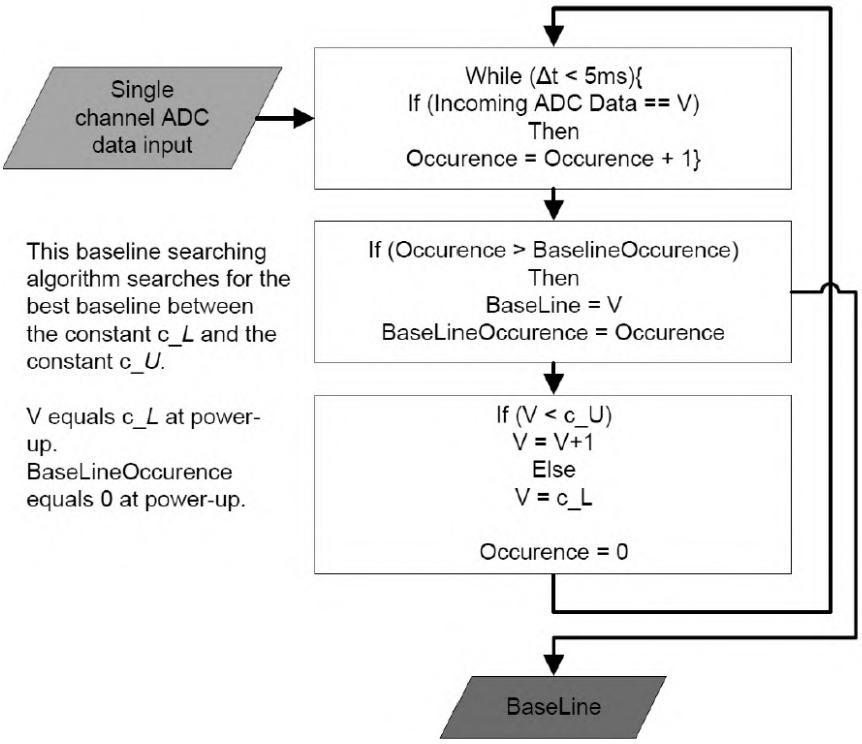

Figure 3.9: Flowchart of the baseline searching algorithm.

channel is searched independently from the other channels; each channel can have a slightly different baseline and this is mainly due to resistor tolerances in the pre-amplifier.

Each integrator outputs a 24-bit number. This number is converted to a 13-bit floating point value (10 significant bits, 3 exponent bits) to lower the amount of data that has to be transferred to the PC. A 140 keV interaction in a NaI(Tl) scintillator results in approximately 5000 light photons that are spread over the PSPMT cathode. We expect that a 13-bit floating point number provides adequate dynamic range for one PSPMT channel; it was not verified if more or less bits improve or deteriorate the performance. The 16 floating point integrator results are stored in a FIFO (first in, first out) memory. Data from the FIFO are then put in an Ethernet packet when 20 events are available. The used Ethernet standard is 1000Base-T (1 Gbit/sec), no additional protocols (e.g. TCP/IP) are used.

3.4 Event positioning software

The Ethernet packets are stored in a list mode file using a C++ program that uses the WinPcap libraries [122]. A contracting grid graphics processing unit (GPU) accelerated MLE algorithm is implemented for the event localization.

3.4.1 Calibration

The MLE algorithm requires calibration and this was done using a positioning robot and a beam source (355 μm beam diameter, 140 keV ^{99m}Tc, see Fig. 3.10). The beam source is scanned on a Cartesian grid (1 mm step, 46 x 46 positions) and 5000 events are measured at each position. The scintillator measures 49 mm x 49 mm but only 45 mm x 45 mm is calibrated with the beam source; this is done because event positioning on the edges of the scintillator shows a large bias and, because the calibration time is slightly reduced by not calibrating the edges of the scintillator.

Events recorded at a position are filtered to remove the scattered events. This is done in a first step by energy windowing and in a second step by using an Anger mask [123]. The Anger mask is a filter that only passes events whose centroid position is within a certain distance (1 mm) of the average centroid position of all the energy-filtered events (a 20% window is used); this is depicted in Fig. 3.11.

A histogram based on the filtered events is then generated for each anode at each robot position and a Gaussian distribution is fit to each histogram.

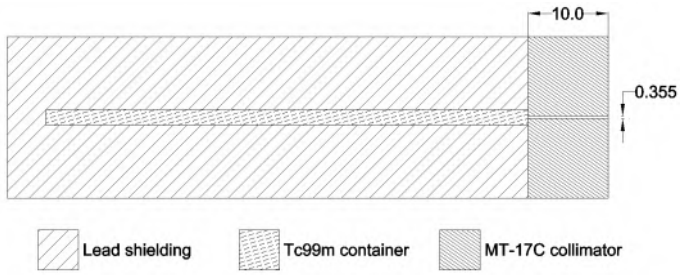

Figure 3.10: The beam source which was used for the calibration and measurements. The hole length of the collimator is 10 mm, the hole diameter is 355 μm . This collimator is made of MT-17C (Midwest Tungsten, USA, see section 2.3 for more information). The ^{99m}Tc container is typically filled with a total activity of about 370 MBq.

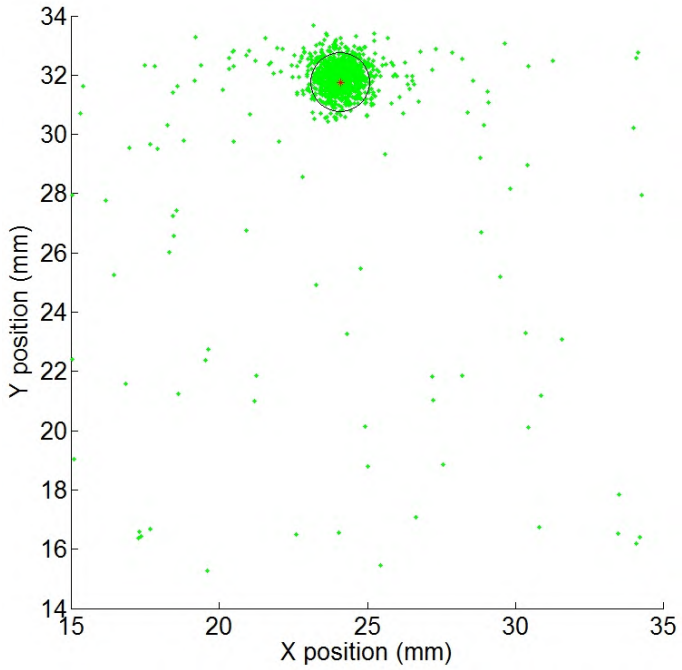

Figure 3.11: All the energy-filtered events of one calibration position are positioned using the COG algorithm (green dots in the graph). The mean position is calculated (red dot in the graph). Events whose position is more than 1 mm away from this mean are not used for the calibration. The black circle depicts this 1 mm border.

The *mean* and *variance* of this Gaussian fit are stored (see Fig. 2.48 and section 2.5.2.7.3).

An energy histogram is made for each robot position. The energy channel containing most events (the *peakchannel*) is stored.

Additional filtering and generation of additional calibration points is done by interpolating the *means*, *the variances* and the *peakchannels* in relation to the calibration position. For this measurement interpolation was used to obtain a 500 μm grid.

3.4.2 Event positioning algorithm and energy windowing

The MLE algorithm calculates the likelihood that an unclassified event occurred at a calibration position; the position having the highest likelihood is selected as the position of interaction (this is explained in section 2.5.2.7.3). The basic MLE algorithm does an exhaustive calculation and calculates the likelihood for every calibration position. We use the contracting grid MLE algorithm [102] which starts by calculating a coarse grid and searching the best position on this coarse grid, the grid is then gradually made finer and smaller. The contracting grid algorithm is faster than the exhaustive search because fewer likelihood calculations have to be done; it exploits the fact that the likelihood surface is convex

When the event has been positioned it is filtered by energy windowing. The energy window is centered on the *peakchannel* of the event position. The energy window width is fixed for the whole detector (a window of 28 KeV, equal to 20% at 140 keV, is used).

Events that interact in the detector outside the 45 mm x 45 mm calibrated area are positioned on the border of the calibrated area by the MLE algorithm. After positioning, an outside border of 1 mm is removed from the detector image to remove those events. This results in a usable detector area of 44 mm x 44 mm.

3.5 Spatial resolution and bias measurements

The spatial resolution and bias are measured by scanning the detector with a beam source (Fig. 3.10, 140 keV ^{99m}Tc) on a Cartesian grid of points, spaced by 5.5 mm (9 x 9 positions). 50000 Events were recorded at each position. The distance from the beam source's collimator to the detector was 1 mm. The resulting data are processed with the MLE contracting grid

algorithm. An energy window of 28 KeV is used. The result is shown in Fig. 3.12.

One dimensional Gaussian functions are fit on horizontal and vertical profiles of the detector image. The spatial resolution of the detector ($FWHM_D$) is then equal to the FWHM of this Gaussian ($FWHM_{Gaussian}$) corrected for the beam diameter (D_{Beam}):

$$FWHM_D = \sqrt{FWHM_{Gaussian}^2 - D_{Beam}^2}. \quad (3.1)$$

A value of 355 μm is used for the beam diameter (D_{Beam}). In reality the beam diameter is slightly larger because of penetration; additional beam broadening takes place because the beam source collimator is at a non-zero distance from the detector. The results that we obtain using eq. 3.1 are thus a slight underestimation of the detector's spatial resolution.

The bias is defined as the distance from the beam position on the robotic stage to the μ (the mean) of the Gaussian fit on the detector image.

Spatial resolution and bias are the best in the center of the detector and worsen towards the edges of the detector; the mean FWHM and bias of all the beams is calculated for the full field of view (FOV) and for the central field of view (CFOV, the length and width of the CFOV are 75% of the length and width of the FOV, 33 mm x 33 mm).

The spatial resolution over the whole FOV is 1.64 $\pm$ 1.13 mm FWHM; the bias is 0.59 $\pm$ 2.25 mm. The worst spatial resolution and bias are positioned in the four corners of the detector; if we ignore those beam positions, then a spatial resolution of 1.42 $\pm$ 0.29 mm and a bias of 0.22 $\pm$ 0.18 mm is obtained.

The results are better for the CFOV because those do not contain the beam measurements close to the edges of the scintillator. In the CFOV a resolution of 1.24 $\pm$ 0.13 mm and a bias of 0.11 $\pm$ 0.05 mm were measured.

The results are summarized in table 3.1.

Fig. 3.13 shows a profile through this detector view at position X equal to 21.5 mm and Fig. 3.14 plots a profile at position Y equal to 21.5 mm. Gaussian functions have been fitted to the peaks in the profiles and these are used to calculate the full width at half maximum (FWHM).

For a comparison, we have also performed COG event positioning. After linearity correction, a spatial resolution of 1.95 mm is found for the central 5x5 beam positions (see Fig. 3.15).

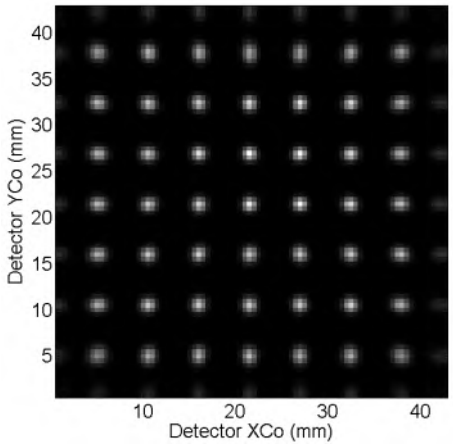

Figure 3.12: Detector view of the 5.5 mm grid scan (9 x 9 positions). The usable detector area is 44 mm x 44 mm.

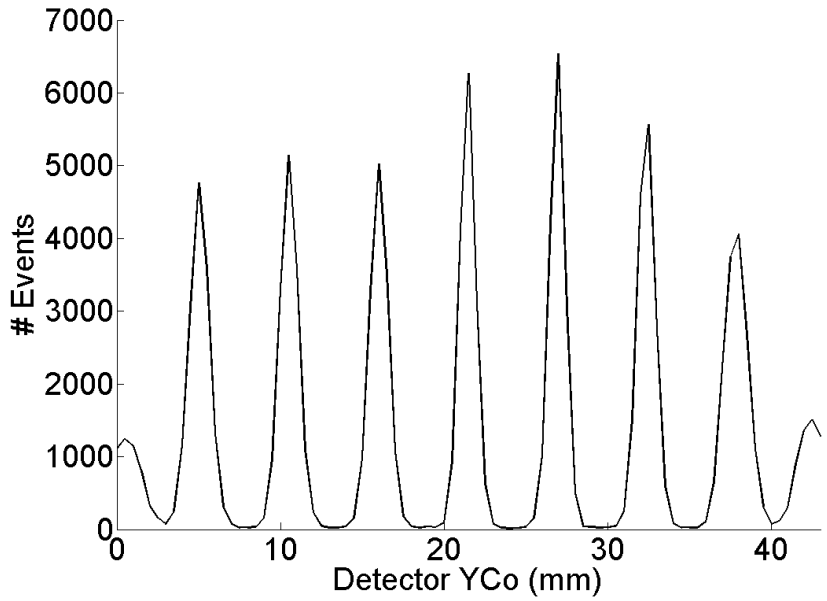

Figure 3.13: Profile of Fig. 3.12 at X=21.5 mm. The peaks have a (beam diameter corrected) FWHM of 2.2 mm, 1.4 mm, 1.3 mm, 1.3 mm, 1.0 mm, 1.0 mm, 1.1 mm, 1.7 mm and 2.0 mm (from left to right).

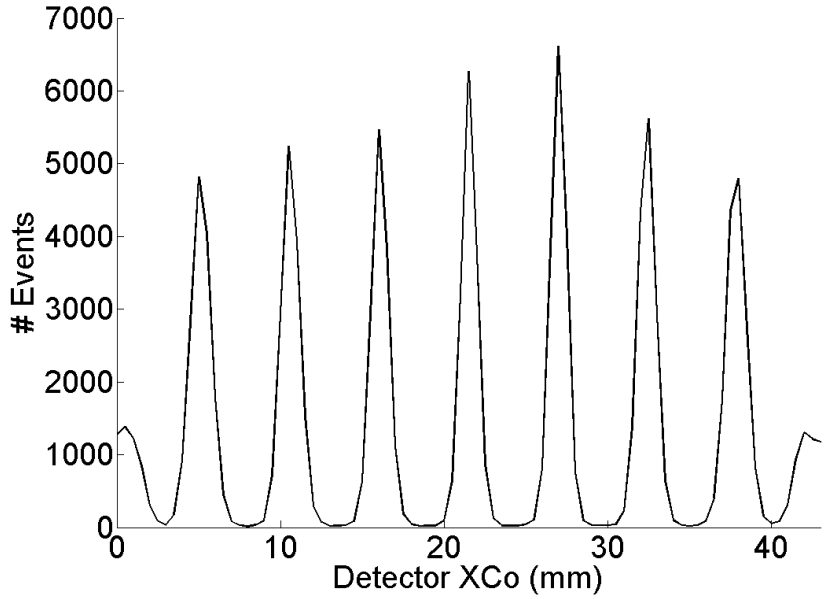

Figure 3.14: Profile of Fig. 3.12 at Y=21.5 mm. The peaks have a (beam diameter corrected) FWHM of 2.1 mm, 1.4 mm, 1.3 mm, 1.1 mm, 1.0 mm, 1.0 mm, 1.1 mm, 1.4 mm and 2.1 mm (from left to right).

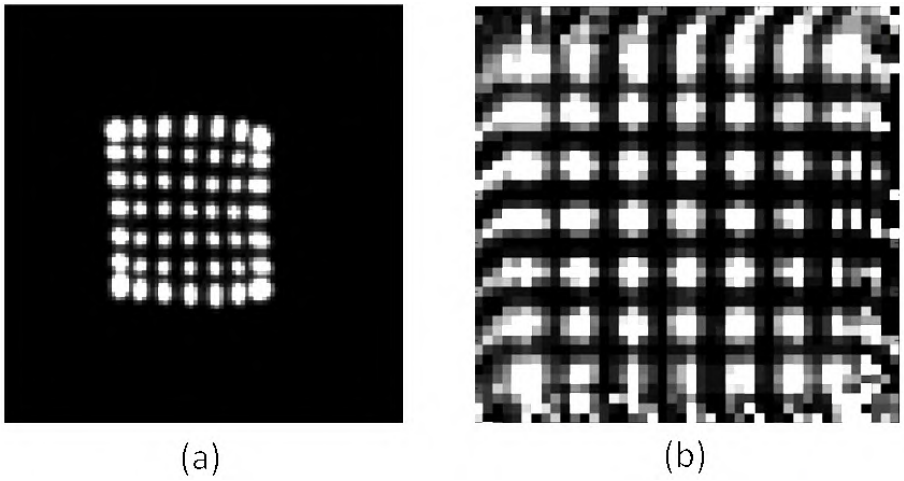

Figure 3.15: COG Event positioning (a) and linearity corrected COG event positioning (b). Only the central 5x5 beam positions can be distinguished. The mean spatial resolution of the central 5x5 beam positions is 1.95 mm.

Table 3.1: Spatial resolution

	NaI(Tl)
Mean FWHM FOV (mm)	1.64 ± 1.13
Mean FWHM FOV, corners excl. (mm)	1.42 ± 0.29
Mean FWHM CFOV (mm)	1.24 ± 0.13
FWHM center (mm)	1.0
Mean bias FOV (mm)	0.59 ± 2.25
Mean bias FOV, corners excl. (mm)	0.22 ± 0.18
Mean bias CFOV (mm)	0.11 ± 0.05

3.6 Energy resolution measurements

An energy spectrum of each measurement on the 5.5 mm grid (section 3.5) is generated. This allows to examine the energy resolution at different positions on the detector.

Fig. 3.16 shows the energy spectrum of a beam source positioned in front of the center of the detector (X=21.5 mm and Y=21.5 mm). A Gaussian function has been fit to the peak of the spectrum and this peak has a FWHM of 9.3%. The energy resolution changes over the detector surface (Fig. 3.17). The average energy resolution over the detector is 9.3 ± 0.04%. The maximum is 9.7% (in the corner of the crystal), the minimum is 9%. The energy resolution degrades close to the edges and corners of the crystal because the light photons experience more reflections before being detected.

3.7 Detector count rate measurements

A syringe filled with 79.55 MBq ^{99m}Tc is positioned in front of a single hole collimator (hole diameter 5 mm, collimator thickness 5 mm). The distance from source to detector was 2 cm. One million events are recorded every 10 minutes; the total acquisition time varies due to the decaying source and was 9 s for the first acquisition and 10 min for the last acquisition. An energy histogram of each file is made and the number of events in a 28 KeV energy window is stored in a vector.

Detector count rate does not show an exponential decay due to detector non-linearity at higher count rates. An exponential decay of ^{99m}Tc is fit to the measurements of the detector count rate at low count rates (the low count rate zone is marked by the red triangles on Fig. 3.18). This

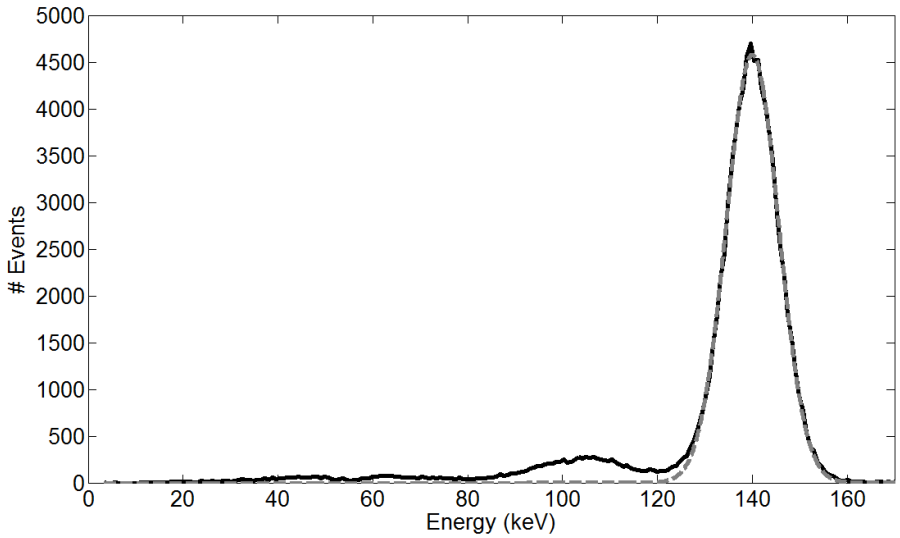

Figure 3.16: Energy spectrum of a ^{99m}Tc beam pointed to the center of the detector (solid line) and Gaussian fit (dotted line). The energy resolution is 9.3% in the center of the detector.

exponential decay fit is the real count rate, Fig. 3.18 compares the real count rate with the measured detector count rate.

The first plot (Fig. 3.18(a)) shows the measured count rate of all the events (CR_A) and an exponential fit ($ExpFitCR_A$).

The second plot (Fig. 3.18(b)) shows the measured count rate of the events in the energy window (CR_{EW}, a 28 KeV energy window is used), an exponential fit ($ExpFitCR_{EW}$) and 80% of the exponential fit ($80ExpFitCR_{EW}$).

The exponential fits ($ExpFitCR_A$ and $ExpFitCR_{EW}$) can be considered as the real count rates.

$80ExpFitCR_{EW}$ equals CR_{EW} at the time point 13h. This time point is marked on both plots with a vertical line. At that time CR_{EW} is 29.7 Kcps and CR_A is 52.3 Kcps. Twenty percent of the energy-windowed events are then lost because 80% of the real energy-windowed count rate ($80ExpFitCR_{EW}$) equals the measured energy-windowed count rate (CR_{EW}).

Two different behaviors can be observed in Fig. 3.18. The first behavior occurs from 0h to 6h; CR_A shows a plateau. This is caused by the limit

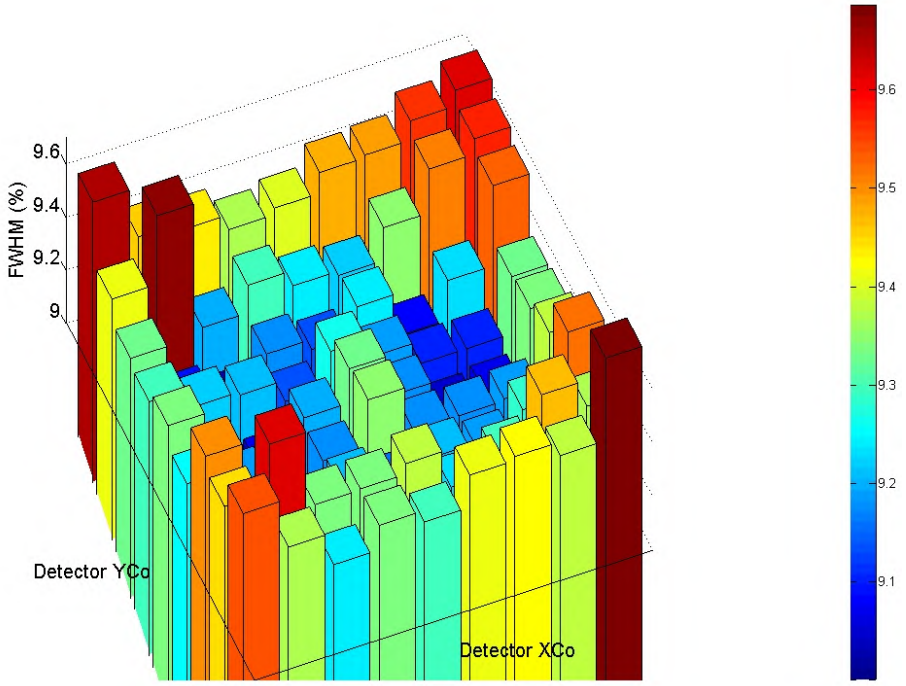

Figure 3.17: The energy resolution changes over the detector surface. The energy resolution degrades close to the edges and corners of the crystal.

in the Ethernet bandwidth. At the same time CR_{EW} increases. This is caused by the decrease in pulse pile-up; pulse pile-up occurs when a second event occurs during the integration time (c_{PD}) of a first event. The second behavior is from 6h to 45h. The measured count rate CR_{EW} approaches the real count rate $ExpFitCR_{EW}$ due to a further decrease in pulse pile-up. This can be concluded from the energy spectra at different time points and is depicted in Fig. 3.20. The decrease in pulse pile-up is observed by looking at the amount of events in channel number 2.2×10^5, this channel contains the events caused by two simultaneous photo-electric events.

The count rate non-linearity is also depicted in Fig. 3.19. This graph shows the measured count rate (CR_{EW}) in function of the real count rate ($ExpFitCR_{EW}$). When the real energy windowed count rate equals 37 Kcps then the detected count rate equals 29.7 Kcps (80% of 37.1 Kcps). This is due to pulse pile-up and can be derived by comparing the spectra at times 10 h and 40 h (see Fig. 3.20); the spectrum at time 10 h shows more counts

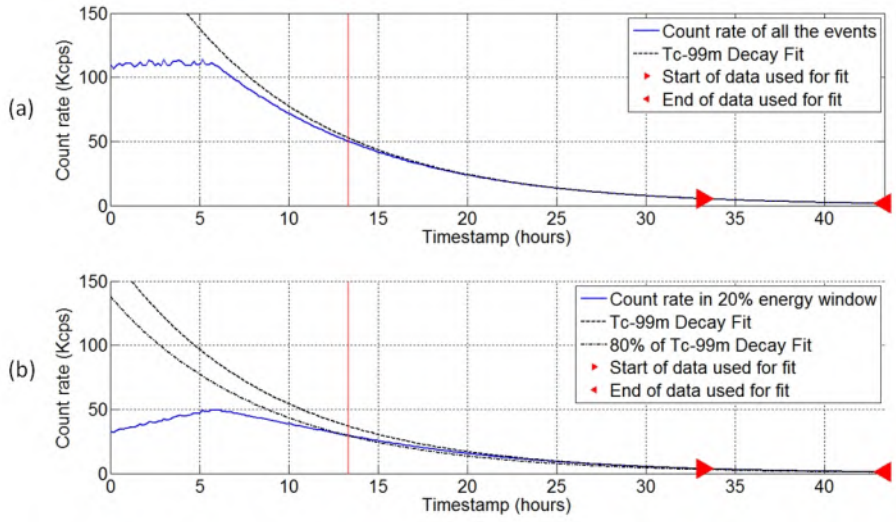

Figure 3.18: (a) Total count rate and (b) energy windowed count rate of a decaying ^{99m}Tc source.

in the pile-up region (*Channel* $> 1.5 \times 10^5$) than the spectrum at time 40 h.

3.8 Discussion

Our NaI(Tl) detector has a spatial resolution (1.24 mm in the CFOV) which is much better than the spatial resolution of a typical clinical detector (3 mm). This is due to the usage of a PSPMT, a thin NaI(Tl) scintillator and the usage of MLE event positioning. The spatial resolution degrades close to the edges of the scintillator. This could be improved by using black (non-reflecting) edges; note however that this could also lead to a worse energy resolution because in that case less light is collected by the PSPMT.

The scintillator that we used here is less thick than the scintillator of a clinical camera, our detector is 5 mm thick and a clinical detector typically is 9.5 mm thick. This was chosen to improve the spatial resolution. This results however in a lower detection efficiency; the 5 mm thick detector has a total detection efficiency of 70.7 % and the clinical detector has a total detection efficiency of 90.3 % for 140 keV gamma photons.

Other researchers have designed detectors that show similarities with our

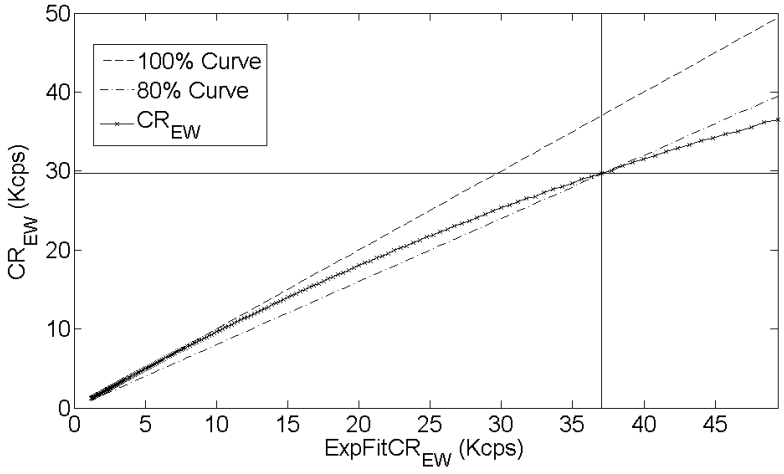

Figure 3.19: The real count rate and the measured count rate.

detector. Kim et al. [124] have coupled a 6 mm thick NaI(Tl) scintillator to an R3941 PSPMT (77mm square PSPMT, 18x16 crossed wire anodes) and used COG event positioning. Using this setup, an energy resolution of 12.9 % and a spatial resolution of 3.1 mm was measured. Our detector outperforms the detector descibed in this paper, this is mainly due to the improved PSPMT (e.g. the H8500 has a better fill factor than the R3941 PSPMT) and the more advanced event positioning algorithm.

More recently, Pani et al. [125] have compared 4 mm thick NaI(Tl) and 4 mm thick $LaBr_3$(Ce). They used these scintillators first coupled to a standard H8500 PSPMT (with a QE of 24%) and then coupled to a super bialkali (SBA) H8500 PSPMT (with a QE of 38.5%, such an SBA PSPMT is more expensive than a standard PSPMT). The glass lightguide of the scintillator's package was 3 mm thick and a modified COG algorithm was used for event positioning. We will not discuss the results obtained with the $LaBr_3$(Ce) detector here but it is interesting to analyze the NaI(Tl) results because their setup shows a lot of similarities with our setup. Such a 4 mm thick NaI(Tl) detector has a probability of 50.7% for photoelectric interactions while our 5 mm thick NaI(Tl) offers a probability of 57.0%.

Using the NaI(Tl) scintillator, an energy resolution of 9.8% and 9.5% was measured, respectively with the standard PSPMT and with the SBA PSPMT. These results are slightly worse than our result (9.3%), this is

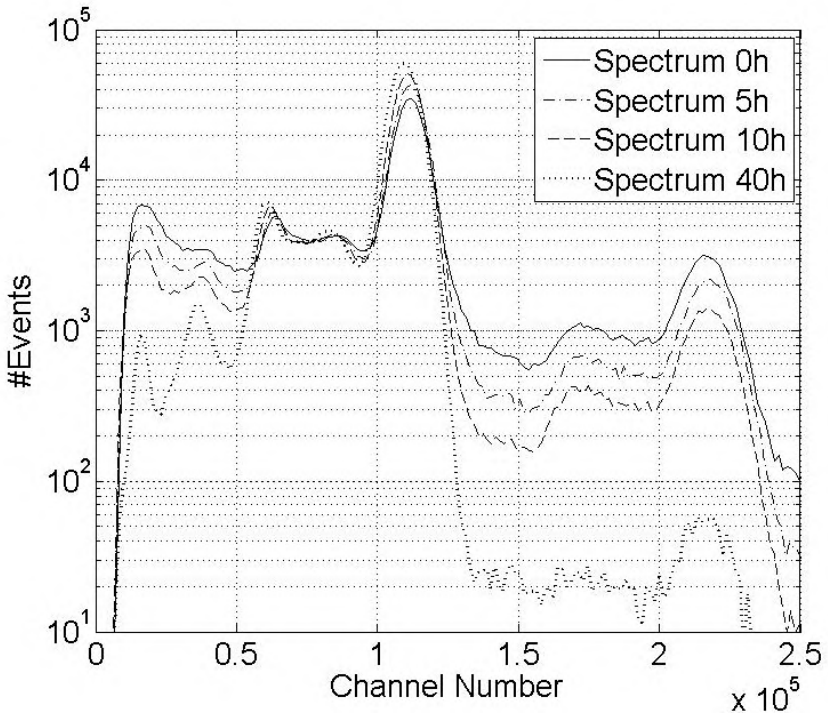

Figure 3.20: Energy spectrum at time 0h, 5h, 10h and 40h (all spectra have been scaled and include the same number of events, a log scale is used on the ordinate axis).

probably due to the fact that their scintillator has black absorbing sides. An intrinsic resolution of 1.15 mm (standard PSPMT) and 0.95 mm (SBA PSPMT) was obtained with the NaI(Tl) scintillator in the center of the detector. These numbers were corrected for the beam diameter and apply to the central region (15 mm x 15 mm) of the detector[1].

Our results show good agreement, we measured a spatial resolution of 1.13 mm in the central 15 mm x 15 mm region of the detector. Additionally, their publication illustrates the improvement that can be made by changing from a standard PSPMT to a more expensive SBA PSPMT (1.15 mm to 0.95 mm).

[1]According to A. Fabbri (personal communication, January 16, 2014)

3.9 Summary and original contributions

In this chapter we described a compact SPECT detector that consists of a 5 mm thick NaI(Tl) scintillator, an H8500 PSPMT and dedicated readout electronics; MLE event positioning is used. The PSPMT provides a good sampling of the small lightspread that is generated by the relatively thin scintillator. This, in combination with the MLE event positioning algorithm, results in a high-resolution detector.

The design of the detector has been presented, this includes hardware (scintillator, PSPMT and read-out electronics), calibration and event positioning. Measurements (spatial resolution, energy resolution and count rate) illustrate the performance of this detector.

In the next chapter we will introduce a new pinhole geometry. This collimator and the NaI(Tl) detector, that was presented here, will then be used in chapter 5 to build a compact SPECT system.

The work described in this chapter has been published as two peer-reviewed journal publications [4, 5] and a conference proceeding [12].

Chapter 4

The lofthole: a novel shaped pinhole geometry for optimal detector usage

4.1 Introduction

In chapter 2 we have introduced the main types of collimators: the pinhole collimator, the parallel hole collimator and the converging beam collimators. Each collimator has its specific advantages and disadvantages. Pre-clinical SPECT systems frequently use multi-pinhole collimators (section 2.4.3.7); such a collimator provides a high sensitivity and a high resolution for a small region close to the apertures. Due to this, the multi-pinhole collimator collimator is well-suited for imaging of small-animals. We have also introduced the concept of multiplexing, where the projections of the different pinholes of the multi-pinhole collimator overlap on the gamma-ray detector. Multiplexing can be used to increase the collimator sensitivity.

The consequences of multiplexing are still under discussion. Some researchers state that multiplexing leads to artifacts [51, 52]. Others state that, under certain conditions, artifacts can be avoided and that multiplexing can be used to improve the image quality [53]. In conclusion, our hypothesis is that multiplexing should be avoided, unless the conditions mentioned by Lin [53] are met. In the latter case, an improved image quality might be obtained without introduction of artifacts.

A first method to avoid overlap is simply obtained by positioning the pinholes far enough from each other such that the different projections do

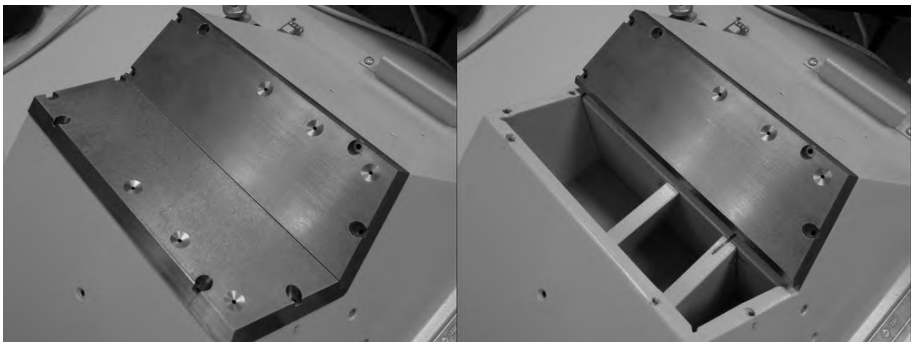

Figure 4.1: (a) A 6-pinhole SPECT collimator and (b) the same collimator with one top plate removed revealing the shielding used to separate the different projections.

not overlap (e.g. FastSPECT [126, 127], GE Alcyone [128]). A drawback of this method is that the typical circular pinholes result in circular projections. As most radiation detectors are rectangular, the detector area can never be optimally used (see Fig. 4.3(a) and [129]). A second solution is to place additional shielding to separate the different projections. This can be done with either slats (see Fig. 4.1 and [130]) or other additional shielding elements behind the pinholes (e.g. [55]). Adding such shielding has the drawback that it increases weight (this could be a problem for rotating systems), design complexity and cost. The use of slats is troublesome and might not be possible when the detector has front-side readout [88].

In this chapter, we investigate a new pinhole geometry, the lofthole, that has a circular aperture but whose entrance and/or exit opening is shaped by the desired irradiated detector area. These can be combined into a multi-lofthole collimator; such a multi-lofthole collimator allows efficient detector usage without using additional shielding.

In the first section (section 4.2) of this chapter we give an introduction to the lofthole geometry and focus on the difference between a conventional pinhole and a lofthole. The second section handles the sensitivity formulas for knife-edge pinholes and loftholes (section 4.3). The proposed formulas are different from the standard formulas (section 2.4.3.2) because they take the penumbra and umbra regions of the pinhole into account. These formulas are verified with simulations in section 4.4. Two pinhole collimators and one lofthole collimator have been produced. A flood phantom and a point source have been measured using these collimators on a standard clinical

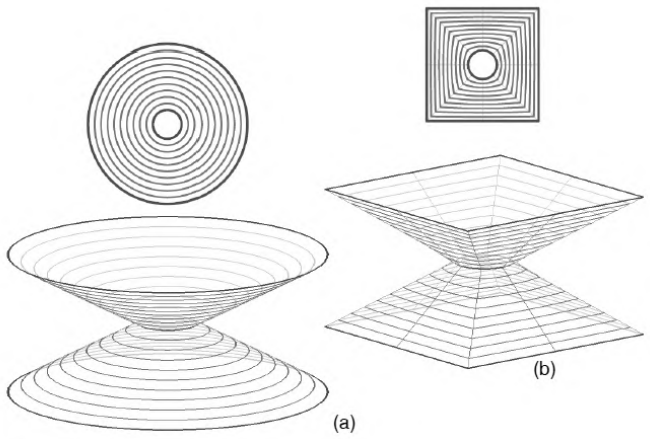

Figure 4.2: (a) Top and side view of a knife-edge pinhole and (b) a lofthole with a square entrance and exit opening. The aperture of both collimating holes is circular. The cross section of this lofthole gradually change from a circle to a square.

gamma camera (Inter Medical Prism 3000XP).

4.2 The lofthole

A knife-edge pinhole has a round aperture and round entrance and exit openings (Fig. 4.2(a)), this results in an hourglass-shaped volume. The lofthole also has a round aperture but, the entrance and exit volumes of the lofthole, defined by the circular aperture and by the entrance and exit squares are complex volumes (the *loftvolume*). Its cross section gradually changes from a circle to a square or polygon. Fig. 4.2(b) shows a lofthole with a square entrance and exit opening.

Let us consider now that a multi-pinhole collimator is used on a large clinical gamma-camera (see Fig. 4.3). This collimator consists of 6 knife-edge pinholes. If overlap is avoided, then only 71.8% of the detector area is used. The second configuration uses the complete detector but 32.9% of the detector sees activity from more than one pinhole which may cause imaging artifacts. The third configuration uses the loftholes. It irradiates the complete detector and has no overlap.

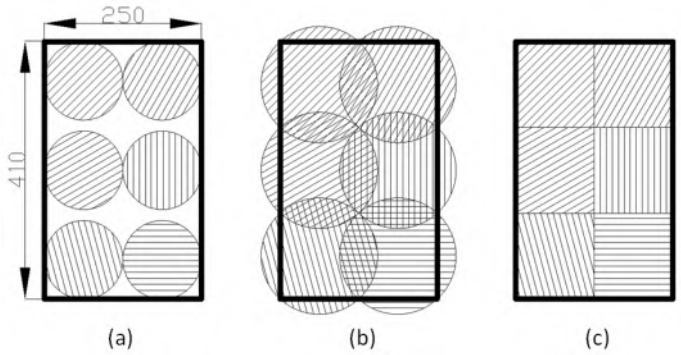

Figure 4.3: 6 Pinholes and a rectangular detector (410 mm x 250 mm). (a) 6 Pinholes without overlap; 71.8% of the detector area is used. (b) 6 Pinholes using the complete detector; 32.9% overlap. (c) 6 Loftholes, the setup with the loftholes uses the whole detector and has no overlap.

4.3 Characterization of sensitivity

4.3.1 The umbra and the penumbra

If we consider an ideal (no penetration) pinhole or lofthole collimator then the detector can be subdivided into three parts. A first part detects photons coming from the whole aperture ($Detector_{HiSens}$ in Fig. 4.4), a second part can only detect photons from a part of the aperture ($Detector_{Penumbra}$) and a third part has no detections ($Detector_{Umbra}$).

The image space can also be divided into three parts. Gamma ray photons originating from the first part of the image space can reach the detector through the whole aperture; this zone is marked as $Image_{HiSens}$ in Fig. 4.4. A second part is called the $Image_{Penumbra}$. Photons originating from this part of the image space can reach the detector only through part of the aperture. Finally, photons of a third part cannot reach the detector ($Image_{Umbra}$).

Knowledge of the detector penumbrae and the sensitivity in the image penumbrae is essential during the design of a multi-pinhole or a multi-lofthole collimator. According to this, one might for example decide to allow or prevent overlapping detector penumbrae. In the following section a sensitivity formula is presented for a pinhole and for a lofthole that takes the penumbra effect into account.

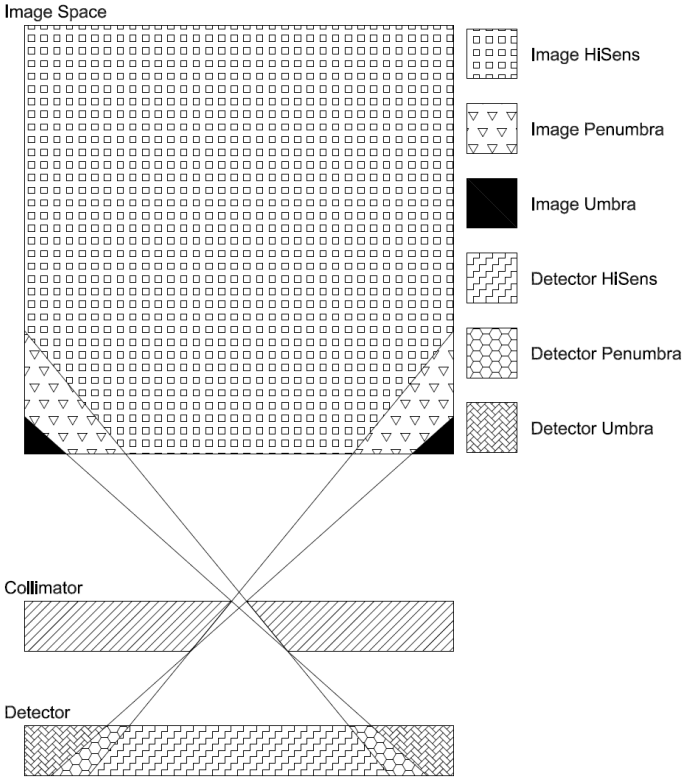

Figure 4.4: The high-sensitive (*HiSens*), low-sensitive (*Penumbra*) and insensitive (*Umbra*) areas on the detector and in the image space.

4.3.2 Analytical sensitivity formulas

The sensitivity for point sources that are positioned in $Image_{HiSens}$ satisfies, to a good approximation (when no penetration is assumed), the geometrical sensitivity formula (see section 2.4.3.2 for the derivation).

$$S = \frac{d^2 sin^3\theta}{16h^2}. \tag{4.1}$$

This geometrical sensitivity depends on d (aperture diameter), θ (angle between the aperture plane and a ray connecting the source and the aperture center) and h (perpendicular distance from the source to the aperture plane). All these parameters are marked in Fig. 4.5. This formula is, how-

ever, not accurate for point sources in the $Image_{Penumbra}$ and $Image_{Umbra}$, where the sensitivity is lower than predicted by (4.1) (and actually becomes zero in the umbra). This problem has been considered before by Barrett and Swindell [64], where a general expression for the point spread function for a cylindrical pinhole was derived, and by Shokouhi et al. [111], where an explicit calculation of the geometric sensitivity in the $Image_{Penumbra}$ was shown for cylindrical and knife-edge pinholes. In this section we present the results for the sensitivity of a knife-edge pinhole and the correction we apply for the square lofthole. In both cases we restrict the calculations to systems with only an aperture and exit opening and with the aperture plane parallel to the exit opening plane, as in Fig. 4.5 and 4.7. Note that these formulas can also be used for collimators that have an entrance opening, provided that this entrance opening is large enough to avoid limiting the field-of-view (FOV) of the aperture in combination with its exit window (see Fig. 4.6 for an example). The usage of both an entrance and exit opening results in a thicker knife-edge, which is beneficial to lower the amount of penetrating photons.

To adapt formula (4.1) for any point source (Src), we note that from all the photons emitted by this source only the ones that pass through both the aperture and the exit opening are going to contribute to the total geometric sensitivity. This number of photons is proportional to the area A_{int}, which is the intersection between the pinhole or lofthole aperture and the exit opening projected from the point source onto the aperture plane (see Fig. 4.5 and 4.7). As such, the geometric sensitivity should be written as

$$S = A_{int} \frac{sin^3\theta}{4\pi h^2}, \tag{4.2}$$

where, according to the division of the image space defined in Fig. 4.4, the intersection area A_{int} can be defined piecewise as

$$A_{int} = \begin{cases} \pi \left(\frac{d}{2}\right)^2, & Src \in Image_{HiSens} \\ A_{int}^{Penumbra}, & Src \in Image_{Penumbra} \\ 0, & Src \in Image_{Umbra} \end{cases}. \tag{4.3}$$

So in order to get the correct results we need to define the boundaries between the three regions and determine an analytic formula for $A_{int}^{Penumbra}$.

Here, we restrict ourselves to the cases where the diameter of the aperture circle is smaller than or equal to the exit opening's projected diameter or side (for a pinhole or lofthole respectively), meaning that there will always be

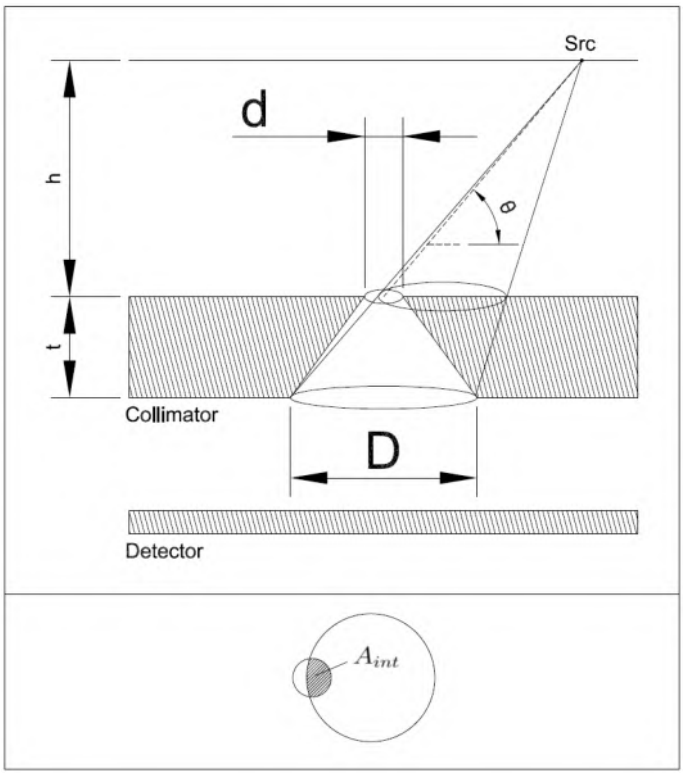

Figure 4.5: Top: Schematic representation of the pinhole and its parameters. Bottom: Intersection of the pinhole aperture circle with the exit circle projected from the point source onto the aperture plane.

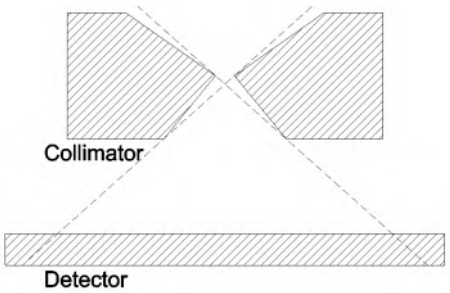

Figure 4.6: The derived sensitivity formulas can also be used for this geometry. The FOV and the sensitivity of the aperture are only limited by the exit opening and not by the entrance opening.

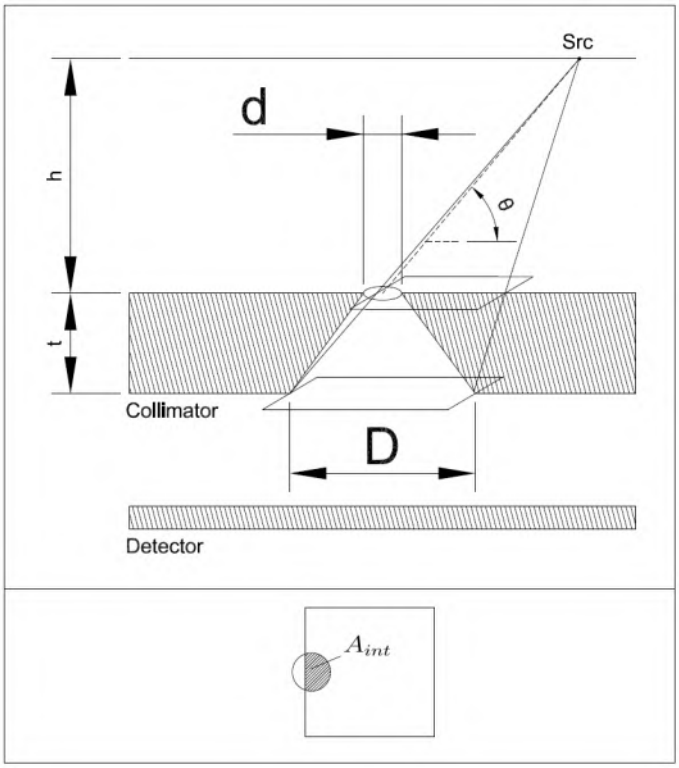

Figure 4.7: Top: Schematic representation of the lofthole and its settings. Bottom: Intersection of the lofthole aperture circle with the exit square projected from the point source onto the aperture plane.

an $Image_{HiSens}$ defined for a given distance h, which is the case for realistic collimators and realistic settings. We include the results and our derivation for the knife-edge pinhole's geometrical sensitivity because it helps to better understand the calculations for the lofthole case.

- Pinhole

To determine the corresponding sensitivity it suffices to know the height h and the distance from the aperture center to the perpendicular projection of the point source *Src* on the aperture plane. As such, we consider a frame of reference in the aperture plane, centered on the aperture and with the x-axis aligned with the perpendicular projection of the point source *Src* on the aperture plane (see Fig. 4.8).

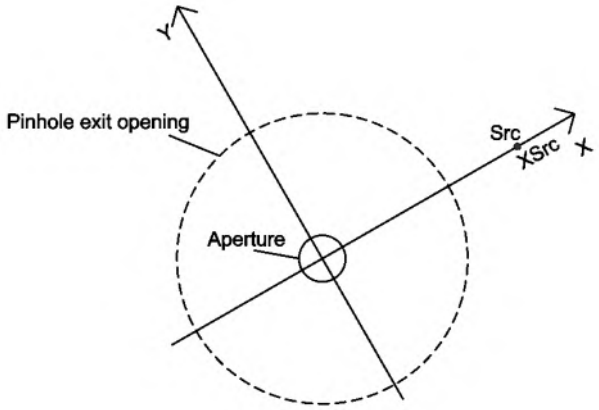

Figure 4.8: A top view on the aperture plane. The reference frame used in the pinhole formulas is centered on the center of the aperture. The x-axis is aligned with the perpendicular projection of the point source *Src* on the aperture plane.

Let us first define the variables $\{x_{Src}\}_{min}$ and $\{x_{Src}\}_{max}$.

$$\{x_{Src}\}_{min} = \frac{h}{t}\left(\frac{D}{2} - \frac{d}{2}\right) - \frac{d}{2} \tag{4.4}$$

$$\{x_{Src}\}_{max} = \frac{h}{t}\left(\frac{D}{2} + \frac{d}{2}\right) + \frac{d}{2} \tag{4.5}$$

The parameter h is the height of the point source above the aperture plane, t is the distance from aperture plane to exit window plane, D is the diameter of the exit window and d is the aperture diameter. These parameters are also explained in Fig. 4.5.

These variables will be used to delineate the $Image_{HiSens}$, the $Image_{Penumbra}$ and the $Image_{Umbra}$. A point source is in the $Image_{HiSens}$ when x_{Src} is smaller than or equal to $\{x_{Src}\}_{min}$, it is in the $Image_{Penumbra}$ when x_{Src} is greater than $\{x_{Src}\}_{min}$ and smaller than or equal to $\{x_{Src}\}_{max}$. If none of these conditions is met, then the point source is in the $Image_{Umbra}$.

The borders of the three regions in image space are defined by the following conditions:

$$Src \in Image_{HiSens} \Leftrightarrow x_{Src} \in [0, \{x_{Src}\}_{min}] \tag{4.6}$$

$$Src \in Image_{Penumbra} \Leftrightarrow x_{Src} \in]\{x_{Src}\}_{min}, \{x_{Src}\}_{max}] \tag{4.7}$$

$$Src \in Image_{Umbra} \Leftrightarrow x_{Src} \in]\{x_{Src}\}_{max}, +\infty[\tag{4.8}$$

Since the pinhole that we are considering is a knife-edge pinhole with only two openings, $A_{int}^{Penumbra}$ is simply an intersection of two circles: the aperture opening circle, of diameter d, and the circular projection of the exit opening, of original diameter D, on that plane (Fig. 4.5). This circular projection has a diameter D'. In [7] we show that $A_{int}^{Penumbra}$ is given by

$$A_{int}^{Penumbra} = \left(\frac{D'}{2}\right)^2 \cos^{-1}\left(\frac{a-x_i}{\frac{D'}{2}}\right) + \left(\frac{d}{2}\right)^2 \cos^{-1}\left(\frac{x_i}{\frac{d}{2}}\right) - a\sqrt{\left(\frac{d}{2}\right)^2 - (x_i)^2}, \tag{4.9}$$

with

$$D' = D \times \frac{h}{h+t}, \quad a = \frac{t}{h+t}x_{Src}, \quad x_i = \frac{a^2 - \left(\frac{D'}{2}\right)^2 + \left(\frac{d}{2}\right)^2}{2a}. \tag{4.10}$$

It can be shown that this formula is equivalent to the formula for cylindrically shaped pinholes [111] when the diameter of the aperture is equal to the diameter of the exit opening.

- Lofthole

The explicit calculations for the lofthole case are more lengthy because there is less symmetry. The area of intersection $A_{int}^{Penumbra}$, as well as the θ values of the $Image_{Penumbra}$ boundaries will now depend on the angle ϕ (see Fig. 4.9). We consider the exit shape to be a square of side D, and only designs such that the side of the projected exit opening (D') is bigger than or equal to the aperture diameter ($D' \geq d$, this is the case for realistic lofthole collimators and realistic settings). Due to the symmetry of the lofthole we can reduce the calculations to point source coordinates (x_{Src}, y_{Src}) in the first quadrant (meaning that we do the transformation $(x_{Src}, y_{Src}) \rightarrow (|x_{Src}|, |y_{Src}|)$).

The intersection of the projected exit opening with $y = 0$ that has the smallest x value is x_1; the intersection with $x = 0$ that has the smallest y value is y_1.

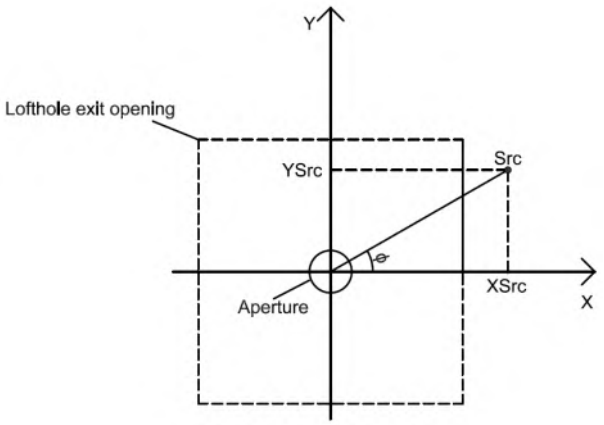

Figure 4.9: A top view on the aperture plane. The reference frame used in the lofthole formulas is centered on the center of the aperture. The axes are aligned with the sides of the exit opening for the lofthole. The coordinates of an arbitrary point source on the aperture plane are (x_{Src}, y_{Src}) at angle ϕ.

$$x_1 = x_{Src} - \frac{h}{h+t}\left(x_{Src} + \frac{D}{2}\right), \tag{4.11}$$

$$y_1 = y_{Src} - \frac{h}{h+t}\left(y_{Src} + \frac{D}{2}\right). \tag{4.12}$$

Point sources in the $Image_{HiSens}$ region have coordinates (x_{Src}, y_{Src}) such that

$$x_1 \leq -\frac{d}{2} \quad \wedge \quad y_1 \leq -\frac{d}{2}, \tag{4.13}$$

and the $Image_{Umbra}$ region is defined by the condition

$$x_1 \geq \frac{d}{2} \quad \vee \quad y_1 \geq \frac{d}{2} \quad \vee \quad \left(\sqrt{x_1^2 + y_1^2} \geq \frac{d}{2} \wedge x_1, y_1 \geq 0\right). \tag{4.14}$$

All other point sources are included in the $Image_{Penumbra}$.

The general formula for the intersection area which includes all possible

cases is derived in [7] and is equal to:

$$\begin{aligned} A_{int}^{Penumbra} &= I\left(\max\left(-\frac{d}{2}, x_1\right), \frac{d}{2}\right) \\ -\mathrm{sgn}(y_1) I\left(\max\left(-\frac{d}{2}, x_1\right), \max(x_-, x_1)\right) \\ -y_1\left(\max(x_+, x_1) - \max(x_-, x_1)\right) \\ -\mathrm{sgn}(y_1) I\left(\max(x_+, x_1), \frac{d}{2}\right), \end{aligned} \tag{4.15}$$

where x_1 and y_1 are defined in formulas 4.11 and 4.12, and

$$x_+ = \begin{cases} \sqrt{\left(\frac{d}{2}\right)^2 - y_1^2}, & \text{if } |y_1| \le \frac{d}{2} \\ 0, & \text{if } |y_1| > \frac{d}{2} \end{cases}, \quad x_- = -x_+, \tag{4.16}$$

$$\mathrm{sgn}(x) = \begin{cases} 1 & \text{if } x \ge 0 \\ -1 & \text{if } x < 0 \end{cases} \tag{4.17}$$

and

$$\begin{aligned} I(x_a, x_b) &= \int_{x_a}^{x_b} \sqrt{\left(\frac{d}{2}\right)^2 - x^2}\, dx \\ &= \left(\frac{d^2}{8}\sin^{-1}\left(\frac{x}{\frac{d}{2}}\right) + \frac{x}{2}\sqrt{\left(\frac{d}{2}\right)^2 - x^2}\right)\Bigg|_{x_a}^{x_b}. \end{aligned} \tag{4.18}$$

4.4 Validation of the sensitivity formulas with simulations

A ray-tracer simulation program has been developed to investigate the sensitivity of the lofthole. This simulation tool tracks photons emitted by a point source in a random direction. Sensitivity is calculated by comparing the number of emitted photons to the number of detected photons. It assumes a perfect collimator (no penetration or scatter are taken into account).

The sensitivity for a point source of a knife-edge pinhole collimator and a lofthole are simulated, calculated using the corrected formulas (formulas

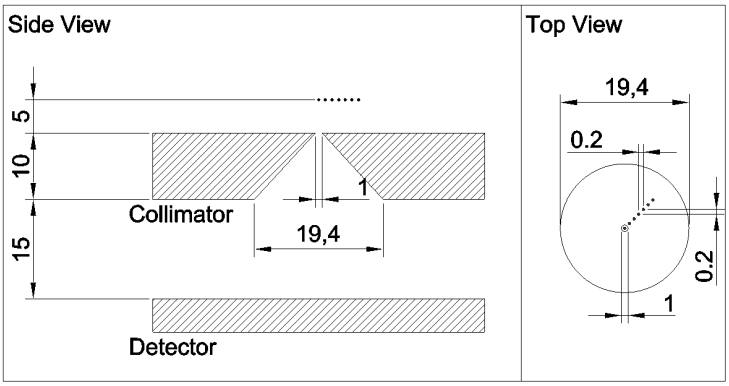

Figure 4.10: A side and top view of the simulated pinhole collimator. Not all simulated point source positions are displayed for clarity reasons.

(4.2), (4.3), (4.9) for the pinhole and (4.2), (4.3), (4.15) for the lofthole) and calculated using the basic formula (formula (4.1)).

The error of the the corrected and the basic sensitivity formula compared to the simulation is calculated in the following way:

$$Error_{Corr} = (S_{Corr} - S_{Sim})/S_{Sim} \tag{4.19}$$

$$Error_{Basic} = (S_{Basic} - S_{Sim})/S_{Sim} \tag{4.20}$$

Note that $Error_{Corr}$ and $Error_{Basic}$ become infinite when S_{Sim} is zero while S_{Corr} or S_{Basic} are non-zero.

The pinhole setup is depicted in Fig. 4.10. It consists of a pinhole collimator with a 1 mm diameter aperture and a circular 19.4 mm diameter exit window; the collimator plate is 10 mm thick. The collimator is positioned 15 mm above the detector. The simulated point sources are positioned 5 mm above the aperture plane. These sources are located on a line that has a $45\,^{\circ}$ angle to the reference frame. This angle has no influence on the pinhole sensitivity due to the symmetry of the pinhole.

The lofthole setup is shown in Fig. 4.11. This setup is similar to the pinhole setup, the difference being that the simulated lofthole collimator has a rectangular exit window with a side of 19.4 mm. The point sources are located on a line that has a $45\,^{\circ}$ angle ($\phi = 45\,^{\circ}$) and on a line that has a $30\,^{\circ}$ angle ($\phi = 30\,^{\circ}$) to the reference frame and the square exit opening.

Each point source position is simulated until 10^6 events are detected or until 10^8 events are emitted by the source.

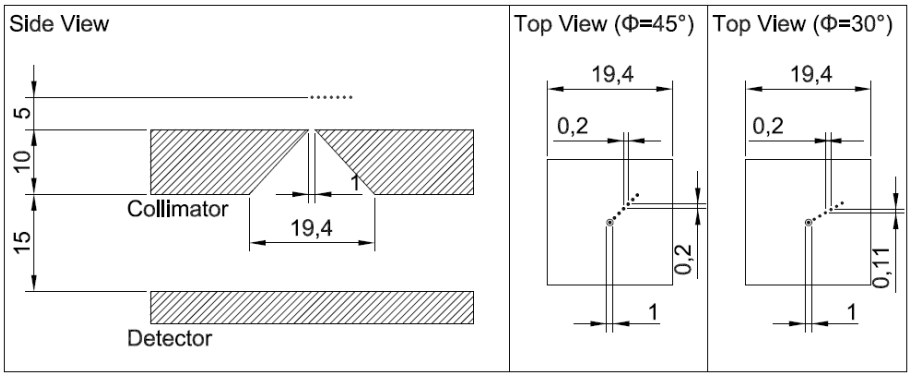

Figure 4.11: A side and top view of the simulated lofthole collimator. The setup is identical to Fig. 4.10 except for the exit opening, the lofthole has a square exit opening. The side length of this square exit opening is equal to the diameter of the pinhole's exit opening. The point sources are located on a line that has a $45\,^\circ$ angle and on a line that has a $30\,^\circ$ angle to the square exit opening.

Fig. 4.12 depicts the validation results. The red traces show the outcome for the pinhole setup, the green traces show the outcome for the lofthole for point sources on a $45\,^\circ$ line and the blue traces are for the lofthole with point sources on a $30\,^\circ$ line.

Fig. 4.12(a) depicts the sensitivity as calculated by the basic formula (4.1), the simulated sensitivity and the sensitivity as calculated by the corrected sensitivity formula (using formulas (4.2), (4.3), (4.9) for the pinhole and (4.2), (4.3), (4.15) for the lofthole).

Fig. 4.12(b) and Fig. 4.12(c) illustrate the error made by the corrected formulas and by the basic formula.

The corrected calculated sensitivity and the simulated sensitivity show good agreement for all point sources on all setups (Fig. 4.12(a)). The largest absolute errors (Fig. 4.12(b)) are all smaller than 0.12%. The basic sensitivity formula does not take the penumbra and umbra into account (Fig. 4.12(a)). This is reflected in a significant error ($> 9\%$, see Fig. 4.12(c)) when the point source is in the $Image_{Penumbra}$ or in the $Image_{Umbra}$.

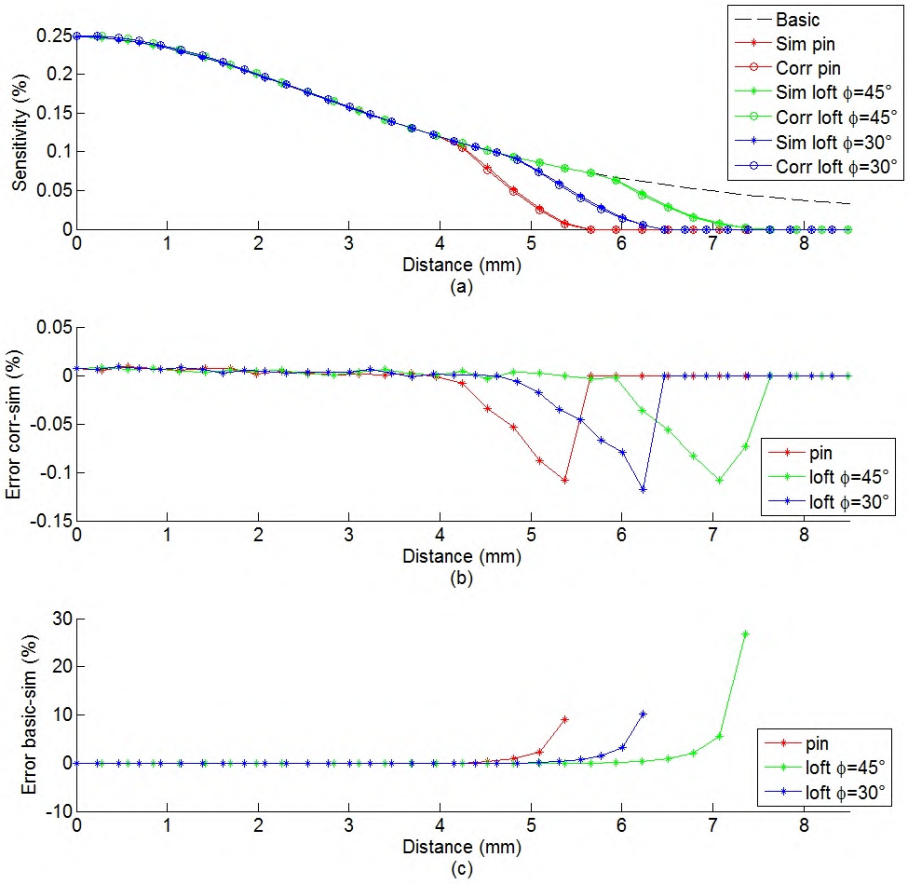

Figure 4.12: There is good agreement between the outcome of the simulations and the outcome of the corrected sensitivity formula. The red traces are the outcome of the pinhole setup, The green traces are for the first lofthole setup ($\phi = 45\,^\circ$) and the blue traces are for the second lofthole setup ($\phi = 30\,^\circ$). (a) The sensitivity calculated with the basic sensitivity formula, the simulated sensitivity and the sensitivity calculated with the corrected formula. The *Basic* traces in the graphs are based on the basic sensitivity formula (4.1); the *Sim* traces are results from simulations and the *Corr* traces are based on the corrected sensitivity formulas ((4.2), (4.3), (4.9) for the pinhole and (4.2), (4.3), (4.15) for the lofthole). (b) The deviation from the calculated sensitivity (based on corrected sensitivity formula) to the simulated sensitivity. (c) The deviation from the calculated sensitivity (based on basic sensitivity formula) to the simulated sensitivity.

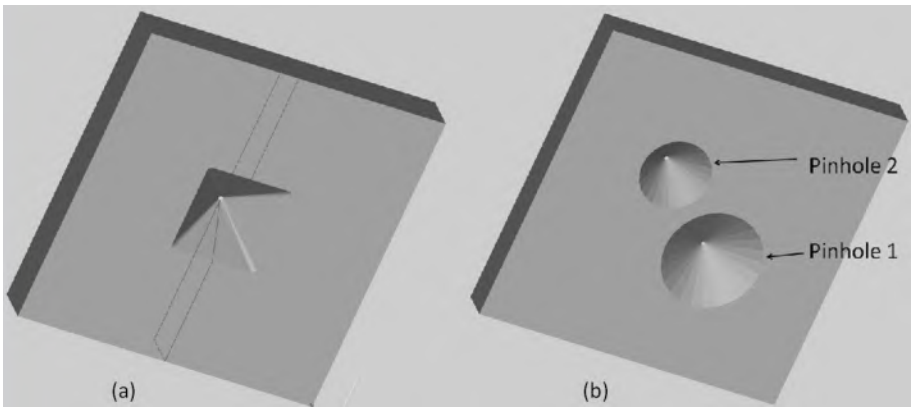

Figure 4.13: (a) The lofthole collimator and (b) the pinhole collimators used for the measurements.

4.5 Comparison of a lofthole and a pinhole collimator

Two collimator plates have been produced, both are 10 mm thick (Fig. 4.13). The plates are made from a 90% tungsten alloy (MT-17C, Midwest Tungsten Service, USA, see table 2.3 for more information) and are produced by milling (VASKON, Belgium). The first collimator plate has a lofthole with a 1 mm diameter aperture. This lofthole has been designed to have a rectangular projection (the exit opening is 19.4 mm by 19.4 mm). Its aperture is positioned on the top of the plate. The other collimator plate has two knife-edge pinholes. The first pinhole (pinhole 1) has a 1 mm aperture and its exit opening has the diameter of the circumscribed circle of the square exit opening of the lofthole (27.4 mm); the opening angle is 106 degrees. The exit opening of the second pinhole (pinhole 2) has the diameter of the inscribed circle of the exit opening of the lofthole (19.4 mm); the opening angle is 85 degrees. The apertures of the pinholes are positioned on the top of the plate. These collimators (lofthole and pinhole 2) are similar to the collimators that were simulated in section 4.4.

All measurements were done on a clinical 3/8 inch thick NaI(Tl) gamma camera (Inter Medical Prism 3000XP). This gamma camera has an intrinsic resolution of 3 mm. An energy window of 20% was used for energy discrimination. We have used these collimators and this detector to evaluate the flood maps and to evaluate the amount of penetration.

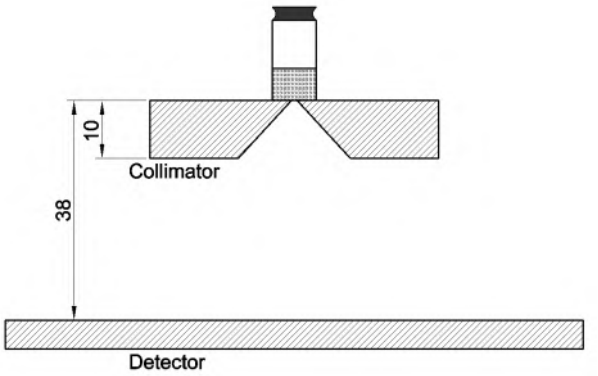

Figure 4.14: The setup used to measure the flood maps. A vial filled with ^{99m}Tc is positioned on top of the aperture. A clinical NaI(Tl) gamma camera was used as detector. Dimensions are in mm.

4.5.1 Flood map comparison

A flood source (a vial filled with ^{99m}Tc) was positioned above the three apertures (pinhole 1, pinhole 2 and lofthole). The distance from aperture to detector was 38 mm (Fig. 4.14). This distance was chosen because it resulted in a flood map that covered a large part of the detector area; the intrinsic detector resolution will have a negligible influence on the flood map measurement due to the large magnification. One million events were recorded for each collimator setup.

The resulting flood map measurements are shown in Fig. 4.15. The lofthole flood map is approximately square, which enables efficient detector usage. The flood map of pinhole 1 is the circumscribed circle and the flood map of pinhole 2 is the inscribed circle of the lofthole flood map.

4.5.2 Penetration comparison

An anion exchange bead (Bio-rad AG1-X2) was immersed in ^{99m}Tc; the total activity after immersion was 15.4 MBq. This small point source was positioned above the center of the three apertures (pinhole 1, pinhole 2 and lofthole) at a height of 10.1 mm (see Fig. 4.16). The distance from aperture to detector was 260.3 mm. This results in a 26.7 times magnified projection of the aperture onto the detector; as a consequence, the influence of the intrinsic resolution on this projection will be very small. The FWHM and FWTM of the point source projection on the detector was calculated

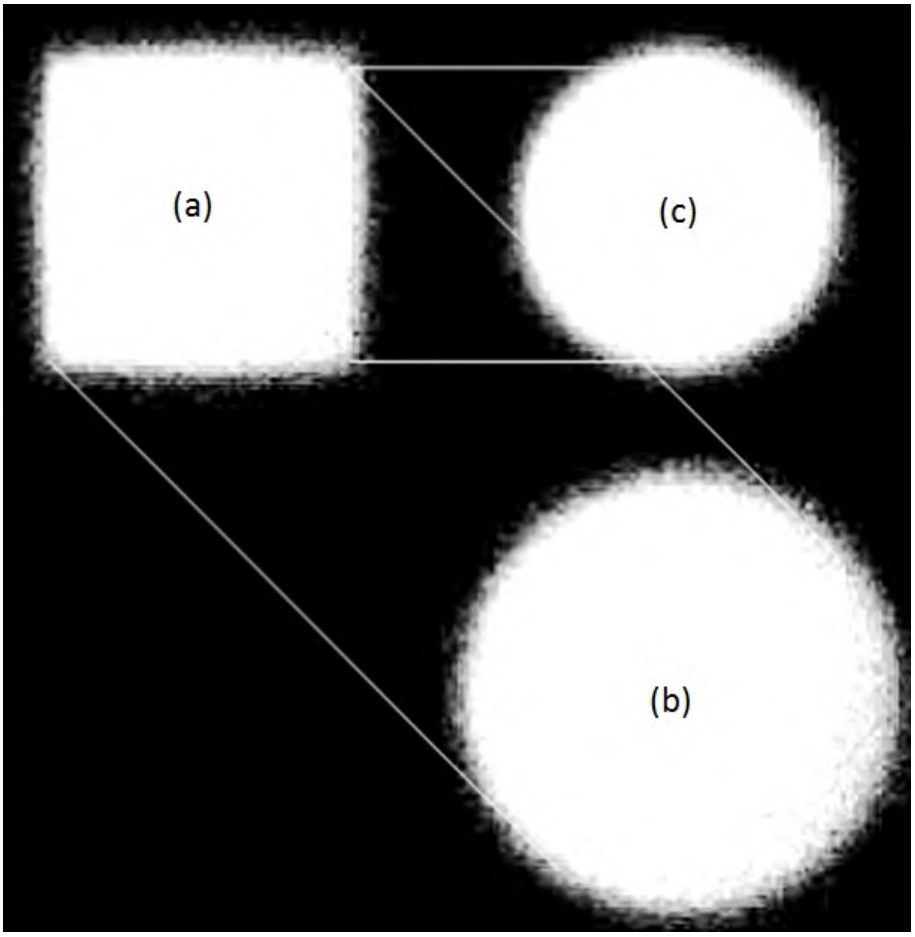

Figure 4.15: (a) Flood maps for the lofthole , (b) pinhole 1 and (c) pinhole 2. These maps were acquired with the setup depicted in Fig. 4.14. The flood map of pinhole 1 is the circumscribed circle of the flood map of the lofthole. The flood map of pinhole 2 is the inscribed circle of the flood map of the lofthole.

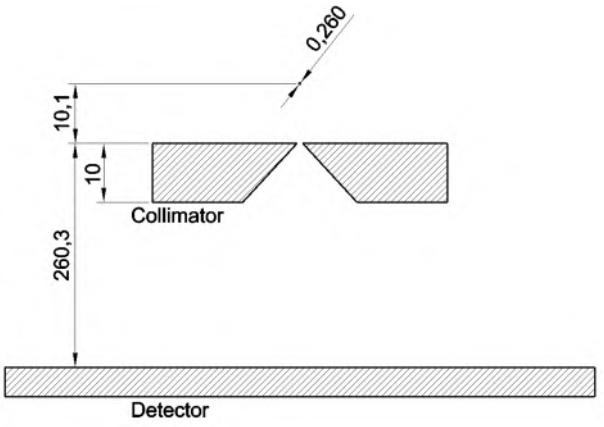

Figure 4.16: The setup used to measure penetration. This setup has a high magnification factor and allows to investigate penetration. Dimensions are in mm.

for two orthogonal profiles and for a diagonal profile. An acquisition of 120 seconds was made for each collimator setup.

The expected FWHM of an ideal collimator ($FWHM_{Ideal}$) without penetration was also calculated for this setup. Fig. 4.17 shows a magnification of the point source and the collimator. The four extreme rays have been drawn; those rays divide the irradiated detector area in two zones (Fig. 4.18). A central zone is able to receive photons from the whole point source, an outer zone is able to receive gamma photons only from a part of the point source. The expected FWHM using a perfect detector ($FWHM_{Aperture}$) is then approximately equal to the distance between the centers of the two outer zones. The intrinsic detector resolution (R_i) can be taken into account by using formula 4.21.

$$FWHM_{Ideal} = \sqrt{FWHM_{Aperture}^2 + R_i^2} \tag{4.21}$$

Fig. 4.19(a) shows the projected image on the detector when the lofthole collimator is used. A vertical, a horizontal and a diagonal profile of the projection data are shown in Fig. 4.20. The profiles are in logarithmic scale.

The FWHM and FWTM of the profiles are shown in tables 4.1 and 4.2; table 4.1 also contains the expected FWHM of an ideal collimator that has no penetration.

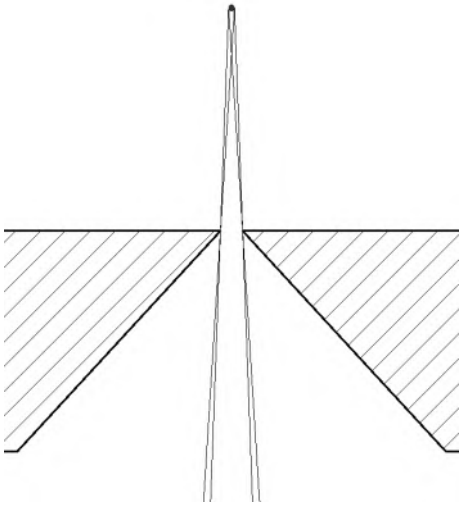

Figure 4.17: The four extreme rays originating from the point source (drawn to scale, according to the dimensions of Fig. 4.16).

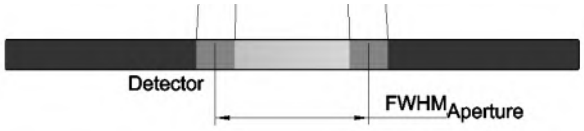

Figure 4.18: The four extreme rays have divided the irradiated detector area in two zones (drawn to scale, according to the dimensions of Fig. 4.16).

	Vert. FWHM (mm)	Hor. FWHM (mm)	Diag. FWHM (mm)
Ideal Coll.	26.9	26.9	26.9
Pinhole 1	36.5	37.4	36.5
Lofthole	31.5	32.3	32.3
Pinhole 2	32	32.4	32.5

Table 4.1: FWHM of the profiles shown in Fig. 4.20

	Vert. FWTM (mm)	Hor. FWTM (mm)	Diag. FWTM (mm)
Pinhole 1	73.6	71.8	71.7
Lofthole	55.8	57.8	64
Pinhole 2	58	58.6	57.2

Table 4.2: FWTM of the profiles shown in Fig. 4.20

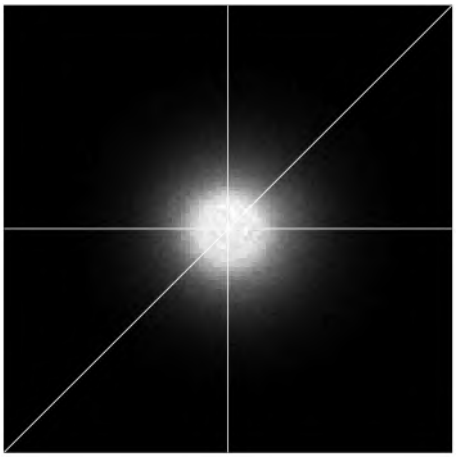

Figure 4.19: Pinhole projection on the detector. Profiles through the vertical, horizontal and diagonal lines are shown in Fig. 4.20.

The FWHM and FWTM of all the profiles of pinhole 2 are smaller than the FWHM and FWTM of the profiles of pinhole 1 indicating that pinhole 2 has less penetrated photons than pinhole 1. This can be explained by the larger opening angle of pinhole 1 which results in a thinner knife-edge. The FWHM of the lofthole and the FWHM of pinhole 2 are roughly similar. The FWTM illustrates that penetration is non-isotropic for the lofthole; the diagonal profile shows a significantly larger FWTM than the horizontal and vertical profile.

This can be explained by considering cuts through the collimators. An edge-to-edge cross-section of the lofthole collimator is identical to a cross-section of pinhole 2. This explains why penetration of pinhole 2 and the lofthole will be similar for the vertical and horizontal profiles. A corner-to-corner cross-section of the lofthole collimator is identical to a cross-section of pinhole 1 so we expect that penetration of the lofthole is similar to the amount of penetration of pinhole 1 for the diagonal profile. In reality the amount of penetration for the diagonal profile is better for the lofthole compared to pinhole 1. This is because penetration in the diagonal profile is not only determined by the diagonal cross-section of the lofthole but also the other non-diagonal cross-sections will contribute to penetration. In those cross-sections the opening angle of the lofthole is smaller than the opening angle of pinhole 1 and this results in a lower amount of penetration for the lofthole.

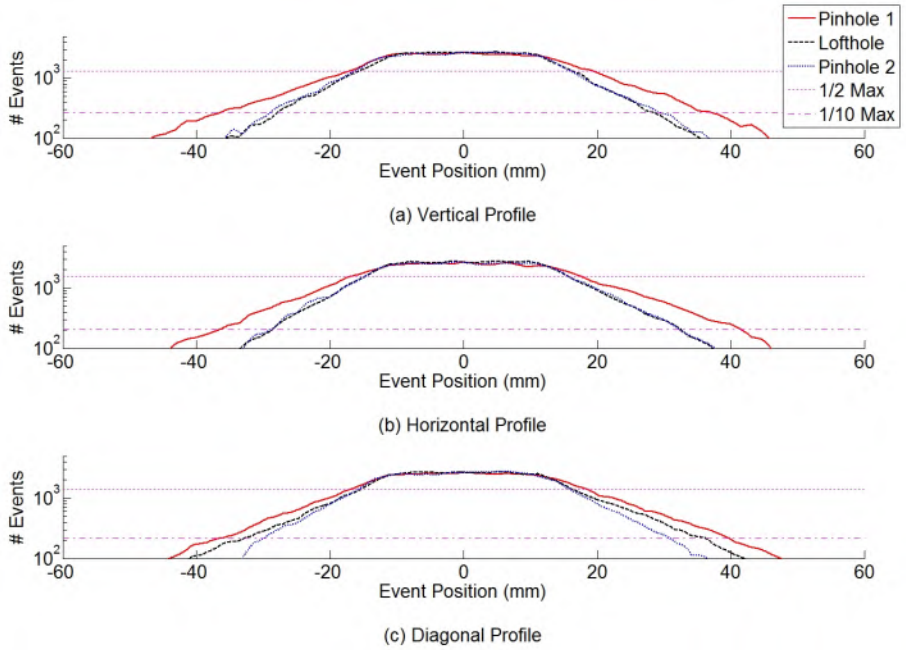

Figure 4.20: (a) A vertical, (b) a horizontal and (c) a diagonal profile (log scale) of the pinhole projection (see Fig. 4.19). The half maximum and the tenth maximum are shown as horizontal lines in each profile graph. The lofthole has less penetration than a knife-edge pinhole that irradiates the same rectangular detector area with full coverage. The abscissa *Event Position* is the distance from the center of the projection.

Additionally the sensitivity of a perfect pinhole collimator (without penetration) was calculated. This sensitivity was then compared to the measured sensitivity of the three collimators.

	# Detections	Sens (%)
Ideal Coll.		0.053
Pinhole 1	1901074 ± 1379	0.103 ± 0.00007
Lofthole	1439849 ± 1200	0.078 ± 0.00006
Pinhole 2	1362621 ± 1167	0.074 ± 0.00006

Table 4.3: Calculated sensitivity of an ideal collimator (without penetration) and measured sensitivities of the three collimators. The standard deviation of the number of detections is based on Poisson statistics.

Table 4.3 lists the calculated (ideal pinhole) and measured sensitivities (pinhole 1, lofthole and pinhole 2). All measured collimators have a higher sensitivity than the ideal collimator and this is due to penetration. The sensitivity of the lofthole is slightly higher than the sensitivity of pinhole 2. The sensitivity of pinhole 1 is significantly higher than the sensitivity of the lofthole and the sensitivity of pinhole 2. This increase in detection efficiency is caused by penetration and will thus be reflected in a worse collimator resolution.

4.6 Discussion

We have derived and validated a sensitivity formula for a lofthole and a knife-edge pinhole that has an aperture and a square exit opening. This formula includes the penumbra effect. The derived formula shows good agreement with the simulations (less than 0.12% difference).

The sensitivity formula could be further improved by incorporating penetration. In section 4.5.2 we have compared the calculated sensitivity of an ideal collimator with the measured sensitivities of three collimators. The measured sensitivities were all significantly larger than the calculated sensitivity of the ideal pinhole collimator. This is due to penetration.

The proposed formula does not allow to calculate the sensitivity for geometries where also the entrance window defines the FOV and sensitivity of the aperture. Currently we design loftholes in such a way that only the exit window defines the FOV and sensitivity of the aperture. We also add an entrance window and we make sure that this entrance window does not further limit the FOV or sensitivity (an example is depicted in Fig. 4.6). In most cases this can be done by making the entrance window slightly larger than the exit window. As a consequence the proposed formulas can be used and the aperture has a true knife-edge which will lower the amount of penetration. The flood map measurements illustrate the square projections of a lofthole with a square exit window. Other geometries are also possible; a pentagonal or hexagonal exit window (Fig. 4.21) could be useful when using, for instance, curved detectors. The point source measurement shows the lower amount of penetration for a lofthole compared to a pinhole. The addition of an entrance opening would further decrease penetration.

SPECT systems with high-resolution detectors need less magnification (sometimes minification can be used), and as a consequence the bottom of the collimator plate is close to the detector. Such systems benefit most from the lofthole. The penumbra is small compared to the total irradiated

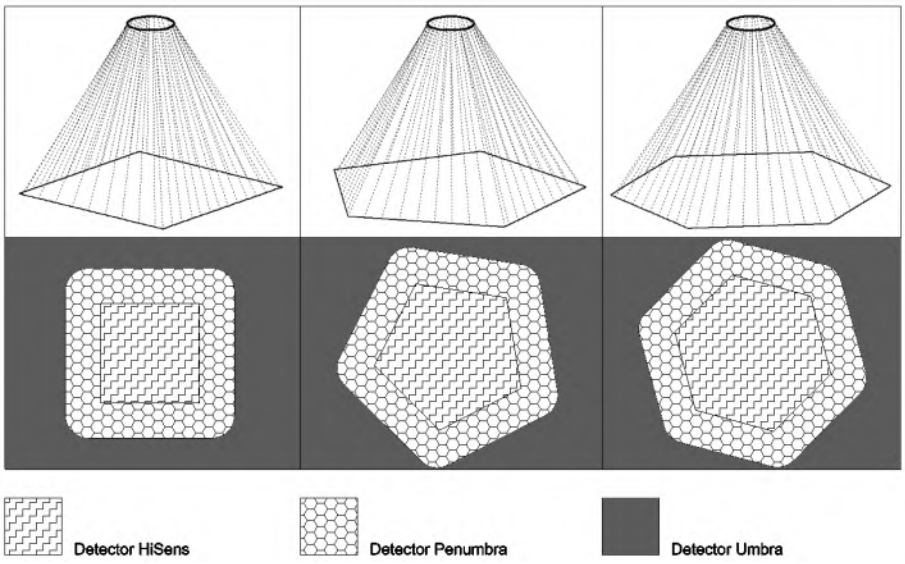

Figure 4.21: Examples of different possible lofthole geometries and the irradiated detector area. The 4-sided lofthole has a square projection on the detector. This geometry is well-suited for use with rectangular detectors. The pentagonal and hexagonal geometries can be useful when curved detectors are used.

area, a lofthole has less penetration than a pinhole and the lofthole has no need for additional shielding to avoid overlap.

4.7 Summary and original contributions

We have presented a new shaped pinhole geometry (the lofthole). This geometry allows for efficient detector usage without overlap and lowers the amount of penetrating gamma photons.

The sensitivity formula has been derived. This formula takes the penumbra effect into account; it does not take penetration into account. The formula is valid for geometries where the field-of-view and the sensitivity of the aperture is solely limited by the exit window.

A prototype lofthole has been studied that has a rectangular flood map projection. This allows for optimal detector usage with multi-pinhole collimators and rectangular detectors. Penetration of a rectangular lofthole is lower than an equivalent knife-edge pinhole that irradiates the same rectangular detector area with full coverage.

The single-lofthole collimator (see Fig. 4.13(a)) will be used in combination with the NaI(Tl) detector (chapter 3) to build a compact SPECT system. The design, calibration and reconstruction of this system, and, measurements using this SPECT system are presented in the next chapter.

In chapter 7 we introduce a new manufacturing method for collimators and use this method to produce a multi-lofthole collimator.

The work described in this chapter has been published in a peer-reviewed journal publication [7] and in a conference proceeding [13]. The pinhole and lofthole sensitivity formulas for the penumbra region (eq. 4.2, eq. 4.3, eq. 4.9 and 4.15) were derived by Lara R. V. Pato.

Chapter 5

FlexiSPECT: A compact SPECT system consisting of a high resolution NaI(Tl) detector and a lofthole collimator

5.1 Introduction

In this chapter, the NaI(Tl) detector (chapter 3) is combined with the single-lofthole collimator (used for the lofthole measurements in chapter 4, see section 4.5) to build a compact demonstrator SPECT system. Two SPECT setups have been made, one that fits rat-size phantoms and one that fits mouse-size phantoms.

This chapter focuses first on the mechanical setup of the SPECT systems. After this, the geometric calibration is explained. This calibration determines the geometric parameters of the system. MLEM image reconstruction is used, this is explained in section 5.4. Finally, we present measurements on the rat and the mouse system. On both setups we have scanned a hot rod phantom and a uniform phantom.

Other researchers have developed compact small-animal SPECT systems. Schramm et al. [131] have developed a compact system that is based on a 2 mm thick NaI(Tl) detector and an ultra high-resolution parallel hole collimator. Using this system they obtained a spatial resolution of 2.5 mm. Another

system, developed by McElroy et al. [132], consists of a pinhole collimator and a gamma-ray detector that is based on a pixelated NaI(Tl) scintillator and PSPMTs. Several pinhole collimators were made with aperture diameters ranging from 0.5 mm to 3 mm, the detector collimator distance f is fixed to 9 cm. Using a radius of rotation of 3 cm (magnification $m = 3$) and the 0.5 mm diameter aperture, they obtained a resolution of approximately 0.95 mm and a sensitivity of 0.0013 %. Kastis et al. [133] build a compact SPECT/CT system that employs a 2 mm thick high-resolution CZT detector (pixel pitch 380 μm) and a tungsten parallel hole collimator (hole pitch 380 μm). Hong et al. [134] developed a compact system that is, similar to our system, based on a NaI(Tl)/PSPMT detector and a pinhole collimator. Using this system, the researchers were able to distinguish the 2.4 mm rods of a Derenzo phantom. Finally, Zeniya et al. [135] developed a compact system that uses a pixelated NaI(Tl) scintillator, an H8500 PSPMT and a pinhole collimator. Using a magnification of 1.3 and a pinhole with a 1 mm diameter they obtained a spatial resolution of 2.8 mm and a sensitivity of 0.00014 % at 3 cm pinhole-source distance.

5.2 Mechanical setup

Fig. 5.1 shows the setup used for the SPECT system. It consists of a high resolution NaI(Tl) detector (presented in chapter 3) with the collimator (depicted in Fig. 5.2) mounted on the detector. A rotation stage in front of the collimator rotates the object.

By positioning the rotation stage at a larger distance from the gamma camera, we are able to enlarge the system FOV (while reducing the magnification). This property is used first to build a rat-size SPECT system (pinhole-COR distance approximately equal to 43 mm) and then to build a mouse-size system (pinhole-COR distance approximately equal to 24 mm). These two systems are schematically depicted in Fig. 5.3. The rat-size system uses minification and the mouse-size system has a magnification factor of approximately 1.

5.3 Geometric system calibration

Accurate knowledge of the SPECT system's geometric parameters is required to perform artifact-free image reconstruction. These parameters are typically acquired by making use of a dedicated phantom measurement. A

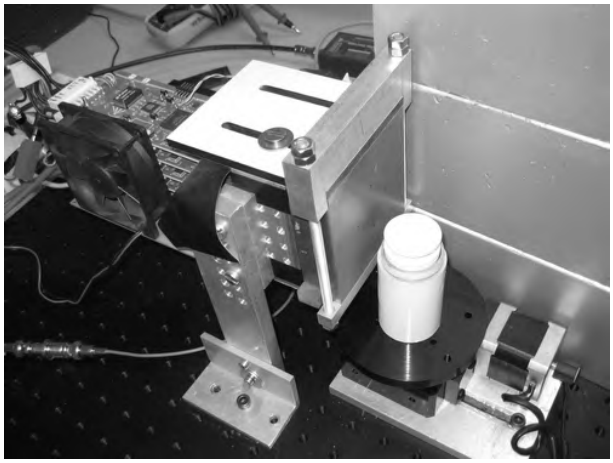

Figure 5.1: The SPECT setup.

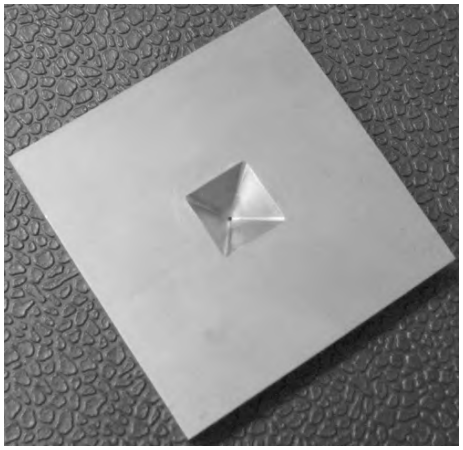

Figure 5.2: The lofthole collimator used for the flexiSPECT setup. This figure shows the exit opening of the collimator. The other side is flat and only contains the circular aperture.

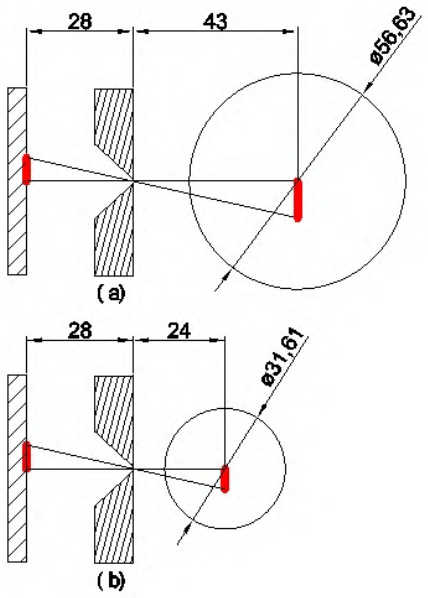

Figure 5.3: (a) The rat-size SPECT system and (b) the mouse size SPECT system. Dimensions are in mm. The circle represents the system FOV.

phantom with three point sources is used here (as proposed by Beque et al. [136]). Two phantoms were made: a mouse-size calibration phantom (Fig. 5.4(a)) and a rat-size calibration phantom (Fig. 5.4(b)); the mouse-size phantom is used to calibrate the mouse-size system and the rat-size phantom is used to calibrate the rat-size system. Both phantoms consist of a polymethyl methacrylate (PMMA) plate with three drilled holes (hole diameter is 1 mm). Approximately 11 MBq ^{99m}Tc is pipetted in each hole.

The calibration phantom is positioned on the rotation stage and acquisitions are made for 60 angles (10 s per acquisition). This is schematically depicted in Fig. 5.5; this figure shows the position of the three rotating point sources for 60 angles (drawn in blue), the pinhole's aperture (green) and the detector (red), the projections of the point sources for the various angles on the detector are marked in black.

A 2D-Gaussian fit is performed on the projection of each point source for each angle, 180 fits have to be done in total. The centers of these Gaussian functions are labeled as the measured point source projection centers $(CtrXm_{i,j}, CtrYm_{i,j})$, with i the point source index ($i \in [1 \quad 3]$) and j the projection angle index ($j \in [1 \quad 60]$).

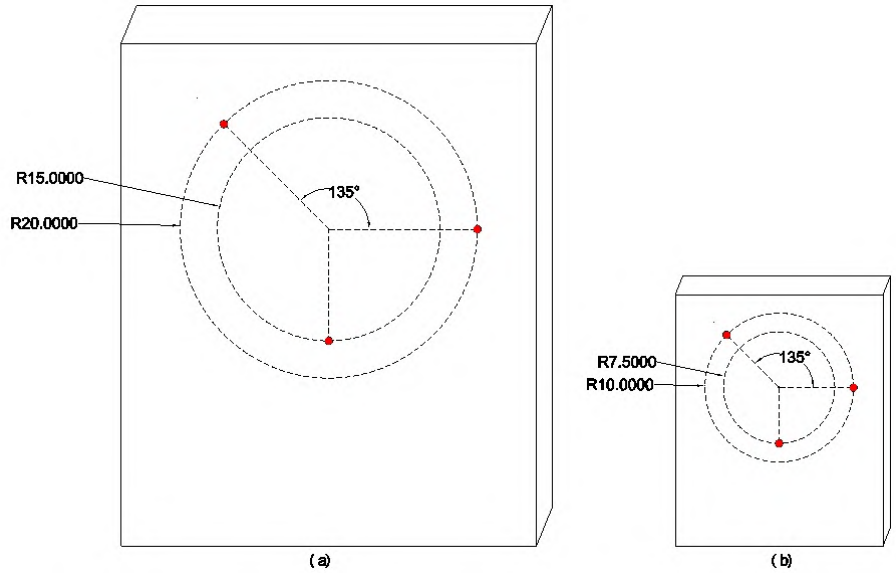

Figure 5.4: (a) The rat-size calibration phantom and (b) the mouse-size calibration phantom. The red circles represent the holes that contain the ^{99m}Tc. Dimensions are in mm.

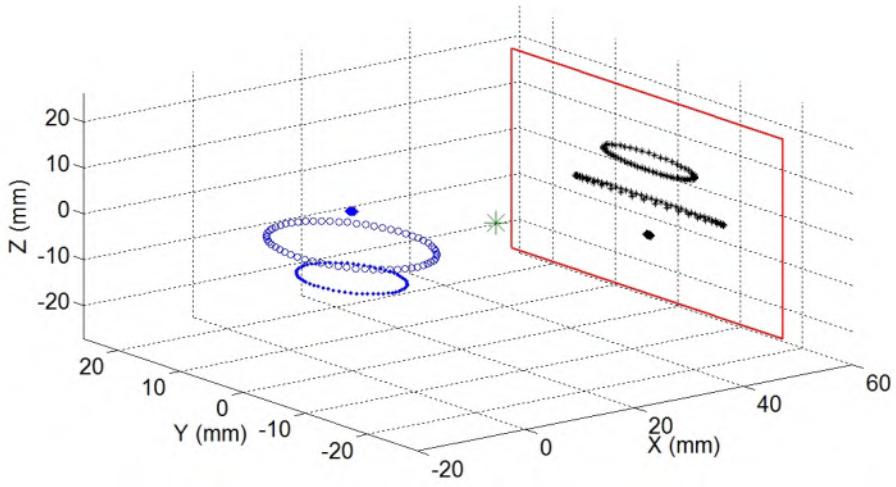

Figure 5.5: The three rotating point sources (blue) project through the aperture (green) onto the detector (red).

An analytical forward projector has been developed that is able to derive the interaction position of a point source on the detector given the system geometry and the point source position. This analytical forward projector is used to calculate the projection centers on the detector $(CtrXc_{i,j}, CtrYc_{i,j})$.

Unconstrained nonlinear optimization (Nelder-Mead simplex algorithm) is then employed to search the different geometric parameters (focal distance, detector offset, pinhole offset, phantom position and initial angle rotation motor) that minimize the Euclidean distance between the measured point source projection centers $(CtrXm_{i,j}, CtrYm_{i,j})$ and the analytically forward projected point source projections $(CtrXc_{i,j}, CtrYc_{i,j})$. The cost function that is used for this optimization is defined as:

$$Cost = \Sigma_{i=1}^{3}\Sigma_{j=1}^{60}\sqrt{(CtrXm_{i,j} - CtrXc_{i,j})^2 + (CtrYm_{i,j} - CtrYc_{i,j})^2}. \tag{5.1}$$

5.4 Image reconstruction

5.4.1 MLEM reconstruction

The GPU accelerated MLEM reconstruction that was developed by Vandeghinste et al. [137] is used here. This reconstruction method makes use of 7-ray based resolution recovery [118]. We used 500 iterations for reconstruction. The reconstructed image is post-filtered with a 1D-Gaussian kernel along the x,y and z direction (standard deviation σ equals 1 voxel). Voxel size is 0.85 mm x 0.85 mm x 0.85 mm for the rat-size system and 0.5 mm x 0.5 mm x 0.5 mm for the mouse-size system.

5.4.2 Sensitivity correction

Sensitivity correction is implemented by combining a flood source measurement and a voxel-aperture distance correction in the reconstruction. A flood source is placed in front of the collimator. This flood source is a plastic rectangular box (12.5 mm thick) that is filled with ^{99m}Tc. The setup is shown in Fig. 5.6. The projection of this flood source needs to be corrected for the thickness of the phantom: an oblique ray passing through the aperture and through the phantom has a larger pathlength inside the phantom and as a result a larger contribution to the projection than a perpendicular ray. This correction is done by multiplying each pixel with the cosine of α (Fig. 5.6), α is the angle formed by a line from pixel to aperture center and

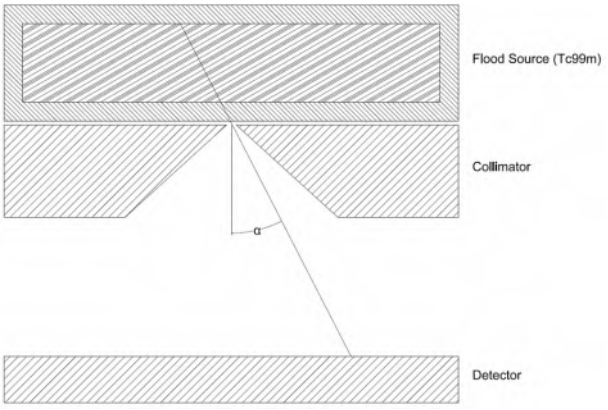

Figure 5.6: Flood source measurement (drawn to scale).

a line perpendicular to the aperture plane.

This flood map is used in reconstruction to correct for the angle-dependent term in the sensitivity. Additionally the distance from voxel to aperture is calculated, this then corrects for the distance-dependent term in the sensitivity.

The advantage of this method compared to using an analytical sensitivity model in the reconstruction is that it will cancel out sensitivity mismatches due to angle-dependent collimator penetration. The sensitivity of a pinhole equals:

$$S_{PinColl} = \frac{d^2 \sin^n \theta}{16h^2}, \tag{5.2}$$

where n is set to 3 (eq. 2.13) for an impenetrable pinhole. Smith et al. [38] have done measurements on several pinhole collimators and conclude that, depending on the pinhole geometry, n can be significantly larger than 3 for a non-ideal penetrable pinhole (values in a range from 3.3 to 4.1 were measured for 140 keV gamma ray photons).

The usage of the flood map was essential for our collimator as collimators that have the aperture located close to the top of the collimator plate have a higher amount of penetration compared to collimators that have the apertures located closer to the center of the plate.

5.5 SPECT system measurements (Rat Setup)

5.5.1 Geometric calibration

The geometric system calibration is made as described in section 5.3, the outcome of this calibration is summarized in table 5.1. The non-calibrated parameters are listed in table 5.2.

The results of the calibration are used to calculate the magnification (m, eq. 2.14), the collimator resolution ($R_P inColl$, eq. 2.16), the detector sensitivity for perpendicular 140 KeV gamma rays (S_{Det}, eq. 2.4), the resolution in the center of the field of view (R_t, eq. 2.15) and the total sensitivity in the center of the field of view (S, eq. 2.27). These are give in table 5.3.

Table 5.1: Outcome of the geometric calibration (rat-size setup)

Detector-aperture distance	f	26.92	mm
Detector shift X		1.14	mm
Detector shift Y		-0.15	mm
Pinhole to ROR	h	42.97	mm
Pinhole shift X		0.65	mm
Pinhole shift Y		0	mm

Table 5.2: Geometric parameters (not calibrated)

Aperture diameter	d	1	mm
Detector intrinsic resolution	R_i	1.24	mm
Detector thickness	T	5	mm

Table 5.3: Derived geometric parameters

Magnification	m	0.63	
Collimator resolution	$R_{PinColl}$	2.60	mm
Det. sens. (P.E. interactions only, 140 keV)	S_{Det}	64	%
Total res. in center of FOV (analytical)	R_{Sys}	3.26	mm
Sens. in center of FOV (analytical)	S	0.0022	%

The magnification factor is 0.63, this SPECT system works in minification mode. Note that the geometric calibration has estimated the detector-aperture distance as 26.92 mm (69.89 mm - 42.97 mm) instead of 25 mm.

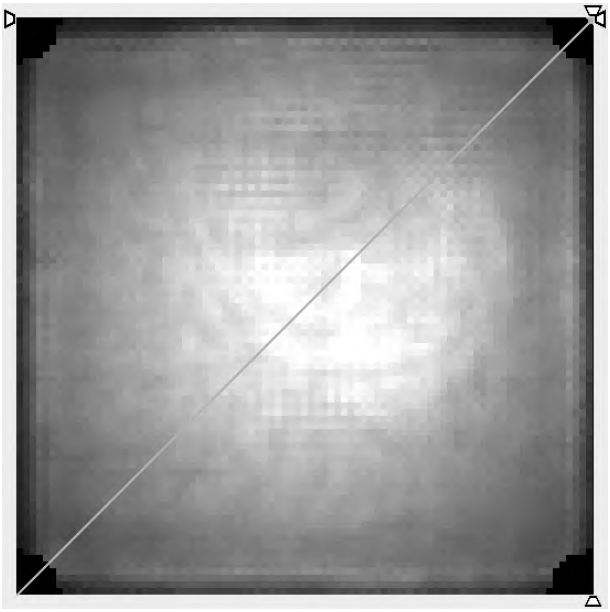

Figure 5.7: The projection of the flood Source on the detector.

This is because the geometric calibration assumes a perfect detector and on average the events interact at a depth of about 2 mm in the scintillator.

5.5.2 Flood source calibration

An acquisition of a flood source is made, this will be used during image reconstruction of the rat-size phantoms (see section 5.4.2). The resulting projection is shown in Fig. 5.7. Fig. 5.8 depicts a profile through the flood source projection and the corrected flood source projection on the line marked in Fig. 5.7. This flood source is corrected for the finite thickness of the flood phantom.

5.5.3 Rat-size hot rod phantom

The setup shown in Fig. 5.1 is used to rotate a micro Deluxe phantom (Data Spectrum, USA) with hot spot inserts (see Fig. 5.9). This phantom is a hot rod phantom with rods of 1.2, 1.6, 2.4, 3.2, 4.0 and 4.8 mm; the cylinder containing the hot rod insert has an outside diameter of 5 cm and an inside diameter of 4.5 cm. The distance between the center of the rods

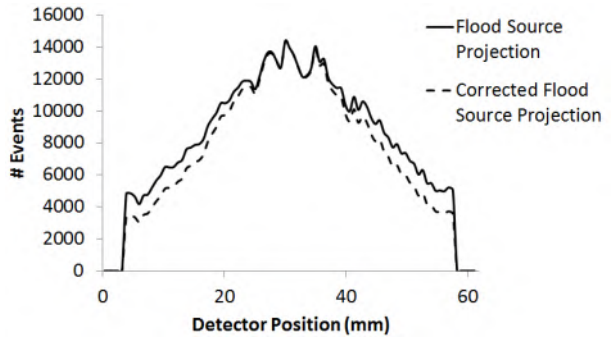

Figure 5.8: Profile through the flood source projection and the corrected flood source projection on the line indicated in Fig. 5.7.

is equal to twice the rod diameter (Fig. 5.9). The hot rod phantom is filled with an activity of 24.75 MBq/ml ^{99m}Tc (the phantom is only partially filled, volume 7 ml, total activity 173.16 MBq).

Data are acquired for 60 angles (120 s for first angle, acquisition times at other angles are adapted to correct for decay).

Once all data is acquired it is processed by the MLE algorithm for event positioning, an energy window of 28 KeV is used. Image reconstruction is done as described in 5.4.

Fig. 5.10 depicts the reconstructed rat-size hot rod phantom (voxel size is 0.85 mm x 0.85 mm x 0.85 mm), the rods of 2.4 mm can be distinguished.

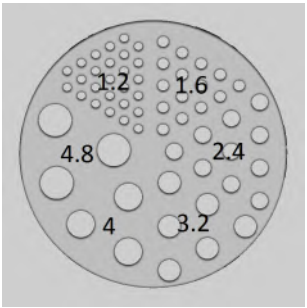

Figure 5.9: The rat-size hot rod phantom.

Figure 5.10: Reconstructed rat-size hot rod phantom.

5.5.4 Rat-size uniform phantom

A uniform phantom (cylindrical container with 4 cm inner diameter) is filled with 7.13 MBq/ml ^{99m}Tc (volume 25 ml, total activity 178.34 MBq). Data are acquired for 60 angles (120 sec for first angle, measurement times at other angles are corrected for decay).

Fig. 5.11 shows the reconstructed rat-size uniform phantom (voxel size is 0.85 mm x 0.85 mm x 0.85 mm); Fig. 5.12 depicts a profile through the reconstructed image at the line indicated in Fig. 5.11(a). The RMS noise is calculated for a cylindrical ROI (the ROI is marked on Fig. 5.11) and is equal to:

$$RMS_{noise} = 100\sigma_{voxel}/\mu_{voxel} = 6.5\%, \tag{5.3}$$

where σ is the standard deviation of the voxels and μ is the mean voxel value.

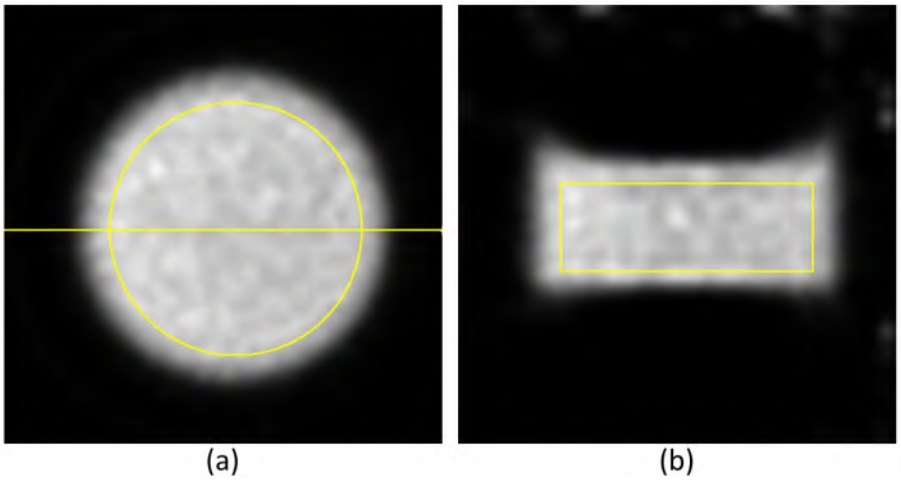

Figure 5.11: (a) Transverse view and (b) coronal view of the reconstructed rat-size uniform phantom

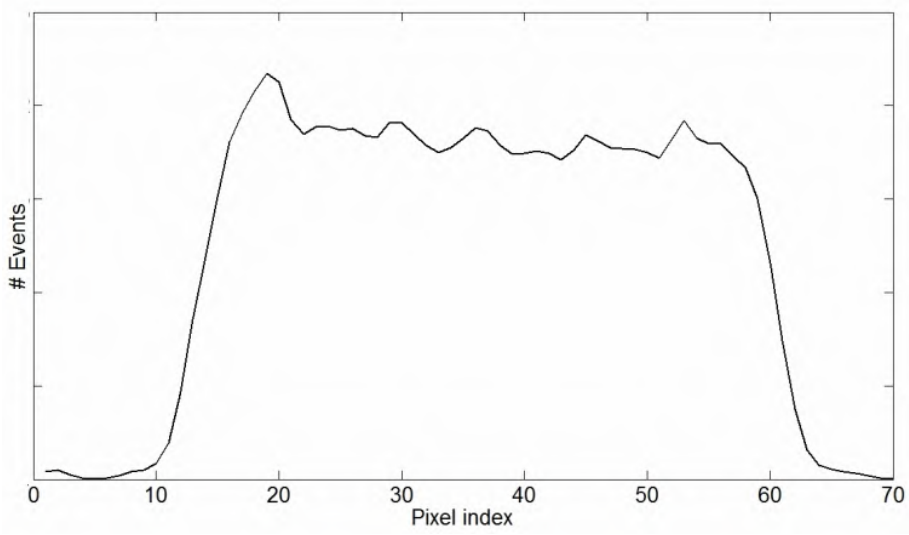

Figure 5.12: Profile view at the line indicated in Fig. 5.11(a).

5.6 SPECT system measurements (Mouse Setup)

5.6.1 Geometric calibration

Geometric system calibration is made as described in 5.3.

The outcome of the geometrical calibration is listed in table 5.4, the non-calibrated parameters are listed in table 5.5 and the derived parameters are listed in table 5.6.

The magnification factor is 1.06 after calibration.

Table 5.4: Outcome of the geometric calibration (mouse-size setup)

Detector-aperture distance	f	27.16	mm
Detector shift X		1.28	mm
Detector shift Y		-0.22	mm
Pinhole to ROR	h	25.71	mm
Pinhole shift X		0.76	mm
Pinhole shift Y		0	mm

Table 5.5: Geometric parameters (not calibrated)

Aperture diameter	d	1	mm
Detector intrinsic resolution	R_i	1.24	mm
Detector thickness	T	5	mm

Table 5.6: Derived parameters

Magnification	m	1.06	
Collimator resolution	$R_{PinColl}$	1.95	mm
Det. sens. (P.E. interactions only, 140 keV)	S_{Det}	64	%
Total res. in center of FOV (analytical)	R_{Sys}	2.27	mm
Sens. in center of FOV (analytical)	S	0.006	%

5.6.2 Flood source calibration

A similar flood phantom measurement as for the rat setup has been acquired (see 5.5.2), this acquisition was corrected for the phantom thickness and the resulting projection will be used during image reconstruction of the mouse-size phantoms.

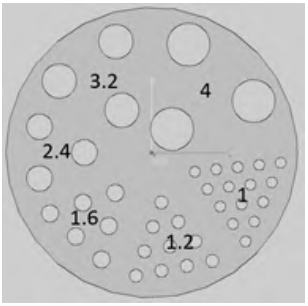

Figure 5.13: The mouse-size hot rod phantom.

5.6.3 Mouse-size hot rod phantom

A mouse-size hot rod phantom with a diameter of 27 mm has been 3D printed (Shapeways, The Netherlands). The density of the phantom material is approximately equal to the density of water. It has rods of 1, 1.2, 1.6, 2.4, 3.2 and 4 mm. The distance between the center of the rods is equal to twice the rod diameter (Fig. 5.13).

The phantom is filled with an activity of 46.62 MBq/ml ^{99m}Tc (the phantom is only partially filled, volume 3 ml, total activity 139.86 MBq). Data are acquired for 60 angles (120 sec for first angle, measurement times at other angles are corrected for decay).

Fig. 5.14 depicts the reconstructed mouse-size hot rod phantom (voxel size is 0.5 mm x 0.5 mm x 0.5 mm), the rods of 1.6 mm can be distinguished.

5.6.4 Mouse-size uniform phantom

A uniform phantom (cylindrical container with 2.7 cm inner diameter) is filled with 11.62 MBq/ml ^{99m}Tc (volume 15 ml, total activity 174.27 MBq). Data are acquired at 60 angles (120 s for first angle, measurement times at other angles are corrected for decay).

Fig. 5.15 depicts the reconstructed mouse-size uniform phantom (voxel size is 0.5 mm x 0.5 mm x 0.5 mm). The top and bottom of the coronal view (Fig. 5.15b) show artifacts. This is due to insufficient axial sampling and would probably be resolved by using multiple bed positions. Fig. 5.16 shows a profile through the reconstructed image at the line indicated in Fig. 5.15(a). The RMS noise is calculated for a cylindrical ROI (the ROI is

Figure 5.14: Reconstructed mouse-size hot rod phantom.

marked on Fig. 5.15):

$$RMS_{noise} = 100\sigma_{voxel}/\mu_{voxel} = 5.7\%. \tag{5.4}$$

5.7 Discussion

The mouse-size FlexiSPECT system has a calculated sensitivity of 0.006% in the center of the FOV and a measured reconstructed resolution of 1.6 mm. The rat-size FlexiSPECT system has a calculated sensitivity of 0.0022% in the center of the FOV and a measured reconstructed resolution of 2.4 mm. Our system's performance is approximately similar to the other compact systems that were listed in the introduction of this chapter (note that it is difficult to compare the systems: some systems have multiple collimators and the sensitivity of the systems was calculated or measured at different positions in the FOV). The resolution and sensitivity of our demonstrator system are however inferior compared to other small animal SPECT systems that have a larger footprint. This is due to the fact that we did not optimize the system geometry: only one lofthole and one detector are used, the

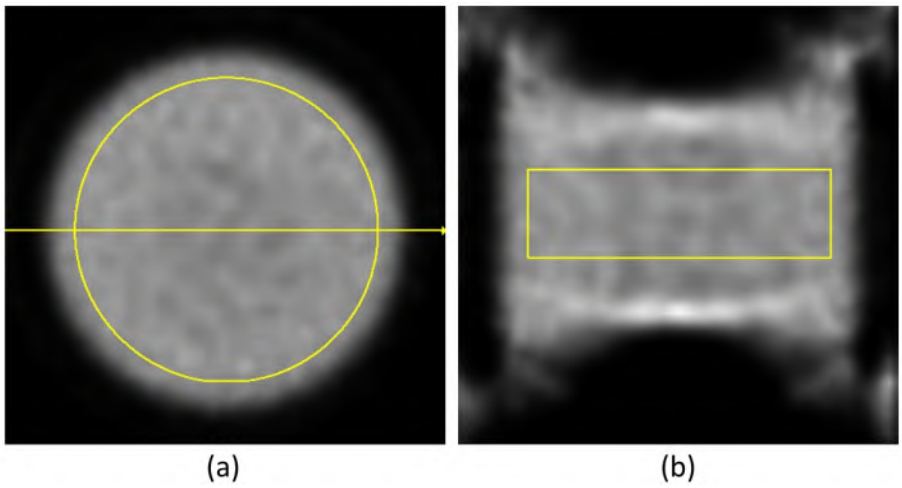

Figure 5.15: (a) Transverse and (b) coronal view of the reconstructed mouse-size uniform phantom.

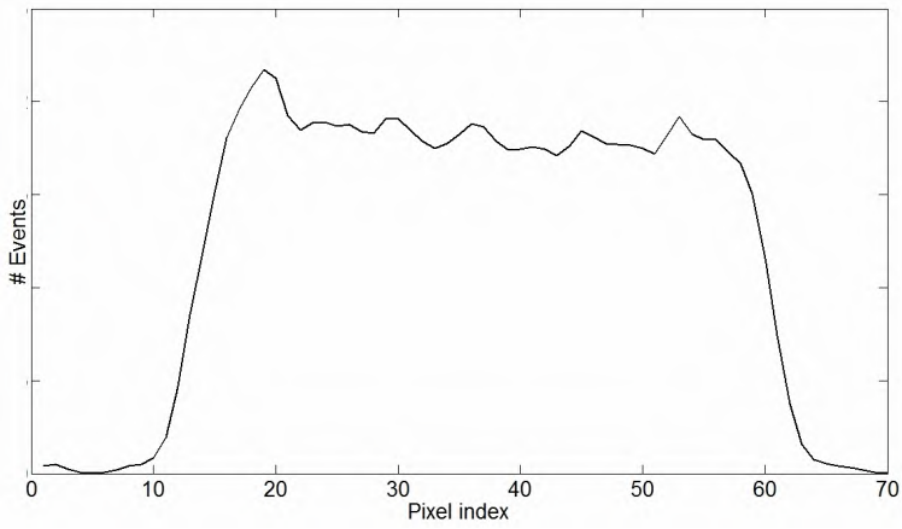

Figure 5.16: Profile view at the line indicated in Fig. 5.15(a).

performance could be improved by using a multi-lofthole collimator and multiple detectors. The U-SPECT-II system [55] has a peak geometric sensitivity of 0.07% and a resolution of 0.35 mm when the high resolution mouse collimator is used. This system can also be equipped with a rat collimator. In that case the sensitivity is 0.09% and the resolution is 0.8 mm. Bioscan's NanoSPECT [138] has a peak sensitivity of 0.0695% and a resolution of 0.4 mm when the mouse high resolution collimator (M UHR) is used. The sensitivity is 0.0998% and the resolution 1.1 mm when the rat high resolution collimator (R UHR) is used.

The collimator has its aperture located on the top of the plate so it has a lot of penetration (see section 5.4.2). This was done to allow bringing the object very close to the aperture (voxels close to the aperture have a high sensitivity and a high resolution). However it is not possible for the two discussed setups to bring a part of the object very close to the aperture, as this would lead to truncation of the field of view. Future versions of the collimator will have the aperture located closer to the center of the plate as was proposed in Fig. 4.6.

5.8 Summary and original contributions

The NaI(Tl) detector (see chapter 3) has been used in combination with a lofthole collimator (see chapter 4) to build two tomographic setups. The tomographic capabilities of these setups are demonstrated by scanning a hot rod phantom and a uniform phantom. These setups use minimal magnification (mouse-size system) and minification (rat-size system), as a consequence the total footprint of the system is small (45 cm x 25 cm).

Our system has a low sensitivity and resolution because the current system uses only one lofthole and one compact detector.

In a first step we will try to further improve the intrinsic detector resolution by using a thinner and denser scintillator (see chapter 6). A thin scintillator has a small light spread and we expect that this will improve the spatial resolution of the detector. By making use of detectors that have a better spatial resolution, one can use less magnification while preserving the same system resolution. Because of this, more detectors and more loftholes can be used, which results in a larger system sensitivity. The current NaI(Tl) scintillator has reflecting top and side surfaces. This was done to obtain a good energy resolution. A drawback is that the spatial resolution near the edges is strongly degraded. The use of black edges will further improve the spatial resolution and the usable detector area. More loftholes can be used

when the detector has a larger usable detector area which also results in an improved system sensitivity.

In a second step, we will introduce a new multi-lofthole collimator, for which a new manufacturing method is introduced (see chapter 7).

The work described in this chapter has been published as part of a peer-reviewed journal publication [5].

Chapter 6

A high resolution LYSO-based SPECT detector

6.1 Introduction

In chapter 3 we have introduced a NaI(Tl) based scintillation detector. This detector has an intrinsic resolution of 1.24 mm in the CFOV.

The advantage of high-resolution gamma-ray detectors is that they can be used to build higher sensitivity systems [1]. When a higher-resolution detector is used then less magnification is required and the detector can be positioned closer to the pinhole. The consequence of this is that more pinholes and detectors can be positioned and due to this the system sensitivity increases.

In order to further improve the spatial resolution, we have now build a new detector based on a 2 mm thick continuous slab of Lutetium Yttrium Orthosilicate (LYSO) [66]. The main advantage of LYSO for SPECT is the high stopping power: 2 mm thick LYSO scintillator has a higher detection efficiency than a 5 mm thick NaI(Tl) scintillator (see table 6.1). Other advantages are the high photo-electric fraction (τ/μ) and its non-hygroscopicity (it does not need packaging and a light guide).

The hypothesis of this study is that such a thin LYSO scintillator will have a small light spread and, as a consequence will also have an improved spatial resolution when coupled to a Hamamatsu H8500 PSPMT. An additional advantage of such a thin LYSO scintillator is that image degradation due to depth of interaction will be smaller compared to the thicker NaI(Tl) scintillator. This effect can be significant for pinhole designs where the an-

gle of incidence is large. The disadvantages of LYSO are the lower light yield (38 photons/keV for NaI(Tl) and 25 photons/keV for L(Y)SO [33]), the intrinsic radioactivity (due to the presence of ^{176}Lu, natural abundance 2.6%, discusses in section 6.4.3) and the moderate energy resolution (section 6.4.2).

In this chapter we compare the 5 mm thick NaI(Tl) scintillator (see chapter 3, note that results might slightly vary due to reassembling the NaI(Tl) detector) to a 2 mm thick LYSO scintillator. A new event positioning algorithm, mean nearest neighbor event positioning (MNN) is used to obtain a high spatial resolution and to enlarge the useful detector area. The advantage of MNN is that it is computationally less demanding than MLE event positioning.

Table 6.1: A comparison of NaI(Tl) and LYSO, absorption data is shown for 140 keV photons and is based on the NIST XCOM database [34]

	NaI(Tl)	LYSO
Density (g/cm^3)	3.67	7.1
Light yield (photons/keV) [33]	38	25
Photoelectric fraction (%)	83.74	91.46
Thickness (mm)	5	2
Tot. abs. for given thickness (%)	70.65	83.36
PE. abs. for given thickness (%)	57.02	73.49
Intrinsically radio-active	×	✓

First, an overview on previous work that considered L(Y)SO for SPECT is given. Second, we compare the mean light spread of a beam source directed to the center of the detector. Third, we compare the energy resolution. Hereafter, the intrinsic activity of the LYSO detector is measured. Finally, the spatial resolution is evaluated with beam-source measurements and with a tungsten resolution collimator.

6.2 Previous work

Others have considered LYSO and the related scintillator Lutetium Orthosilicate (LSO) for SPECT before. Seidel et al. [139] have built a prototype miniature gamma camera based on a 23.7 mm diameter and 4.7 mm thick continuous LSO scintillator. This scintillator was coupled to a Hamamatsu R3941 PSPMT (66 mm x 55 mm active area, 18x16 crossed wire anodes). Using COG event positioning, they measured a resolution of 2.3 mm for 140

keV gamma photons and a useful detector area of 10 mm diameter. At that time LSO was not available in larger sizes so they were not able to cover the whole PSPMT with scintillator material. Cardi et al. [140] were the first to use a collimator in a prototype LYSO-based PET scanner. By using an existing PET scanner they were bound to the 10 mm thick pixelated LYSO crystals that were designed for use with 511 keV PET tracers. By raising the high voltage of the PMTs, to compensate for the lower amount of light photons that is generated by a 140 keV gamma photon, they were able to adequately detect and position the events. Dhanasopon et al. [141] used thin pixelated LSO (pixel size 2 mm x 2 mm, 3 mm thick) and an H8500 PSPMT to build a miniature gamma ray camera. A pixelated scintillator was chosen because it provides a better linearity than a continuous scintillator that uses COG event positioning. Lois et al. [142] coupled a 51 mm x 51 mm x 4 mm continuous LYSO crystal to a Hamamatsu H8500 PSPMT and measured an LYSO background of 21 cps/cm^3 in a 100-180 keV window. They conclude that the LYSO background should not deteriorate the performance of a SPECT system. Related to this, Monte-Carlo simulations were done to evaluate an MR-compatible PET or SPECT detector based on LYSO and Silicon Photomultipliers (SiPMs) [143]. Background measurements were also done by Liang et al. to evaluate a gamma camera that consists of pixelated LYSO (pixel size 2 mm x 2 mm) for positron and scinti-mammography [144]. Yao et al. used a collimator in a PET detector ring and they proposed a background subtraction method to correct for the LYSO intrinsic activity [145].

6.3 Detector

6.3.1 Scintillators, PSPMT and readout electronics

Table 6.2 describes the two setups that were used for this study.

The NaI(Tl) scintillator is the same scintillator as was used in chapter 3. Note that the detector was reassembled for the measurements done in this chapter.

The LYSO scintillator (Hilger Crystals, UK) has a 49 mm x 49 mm surface and is 2 mm thick. It has black edges and a reflecting top surface, this was chosen to enlarge the useful detector area. The LYSO scintillator is not packaged because it is not hygroscopic.

Fig. 6.1 depicts the dimensions of the NaI(Tl) scintillator and the LYSO scintillator.

Table 6.2: Details of the NaI(Tl) setup and the LYSO setup

	NaI(Tl)	LYSO
Surface area (mm^2)	49x49	49x49
Thickness (mm)	5	2
Top surface	reflective	reflective
Side surfaces	reflective	black
Light guide thickness (mm)	2 mm	n.a.
Optical grease	St. Gobain BC630	
PSPMT	H8500	
PSPMT high voltage (V)	900	1000

The Hamamatsu H8500 PSPMT is used as photodetector. The PSPMT high voltage is 1000 V for the LYSO detector and 900 V for the NaI(Tl) detector. The high voltage of the LYSO detector is set higher because LYSO has a lower light yield than NaI(Tl) (see table 6.1). The SPECTatress electronics boards (see section 3.3) were used for the PSPMT readout. There was no difference between the electronics used for the NaI(Tl) detector and the electronics used for the LYSO detector.

Saint-Gobain BC630 was used to optically couple the scintillators to the PSPMTs.

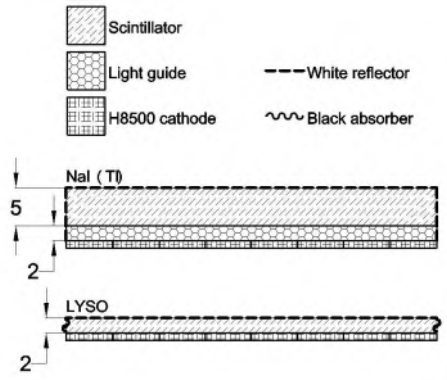

Figure 6.1: The NaI(Tl) and LYSO scintillators (drawn to scale, dimensions are in mm). The light guide cannot easily be omitted because NaI(Tl) is hygroscopic and hermetic sealing is required.

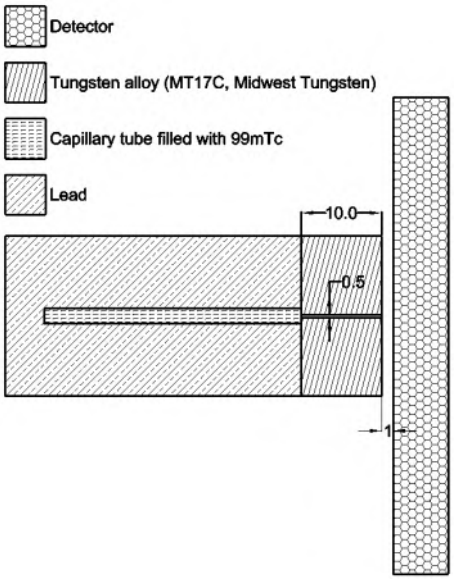

Figure 6.2: The beam source used for detector calibration and resolution measurements (dimensions are in mm). The capillary tube is filled with approximately 370 MBq ^{99m}Tc at the start of the calibration.

6.3.2 MNN calibration

Both detectors were calibrated using the same method.

Calibration data are acquired by using a positioning robot and a beam source (see Fig. 6.2). The beam source scans a Cartesian grid (1 mm step, 50 x 50 positions) and an acquisition is done at each position (a total of 2500 acquisitions is made); this results in a calibration file for each grid position. The acquisition time is 10 s for the first calibration position and is adapted for the other positions to correct for decay of the ^{99m}Tc beam source.

The events of each acquisition are filtered by energy windowing (window width is 20 % for the NaI(Tl) detector and 42 % for the LYSO detector) and by Anger masking (see section 3.4.1).

A histogram of the normalized[1] values of each anode k is then made for each calibration position j (64 histograms per calibration position, 2500 calibration positions). A Gaussian function is fit to this histogram (Fig. 6.3)

[1]The anode values are normalized to energy, see eq. 2.40

and the mean ($\mu_{j,k}$, position index $j \in [1, 2500]$, anode index $k \in [1, 64]$) of this function is stored. Additionally, the energy of each calibration event is calculated by summing the 64 anode values and, an energy histogram is made for each calibration position j. The energy channel with most occurrences is labeled as PC_j (photopeak channel). The PC will vary over the detector surface because of non-uniform light-collection and PSPMT gain mismatches.

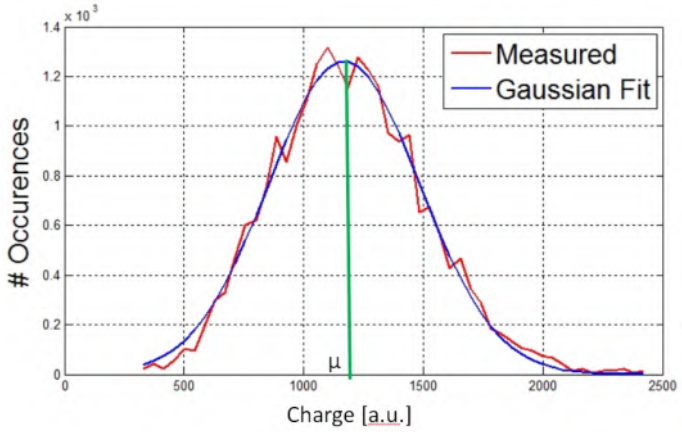

Figure 6.3: A histogram of the charge of a PSPMT channel for a measurement grid position. The histogram is fit with a Gaussian function.

Interpolation is then used to obtain μ and PC values for a 250 μm grid (38809 positions[2]). Index j will be used when we refer to the measurement grid (1 mm steps) and index m will be used when we refer to the interpolated grid (250 μm steps). The coordinates of the measurement grid are (X_j, Y_j) with $j \in [1, 2500]$, the coordinates of the interpolated grid are (X_m, Y_m) with $m \in [1, 38809]$.

An interpolated $\mu_{m,k}$ value is associated with a coordinate (X_m, Y_m) on the interpolated grid. To derive this interpolated value, we first search the 25 nearest calibration positions on the measurement grid. Each one of these positions (X_j, Y_j) has a $\mu_{j,k}$ value associated with it. A second degree bivariate polynomial is then fit to these 25 $\mu_{j,k}$ values; this polynomial is a function of the two robot coordinates X_j and Y_j. $\mu_{m,k}$ Is then calculated by evaluating this polynomial for (X_m, Y_m). Measured and interpolated μ values are depicted in Fig. 6.4.

[2] $((50 \times 4) - 3)^2 = 197^2 = 38809$

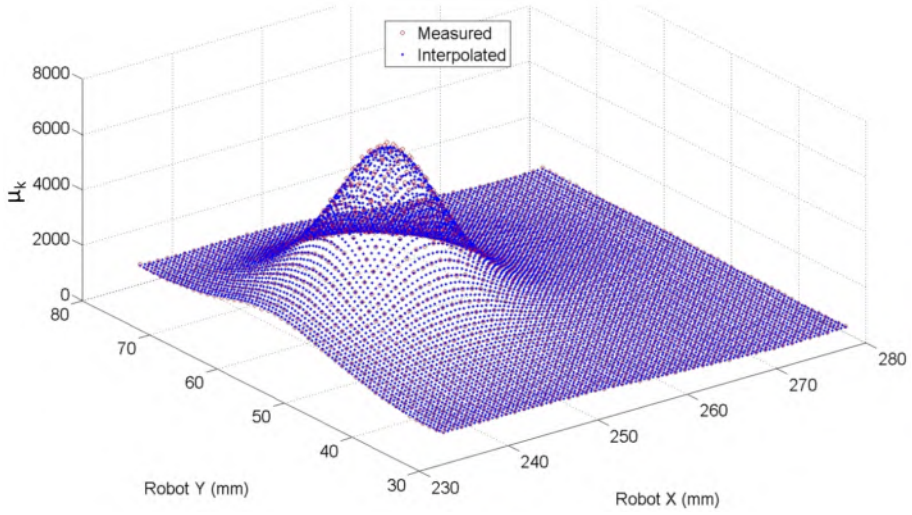

Figure 6.4: The mean value of a PSPMT anode. The measured and interpolated values are shown.

The same interpolation method is used to derive PC_m values.

Hereafter, all the acquired calibration files are reprocessed. The maximum squared distance (MD) of the events to the mean light spread is calculated for each calibration file (see equation 6.1); this will be used during event positioning to perform distance thresholding.

$$MD_j = \max_{i \in 1 \rightarrow N_j} \left(\sum_{k=1}^{64} (CAV_{i,j,k} - \mu_{n,k})^2 \right) \tag{6.1}$$

N_j is the number of events obtained after energy filtering and Anger masking for calibration position j. $CAV_{i,j,k}$ is the normalized value of anode k for calibration event i of calibration position j, and, $\mu_{n,k}$ is the mean normalized value of anode k for position n on the interpolated grid. Index n is defined as the index on the interpolated grid that has the same coordinates as index j on the measurement grid.

Finally, interpolation is used to obtain MD_m values for a 250 μm grid. The interpolation mechanism is the same as the method used to calculate the interpolated $\mu_{m,k}$ and PC_m values.

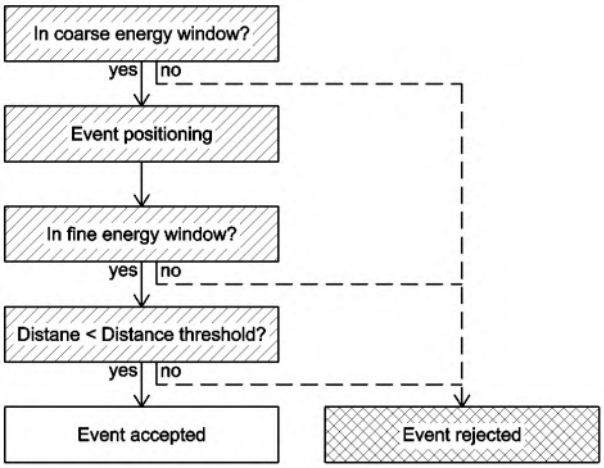

Figure 6.5: The processing steps performed for each detected event. Each event has to be accepted by a coarse energy window before it is positioned. Afterwards a fine energy window and a distance threshold are applied.

6.3.3 Event positioning

Fig. 6.5 shows the processing steps that are performed for each detected event. Each event has to be accepted by a coarse energy window before it is positioned. Once the position is determined, a fine energy window and a distance threshold are applied. All these steps are explained in detail in the following paragraphs.

6.3.3.1 Coarse energy windowing

A coarse energy window is applied before positioning an event to reduce computation time. The two energy thresholds used by this coarse window are described by equations 6.2 and 6.3.

$$CT_L = \frac{(100 - \frac{EW}{2})}{100} min(PC_m) \tag{6.2}$$

$$CT_H = \frac{(100 + \frac{EW}{2})}{100} max(PC_m) \tag{6.3}$$

EW is the width of the energy window in percent. A 20% window is used for the NaI(Tl) setup; a 42% window is used for the LYSO detector. The size of the energy window is approximately twice the energy resolution of the detector.

6.3.3.2 Mean nearest-neighbor event positioning (MNN)

MNN calculates the square of the Euclidean distance ($D_{i,m}$) for an event i to the mean light spread of grid position m. This distance is a measure for the similarity between the light spread of event i and the mean light spread of position m.

$$D_{i,m} = \sum_{k=1}^{64} (AV_{i,k} - \mu_{m,k})^2 \tag{6.4}$$

$AV_{i,k}$ is the normalized value of anode k for event i.

The interaction position (P_i) of event i is set to the grid position m which has the smallest square distance:

$$P_i = \arg\min_m (D_{i,m}). \tag{6.5}$$

This algorithm was implemented on a graphics processing unit (GPU). Computation time is drastically reduced by applying a contracting grid search instead of an exhaustive search [102].

6.3.3.3 Fine energy windowing

When the event has been positioned it is filtered by a fine energy window. The energy window is centered on the PC_m of the event position P_i (equations 6.6 and 6.7). The energy window width (EW) is fixed for the whole detector.

$$FT_{i,L} = \frac{(100 - \frac{EW}{2})}{100} (PC_{P_i}) \tag{6.6}$$

$$FT_{i,H} = \frac{(100 + \frac{EW}{2})}{100}(PC_{P_i}) \tag{6.7}$$

6.3.3.4 Distance thresholding

Additional filtering is done by using a maximal distance threshold. Event i is accepted when D_{i,Pos_i} (the minimal distance) is smaller then MD_{Pos_i} (eq. 6.1), otherwise it is rejected.

The usage of distance thresholding will partly remove multiple interactions (e.g. Compton scatter interaction followed by a photo-electric interaction) which end up in the energy window. For the LYSO detector it will also partly remove the events that are caused by combinations of intrinsic LYSO radioactivity (see section 6.4.3) and (intrinsic LYSO or extrinsic Compton scattered) gamma photons. Such events show little similarity to the energy filtered and Anger masked calibration events; due to this their Euclidean distance to the mean detector response is large and, they can be filtered out by using a distance threshold.

This distance thresholding is related to likelihood thresholding [100]; both methods remove events whose light spread shows no similarity to the light spreads obtained during calibration.

6.4 Evaluation of detector performance

All measurements except the intrinsic radioactivity measurement are done for the NaI(Tl) and the LYSO detector. The intrinsic radioactivity measurement is only performed for the LYSO detector.

6.4.1 Mean light spread

The beam source (see Fig. 6.2, ^{99m}Tc, approximately 387 MBq for the NaI(Tl) detector and approximately 370 MBq for the LYSO detector) is directed to the center of the detector and an acquisition of 60 s is made. 87420 And 101546 events were used to calculate the average light spread of respectively the NaI(Tl) detector and the LYSO detector.

The average light spreads are shown in Fig. 6.6(a) (NaI(Tl) detector) and Fig. 6.6(b) (LYSO detector).

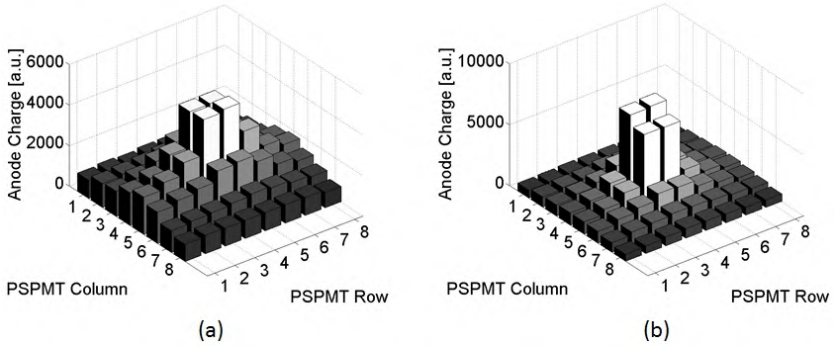

Figure 6.6: The mean light spread of events interacting in the center of the scintillator (measured on an 8x8 channel H8500 PSPMT). (a) The NaI(Tl) measurement and (b) the LYSO measurement.

The mean light spread of the LYSO detector (11.1 mm FWHM) is by far narrower than the mean light spread of the NaI(Tl) detector (16.6 mm FWHM). The main reason for this is the difference in thickness of the scintillators and the usage of a light guide on the NaI(Tl) detector. Our hypothesis is that this leads to a better spatial resolution when the light sampling is fine enough.

6.4.2 Energy resolution

The detector is scanned with the beam source (Fig. 6.2, same activity as in section 6.4.1) on a Cartesian grid (step size 5.5 mm). This results in 81 acquisitions. Acquisition time is 30 s. An energy histogram is generated for each grid position and the full width at half maximum (FWHM) is derived by fitting a Gaussian function to the energy histogram.

The energy resolution of the LYSO detector is position dependent (see Fig. 6.7(b)). The best energy resolution (20.1%) is obtained in the center of the detector; the worst energy resolution (24.4%) is obtained at a corner of the detector. This position dependence is less pronounced for the NaI(Tl) detector due to the absence of black edges (Fig. 6.7(a)). The best energy resolution (9.0%) is obtained at row 7, column 6; the worst energy resolution (9.7%) is obtained at a corner of the detector.

Fig. 6.8 and Fig. 6.9 show the energy spectra of the two acquisitions of section 6.4.1 (beam at center detector, 300 s acquisition time). The spectrum of the LYSO detector shows an X-ray escape peak at 86 keV.

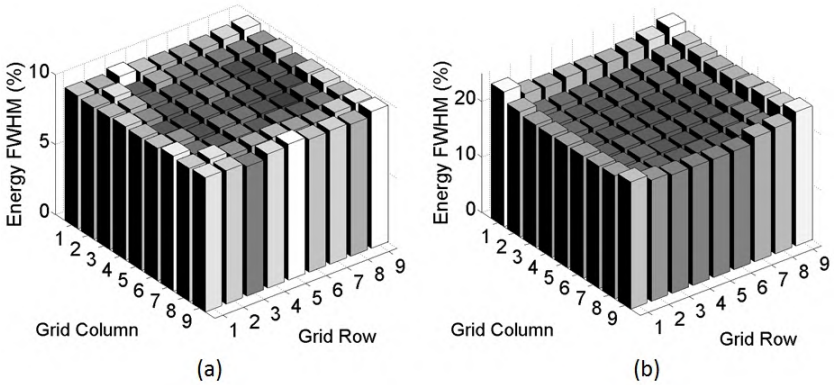

Figure 6.7: The energy resolution measured with the beam source positioned on a Cartesian grid. (a) The NaI(Tl) measurement and (b) the LYSO measurement.

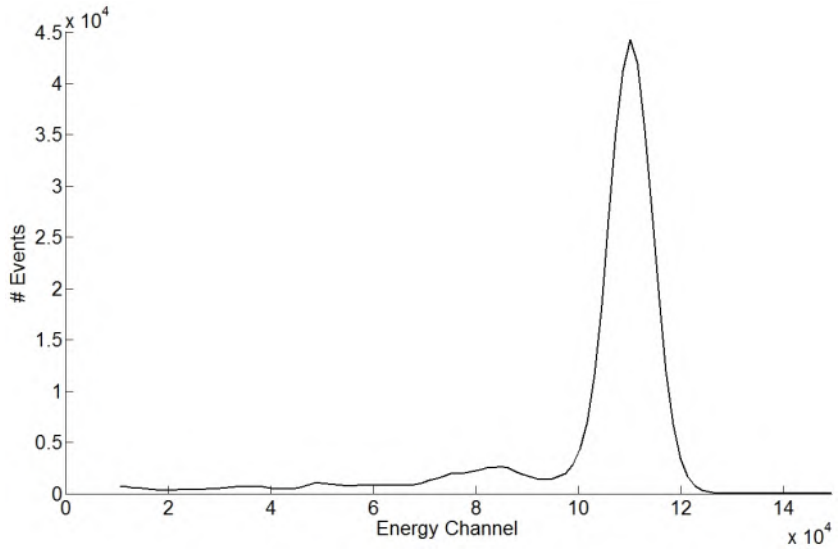

Figure 6.8: The energy spectrum measured with a beam source pointing to the center of the detector (NaI(Tl)).

Table 6.3: The minimum, maximum and mean energy resolution

	NaI(Tl)	LYSO
Min. En. Res. (%)	9.0	20.1
Max. En. Res. (%)	9.7	24.4
Mean En. Res. (%)	9.3 ± 0.2	21.3 ± 1.1

When a gamma photon ($E_\gamma = h\nu$) undergoes photoelectric interaction, then a photo electron is ejected ($E_e = h\nu - E_b$, E_b is the binding energy of the electron) and a characteristic X-ray (E_X) is emitted. In most cases, this characteristic X-ray is immediately absorbed in the detector and the full gamma-ray energy is detected ($E_{Det} = E_e + E_X = h\nu$). When this photoelectric interaction occurs near a surface of the scintillator then it is possible that the X-ray escapes from the scintillator. In that case only a part of the gamma-ray energy will be detected ($E_{Det} = E_e$) and this results in a second peak in the energy spectrum. Here, the X-ray escape peak is caused by $K\alpha_1$ X-ray escape of lutetium. The X-ray escape peak is positioned at $E_{Det} \approx h\nu - E_b = 140keV - 54keV = 86keV$. X-ray escape has a higher

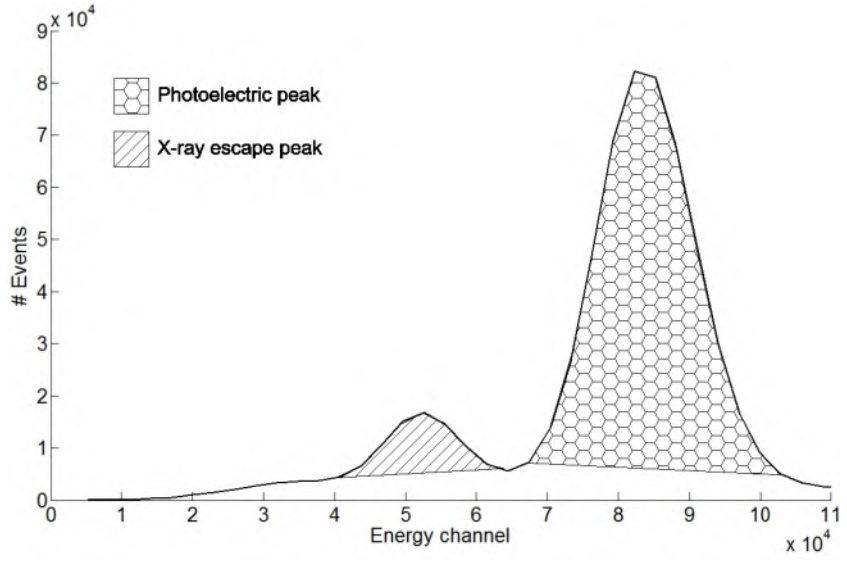

Figure 6.9: The energy spectrum measured with a beam source pointing to the center of the detector (LYSO). Note the X-ray escape peak at 86 KeV; this peak is caused by $K\alpha_1$ X-ray escape of lutetium. The high-energy tail in the LYSO spectrum is caused by the LYSO intrinsic radioactivity.

probability for thin and dense crystals and for low energy gamma photons because in those cases the photoelectric interaction occurs closer to the surface of the scintillator. This effect is discussed in detail in [33].

A consequence of X-ray escape is that the detection efficiency of the LYSO detector will decrease because some photoelectric events will be detected outside of the energy window and will thus be rejected. Consider that the sum of the areas of the two hatched peaks in Fig. 6.9 is 100 % then the photoelectric peak is 90.8 % and the X-ray escape peak is 9.2 %.

6.4.3 Intrinsic radioactivity

The LYSO intrinsic radioactivity is measured by doing a long acquisition (approximately 9 h) without external activity. The events are positioned by the MNN method.

Fig. 6.10(a) depicts the positioned intrinsic activity when no distance thresholding is used. Image (b) is obtained by using distance thresholding. The use of distance thresholding results in a lower LYSO background (7.4% less, see table 6.4) and in a more uniform background image.

The intrinsic count rate is low (125.6 cps, 0.024 cps/mm^3, see table 6.4) in a 110.6 keV to 169.4 keV window.

Table 6.4: Intrinsic LYSO events

Acquisition time (min)	531	
Energy window center (keV)	140	
Energy window (%)	42	
Energy window (keV)	110.6 to 169.4	
	MNN without dist. thresh.	**MNN with dist. thresh.**
Nbr. of events in energy window	4001824	3705634
Nbr. of events in energy window (%)	100	92.6
Count rate (cps)	125.6	116.3
Count rate / vol. scint. (cps/mm^3)	0.026	0.024

The intrinsic radioactivity of LYSO is caused by the presence of ^{176}Lu (natural abundance 2.6%, half-life 3.78 $\times$ 10^{10} years) in the scintillator. The decay scheme of ^{176}Lu is shown in Fig. 6.11 [146]. Intrinsic events

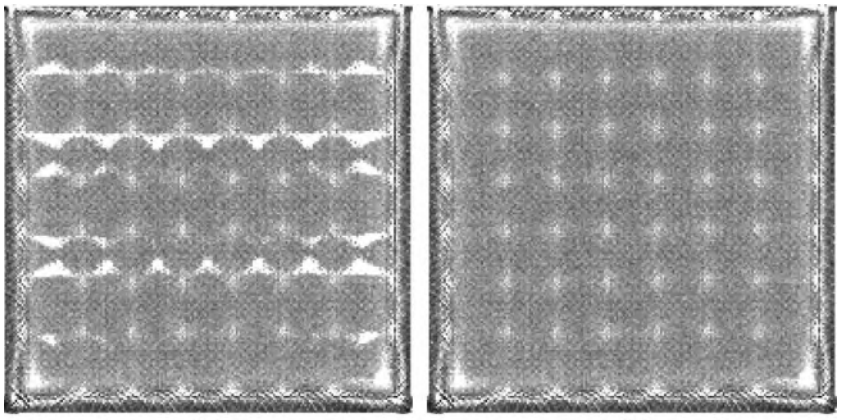

Figure 6.10: This LYSO background image was obtained during a 531 min acquisition without external activity. Image (a) shows the positioned intrinsic activity when no distance thresholding is used. Image (b) is obtained by using distance thresholding. The use of distance thresholding results in a lower LYSO background (7.4% less, see table 6.4) and in a more uniform background image. The intrinsic count rate is low (0.024 cps/mm^3, see table 6.4).

in a 140 keV centered energy window consist of β^- decays in combination with escaping γ decays, combinations of β^- decay and Compton scattered γ decays and combinations of β^- decay and photoelectrically absorbed 88 keV γ decays.

6.4.4 Spatial resolution measurements

A uniformity map is acquired before performing the actual resolution measurements. This is done by measuring a point source (^{99m}Tc, 118 MBq) at large distance (90 cm) from the detector.

6.4.4.1 Beam source measurement

The events from the energy resolution acquisitions (see section 6.4.2: beam source on 5.5 mm grid) are positioned and merged into one image. This image is corrected for uniformity by dividing it by the uniformity map. This is depicted in Fig. 6.12. Profiles are shown in Fig. 6.13.

The mean FWHM of all the beams is calculated for the full field of view (FOV) and for the central field of view (CFOV, the length and width of

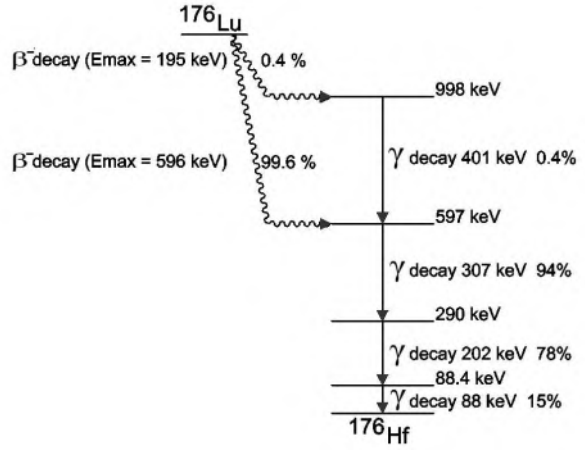

Figure 6.11: The decay scheme of ^{176}Lu [146]. The β^- decay has a continuous spectrum, it is the main contributor to events in a 140 keV centered energy window.

.

the CFOV are 75% of the length and width of the FOV). The results were corrected for the beam diameter by using equation 3.1. Additionally, the bias is calculated for each beam position.

The mean spatial resolution over the whole FOV is 1.72 $\pm$ 0.56 mm for the NaI(Tl) detector and 1.02 $\pm$ 0.32 mm for the LYSO detector. The results improve if we only consider the CFOV because the worst spatial resolution is obtained at the edges of the scintillator. Here, the mean spatial resolution is 1.28 $\pm$ 0.12 mm for the NaI(Tl) detector and 0.78 $\pm$ 0.04 mm for the LYSO detector.

A summary of the results, including the bias, is given in table 6.5.

Table 6.5: Spatial resolution

	NaI(Tl)	LYSO
FWHM FOV (mm)	1.72 $\pm$ 0.56	1.02 $\pm$ 0.32
FWHM CFOV (mm)	1.28 $\pm$ 0.12	0.78 $\pm$ 0.04
FWHM center (mm)	1.18	0.75
Mean bias FOV (mm)	0.10 $\pm$ 0.11	0.04 $\pm$ 0.03
Mean bias CFOV (mm)	0.03 $\pm$ 0.01	0.03 $\pm$ 0.02

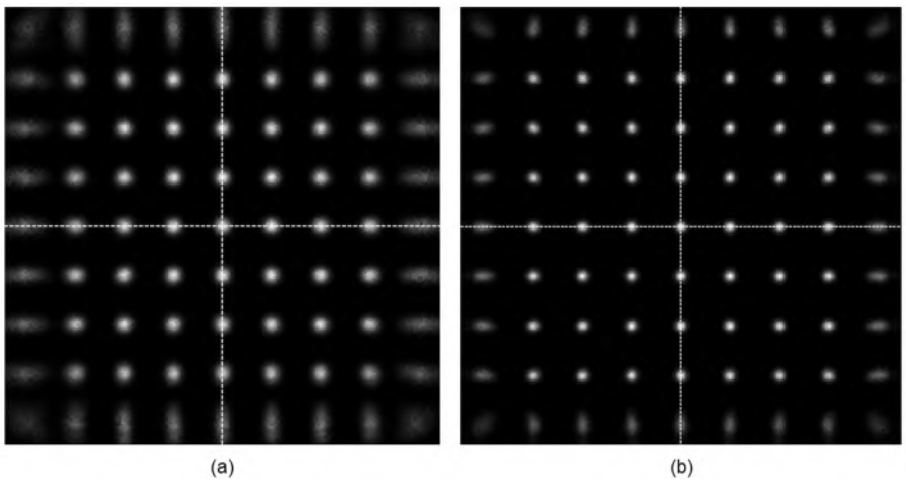

Figure 6.12: Result of the beam source measurement on (a) the NaI(Tl) detector and (b) the LYSO detector. The grid spacing is 5.5 mm. Profiles on the dotted lines are depicted in Fig. 6.13

.

6.4.4.2 Tungsten resolution collimator measurement

The tungsten resolution collimator is shown in Fig. 6.14. The measurement setup is depicted in Fig. 6.15, it consists of a source (^{99m}Tc, 25.9 MBq) that is positioned at large distance (46 cm) from the resolution collimator. The resolution collimator is positioned on the scintillator. The acquired image is corrected for uniformity by dividing it by the uniformity map.

Fig. 6.16(a) shows the image obtained using the resolution collimator on the NaI(Tl) detector; Fig. 6.16(b) is obtained with the LYSO detector. These images clearly indicate the higher resolution of the LYSO detector; the 0.6 mm holes can be resolved on the LYSO detector.

6.5 Discussion

Three factors contribute to the energy resolution of a scintillator: Poisson statistics during the production of light photons in the scintillator (section 2.5.1.2), activator concentration gradients (the light yield becomes position dependent when the activator is not uniformly distributed) and an intrinsic contribution [147]. The latter factor is due to the non-linearity of the light

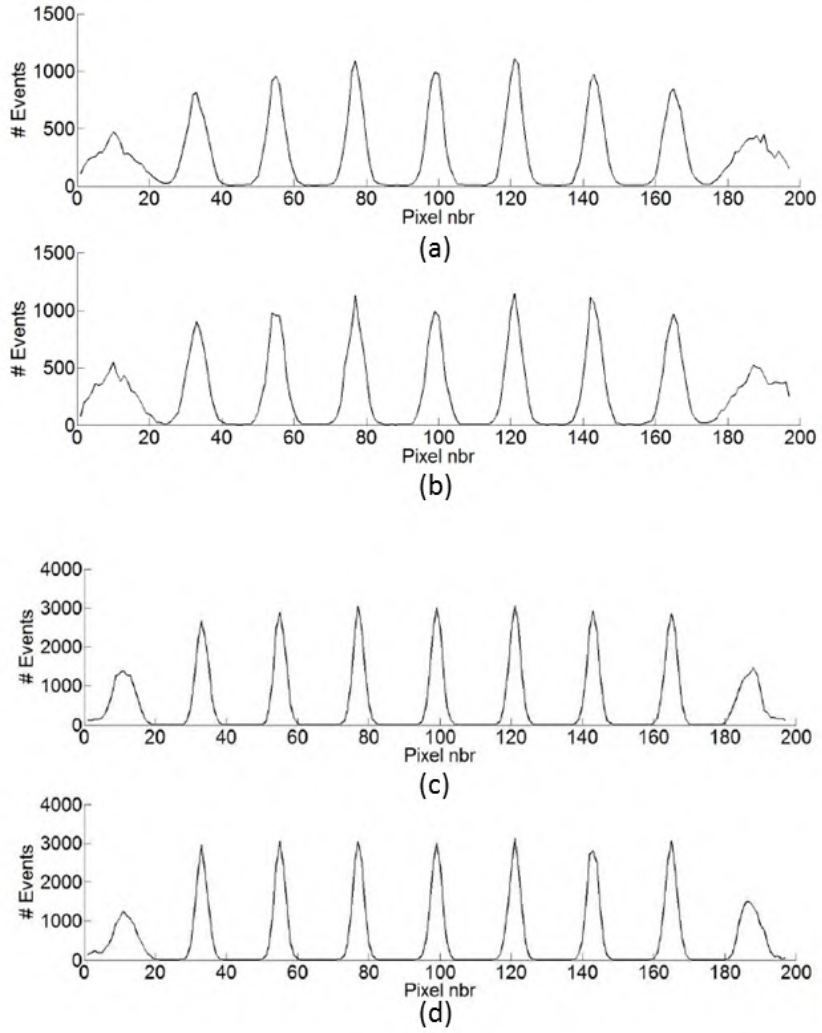

Figure 6.13: (a) Horizontal and (b) vertical profile view of the beam source measurement on the NaI(TI) detector. The FWHM of the central beam position is 1.18 mm. (c) Horizontal and (d) vertical profile view of the beam source measurement on the LYSO detector. The FWHM of the central beam position is 750 μm. The pixel size is 250 μm.

.

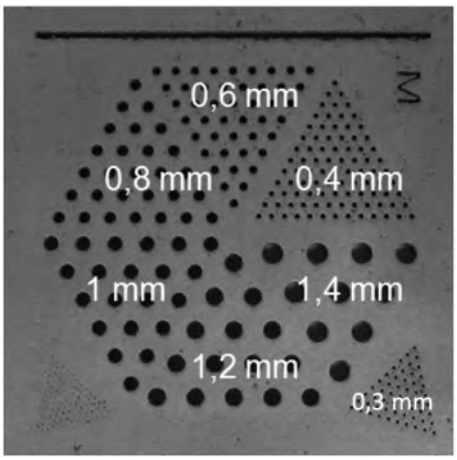

Figure 6.14: The resolution collimator is a 2 mm thick tungsten plate and contains groups of parallel holes of different diameters.

yield of the scintillator.

The energy resolution of the NaI(Tl) detector (9.3%) is superior to the energy resolution of the LYSO detector (21.3 %). This is partially due to Poisson statistics (LYSO has a lower light yield than NaI(Tl) [148]) which results in a larger statistical contribution to the energy resolution for LYSO and, partially due to the worse intrinsic energy resolution of LYSO (discussed by Dorenbos et al. for LSO [147]). L(Y)SO shows significant non-linear behavior for low energy gamma-rays ($E_\gamma < 60keV$). Low energy non-proportional behavior also influences the energy resolution for higher energy gamma photons (such as 140 keV ^{99m}Tc). A photoelectric interaction of a 140 keV gamma ray in a scintillator generates secondary radiation (characteristic X-rays and/or Auger electrons, having a low energy) and a photo-electron. The photo-electron then looses its energy along its track with a series of small energy deposits. All these energy quanta are of a low energy and its energy composition varies, which leads to a worse energy resolution when the scintillator's response is not linear [149].

The energy resolution of the LYSO detector is worst at the edges and corners of the crystal; this is caused by the black side edges of the LYSO scintillator. The mediocre energy resolution might pose problems for standard clinical SPECT imaging because such acquisitions typically contain a high quantity of scattered photons. High spatial resolution detectors are however mostly interesting for pinhole imaging, this is typically used for

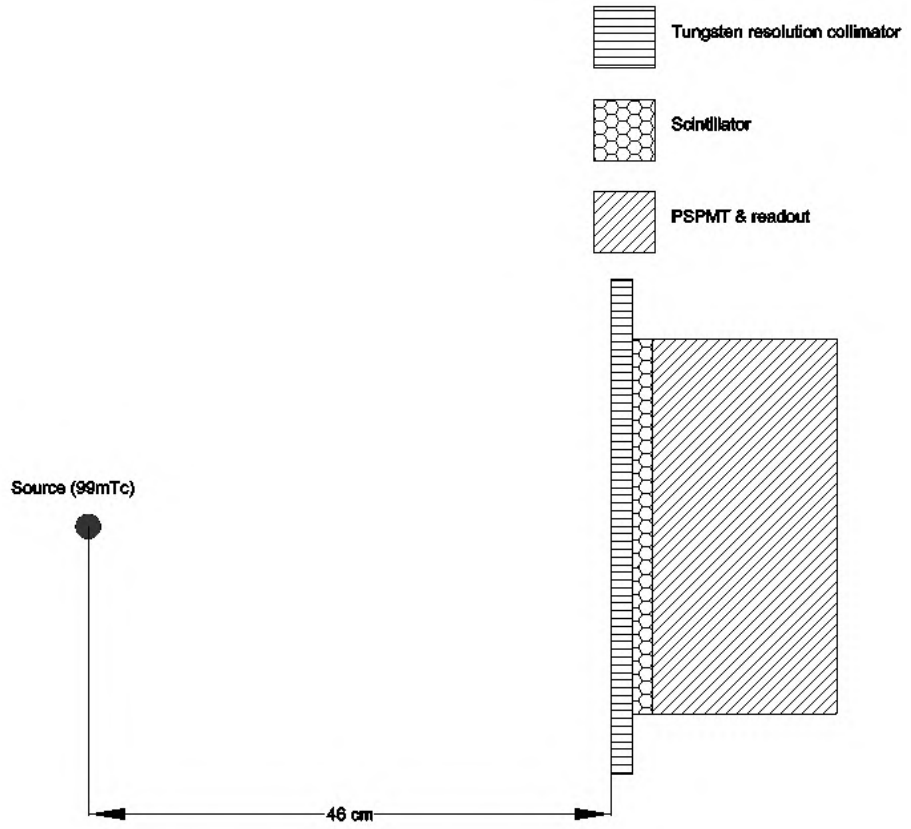

Figure 6.15: The setup used to obtain a projection of the resolution collimator (not drawn to scale)

pre-clinical imaging and energy resolution is less important for such studies due to the lower amount of scattered photons [150]. It does however limit the possibilities to perform multi-isotope SPECT studies.

The intrinsic radioactivity of LYSO is low and is probably not a problem for typical SPECT imaging. Eventually, a background subtraction method (proposed by Yao et al for LSO [145]) can be used to compensate for the intrinsic radioactivity. Our measured background activity (0.024 cps/mm^3 for a 60 keV wide window, centered at 140 keV) is slightly less than what would be expected from the measurements of Lois et al. [142] (0.021 cps/mm^3 for an 80 keV wide window, centered at 140 keV). This is likely due to the different scintillator geometry (49 mm x 49 mm x 2 mm for our setup, 51 mm x 51 mm x 4 mm for the setup used by Lois et al.). The

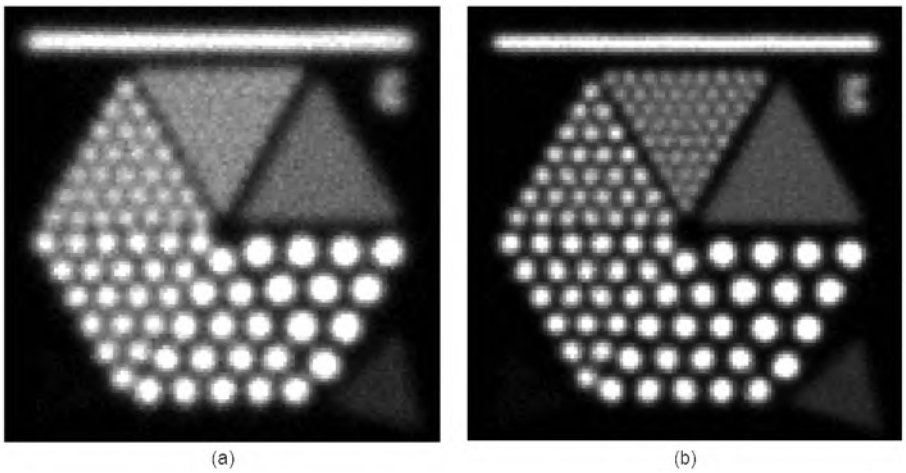

Figure 6.16: The image acquired using the resolution collimator on (a) the NaI(Tl) detector and (b) the LYSO detector (only the detector area uncovered by the collimator holes is shown). The 0.8 mm holes can be resolved on the NaI(Tl) detector, the 0.6 mm holes can be resolved on the LYSO detector.

.

background map (Fig. 6.10(b)) is not uniform. The background events are more prominent at the edges of the scintillator, where the probability that the ^{176}Lu gamma decays are able to escape the scintillator without interaction is higher [142]. Additionally, a grid pattern is observed. This pattern is caused by detector uniformity; it is also visible in the uniformity map. The pattern is not a consequence of the MNN positioning algorithm; a similar pattern is observed when using COG or MLE event positioning (Fig. 6.17). It is our hypothesis that the pattern results from the detector's spatial resolution which is limited by the PSPMT's anode pixel size. Because of this limitation, the resolution will be slightly better when the event interacts above the gap between two pixels than when the interaction takes place above the center of a pixel. This resolution non-uniformity then gives rise to detector non-uniformity.

The LYSO scintillator outperforms the NaI(Tl) scintillator with respect to spatial resolution (NaI(Tl) 1.28 mm, LYSO 0.78 mm). The spatial resolution degradation near the edges of the crystal is worse for the NaI(Tl) detector than for the LYSO detector; this is due to the reflecting edges of the NaI(Tl) package and the thicker NaI(Tl) crystal. The spatial resolution of 0.78 mm obtained with the continuous 2 mm thick LYSO scintillator

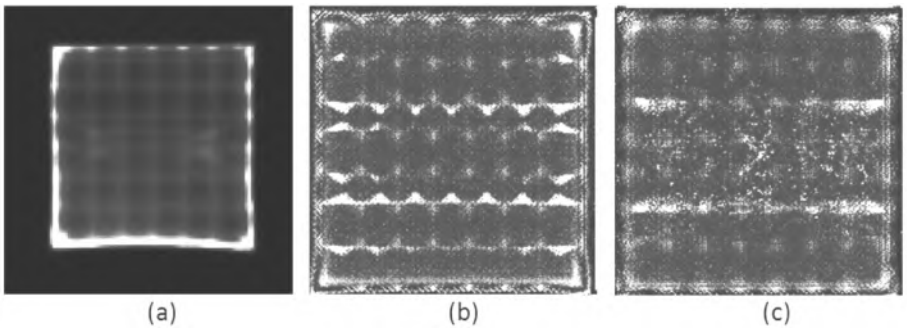

Figure 6.17: The LYSO background image, processed with (a) COG, (b) MNN and (c) MLE event positioning. No distance thresholding or likelihood thresholding has been used.

and the MNN event-positioning algorithm is substantially better than the spatial resolution of other existing SPECT L(Y)SO-based detectors (an enumeration was given in the introduction of this chapter where the highest resolution was 2 mm, obtained by making use of a pixelated LYSO scintillator).

We used MNN to calculate the event position. Previously, MLE event positioning has been used [5, 100, 101]. The use of MLE results in an improvement in spatial resolution (see table 6.6). The advantage of MNN is that it is computationally less demanding than MLE event positioning. A measurement containing 117340 events is positioned in 3.5 s by MNN event positioning (33500 events/s); the same dataset takes 6.0 s using MLE event positioning (19500 events/s).

At first sight, one might expect that the count rate capability of the LYSO detector is higher than that of the NaI(Tl) detector because LYSO is a much faster scintillator (230 ns decay time for NaI(Tl) and 40 ns decay time for LYSO). However, in our setup the count rate is limited by the electronics (by the Ethernet bandwidth and the analog pre-amplifiers) and, as a result both the LYSO and NaI(Tl) scintillator would show approximately the same count rate capability. The count rate performance of the electronics was characterized in a previous chapter (see section 3.7).

LYSO is also interesting for SPECT studies that involve high-energy isotopes (e.g. ^{131}I and ^{111}In) because of its high stopping power. Note however that a thicker scintillator would be required for such applications which would probably result in worse spatial resolution.

Table 6.6: Spatial resolution

	NaI(Tl)	
	MNN	MLE
FWHM FOV (mm)	1.72 ± 0.56	1.63 ± 0.56
FWHM CFOV (mm)	1.28 ± 0.12	1.20 ± 0.13
FWHM center (mm)	1.18	1.14
Bias FOV (mm)	0.10 ± 0.11	0.15 ± 0.11
Bias CFOV (mm)	0.03 ± 0.01	0.08 ± 0.04
	LYSO	
	MNN	MLE
FWHM FOV (mm)	1.02 ± 0.32	1.00 ± 0.37
FWHM CFOV (mm)	0.78 ± 0.04	0.74 ± 0.05
FWHM center (mm)	0.75	0.64
Bias FOV (mm)	0.04 ± 0.03	0.05 ± 0.03
Bias CFOV (mm)	0.03 ± 0.02	0.04 ± 0.03

6.6 Summary and original contributions

We have described two SPECT detectors: the first one is based on 5 mm thick NaI(Tl) scintillator and the second one is based on 2 mm thick LYSO scintillator, both scintillators are coupled to a Hamamatsu H8500 PSPMT. The main detector components were described, MNN calibration and event positioning was explained and, measurements of spatial resolution and energy resolution were presented. The NaI(Tl) detector has an energy resolution of 9.3% and a spatial resolution of 1.28 mm (CFOV); the LYSO detector has an energy resolution of 21.3% and a spatial resolution of 1.02 mm (FOV) and 0.78 mm (CFOV). The LYSO background is low (0.024 cps/mm^3 in a 110.6 to 169.4 keV window) and can probably be ignored for typical SPECT studies.

Due to the high spatial resolution of the LYSO detector, magnification can be small or minification can be used and, as a consequence, more pinholes and detectors can be positioned, which finally results in a higher system sensitivity [1]. A collimator has been designed specifically for our LYSO detector [1]. This collimator has a complex geometry and would be very expensive or impossible to manufacture using the traditional machining techniques like milling, drilling and EDM. Therefore, we introduce in the next chapter a new manufacturing technique for complex tungsten collimators.

The work described in this chapter has been published as a peer-reviewed journal publication [8].

Chapter 7

Rapid additive manufacturing of collimators with selective laser melting of tungsten powder

7.1 Introduction

In chapter 2 we have presented an overview of several collimator types. For the majority of clinical studies a parallel hole collimator is used, but there is an increased use and need for more complex shaped collimators for imaging specific organs (heart, brain [151, 152]) or small objects (mice, rats). Especially in cardiac [153–155] and small animal imaging [156, 157], systems with complex collimator geometries have been designed. These systems often have a high number of pinholes (e.g. 75 pinholes in the U-SPECT II system [158], 300 pinholes in the VECTor system [42]).

The production of complex multi-pinhole and multi-lofthole collimators can be a daunting task. Especially when they have to be made out of tungsten, which is a very hard and brittle material. An overview of different collimator production techniques is given in section 2.4.5. The most commonly used techniques are casting of lead, drilling and milling of lead or tungsten alloys and, electric discharge machining (EDM) of tungsten or tungsten alloys.

In this chapter we present a novel direct additive manufacturing technique for the construction of collimators, based on selective laser melting (SLM)

of high density tungsten powder. Selective laser melting uses a focused laser to melt powder. The laser scans a cross-section of the collimator on the surface of a powder bed. After this the powder bed is lowered and a new uniform powder layer is distributed on top of the previous layer. This process is repeated until the whole collimator is produced.

The traditional techniques are based on removing material from a plate (*subtractive* manufacturing) by making use of mills, drills or EDM. This new *additive* manufacturing technique effectively only adds material where the CAD design file specifies material. This has the added benefit that less material is wasted which might in some cases lead to an additional cost reduction.

We have evaluated this new technique by performing measurements on three sample plates and on two collimators. The plates and the first-generation collimator were produced with the same processing parameters. After this, the processing parameters and post-processing were updated to improve the density and the accuracy, and, the second-generation collimator was produced.

First we measured the density and gamma photon attenuation of the three sample plates. Measurements were done on the first-generation collimator: the density was measured, point source measurements were done and the production accuracy was verified. Finally we measured the density and production accuracy of the second-generation collimator.

7.2 Collimator design

Two collimators have been produced using additive manufacturing. The first-generation collimator was the first design that was produced using this technique. Consequent SPECT simulations indicated that some geometrical changes were required, this resulted in a new design: the second-generation collimator. The latter collimator was also produced using additive manufacturing but some processing parameters and post-processing were updated in order to further improve the accuracy and density of the collimator.

7.2.1 First-generation collimator

We have extended the single lofthole (section 5) to a multi-lofthole collimator for mouse imaging [1]. The collimator has 20 loftholes that focus on different small regions in the mouse. The loftholes have no entrance opening and due to this, the apertures are positioned on the top of the collimator

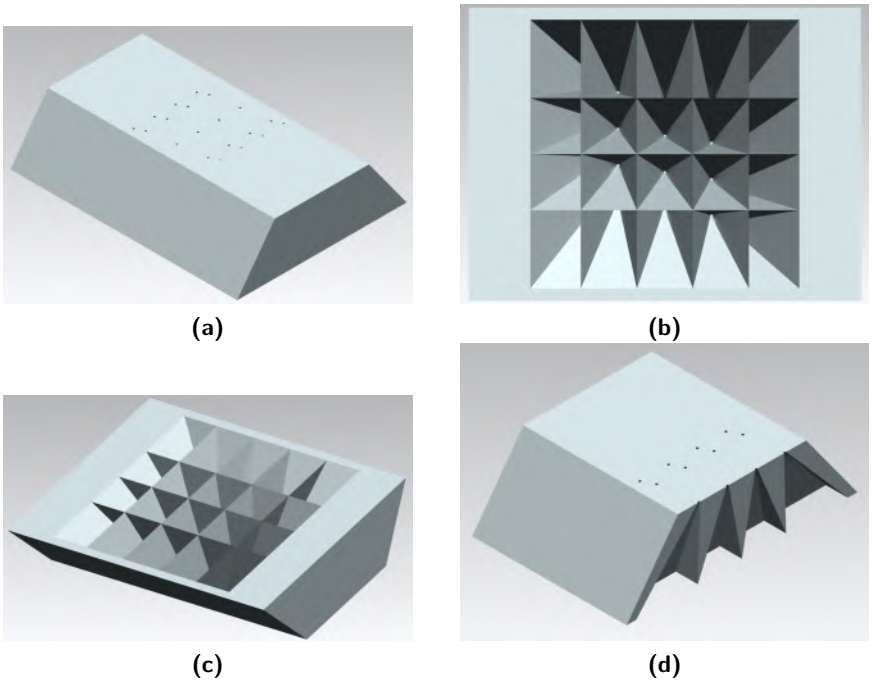

Figure 7.1: The first-generation collimator (CAD rendering). (a) The top side of the collimator. The top of the plate contains 20 apertures, the loftholes do not have an entrance opening. (b) The bottom side of the collimator. This view depicts the exit openings of the loftholes. (c) A side view of the collimator. (d) A profile view shows the sharp edges between the different loftholes.

plate; the exit openings of the loftholes form a grid of sharp edges. This results in a collimator with a complex shape (see Fig. 7.1); the collimator is 16 mm thick and measures 70 mm by 52 mm. The production of such a collimator is very expensive or might even be impossible to produce using drilling, milling or electric discharge techniques due to the large number of loftholes and the obliqueness of these. Therefore additive manufacturing was investigated for producing this design.

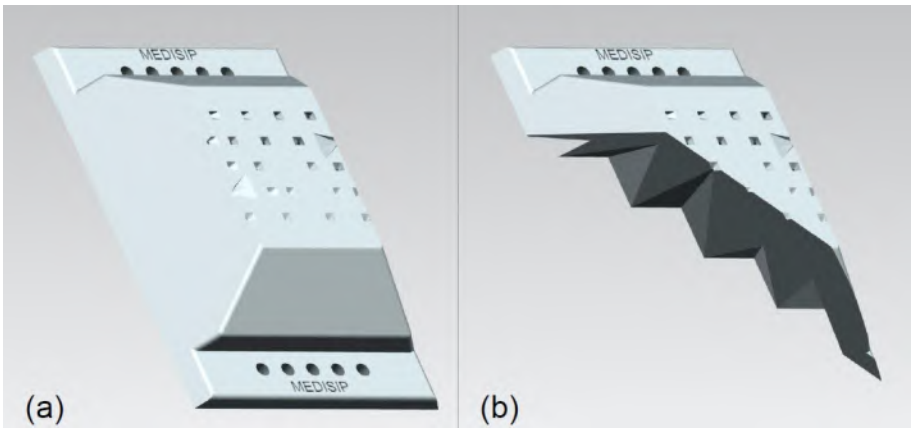

Figure 7.2: (a) A CAD rendering of the second-generation collimator and (b) a profile view.

7.2.2 Second-generation collimator

The second-generation is approximately similar to the first-generation collimator. The differences are that the loftholes have a small entrance opening, to improve penetration performance and, that the apertures are differently positioned. Additionally, the sides of the collimator were made thinner to reduce the amount of tungsten required. A CAD rendering is shown in Fig. 7.2.

7.3 Collimator production

Additive manufacturing is a broad term used for a variety of production techniques in which material is built up in thin layers by a 3D-printer based on a 3D CAD design (STL file). This procedure is repeated layer by layer, until the complete object is built. Components can be built in a large variety of materials; mostly plastics and some metals.

In the past tungsten-carbide alloys have been produced with additive manufacturing but this is the first report on additive manufacturing of pure tungsten. A general illustration of the technique is shown in Figure 7.3.

The build-up process starts with a base plate on the object piston (Fig. 7.3(e)). Metal particles are distributed over this solid piece by the powder delivery system: the powder table (Fig. 7.3(d)) moves up and the powder

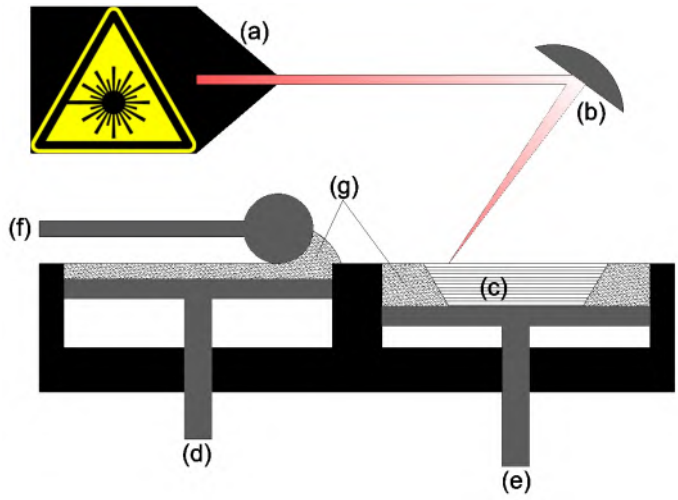

Figure 7.3: Illustration of the production process: (a) laser source, (b) scanner system, (c) collimator, (d,f) powder delivery system, (e) object piston and (g) powder.

distributor (Fig. 7.3(f)) spreads a thin layer of powder (Fig. 7.3(g)). In a next step the laser scanner system (Fig. 7.3(a) and (b)) draws the desired cross section on the powder bed. A raster scan is used for the trajectory of the laser beam; the scan speed is not varied. The laser is switched on at the locations where the powder has to be melted (Fig. 7.3(c)). In the other regions, the powder remains unaffected and can be used again after the process. Each subsequent layer is then melted on the previous layer. The current production process allows volumes with base planes of 25 cm x 25 cm. The different processing parameters (thickness of each powder layer, the laser power, the laser spot size and the laser scanning speed) are determined by performing parameter studies and material testing.

For this application, tungsten powder with a grain size below 63 μm and average diameter of 35 μm was used. A tungsten support structure was melted on top of the base plate. The collimator was built on top of the support structure. The process was started on the end plane of the collimator that contains the apertures. Afterwards, the support structure was removed from the base plate by electric discharge machining (EDM) and the collimator was removed manually from the support structure.

The geometry of the collimator was obtained by simulations [1]. Siemens NX was used to make a CAD model of the geometry. This CAD design

was sent to the additive manufacturing company (Layerwise, Belgium) and within 2 weeks the collimator was produced (Figs. 7.4, 7.5 and 7.6). Layerwise has built their own laser melting machine. This machine uses a solid state laser with a wavelength in the infrared region. Typically used laser powers are in the range of 100 to 200 Watt. The total manufacturing time of a collimator was 26 hours.

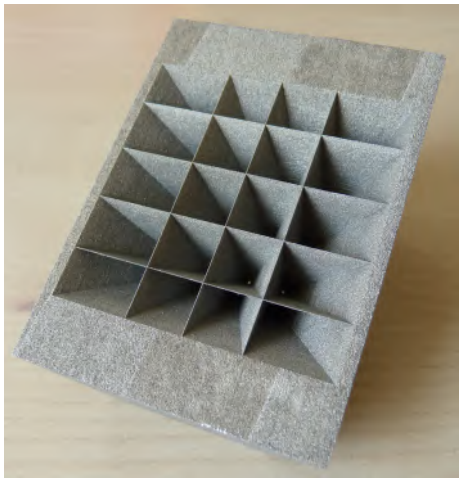

Figure 7.4: Bottom view of the produced first-generation multi-lofthole collimator (16 mm thick and 70 mm x 52 mm transverse size)

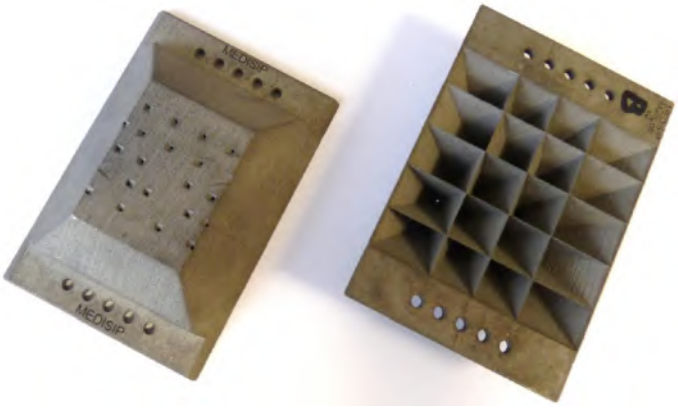

Figure 7.5: The manufactured second-generation collimator

7.4 Measurements on printed sample pieces

A solid tungsten block was made by selective laser melting. Three plates (250 μm, 500 μm and 750 μm thick) were cut from this solid block by use of wire electric discharge machining (WEDM).

7.4.1 Density

The density of each plate was calculated by measuring the mass (Mettler Toledo EL104) and the volume. The volume was calculated by measuring the dimensions of the samples with a caliper (Moore & Wright), the thickness of the plates was measured with a micrometer (Etalon Microselect 25).

Tables 7.1 and 7.2 show the weight, dimensions and density of the three different tungsten plates. There is a noticeable difference between the density of sample number 1 and the densities of sample numbers 2 and 3. We had not expected this because all three plates were machined from the same printed tungsten block. It might be caused by the thickness of this plate in combination with its roughness. The roughness of the plate has minimal influence on the volume of the thicker plates but might have a substantial influence on the volume of the thin plate. The density of the plates is lower than the density of pure tungsten because there are microscopic air cavities in the plates.

Sample Nbr	Thick. (mm)	Dim. 1 (mm)	Dim. 2 (mm)
1	0.24	9.63	10.1
2	0.48	9.64	10.09
3	0.73	9.67	10.13

Table 7.1: Dimensions of the three tungsten plates

Sample Nbr	Weight (g)	Dens. (g/cm^3)
1	0.3635	15.6
2	0.821	17.6
3	1.265	17.7

Table 7.2: Densities of the three tungsten plates

7.4.2 Attenuation

A 140 keV ^{99m}Tc beam source was used to irradiate the sample plates. The measurement setup is depicted in Fig. 7.7. The beam source has a 355 μm diameter hole and a hole length of 10 mm. The NaI(Tl) detector described in chapter 3 is used.

First a measurement was made without an attenuating sample piece. This was followed by a measurement with an attenuating sample piece. An acquisition time of 60 seconds and an energy window of 20% was used for each measurement. These measurements were repeated 10 times for each sample piece, the beam was not moved in between the 10 measurements. The detected events were filtered by position (only events located in a radius of 2 mm around the position of the peak in the detector measurement were used) to obtain a narrow beam measurement that minimizes the contribution of scatter.

The energy and position filtered data were then used to calculate the attenuation of the sample pieces for 140 keV gamma rays; the outcome was compared to the expected attenuation calculated by the Lambert-Beer law. This calculation uses the measured density (section 7.4.1) and the mass attenuation coefficient of tungsten for 140 keV (NIST XCOM database, 1.88 cm^2/g).

The expected and measured attenuation of the three plates is given in table 7.3, the standard deviation was calculated from the 10 attenuation measurements that were done for each plate, the expected and measured attenuation are in good agreement. As a comparison we also calculated the expected attenuation of pure tungsten plates (density 19.25 g/cm^3, μ_m 1.88 cm^2/g) and pure lead plates (density 11.34 g/cm^3, μ_m 2.39 cm^2/g) having the same thicknesses as the measured plates (table 7.4).

Sample Nbr	Expected Att. (%)	Meas. Att. (%)	StDev (%)
1	50.5	50.3	1.2
2	79.6	79.7	0.4
3	91.2	91.5	0.3

Table 7.3: Expected attenuation and measured attenuation for 140 keV gamma ray photons. The expected attenuation uses the dimensions and densities from tables 7.1 and 7.2.

Additionally a transmission scan of each plate was made to check the uniformity of the plates. This was done using a GE eXplore Locus SP micro-CT (90kVp, 60uA, averaged over 3 frames, 3 seconds exposure time).

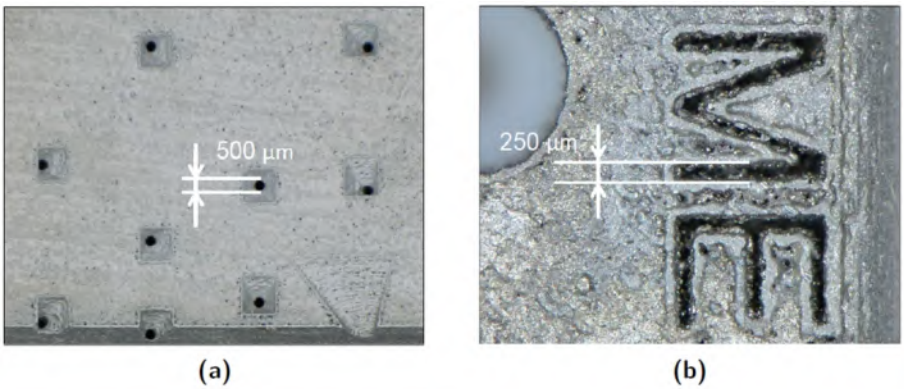

Figure 7.6: Some details of the second-generation collimator. (a) A microscopic view of the entrance openings and apertures. (b) The resolution of the manufacturing process allows for fine details such as text.

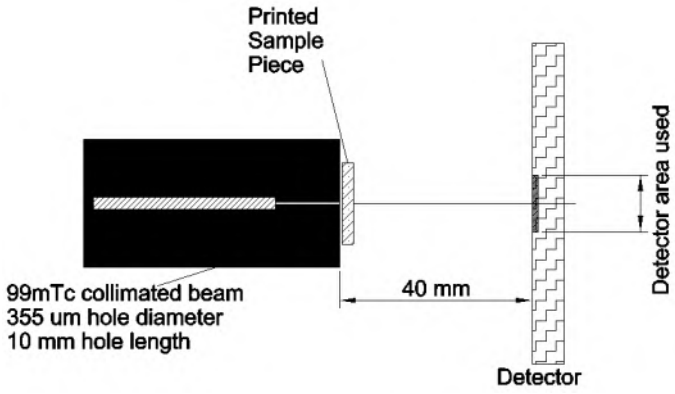

Figure 7.7: The setup used to measure attenuation. Three sample plates were made (250 μm, 500 μm and 750 μm thick). The detected events were energy and position filtered to obtain a narrow beam measurement that excludes scatter.

Sample Nbr	Att. Pure W	Att. Pure Pb
1	58.1	47.8
2	82.4	72.8
3	92.9	86.2

Table 7.4: The attenuation factors of pure tungsten plates (density 19.25 g/cm^3, μ_m 1.88 cm^2/g) and pure lead plates (density 11.34 g/cm^3, μ_m 2.39 cm^2/g) for the thickness of the three plates are given for comparison.

The transmission images are shown in Fig. 7.8(a), (b) and (c). A horizontal profile through the center of these images is shown in Fig. 7.8(d), (e) and (f). These flat profiles indicate that the plates have uniform attenuation.

7.5 Collimator measurements (first-generation collimator)

7.5.1 Density

The volume of the collimator was measured by using the Archimedes suspension method [159] and the density was determined by determining the mass with a precision balance (Kern EMB 1200-1). This measurement was repeated 10 times.

The volume of the collimator was 32.0 $\pm$ 0.18 cm^3, the mass was 553.89 $\pm$ 0.19 g. The density of the collimator was 17.31 $\pm$ 0.10 g/cm^3. This corresponds to 89.92 $\pm$ 0.50 $\%$ of pure tungsten (density 19.25 g/cm^3). The density is not 100 $\%$ of pure tungsten because there are microscopic air cavities in the tungsten walls.

7.5.2 Production accuracy

The collimator was scanned using a GOM ATOS II Triple Scan optical scanner. The outcome of this measurement was compared with the original CAD design file.

Using this technique we were able to measure most surfaces of the collimator. It did not allow us to measure the apertures, the deepest parts of the loftholes and the sharp edges that separate the different loftholes. The result of the collimator measurements is shown in Fig. 7.9. The deviations are not uniformly spread over the collimator, there is a defect that continues

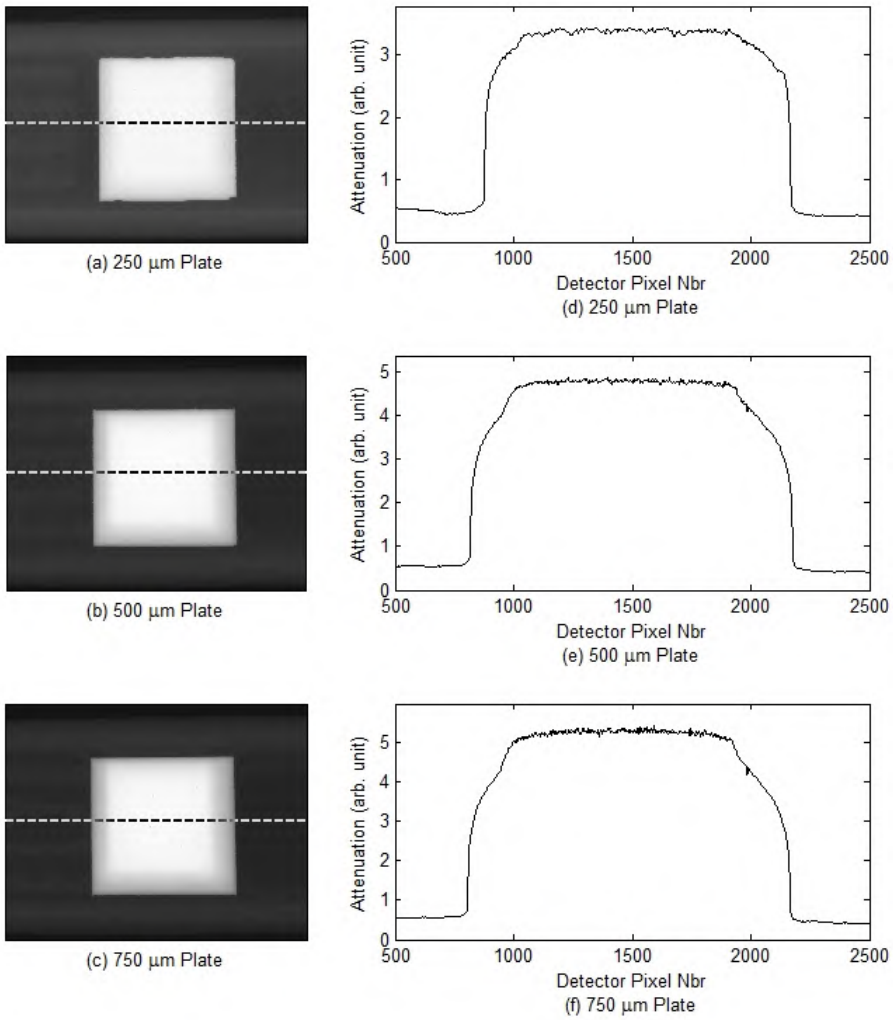

Figure 7.8: (a)(b)(c) Transmission scan of the three plates (GE eXplore Locus SP micro-CT). (d)(e)(f) Profiles of the transmission images on the dashed lines, the profiles show the uniform attenuation of the plates.

along the length of the collimator, it is marked with a black rectangle in Fig. 7.9. Fig. 7.10 zooms in on the maximum and minimum deviation. The maximum deviation is +0.650 mm, the minimum deviation is -0.260 mm. A histogram of the deviations is depicted in Fig. 7.11. The part has a positive bias due to the roughness of the collimator surfaces.

The absolute position of the apertures (referenced to a corner of the collimator) was measured with a Nikon AZ100M microscope. The apertures were measured with an Olympus IMT200 microscope. The Olympus IMT200 is an inverted microscope: light is generated under the aperture and the microscope looks to the collimator from the lofthole side. This resulted in images where the contours of the apertures can be seen in detail. This technique was used for the three central rows of apertures; it could not be used for the top and the bottom row because of the obliqueness of these holes. The apertures were segmented from the acquired microscopic images, their area was calculated and this area was then used to calculate the average diameter of the aperture.

The aperture positions have a mean deviation of 5 μm, the maximum deviation was 174 μm and the minimum deviation was -122 μm. The mean aperture diameter is 464 $\pm$ 19 μm. The measured diameters are shown in table 7.5.

	Col. 1	Col. 2	Col. 3	Col. 4
Row 2	472 μm	485 μm	482 μm	456 μm
Row 3	441 μm	494 μm	445 μm	433 μm
Row 4	465 μm	482 μm	454 μm	454 μm

Table 7.5: Measured diameters of the pinholes. See Fig. 7.13 for the nomenclature.

The microscopic images revealed that the circularity of the apertures is not good. This is shown in Fig. 7.12.

7.5.3 Sensitivity measurement

The collimator was positioned on top of the NaI(Tl) detector (described in chapter 3). A ^{99m}Tc point source was made with an anion-exchange bead (Bio-Rad AG1-X2, total activity 5.4 MBq) and, was positioned in front of the center of the collimator (depicted in Fig. 7.13). The point source was moved in steps of 1 mm from a height of 5 mm to a height of 34 mm above the aperture plane. At each position an acquisition of 60 seconds was made, an energy window of 20 % was used. The number of detections

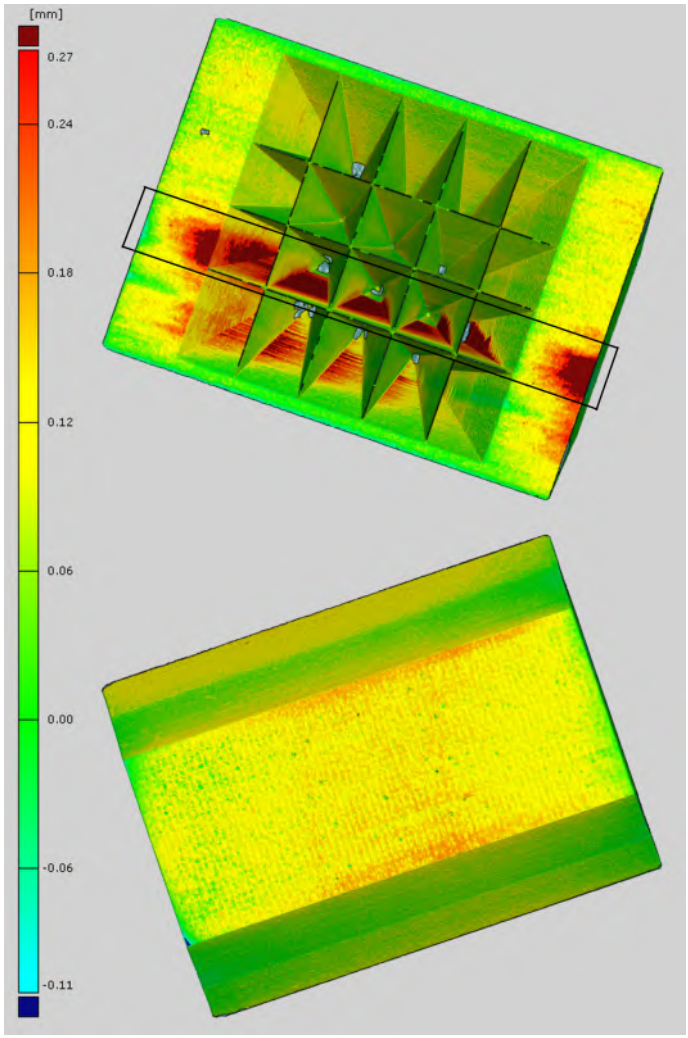

Figure 7.9: The deviation between the first-generation collimator and the CAD design (positive deviations in red, negative deviations in blue). The top figure shows the bottom side of the collimator; this is the surface that contains the exit opening of the loftholes. The bottom figure shows the top side of the collimator, this surface contains the apertures. The used measurement technique did not allow us to measure the apertures, the deepest parts of the loftholes and the sharp edges that separate the different loftholes.

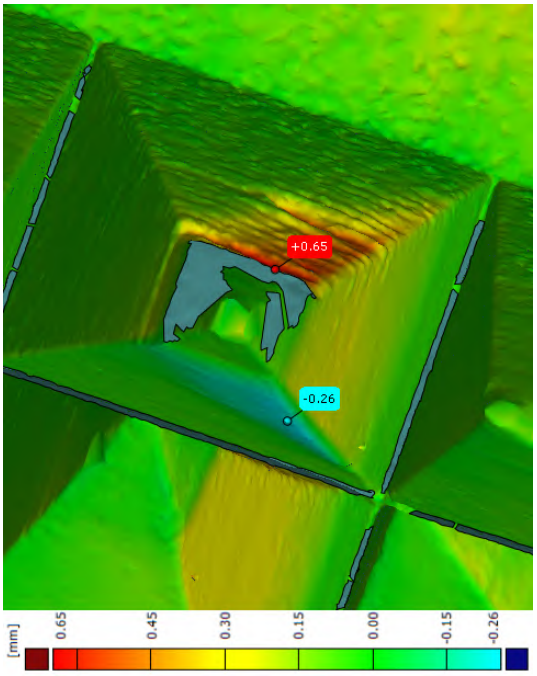

Figure 7.10: A magnified view of the collimator depicting the largest deviations. The biggest deviations are found in the same lofthole.

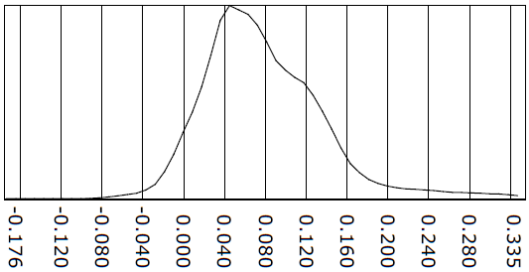

Figure 7.11: A histogram of the deviations across the whole collimator (unit is mm)

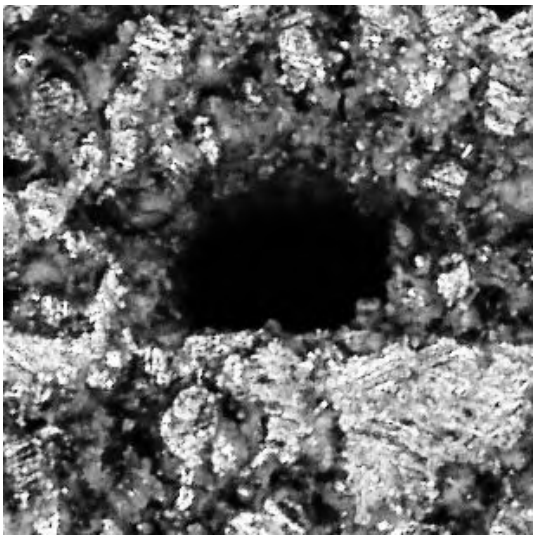

Figure 7.12: A microscopic image of the aperture at row 1, column 1 (first-generation collimator).

was measured and calculated for the central apertures (the apertures at row 2,3,4 columns 2 and 3, see Fig. 7.13 for the nomenclature).

The expected number of detections was calculated based on the pinhole sensitivity formula (equation 2.13) and the detector sensitivity. The detector sensitivity is based on the Lambert-Beer law (see equation 7.1), it uses μ (attenuation coeffient of the detector material), T_{Det} (thickness of the detector) and α (the angle of incidence).

$$S_{Detector} = 1 - \exp\left[\frac{\mu T_{Det}}{cos(\alpha)}\right] \tag{7.1}$$

The expected number of detections depends on the activity of the source (Act_{Src}), the acquisition time (T_{Acq}), the sensitivity of the pinhole ($S_{Pinhole}$) and the sensitivity of the detector ($S_{Detector}$).

$$NbrOfDetections = Act_{Src} \times T_{Acq} \times S_{Pinhole} \times S_{Detector} \tag{7.2}$$

The expected number of detections (eq. 7.2) was calculated using the

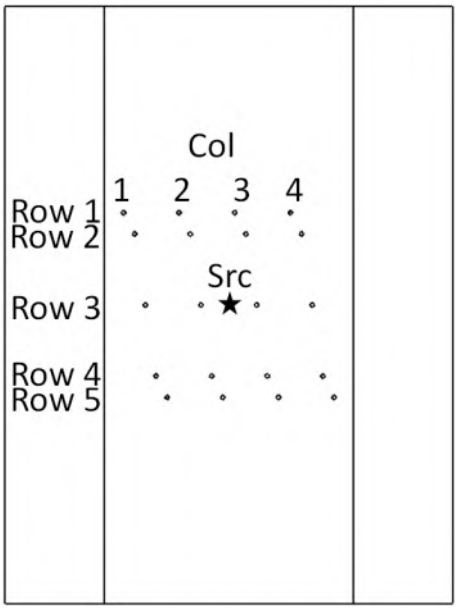

Figure 7.13: The setup used to measure sensitivity. A small point source was positioned in front of the center of the collimator. The point source was moved from a height of 5 mm to a height of 34 mm above the aperture plane. This was done in steps of 1 mm.

ideal pinhole diameters (500 μm) and using the measured pinhole diameters.

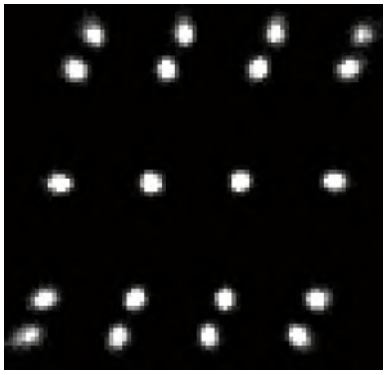

Figure 7.14: Measurement of a point source at a height of 34 mm above the aperture plane, the point source is seen by all the apertures.

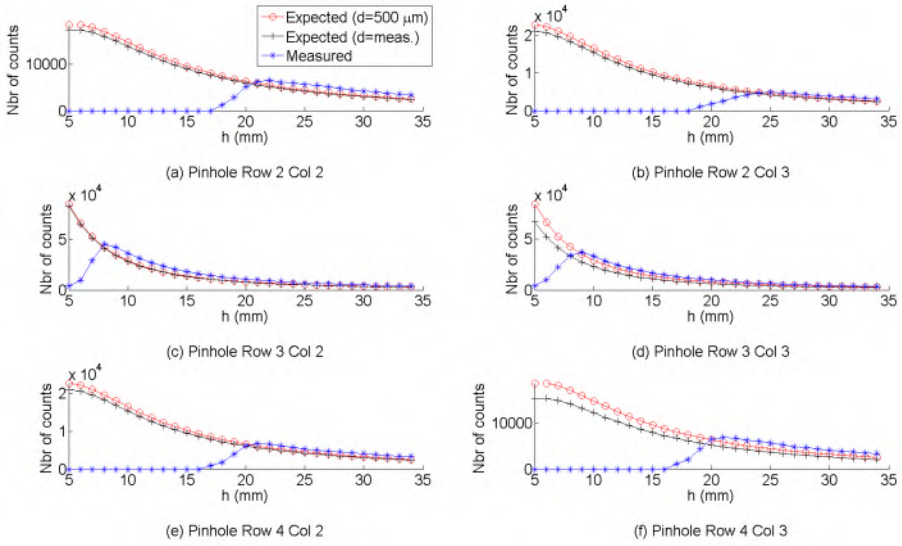

Figure 7.15: Measured and expected number of counts. The expected number of counts was calculated using the ideal pinhole diameters (500 μm) and using the measured pinhole diameters (see table 7.5).

The resulting detector measurement of a point source at a height of 34 mm is shown in Fig. 7.14.

The expected number of counts fits well to the measured number of counts when the point source is in the field-of-view of the lofthole (Fig. 7.15).

7.6 Collimator measurements (second-generation collimator)

7.6.1 Density

The volume of the collimator was measured by using the Archimedes suspension method [159] and the density was determined by determining the mass with a precision balance (Kern EMB 1200-1). This measurement was repeated 10 times.

The volume of the collimator was 18.18 $\pm$ 0.08 cm^3, the mass was 337.37 $\pm$ 0.07 g. The density of the collimator was 18.56 $\pm$ 0.08 g/cm^3. This corresponds to 96.4 $\pm$ 0.42 $\%$ of pure tungsten (density 19.25 g/cm^3).

The density of the second-generation collimator is higher than the density of the first-generation collimator because different processing parameters were used during the manufacturing.

7.6.2 Production accuracy

The collimator was also measured using the GOM ATOS II Triple Scan optical scanner. The outcome of this measurement was compared with the original CAD design file.

The result of the collimator measurements are shown in Fig. 7.16. The accuracy has greatly improved with reference to the first-generation collimator due to different processing parameters and different post-processing. The maximum deviation is +0.180 mm, the minimum deviation is -0.137 mm. A histogram of the deviations is also depicted in Fig. 7.16. The part also has a small positive bias.

The diameter of each aperture was measured using a microscope. The mean aperture diameter is 509 $\pm$ 21 μm, the maximum diameter is 542 μm, the minimum diameter is 457 μm. A microscopic view of some collimator holes is depicted in Fig. 7.17.

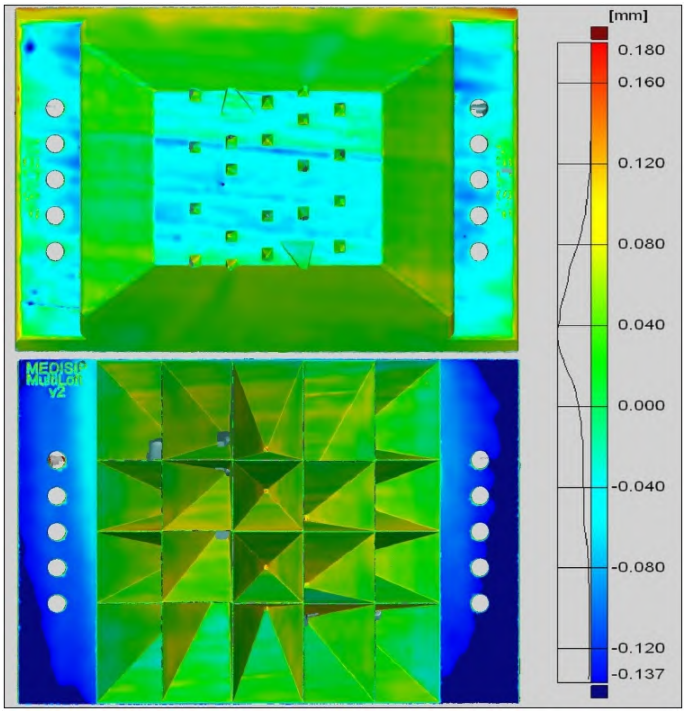

Figure 7.16: The deviation between the second-generation collimator and its CAD design (positive deviations in red, negative deviations in blue). The top figure shows the top side of the collimator; this is the surface that contains the entrance opening of the loftholes. The bottom figure shows the bottom side of the collimator, this surface contains the exit openings.

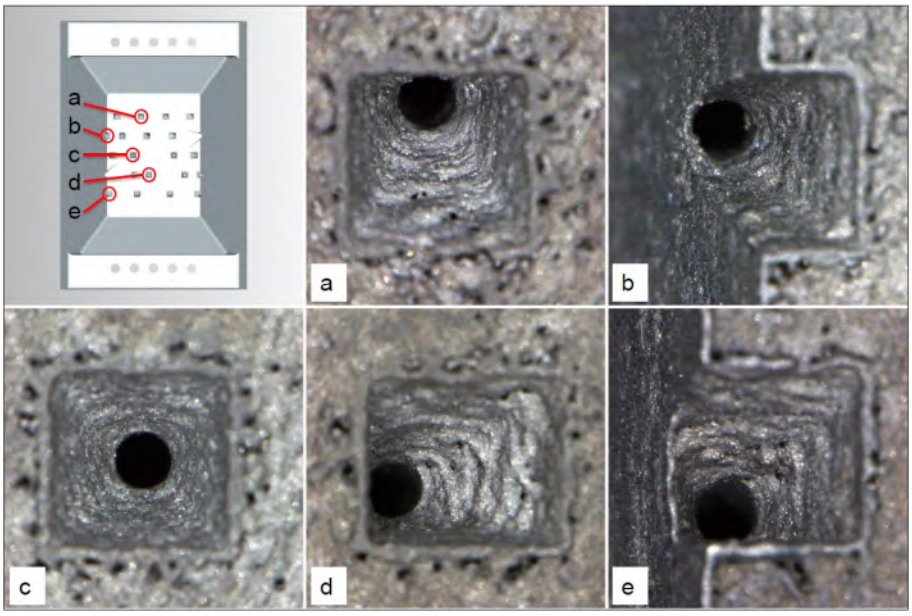

Figure 7.17: A microscopic view of the entrance openings and apertures of the second-generation collimator

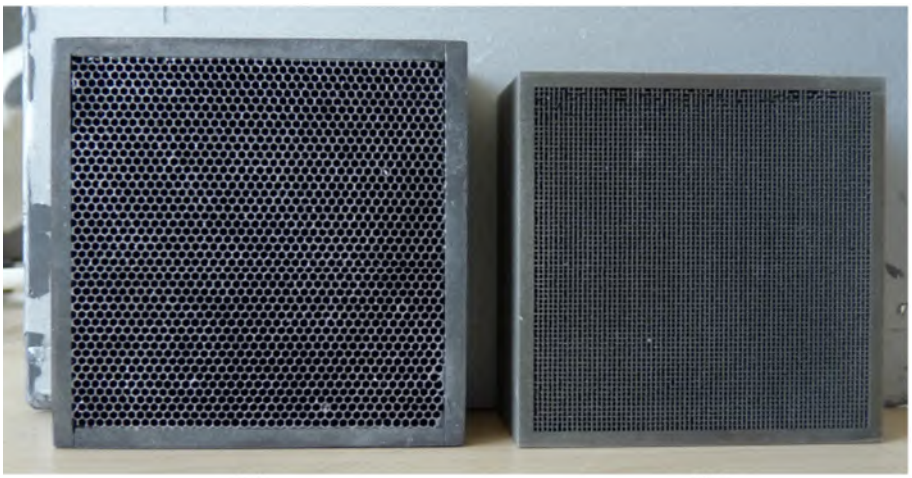

Figure 7.18: (a) A casted lead parallel hole collimator and (b) a tungsten parallel hole collimator made by additive manufacturing. The tungsten collimator allows the usage of smaller holes and thinner septa. The tungsten collimator has a hole size of 525 μm and the septal thickness is 150 μm, the hole length is 25 mm.

7.7 Discussion

Additive manufacturing is a new technique to produce pure tungsten collimators. This technique can be used for new collimator geometries that would be impossible or very expensive to build using the conventional subtractive manufacturing methods such as drilling, milling or EDM.

This chapter has focused on the production of a complex multi-lofthole collimator but the additive manufacturing technique can also be used for the construction of other collimators like parallel hole (see Fig. 7.18), fan beam or cone beam [160]. By making use of tungsten additive manufacturing, one can produce collimators with a smaller septal thickness and a smaller hole diameter. Additionally, one can easily build different hole geometries (triangular, circular, pentagonal or hexagonal holes). We have recently produced a tungsten parallel hole collimator with square holes (25 mm long, 525 μm side length) and a septal thickness of 150 μm (Fig. 7.18).

Three tungsten plates with different thicknesses have been produced. These plates attenuate slightly less than a solid tungsten plate with the same dimensions. The thinnest plate deviates in density from the other two plates which may be caused by the thickness (240 μm) and the roughness

of this plate.

Two 20-lofthole collimator have been produced. The density and accuracy have greatly improved in between both generations. The second-generation collimator has a density of 96.4% of pure tungsten and an accuracy of $[-137\mu m + 180\mu m]$. Additionally, the overall finish of the second-generation is better than that of the first-generation collimator, this is most noticeable when comparing the first-generation aperture depicted in Fig. 7.12 with the second-generation apertures of Fig. 7.17.

The additive manufacturing technique can also be used for applications in other domains where complex structures in high density material are needed. The shielding of irradiation in radiotherapy to specific organs is a possible application field where patient specific geometries are sometimes needed. The proposed technique might also be interesting for CT anti-scatter grids.

7.8 Summary and original contributions

The proposed additive manufacturing technique permits the fabrication of complex high density tungsten collimators, it allows a fast production cycle and, it makes novel geometries, which could not be produced or would be very expensive with the conventional techniques, possible.

At this point, we have presented the two key components which will be used for a second compact SPECT system that is presented in the next chapter. This system is based on the first demonstrator SPECT system (described in chapter 5). By now, we have an improved detector (chapter 6) and a multi-lofthole collimator (presented in this chapter) and the combination of those should result in a compact high-resolution SPECT system with high sensitivity.

The work described in this chapter has been published in a peer-reviewed journal publication [6].

Chapter 8

A multi-lofthole collimator based SPECT system

8.1 Introduction

Our previous SPECT system (chapter 5) had an analytical resolution of 2.25 mm and a sensitivity of 0.006 % (60 cps/MBq) in the center of the FOV. The reason for this moderate performance is mainly due to the fact that the collimator uses only one lofthole. By now, we have an improved detector based on an LYSO scintillator (chapter 6) and a collimator production technique (chapter 7) that allows us to produce complex multi-lofthole collimators. These two tools will be used in this chapter to build a SPECT system that offers an improved performance compared to our first SPECT system.

The new system is based upon a SPECT system optimization procedure developed by Van Holen et al. [23], that calculates the cylindrical geometry (detectors and pinhole apertures are on the surface of a cylinder) that results in the highest point sensitivity, taking into account a certain target system resolution and detector resolution and, taking into account that the pinhole or lofthole projections should not overlap. This procedure is used here to design a SPECT system that has a FOV which is sufficiently large to image a mouse or a rat brain.

The method used to calculate the optimal sensitivity of a cylindrical SPECT setup is schematically depicted in Fig. 8.1. It uses the detector intrinsic resolution R_i, the system target resolution R_t, the detector distance L, the pinhole distance l, the detector size H, the transaxial FOV d_{tx}

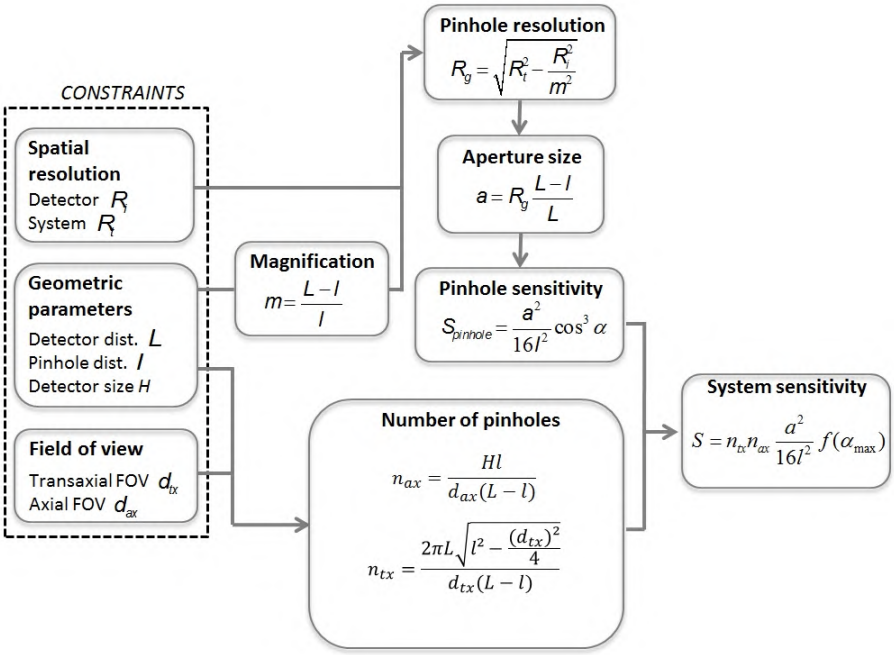

Figure 8.1: The design procedure for cylindrical SPECT geometries [1].

and the axial FOV d_{ax}. In a first step, the number of axial and transaxial pinholes (or loftholes) is calculated [161]. Hereafter, the magnification m is calculated and this can then be used to calculate the required collimator resolution R_g. Based on the collimator resolution, one can calculate the aperture diameter a. This enables us to calculate the single pinhole sensitivity $S_{pinhole}$ for a point in the center of the FOV. The total system sensitivity equals the pinhole sensitivity multiplied by the number of pinholes $n_{ax}n_{tx}$, $f(\alpha_{max})$ is a correction factor for the sensitivity decrease due to the non-zero incidence angle α of axially off-center pinholes [161]. Note that a real solution is not possible when $R_t^2 < R_i^2/m^2$.

One can now calculate the optimal sensitivity for different values of l and L (Fig. 8.2); the minimum pinhole distance l is set to 20 mm in order to be able to position a mouse in the collimator bore. The system that shows the largest optimal sensitivity is then selected as the optimal system (marked with a red asterisk in Fig. 8.2).

This optimal cylindrical system, which consists of a cylindrical detector and multi-pinhole collimator, is then used as a guideline to design a re-

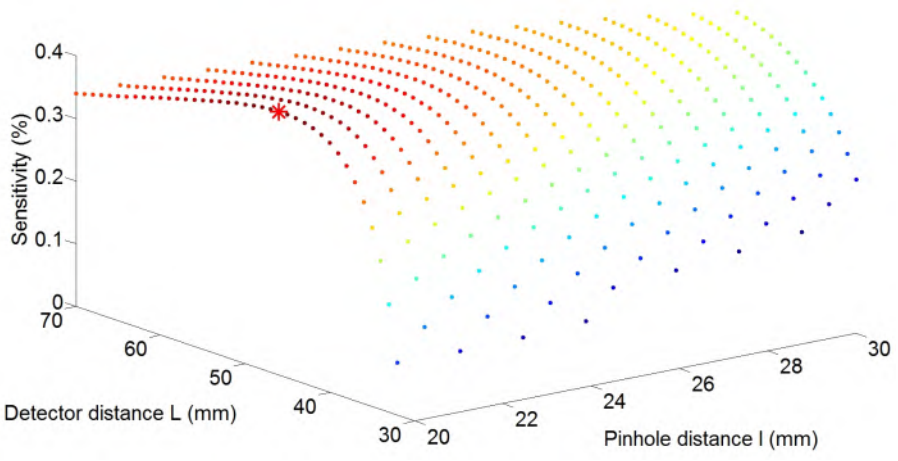

Figure 8.2: The optimal sensitivity for different values of detector distance *L* and pinhole distance *l*. The optimal system is the system that has the largest optimal sensitivity and is marked by a red asterisk in this scatter plot.

alistic pentagonal system that employs flat rectangular detectors and flat multi-lofthole collimators. Additionally, the pinhole's FOV is changed in such a way that each sees a slightly different portion of the system FOV. Simulations indicate that the subject and the gamma cameras can remain completely stationary to reconstruct a 30 mm diameter and 12 mm long cylindrical FOV artifact-free [23].

A CAD rendering of the system is shown in Fig. 8.3; its geometric properties are given in table 8.1. This system uses a total of 100 loftholes (400 μm aperture diameter), a minification factor of 0.88 is used. Fig. 8.3 shows five high-resolution detectors, consisting of a PSPMT and a thin LYSO scintillator (drawn in purple), that were described in chapter 6. It also depicts five second-generation multi-lofthole collimators (chapter 7), each collimator consists of 20 loftholes and irradiates the central 48 mm x 48 mm of a detector. Fig. 8.4 shows a cross-section view of one gamma camera in the axial plane, Fig. 8.5 depicts how the collimator subdivides the detector in 20 sub-detectors.

A demonstrator system was built consisting of a single LYSO detector and a single multi-lofthole collimator; it is depicted in Fig. 8.6. The demonstrator system has 20 500 μm diameter pinholes, a minification of 0.88 is used. The transaxial FOV is 30 mm, the axial FOV is 12 mm.

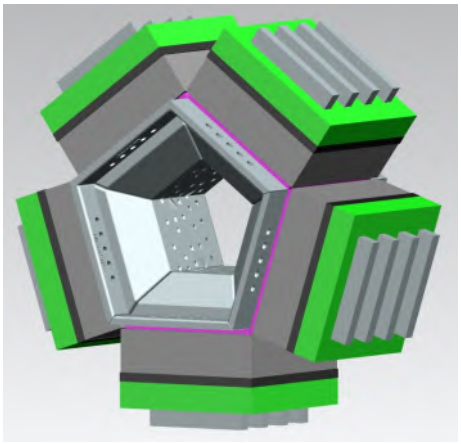

Figure 8.3: A CAD rendering of the system designed by Van Holen et al. [1].

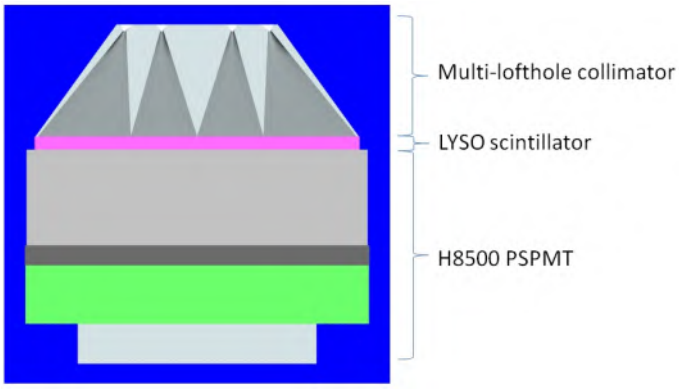

Figure 8.4: A cross-sectional view of a gamma camera (section made in a plane that is perpendicular to the aperture plane and that intersects with the apertures of lofthole row 3).

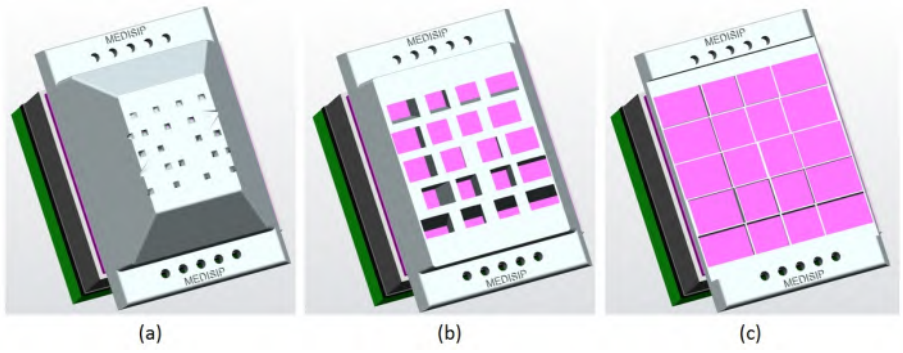

Figure 8.5: The collimator subdivides the detector in 20 sub-detectors. (a) The gamma camera, (b) the gamma camera with a cross-sectional view of the collimator at a height of 5 mm above the scintillator plane and (c) the gamma camera with a cross-sectional view of the collimator at a height of 1 mm above the scintillator plane. Each collimator consists of 20 loftholes and irradiates the central 48 mm x 48 mm of a detector.

A rotation stage is used to rotate phantoms, and, this rotation stage can be attached to a linear stage thus allowing multiple *bed* positions. By rotating in steps of 72°, we can emulate the stationary system of Fig. 8.3. Additionally acquisitions of more angles and, by moving axially, multiple bed positions can be done to study possible improvements in image quality.

MLEM is used to reconstruct the images, forward and back-projection are based on a system matrix. The system matrix is calculated in advance requiring several calibration steps.

Table 8.1: Parameters of the simulated pentagonal system

Nbr. of pinholes per gamma camera	20
Pinhole diameter	400 μm
Magnification	0.88
Axis of rotation - pinhole distance	17.9 mm
Axis of rotation - detector distance	33.7 mm
Transaxial FOV	30 mm
Axial FOV	12 mm
Volume sensitivity	0.107 %
Reconstructed spatial resolution	700 μm

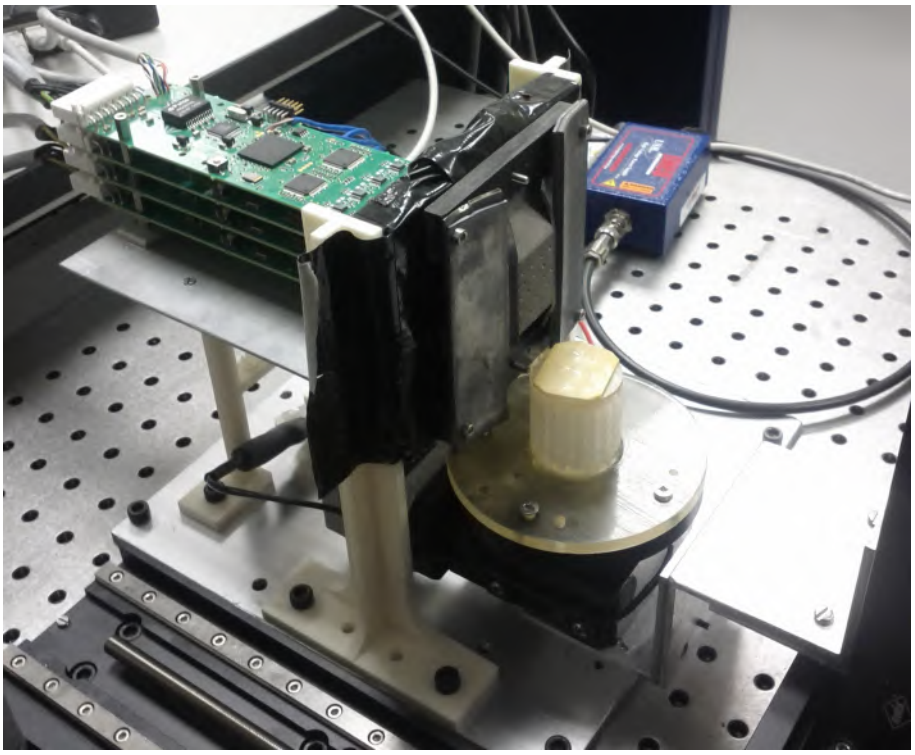

Figure 8.6: The prototype system consists of one detector and one second-generation collimator. A rotation stage is used to rotate phantoms.

8.2 SPECT system calibration

The system calibration is a multi-step process, which results in a system matrix for one angle of the voxel grid. Therefore, we will have to rotate the image around the axis of the rotation stage during image reconstruction. An additional calibration step to derive the coordinates of the axis of rotation is required.

8.2.1 System matrix calculation

The system matrix contains the detector response of each voxel. One could consider measuring the complete system matrix by measuring the projections of a small point source that is sequentially positioned in the center of each voxel (we use 121 x 121 x 97 voxels, 250 μm voxel size); the detector

response for a point source is commonly known as a point spread function (PSF). Even with an intense ($Activity > 37MBq$) non-decaying 140 keV gamma ray point source and measuring only 1 s at each voxel coordinate, the total acquisition time would be 394 h or 16 days. This is practically not feasible and, due to this, we acquire projections of a point source on a coarse grid. Hereafter, the system matrix is calculated, based on the coarse grid acquisitions.

The computation of a system matrix based on point source acquisitions was considered before. Chen et al. [162] have developed two system matrix calculation methods for the FastSPECT II [157] small-animal SPECT system. The first method employs Gaussian fitting to each measured PSF and then uses interpolation of the Gaussian parameters to calculate the PSF for a source at an arbitrary position. A second method is based on the fact that PSFs of adjacent measured source locations have the same properties in their Fourier transforms, interpolation of the magnitudes and phases in the Fourier domain is used to calculate the response of an arbitrary point source. Unlike our system, the FastSPECT II system matrix calculation is not complicated by pinhole penumbrae because each pinhole sees the complete transaxial FOV.

The U-SPECT II system is another system that uses a pre-calculated system matrix that is based on point source acquisitions. It employs three large gamma camera's and a multi-pinhole collimator [119]. The circular projections of the pinholes are transformed to rectangular projections by making use of an additional shielding tube; due to this the U-SPECT II system has non-overlapping pinhole penumbrae. A cylindrical reservoir (filled with ^{99m}Tc) is measured and the resulting flood map is used during system matrix calculation to model these penumbrae. Measured PSFs are first divided by the flood map. Hereafter, the PSFs are used to derive the system geometry. Then a model for the sensitivity and resolution is derived. The PSF for an arbitrary point source location is calculated by displacing (based on ray-tracing), stretching (based on the resolution model) and scaling (based on the sensitivity model) the measured PSF whose point source location is nearest to the arbitrary point source's location. The resulting PSF is then multiplied by the flood map to obtain the final PSF.

Our system matrix calculation is partially based on the method proposed by Van der Have et al. [119] and is schematically depicted in Fig. 8.8. A particular problem with the calculation of the system matrix of our system is the presence of overlapping lofthole penumbrae due to intrinsic detector resolution and the non-zero DOI of the detector. The effect of non-zero DOI

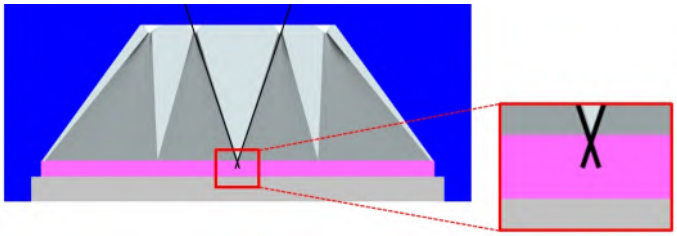

Figure 8.7: A cross-section of the gamma camera. The path of two possible gamma-rays is drawn in black; these gamma-rays illustrate that there is a small amount of overlap due to the non-zero DOI.

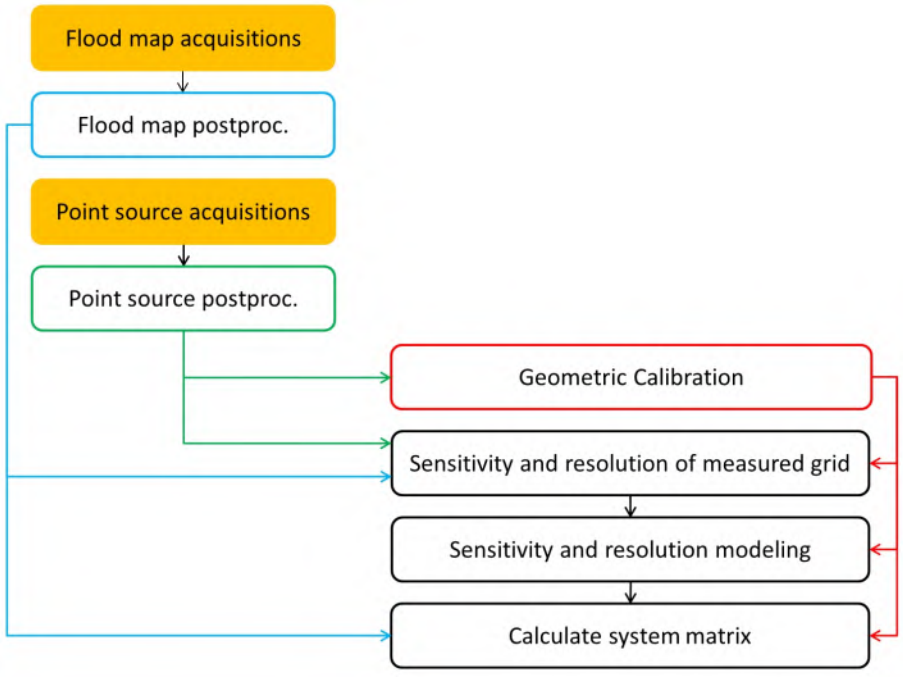

Figure 8.8: The different calibration steps that are done before the calculation of the system matrix. The calculations are based on the acquisition of a flood map of each lofthole and on point source measurements.

is shown in Fig. 8.7: oblique rays can be detected outside a lofthole's exit window because the depth of interaction is non-zero (the average DOI for perpendicular 140 keV gamma rays in a 2 mm thick LYSO scintillator is 0.7 mm). In order to model those we first acquire a flood map of each lofthole, this is done sequentially because the flood maps of the different loftholes show overlap. This flood map will then be used during the actual system matrix calculation. Point source measurements (section 8.2.1.2) are used first to derive the system geometry (section 8.2.1.3) and then to develop a model for the resolution and sensitivity (section 8.2.1.4 and 8.2.1.5). This model, together with the result of the geometric calibration, allows to calculate the gamma camera response for a point source at an arbitrary position. The full system matrix can now be composed by calculating the PSF for a source positioned at the center of a voxel, this is done sequentially for each voxel of the voxel grid (section 8.2.1.6).

8.2.1.1 Flood map acquisitions and derivation of the lofthole borders

Each lofthole aperture is sequentially irradiated by a flood source to derive the delineation of each sub-detector. This is done by filling a flood phantom (a rectangular box that measures 50 mm x 50 mm x 12 mm) with 190 MBq ^{99m}Tc; a tungsten alloy plate (1 mm thick) with a 5 mm diameter hole is attached to the flood phantom (Fig. 8.9). This assembly is then attached to a robotic stage and positioned in such a way that the 5 mm hole in the tungsten plate allows irradiation of a collimator aperture.

The 20 resulting acquisitions are corrected for uniformity (by dividing them by the detector's intrinsic uniformity map[1]) and median filtered (1D median filtering is used, first in the detector's X direction then in the detector's Y direction, a kernel size of 9 is used). A typical flood map is shown in Fig. 8.10. $\mathbf{Flood_s}$ is used in the remainder of the chapter to label the uniformity corrected and filtered flood map of lofthole s ($s \in [1, 20]$).

The row pixel sum (Fig. 8.11(c)) and the column pixel sum (Fig. 8.11(b)) of each $\mathbf{Flood_s}$ (Fig. 8.11(a)) is calculated. The vertical sub-detector borders are positioned where the row sum drops to 5% of the maximum value of the row sum; the horizontal sub-detector borders are positioned where the column sum drops to 5% of the maximum value of the column sum. The borders are marked by a red rectangle on Fig. 8.11(a) and, by

[1] A uniformity map is acquired using a point source (^{99m}Tc, 118 MBq) at large distance (90 cm) from the detector, without the collimator.

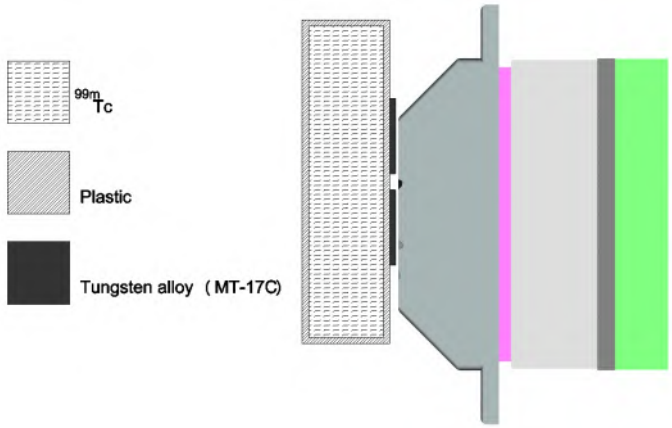

Figure 8.9: The setup used to measure the flood maps. The flood source and the tungsten alloy plate with the 5 mm diameter hole are attached to a robotic stage. By doing so, we can sequentially irradiate the lofthole apertures.

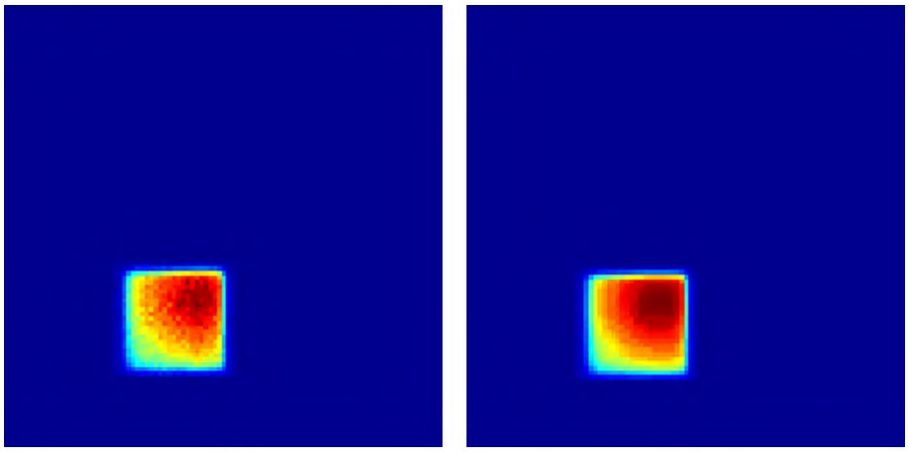

(a) (b)

Figure 8.10: (a) A flood image of a lofthole and (b) the median filtered flood image

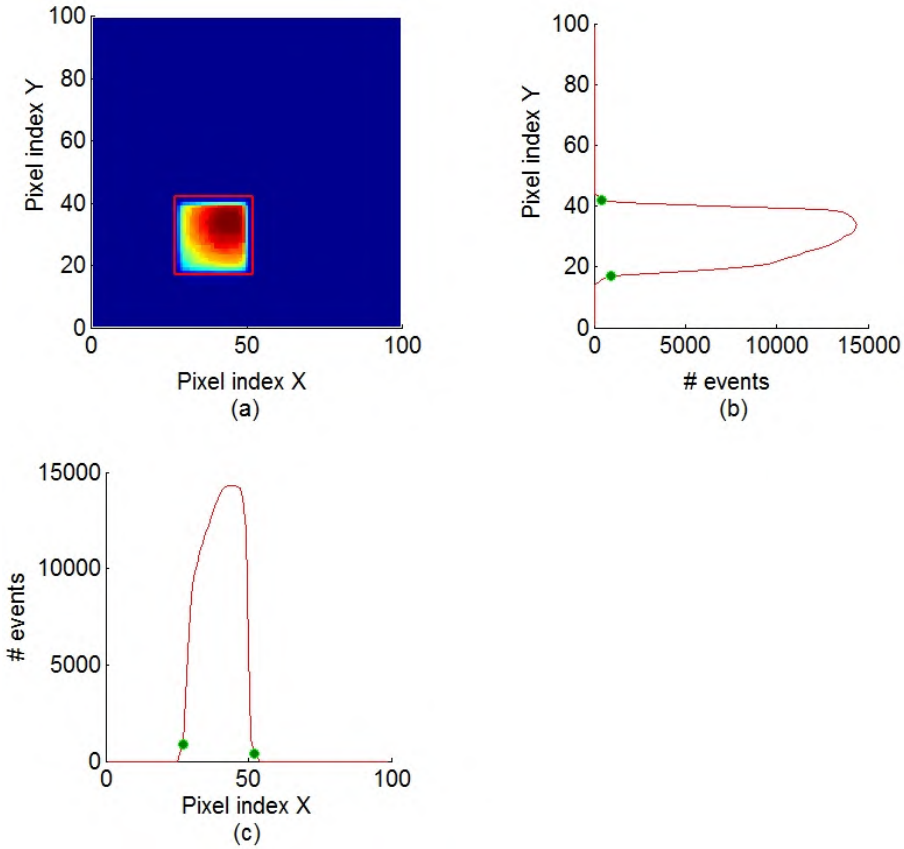

Figure 8.11: (a) A flood image of a lofthole, (b) the column sum and (c) the row sum. The sub-detector borders are marked with red lines in (a) and with green circles in (b) and (c).

green dots on Fig. 8.11(b) and Fig. 8.11(c).

Fig. 8.12 shows the sum of the 20 flood maps ($\sum_{s=1}^{20} \mathbf{Flood_s}$); the sub-detector delineation is also shown and reveals the overlap on the detector.

8.2.1.2 Point source acquisitions

The source that we use for the PSF measurement is an anion exchange bead (Bio-rad AG1-X2, 180 μm - 500 μm bead diameter). Drops of ^{99m}Tc are pipetted on the bead, the liquid is evaporated by making use of an infrared

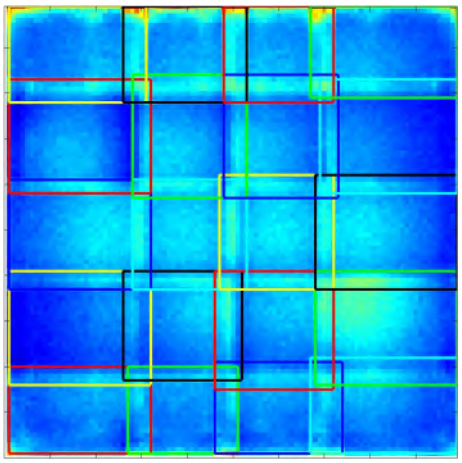

Figure 8.12: The sum of all the median filtered flood images reveals the overlap under the lofthole edges. The rectangles represent the derived sub-detector delineation.

heating lamp. Typically, approximately 185 MBq ^{99m}Tc is pipetted. The total activity in the bead after evaporation is 11.1 MBq. After this, the source is glued to the end of a small extension arm which in turn is attached to a 3D robotic stage. The measurement setup is depicted in Fig. 8.13.

Using this setup we have measured PSFs on a coarse 2.5 mm grid. The measured positions are shown in Fig. 8.14; the grid has an axial length of 20 mm and a diameter of 30 mm. An example of a measured PSF is shown in Fig. 8.15(a).

The acquisition time is 10 s for the first grid position and is adjusted for decay for the other grid positions; the total acquisition time was 4 h.

All the acquired PSFs are first corrected for uniformity by dividing them by the detector uniformity map. In the remainder of this chapter we will use $\mathbf{PSF_p}$ to label the uniformity corrected *PSF* of a point source at position p. Each $\mathbf{PSF_p}$ is now divided into 20 sub-PSFs where each sub-PSF is associated with a sub-detector and its associated lofthole aperture.

During system matrix calculation (section 8.2.1.6) we will multiply the calculated sub-PSFs with the floodmaps to model the lofthole penumbrae. This multiplication should however not have an influence for sub-PSFs whose centroid is not near the sub-detector's edges. For this reason, each measured sub-PSF is first divided by its associated $\mathbf{Flood_s}$.

$\mathbf{SubPSF_{p,s}}$ will be used to indicate the flood corrected sub-PSF s ($s \in$

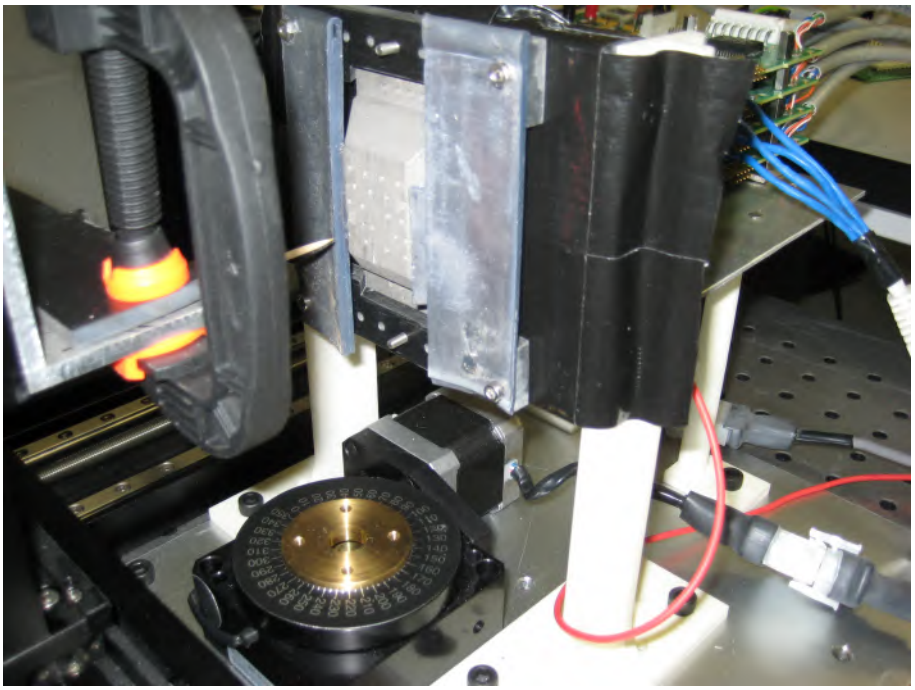

Figure 8.13: A small point source is fixed to a robotic stage and positioned in the system FOV.

$[1, 20]$) of a point source at position p.

8.2.1.3 Geometric calibration

The measured PSFs are first used to derive the position of the collimator apertures and the position and orientation of the detector. By doing so, we will be able to calculate the average interaction (or centroid) positions on the detector for a point source at an arbitrary position (x_S, y_S, z_S).

In a first step, rotated bivariate Gaussian functions are fit to each $\mathbf{SubPSF_{p,s}}$.

A mask is now employed on the detector, this mask is marked in red in Fig. 8.15(b). Gaussian fits, whose center is inside the detector mask, are used for the geometric calibration. An example is depicted in Fig. 8.15(b), the centers that are in the detector mask are marked with a green asterisk; each center s has detector coordinates $(\xi'_{s,i}, \eta'_{s,i})$ (sub-detector index $s \in [1, 20]$, measurement grid index i). The masked zones are not overlapping (i.e. the

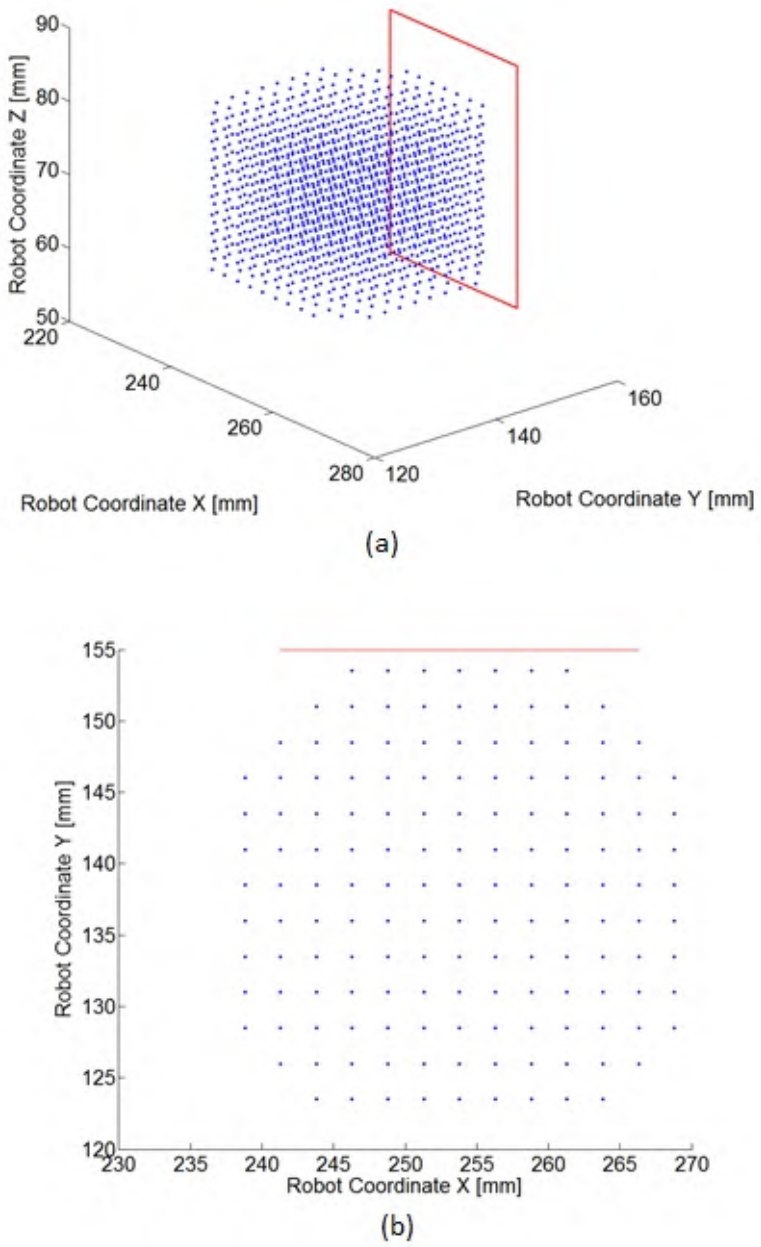

Figure 8.14: The point source is moved to several positions in the system FOV. These positions are marked with blue dots in the drawing, the front of the collimator is marked with a red rectangle ((a) side view and (b) top view).

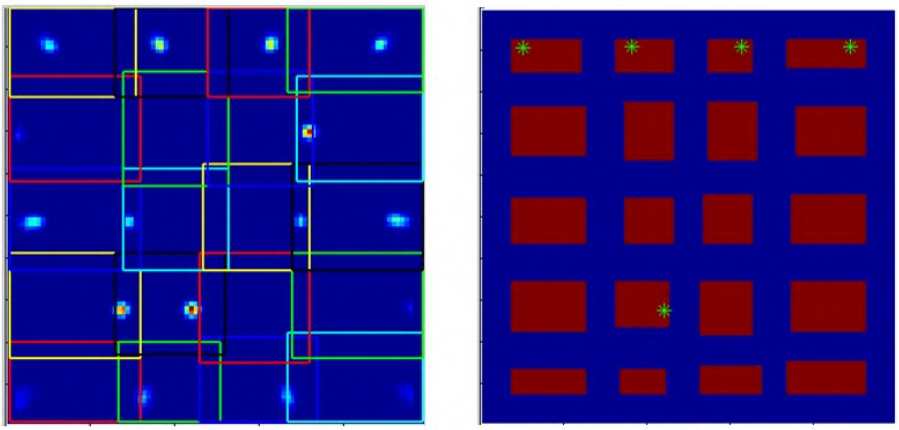

Figure 8.15: (a) The PSF acquired when the point source is in the center of the measurement grid (253.8 mm, 138.5 mm, 73.5 mm). (b) The detector mask used for geometric calibration.

aperture associated with the projection can be unambiguously resolved) and do not include detector edges which suffer from a worse detector resolution and event positioning bias.

Each sub-detector/lofthole pair is calibrated independently (without considering the other sub-detectors and apertures) using the method proposed by Van der Have et al. [119], which is explained in the following paragraphs.

The nomenclature that we will use is depicted in Fig. 8.16. A center of a sub-PSF is positioned at (x_D, y_D, z_D) in the 3D voxel coordinate system, which is at (ξ, η) in the 2D detector coordinate system. The aperture is positioned at (x_A, y_A, z_A), the point source is at (x_S, y_S, z_S) and the origin of the detector at (x_T, y_T, z_T).

The pinhole, the detector interaction coordinate and the source are on a line and this line is defined by:

$$\frac{x_S - x_A}{x_A - x_D} = \frac{y_S - y_A}{y_A - y_D} = \frac{z_S - z_A}{z_A - z_D}. \tag{8.1}$$

The voxel coordinate system and the detector coordinate system are related in the following way:

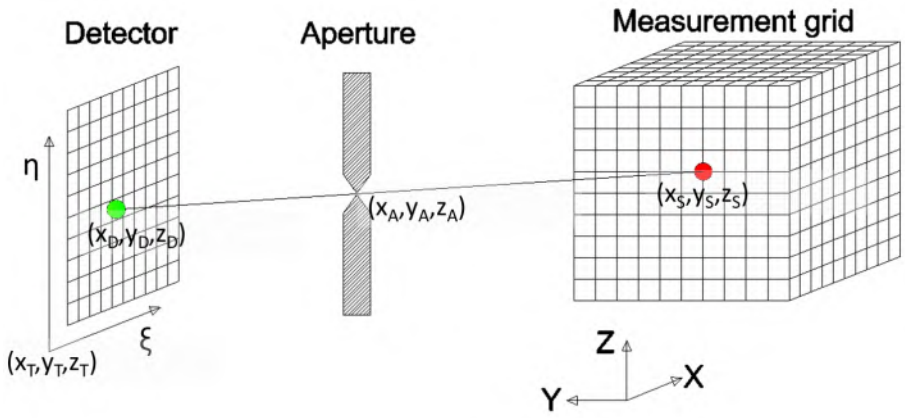

Figure 8.16: The detector coordinate system (ξ, η) and the voxel coordinate system (x, y, z).

$$\mathbf{R} \begin{bmatrix} \xi \\ 0 \\ \eta \end{bmatrix} + \begin{bmatrix} x_T \\ y_T \\ z_T \end{bmatrix} = \begin{bmatrix} x_D \\ y_D \\ z_D \end{bmatrix} \tag{8.2}$$

where R is a rotation matrix expressed in terms of the Euler angles α, β and γ. This rotation matrix represents the alignment of the detector to the voxel grid.

$$\mathbf{R} = \mathbf{R_z}(\gamma)\ \mathbf{R_y}(\beta)\ \mathbf{R_x}(\alpha) \tag{8.3}$$

with

$$\mathbf{R_z}(\gamma) = \begin{bmatrix} \cos\gamma & -\sin\gamma & 0 \\ \sin\gamma & \cos\gamma & 0 \\ 0 & 0 & 1 \end{bmatrix} \tag{8.4}$$

$$\mathbf{R_y}(\beta) = \begin{bmatrix} \cos\beta & 0 & \sin\beta \\ 0 & 1 & 0 \\ -\sin\beta & 0 & \cos\beta \end{bmatrix} \tag{8.5}$$

$$\mathbf{R_x}(\alpha) = \begin{bmatrix} 1 & 0 & 0 \\ 0 & \cos\alpha & -\sin\alpha \\ 0 & \sin\alpha & \cos\alpha \end{bmatrix} \tag{8.6}$$

Equations 8.1 and 8.2 can be combined and x_D, y_D and z_D can be eliminated. By doing so, the interaction coordinates (ξ, η) on the detector can be calculated using the aperture position (x_A, y_A, z_A), the source position (x_S, y_S, z_S) and, the detector position (x_T, y_T, z_T) and orientation (α, β, γ):

$$\xi = f(x_A, y_A, z_A, x_S, y_S, z_S, x_T, y_T, z_T, \alpha, \beta, \gamma) \tag{8.7}$$

$$\eta = g(x_A, y_A, z_A, x_S, y_S, z_S, x_T, y_T, z_T, \alpha, \beta, \gamma) \tag{8.8}$$

The complete equations are of substantial length and have been replaced here by two functions f and g.

We will now estimate the geometric parameters (x_A, y_A, z_A), (x_T, y_T, z_T) and (α, β, γ) of our system by making use of an iterative optimization algorithm. An initial estimate of the geometric parameters is based upon the CAD design file of the collimator and assumes a perfect alignment of voxel grid and detector grid ($\alpha = \beta = \gamma = 0$). The position of the gamma camera with reference to the point source grid is first estimated by making use of a ruler. These estimates are used to calculate the expected interaction coordinates on the detector (ξ_i'', η_i'') for each point source position i of the measurement grid (eq. 8.7 and 8.8).

A cost function that will be used for unconstrained nonlinear optimization is now defined as:

$$Cost = \Sigma_{i=1}^{I} C_i, \tag{8.9}$$

I is the number of measured point source positions. C_i is defined by:

$$C_i = (\xi_i'' - \xi_{s,i}')^2 + (\eta_i'' - \eta_{s,i}')^2 \tag{8.10}$$

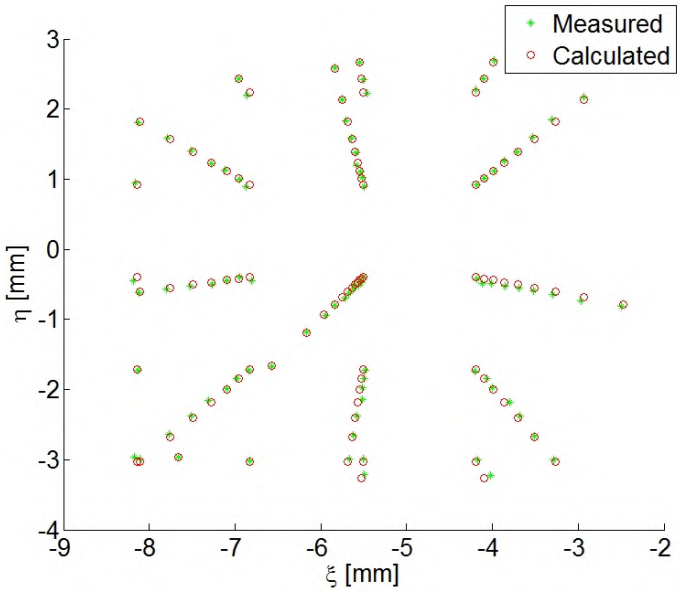

Figure 8.17: An optimization algorithm searches the geometric parameters that result in the best fit between the measured interaction position and the calculated interaction position. The result of this optimization is shown for the lofthole at row 3 an column 2 (see Fig. 7.13 for the lofthole indexing). The measured and calculated centroid positions show good agreement.

when $(\xi'_{s,i}, \eta'_{s,i})$ is in the detector mask and, C_i is set to zero ($C_i = 0$) when $(\xi'_{s,i}, \eta'_{s,i})$ is not in the detector mask. C_i Is the square of the Euclidean distance from the measured centroid position (ξ'_s, η'_s) to the calculated centroid position (ξ'', η''). The sub-detector index s should be set to the index of the sub-detector that is being calibrated.

Unconstrained nonlinear optimization (using the Nelder-Mead simplex algorithm) is then used to find the geometric parameters $(x_A, y_A, z_A, x_T, y_T, z_T, \alpha, \beta, \gamma)$ that result in the lowest cost. The result of this optimization is shown in Fig. 8.17 for the lofthole at row 3 and column 2 (see Fig. 7.13 for the lofthole indexing).

8.2.1.4 Sensitivity and resolution of measured grid

The geometry of each sub-detector/lofthole pair is now calibrated, this enables us to calculate the projection centers (ξ_s, η_s) (sub-detector index $s \in [1, 20]$) for a source at an arbitrary position (x_S, y_S, z_S). Information

on sensitivity and resolution is still missing in order to calculate a PSF.

To obtain this, we start by analyzing the measured PSFs again; this is also done independently for each sub-detector/lofthole pair. Ray-tracing (using eq. 8.7 and 8.8) is used to calculate (ξ_s, η_s), for a point source at location p. If the calculated (ξ_s, η_s) is within the lofthole borders that were determined in section 8.2.1.1 and the distance from (ξ_s, η_s) to the lofthole borders is more than 4 mm, then a rotatable bivariate Gaussian function is fit to $\mathbf{SubPSF_{p,s}}$. The parameters of this bivariate Gaussian function ($\sigma'_{x,p,s}$, $\sigma'_{y,p,s}$ and $S'_{p,s}$) and the associated source position p (x_S, y_S, z_S) are stored for later use. $\sigma'_{x,p,s}$ And $\sigma'_{y,p,s}$ are related to the system resolution for a source at position p; $S'_{p,s}$ represents the volume under the Gaussian function, this value is related to the sensitivity of the aperture s for a source at position p.

8.2.1.5 Sensitivity and resolution modeling

In the previous section we have obtained the Gaussian parameters ($S'_{p,s}$, $\sigma'_{x,p,s}$, $\sigma'_{y,p,s}$) for the associated source position p (x_S, y_S, z_S). These are now used to fit a sensitivity function and a resolution function; these functions will allow us to calculate the sensitivity and resolution for a point source at an arbitrary position.

The sensitivity function for sub-detector s equals:

$$S_{p,s} = A_s(\cos\theta)^{n_s}/h^2, \tag{8.11}$$

where A_s is a scaling factor and n_s is a factor which incorporates the angular dependency of the sensitivity. The height of the point source above the aperture h is defined as:

$$h = y_A - y_S. \tag{8.12}$$

The angle θ is the angle between a line perpendicular to the aperture plane and a line that connects the center of the aperture and the source:

$$\theta = \arctan \frac{\sqrt{(x_S - x_A)^2 + (z_S - z_A)^2}}{y_A - y_S}. \tag{8.13}$$

Unconstrained nonlinear optimization (Nelder-Mead simplex algorithm) is used to derive the A_s and n_s that provide the best fit between the calculated $S''_{p,s}$, and, the measured $S'_{p,s}$. $S''_{p,s}$ is calculated by making use of eq. 8.11

for each point source position p. The cost function that is minimized is:

$$Cost = \Sigma_{p=1}^{P} \left(\frac{S'_{p,s} - S''_{p,s}}{S''_{p,s}} \right)^2, \tag{8.14}$$

where P is the number of point source measurements that have a projection for detector/lofthole s.

The resolution function for sub-detector s equals:

$$\sigma_{p,s} = \frac{\sqrt{(d_s(f+h)/h)^2 + R_i^2}}{2.35}, \tag{8.15}$$

f is the distance from detector to collimator plane and is defined as:

$$f = y_D - y_A. \tag{8.16}$$

Unconstrained nonlinear optimization (Nelder-Mead simplex algorithm) is used to derive the optimal d_s that provides the best fit between the calculated $\sigma''_{p,s}$, and, the measured $\sigma'_{p,s}$, with $\sigma'_{p,s}$ being the mean of $\sigma'_{x,p,s}$ and $\sigma'_{y,p,s}$. The cost function that is minimized is:

$$Cost = \Sigma_{p=1}^{P} \left(\frac{\sigma'_{p,s} - \sigma''_{p,s}}{\sigma''_{p,s}} \right)^2. \tag{8.17}$$

8.2.1.6 System matrix calculation

The PSF of a point source at an arbitrary location p can now be calculated, this is done by summing the 20 subPSFs:

$$\mathbf{PSF_p} = \sum_{s=1}^{20} \mathbf{subPSF_{p,s}} \tag{8.18}$$

This equation uses $subPSF_{p,s}$ and this is calculated in the following way: in a first step, the detector interaction positions in the detector coordinate system (ξ_s, η_s) are calculated using eq. 8.7 and eq. 8.8. If coordinate (ξ_s, η_s) is within the sub-detector's borders (section 8.2.1.1), then a 2D Gaussian function has to be positioned at (ξ_s, η_s). This 2D Gaussian function has a σ which is defined by eq. 8.15 and the fit parameter d. The number of counts contained in this Gaussian is calculated by making use of eq. 8.11 and the fit parameters A_s and n_s. The tails of this Gaussian

($< 10\%$ of maximum value Gaussian) are set to zero in order to make the system matrix more sparse. The resulting $\mathbf{SubPSF_{p,s}}$ is multiplied by the associated flood map $\mathbf{Flood_s}$. By doing so we model, to a certain extent, the cut-off of the lofthole's exit window.

This procedure is employed to calculate the PSF of a point source positioned at the center of each voxel. The voxel grid is 121 x 121 x 97 voxels large, the voxel size is 250 μm. All the resulting PSFs are merged into the system matrix (H_d).

8.2.2 Center of rotation in image space (COR_{Im})

The center of rotation in image space (COR_{Im}), which is defined by the X and Y-coordinate of the axis of the rotation stage in image space, is an important parameter for image reconstruction. A deviating COR_{Im} will lead to resolution loss and to image artifacts. A point source, which is fixed to the rotation stage at a height Src_Z (which is visually at the same height as the third aperture row) and at a radius R_p, is used for the COR_{Im} calibration.

The projections of only one rotating point source provide enough information to derive the COR_{Im} because our collimator has multiple apertures and because we have already derived the system geometry by making use of the point source acquisitions (section 8.2.1.3). This is explained and illustrated in Fig. 8.18.

An acquisition of the rotating point source is made for 50 angles (resulting in 50 $\mathbf{PSF_p}$). Rotated bivariate Gaussian functions are fit to each $\mathbf{SubPSF_{p,s}}$. The centroids of these Gaussian functions represent the measured $(\xi'_{s,a}, \eta'_{s,a})$ (sub-detector index $s \in [1, 20]$, angle index $a \in [1, 50]$).

The unknown parameters of this setup are the radius R_p, the coordinates of the COR_{Im} (COR_X, COR_Y), the initial angle of the phantom δ and the source height Src_Z; only COR_X and COR_Y will be used by the image reconstruction algorithm.

Eq. 8.7 and eq. 8.8 will be used here again to calculate the expected interaction coordinates $(\xi''_{s,a}, \eta''_{s,a})$ for each point source location. The square of the Euclidean distance between the calculated $(\xi''_{s,a}, \eta''_{s,a})$ and measured $(\xi'_{s,a}, \eta'_{s,a})$ is used as a cost function to derive the unknown parameters (R_p, (COR_X, COR_Y), δ and Src_Z) by making use of unconstrained nonlinear optimization (Nelder-Mead simplex algorithm). The cost function that is used

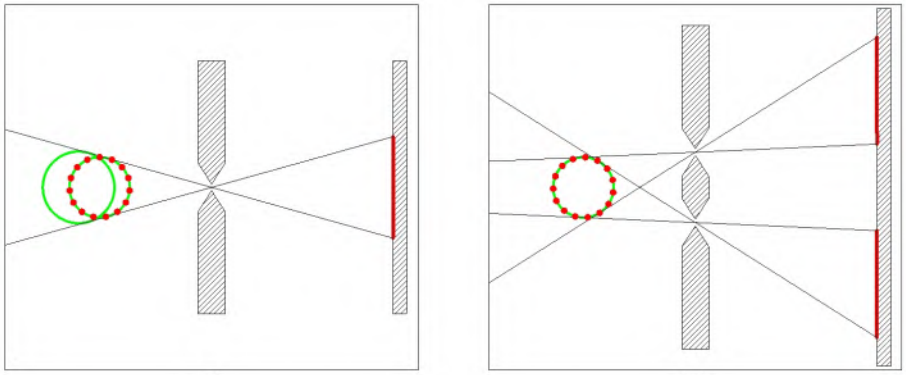

Figure 8.18: (a) A single-aperture collimator. A point source rotates to multiple angles (red dots) and this results in a projection on the detector (red line). We are not able to resolve the COR_{lm} because multiple circular point source paths (green circles) can be found that agree with the backprojected detector data. (b) A multi-aperture collimator. A point source rotates to multiple angles (red dots) and this results in two projections on the detector (red lines). Only one circular point source path (green circle) exists that agrees with the backprojected detector data.

is defined as:

$$Cost = \Sigma_{a=1}^{50} \Sigma_{s=1}^{20} C_{s,a}. \tag{8.19}$$

$C_{s,a}$ is defined as:

$$C_{s,a} = ((\xi''_{s,a} - \xi'_{s,a})^2 + (\eta''_{s,a} - \eta'_{s,a})^2) \tag{8.20}$$

when the distance between $(\xi'_{s,a}, \eta'_{s,a})$ and the lofthole border (section 8.2.1.1) is more than 5 detector pixels and,

$$C_{s,a} = 0 \tag{8.21}$$

when the distance between $(\xi'_{s,a}, \eta'_{s,a})$ and the lofthole border is less than or equal to 5 detector pixels. This is done to avoid inaccuracies which are due to the lofthole borders.

8.3 Image reconstruction

MLEM is used for image reconstruction. The implementation of the algorithm is however slightly different than explained in section 2.6 due to the fact that we only have a system matrix H_d for one angle.

Projection data are acquired for multiple angles. β_a Is the angle associated with projection a ($a \in [1, A]$).

Forward projection j is implemented by first rotating the image by an angle β_a around (COR_X, COR_Y), followed by a forward projection using the H_d matrix. Image rotation is implemented using tri-linear interpolation.

The forward projected image is then compared with the measured projection; the comparison is backprojected using the $\mathbf{H_d}$ matrix. The backprojected image has to be rotated by an angle $-\beta_a$, resulting in an image correction factor $\mathbf{Backproj_{k,a}}$. The image correction factor of voxel k for all angles ($\mathbf{BackProj_k}$, see eq. 2.54) is equal to:

$$\mathbf{BackProj_k} = \sum_{a=1}^{A} \mathbf{Backproj_{k,a}} \tag{8.22}$$

A 2 pixel (1 mm thick) outside border of the detector, where the positioning bias and detector resolution degrade detector performance, is not used to reduce reconstruction artifacts.

The reconstructed images are post-filtered with a 1D-Gaussian kernel along the x,y and z direction ($\sigma = 0.6$ *voxels*, voxel size = 250x250x250 μm^3).

8.4 Measurements

We have measured and reconstructed two phantoms: A Derenzo phantom and a uniform phantom. The Derenzo phantom has several clusters of hot rods with diameter from 0.7 mm to 1.5 mm. This phantom is used because it allows us to evaluate the reconstructed system resolution. The uniform phantom is used because it easily reveals artifacts that might be unperceived when reconstructing a sparse phantom such as the Derenzo phantom.

Both phantoms were scanned using four different scan protocols: 5 angles / 1 bed position, 50 angles / 1 bed position, 5 angles / 10 bed position and 50 angles / 10 bed position. The 5 angles/ 1 bed position protocol emulates the stationary system that was simulated by Van Holen et al. [23].

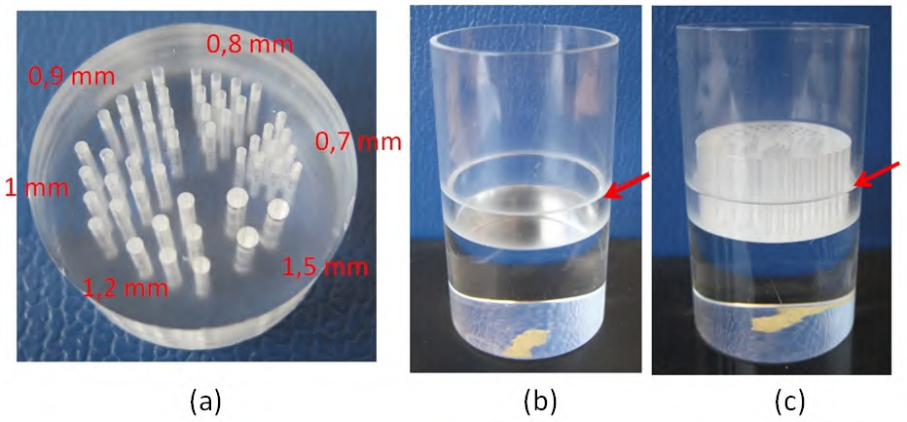

Figure 8.19: (a) The Derenzo insert is positioned in (b) the recipient, (c) depicts the complete phantom. The recipient has an inner diameter of 24 mm; the inner diameter widens to 26 mm at a height of 6 mm, this is marked with an arrow in (b) and (c).

The scan settings are summarized in table 8.2 for the Derenzo phantom and in table 8.3 for the uniform phantom.

8.4.1 Derenzo phantom

The Derenzo phantom is depicted in Fig. 8.19(c). It consists of an insert (Fig. 8.19(a)) and a recipient (Fig. 8.19(b)). The insert has a diameter of 24 mm. The rods have diameters of 0.7, 0.8, 0.9, 1, 1.2 and 1.5 mm, the distance between the rods is twice the rod diameter. The recipient has an inner diameter of 24 mm; the inner diameter widens to 26 mm at a height of 6 mm, this is marked with an arrow in Fig 8.19b and c. The Derenzo phantom was scanned using four different acquisition protocols which are described in table 8.2.

8.4.1.1 Scan 1: one bed position, five angles

The Derenzo phantom (Fig. 8.19)(c) is filled with 2 ml ^{99m}Tc. By doing so, the insert is submerged for approximately 1 mm, the rest of the phantom is not filled. The total activity is 133.0 MBq (66.5 MBq/ml).

The first scan protocol uses 5 angles and 1 bed position. An acquisition time of 10.4 min is used for the first angle, the acquisition time is adjusted

Table 8.2: Acquisitions of the Derenzo phantom

	Scan 1	Scan 2	Scan 3	Scan 4
Activity (MBq)	133.0	107.7	230.9	206.9
Volume (ml)	2	2	2	2
MBq/ml	66.5	53.8	115.4	103.4
# Angles	5	50	5	50
# Bed pos.	1	1	10	10
# Proj.	5	50	50	500
Bed step size (mm)	n/a	n/a	1.3	1.3
Total bed travel (mm)	n/a	n/a	12	12
Axial length phantom (mm)	6.5	6.5	13	13
Acq. time 1^{st} angle (min)	10.4	1.3	1	0.11
Total acq. time (min)	54.2	69.3	52.5	58.1

for decay for the subsequent angles resulting in a total acquisition time of 54.2 min. By doing so, the stationary system which is depicted in Fig. 8.3 is emulated. The results for 100, 300 and 500 iterations are shown in Fig. 8.20.

The 900 μm rods can be distinguished in the image that was reconstructed using 500 iterations, but, the image is obscured by artifacts that are probably caused by mismatches between the calculated system matrix and the real system behavior. The artifacts are probably not caused by insufficient angular sampling because the simulations did not show these artifacts [1].

The axial top part of the phantom can not be reconstructed (marked with a red rectangle in Fig. 8.20) which is due to insufficient axial sampling.

8.4.1.2 Scan 2: one bed position, fifty angles

The same Derenzo phantom, which was used during the previous section has, at the start of this new acquisition decayed to 107.7 MBq (53.8 MBq/ml). Now 50 angles and 1 bed position are used. We compensate for the decayed source by increasing the total acquisition time to 69.3 min, an acquisition time of 1.3 min is used for the first angle.

The reconstructed images are shown in Fig. 8.21.

The resulting images are definitely superior to the images of the previous section, all the 800 μm rods can be distinguished. It is our hypothesis that the mismatches between system matrix and system behavior get averaged out by using more acquisition angles. The axial sampling is, similar to scan

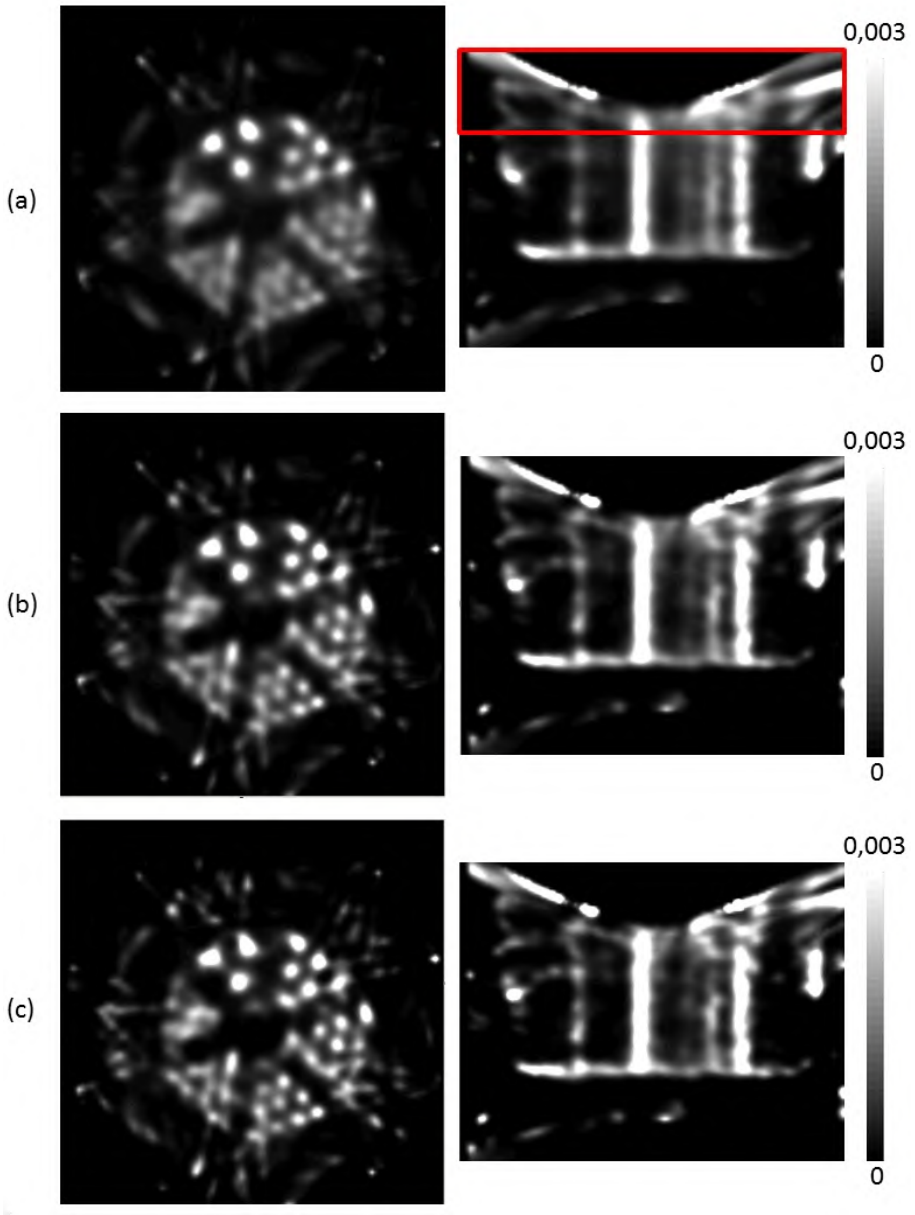

Figure 8.20: The reconstructed Derenzo phantom (acquisition for 5 angles, 1 bed position) after (a) 100 iterations, (b) 300 iterations and (c) 500 iterations. The transaxial and coronal view are depicted.

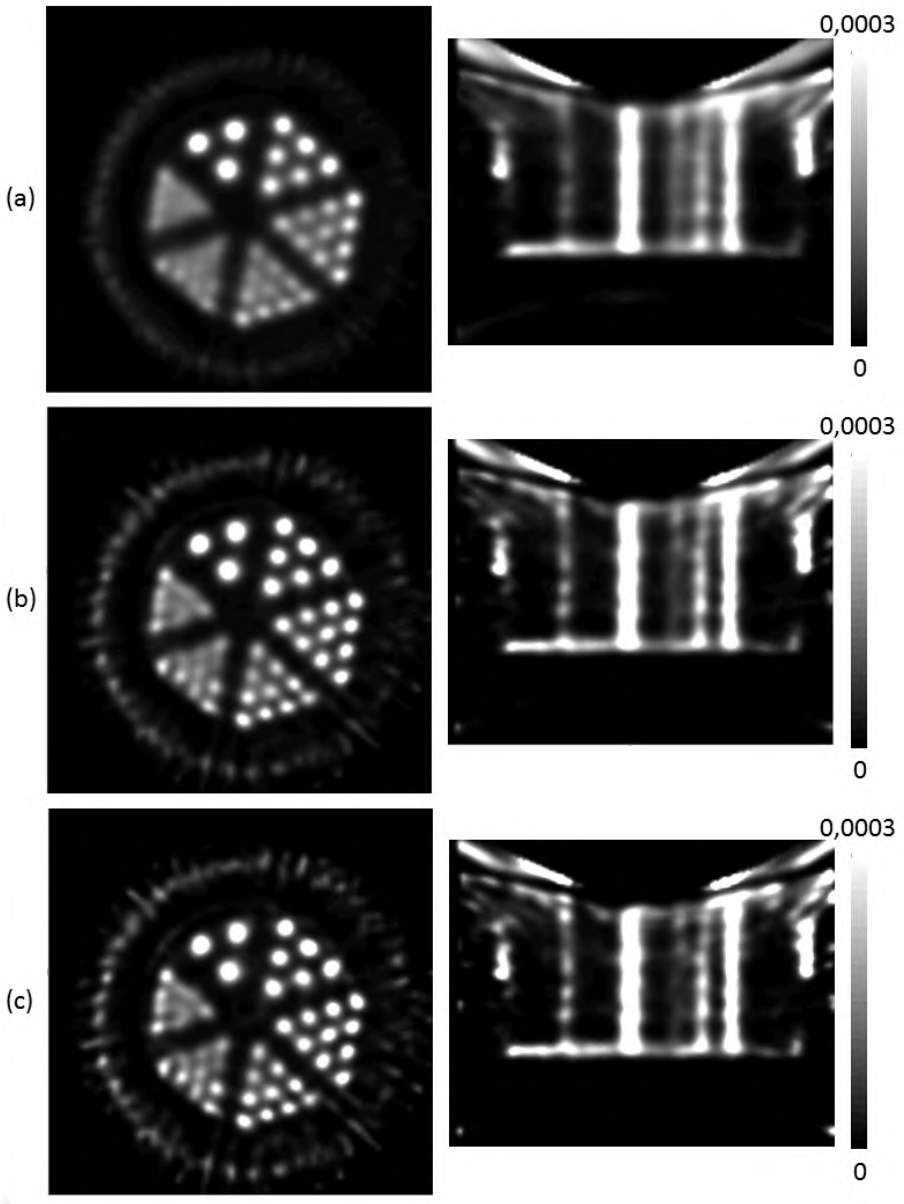

Figure 8.21: The reconstructed Derenzo phantom (acquisition for 50 angles, 1 bed position) after (a) 100 iterations, (b) 300 iterations and (c) 500 iterations. The transaxial and coronal view are depicted.

1, insufficient to reconstruct the top part of the phantom.

8.4.1.3 Scan 3: ten bed positions, five angles

The third scan protocol uses 10 bed positions (1.3 mm bed step size) and 5 angles. The Derenzo phantom was refilled with 230.9 MBq for the multiple bed positions scan. The total acquisition time is 52.5 min, an acquisition time of 1 min is used for the first angle. In order to perform this multiple bed positions measurement we had to attach the rotation stage to a linear stage (depicted in Fig. 8.6).

The Derenzo phantom is filled for approximately 13 mm. The total bed travel equals 12 mm; resulting in 1.33 mm per bed position.

The main reason to use more bed positions is to improve the axial sampling, and by doing so, enlarge the axial volume which can be reconstructed. The effect can be seen by comparing the coronal views of Fig. 8.22 and Fig. 8.20.

Additionally, it can be concluded that there are also less artifacts present in the transaxial views (8.22 compared to Fig. 8.20). Also here mismatches between system matrix and real system behavior are averaged out by making use of additional projections.

8.4.1.4 Scan 4: ten bed positions, fifty angles

Finally, the Derenzo phantom was scanned using 50 angles and 10 bed positions (1.3 mm bed step size). The bed positions are similar to those used for scan 3.

The same Derenzo phantom, which was used for scan 3 has, at the start of this new acquisition decayed to 206.9 MBq (103.4 MBq/ml). We compensate for the decayed source by increasing the total acquisition time to 58.1 min, an acquisition time of 6.6 s is used for the first angle.

A total of 500 projections is used here (50 angles and 10 bed positions), this results in relatively artifact-free images of the Derenzo phantom. The resolution of the 50 angles, 10 bed position image seems to be slightly worse than the resolution of the 50 angles, 1 bed position. This is probably due to deviations caused by the more demanding mechanical setup that also requires a linear stage.

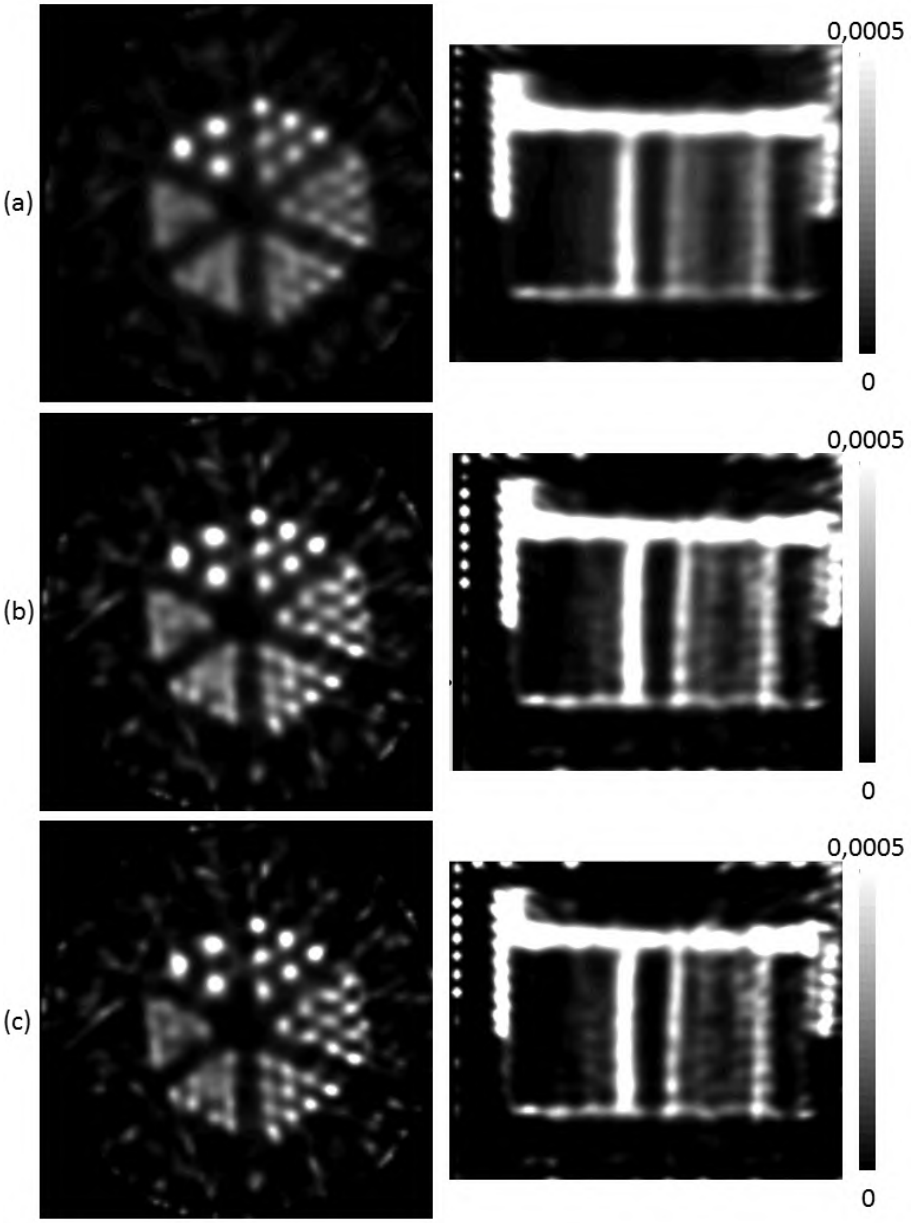

Figure 8.22: The reconstructed Derenzo phantom (acquisition for 5 angles, 10 bed positions) after (a) 100 iterations, (b) 300 iterations and (c) 500 iterations. The transaxial and coronal view are depicted.

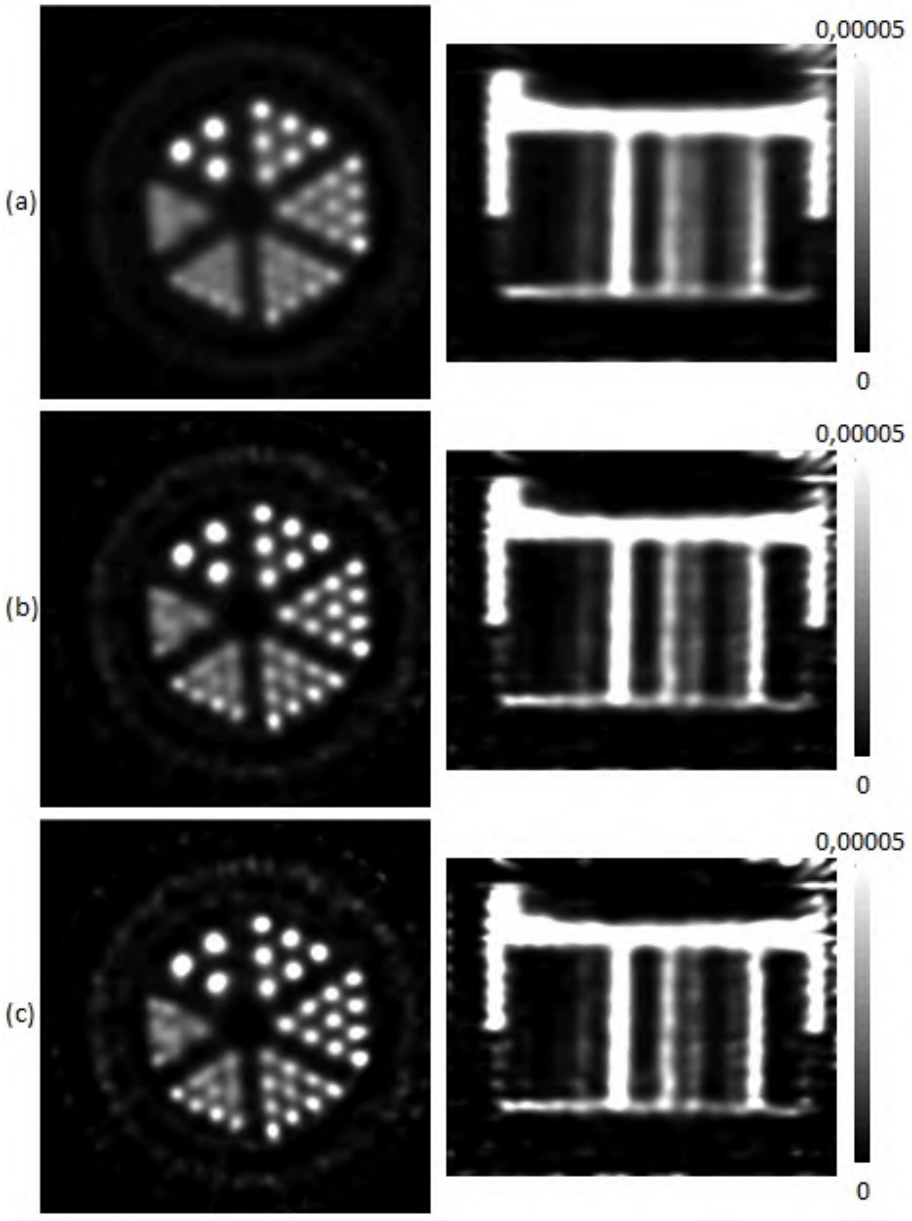

Figure 8.23: The reconstructed Derenzo phantom (acquisition for 50 angles, 10 bed positions) after (a) 100 iterations, (b) 300 iterations and (c) 500 iterations. The transaxial and coronal view are depicted.

Table 8.3: Acquisitions of the uniform phantom

	Scan 5	Scan 6	Scan 7	Scan 8
Activity (MBq)	97.0	78.6	151.3	134.0
Volume (ml)	3	3	3	3
MBq/ml	32.3	26.2	50.4	44.7
# Angles	5	50	5	50
# Bed pos.	1	1	10	10
# Proj.	5	50	50	500
Bed step size (mm)	n/a	n/a	0.89	0.89
Total bed travel (mm)	n/a	n/a	8	8
Axial length phantom (mm)	6.7	6.7	6.7	6.7
Acq. time 1^{st} angle (min)	10.4	1.3	1	0.11
Total acq. time (min)	54.2	69.3	52.5	58.1

8.4.2 Uniform phantom

The recipient of the Derenzo phantom (Fig. 8.19(b)) is filled with 3 ml ^{99m}Tc, the active axial length of the resulting phantom is approximately 7 mm. It is scanned using four different scan protocols. The details of each scan are listed in table 8.3.

8.4.2.1 Scan 5: one bed position, five angles

The total activity for scan 5 is 97 MBq (32.3 MBq/ml). The scan protocol uses 5 angles and 1 bed position. An acquisition time of 10.4 min is used for the first angle, the acquisition time is adjusted for decay for the subsequent angles, resulting in a total acquisition time of 54.2 min. The results for 100, 300 and 500 iterations are shown in Fig. 8.24; profiles are shown in Fig. 8.25.

The resulting images show severe streak artifacts; an example is marked by the red arrow in Fig. 8.24. Some activity is positioned outside the phantom (marked by the green arrow in Fig. 8.24).

8.4.2.2 Scan 6: one bed position, fifty angles

The uniform phantom, which was used during the previous section has, at the start of this new acquisition, decayed to 78.6 MBq (26.2 MBq/ml). Now 50 angles are used, an acquisition time of 1.3 min is used for the first

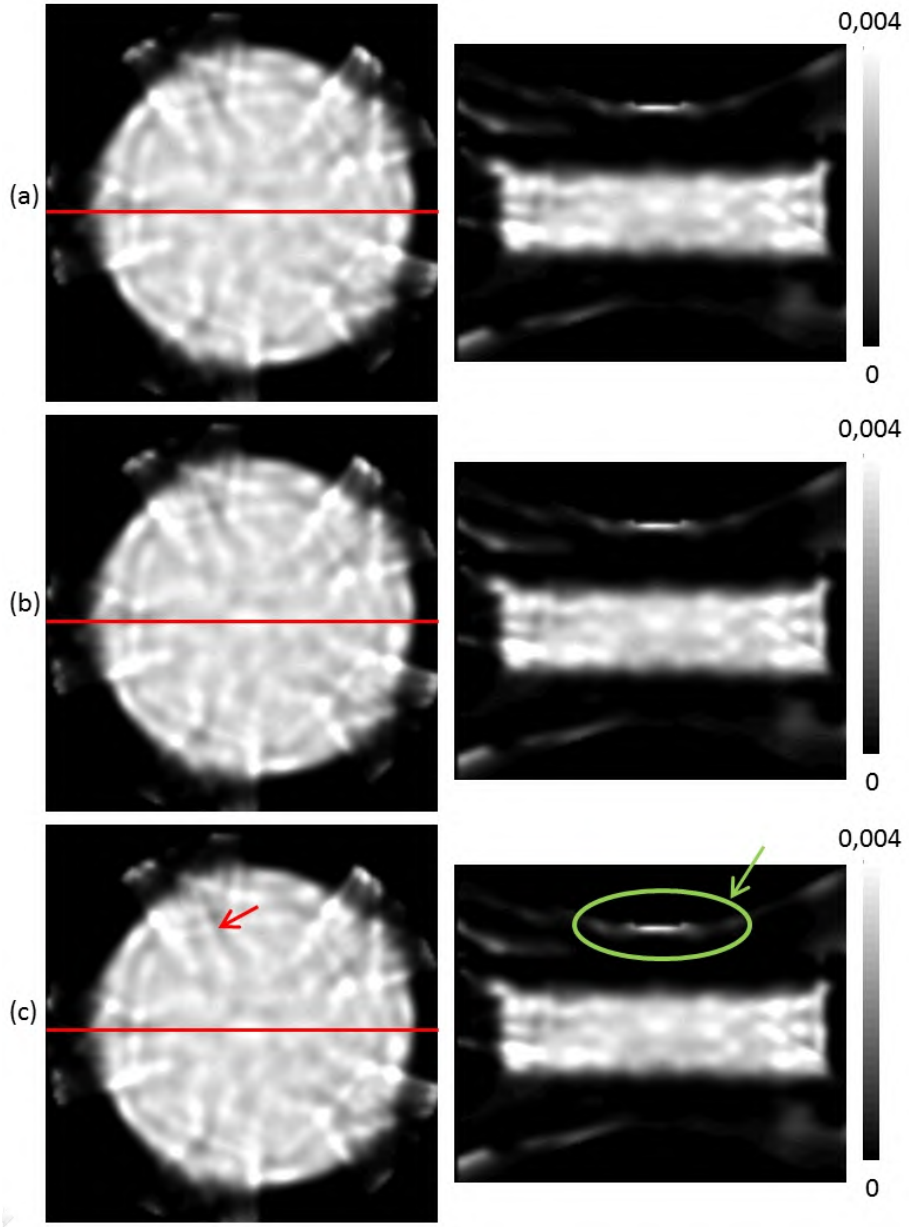

Figure 8.24: The reconstructed uniform phantom (acquisition for 5 angles) after (a) 100 iterations, (b) 300 iterations and (c) 500 iterations. The transaxial and coronal view are depicted. Profiles are shown in Fig. 8.25

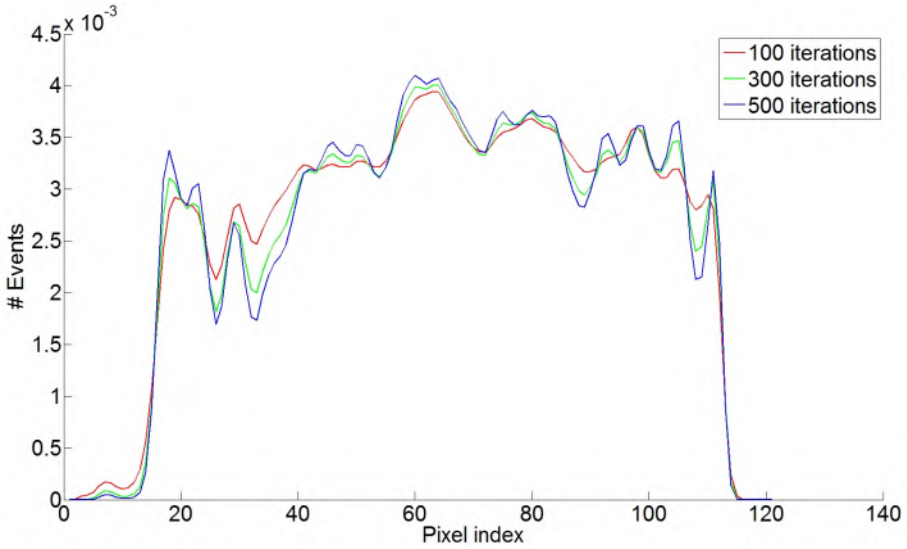

Figure 8.25: Profile views of the reconstructed uniform phantom (acquisition for 5 angles, 1 bed position) depicted in Fig. 8.24 for 100, 300 and 500 iterations.

angle, the total acquisition time is 69.3 min. The results for 100, 300 and 500 iterations are shown in Fig. 8.26; profiles are shown in Fig. 8.27.

Similar to the Derenzo phantom, we see that the reconstruction artifacts are less pronounced when more acquisition angles are used. Two kinds of artifacts can be observed: ring artifacts (blue arrow in Fig. 8.26) and streak artifacts at the outside border of the phantom (red arrow in Fig. 8.26).

8.4.2.3 Scan 7: ten bed positions, five angles

The uniform phantom has been refilled to an activity of 151.3 MBq, it has an axial length of approximately 6.7 mm. Here we scan it using 10 bed positions (total bed travel is 8 mm, one step is 889 μm). The results for 100, 300 and 500 iterations are shown in Fig. 8.28; profiles are shown in Fig. 8.29.

As expected, we see that the usage of more bed positions improves the axial sampling, and, enlarges the axial volume that can be reconstructed (Fig. 8.24 vs. Fig. 8.28). Additionally, system matrix mismatches are averaged out and due to this, the artifacts are suppressed.

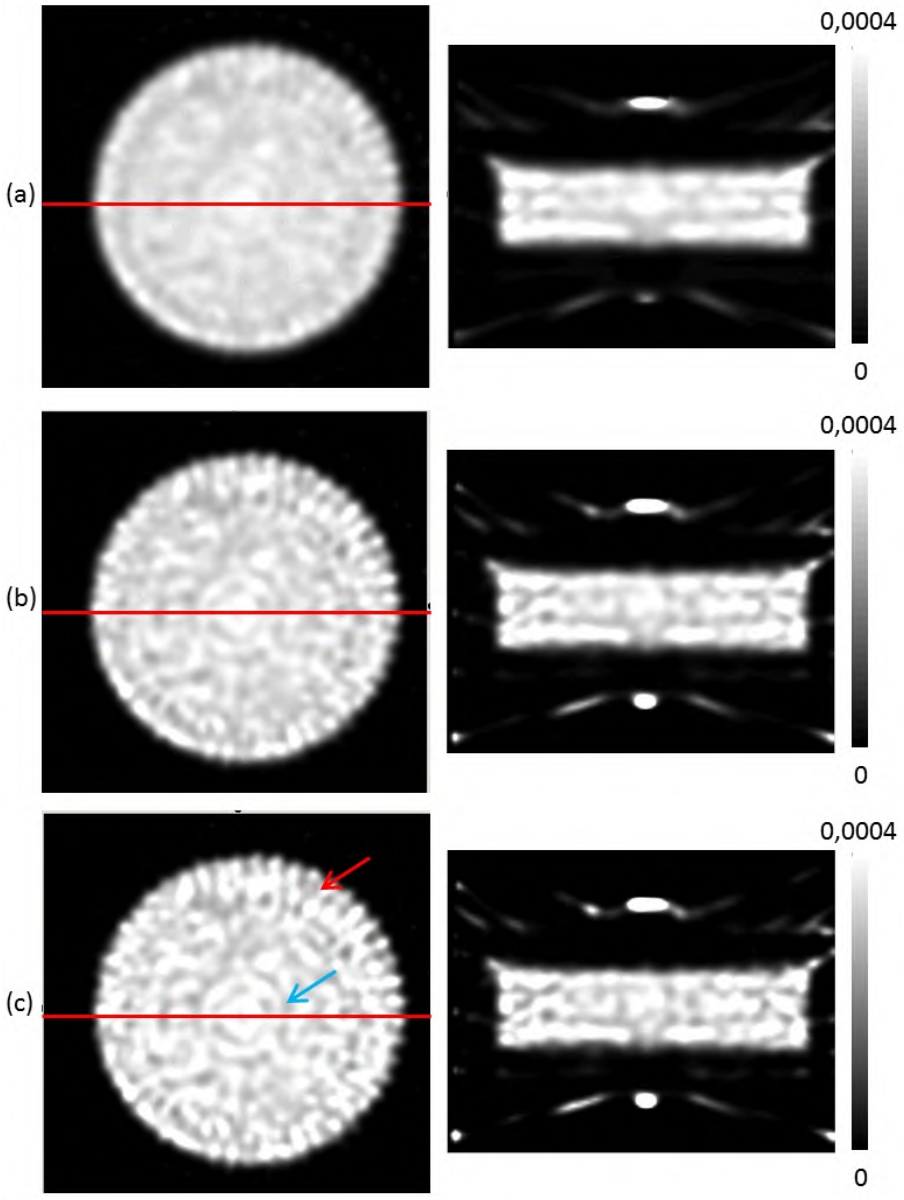

Figure 8.26: The reconstructed uniform phantom (acquisition for 50 angles, 1 bed position) after (a) 100 iterations, (b) 300 iterations and (c) 500 iterations. The transaxial and coronal view are depicted. Profiles are shown in Fig. 8.27.

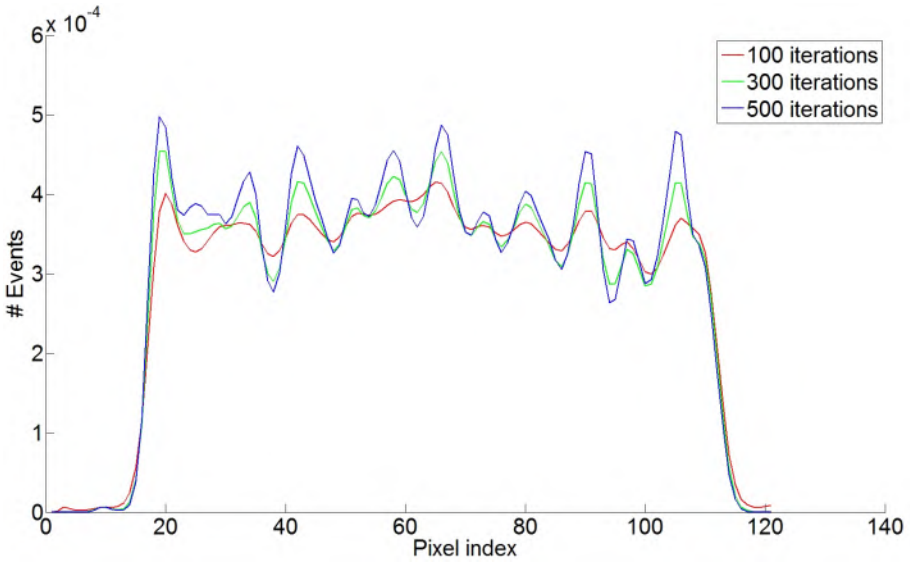

Figure 8.27: Profiles of the reconstructed uniform phantom (acquisition for 50 angles, 1 bed position) depicted in Fig. 8.26 for 100, 300 and 500 iterations.

8.4.2.4 Scan 8: ten bed positions, fifty angles

The uniform phantom used in the previous section has decayed to 134 MBq, the acquisition time has been enlarged to compensate for this.

In this section an acquisition is done using 10 bed positions and 50 angles. The total bed travel is 8 mm, the step size is 889 μm.

The reconstructed images are superior to the images acquired using less projections; there is however still a bright spot on the center of rotation (see Fig. 8.31) and some activity is positioned outside the phantom.

8.5 Discussion

The presented SPECT system is based on a design by Van Holen et al. [23]. Simulations of the system indicate that it should be able to reconstruct objects, artifact-free, that are acquired using only five acquisition angles and one bed position. By doing so, the system and object can remain stationary.

The measurements presented here do not show artifact-free images. The main reason for this is probably a mismatch between the system matrix

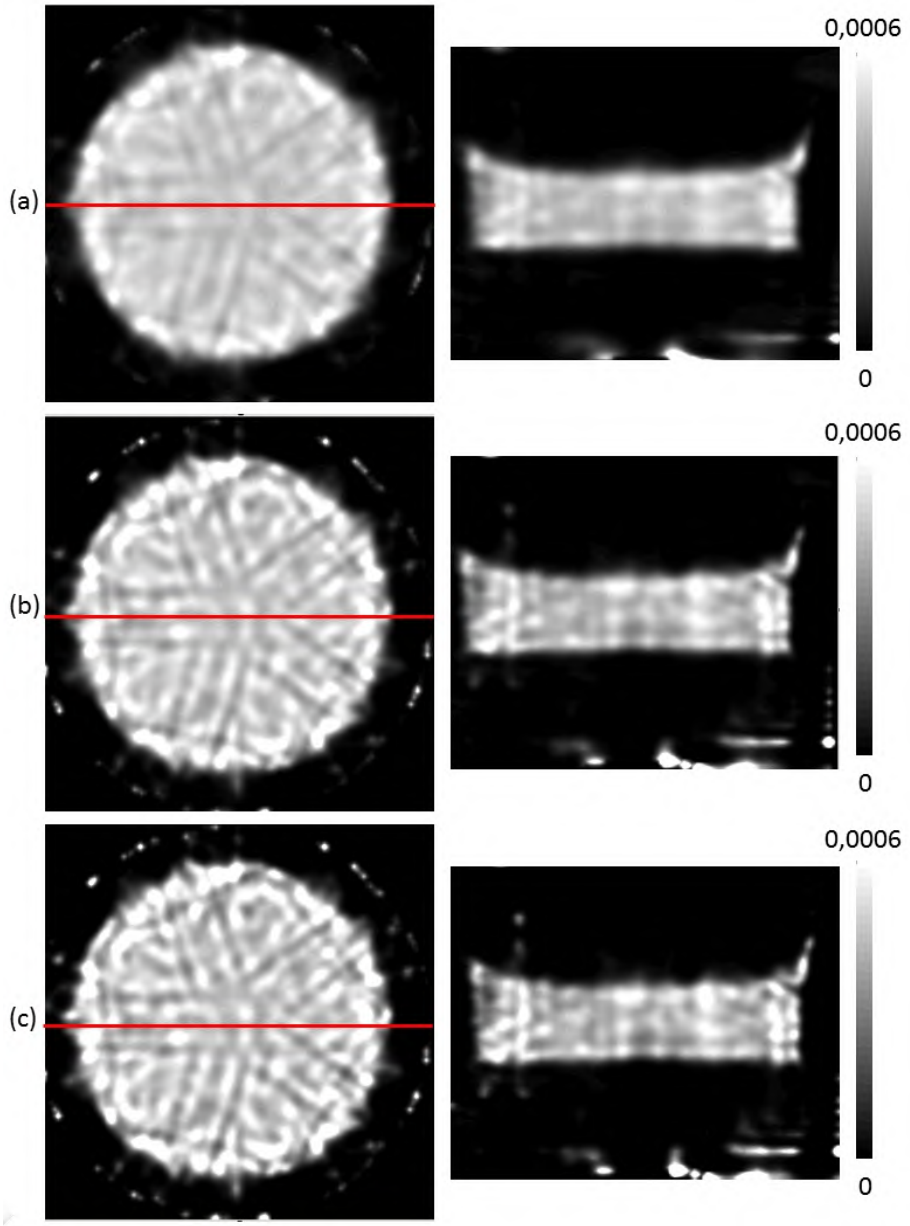

Figure 8.28: The reconstructed uniform phantom (acquisition for 5 angles, 10 bed positions) after (a) 100 iterations, (b) 300 iterations and (c) 500 iterations. The transaxial and coronal view are depicted.

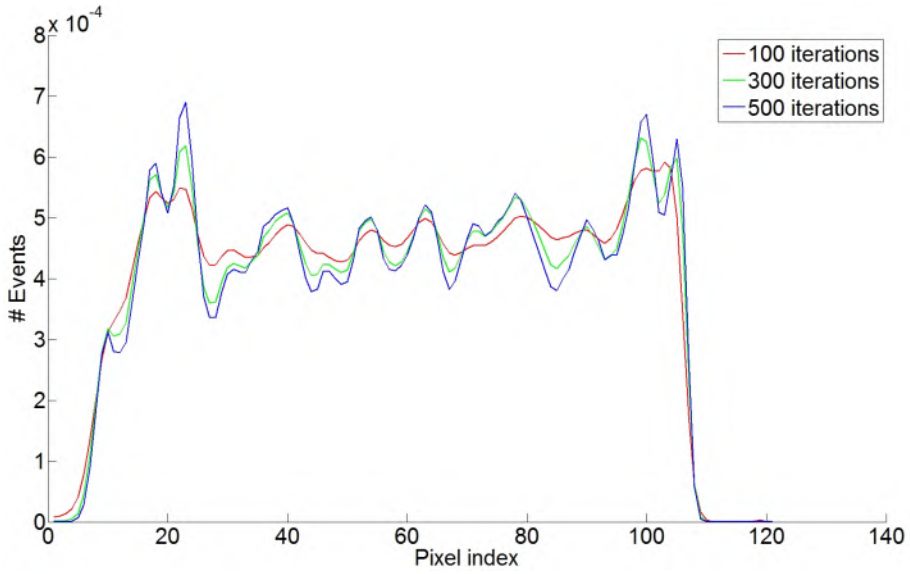

Figure 8.29: Profiles of the reconstructed uniform phantom (acquisition for 5 angles, 10 bed positions) depicted in Fig. 8.28 for 100, 300 and 500 iterations.

and the real system behavior; such a mismatch is not present in the simulations. It is difficult to determine a main reason for this mismatch (e.g. wrong COR_{lm}, inaccurate aperture positions, noisy flood maps, system matrix calculation method, ...), because different causes result in similar artifacts. From simulations, we have noticed that a mismatch in COR_{lm}, and, a mismatch in aperture position, leads to similar ring and streak artifacts. Additionally, we should note that simulations always differ from real-world circumstances. The simulations used for the design of the system ([23]) do for example not include detailed aperture penetration modeling and a detailed model for detector DOI.

Using more angles and more bed positions definitely improves the image quality. In a system setting, this would mean that the detectors and collimators should be mounted on a rotating gantry, and, that the animal should be positioned on a motorized bed.

Further improvements are however still possible. A more accurate system matrix has the potential to further improve the image quality. To accomplish this one could for example first calibrate the geometry using point source measurements and then generate a system matrix for the calibrated geometry using Monte-Carlo simulations.

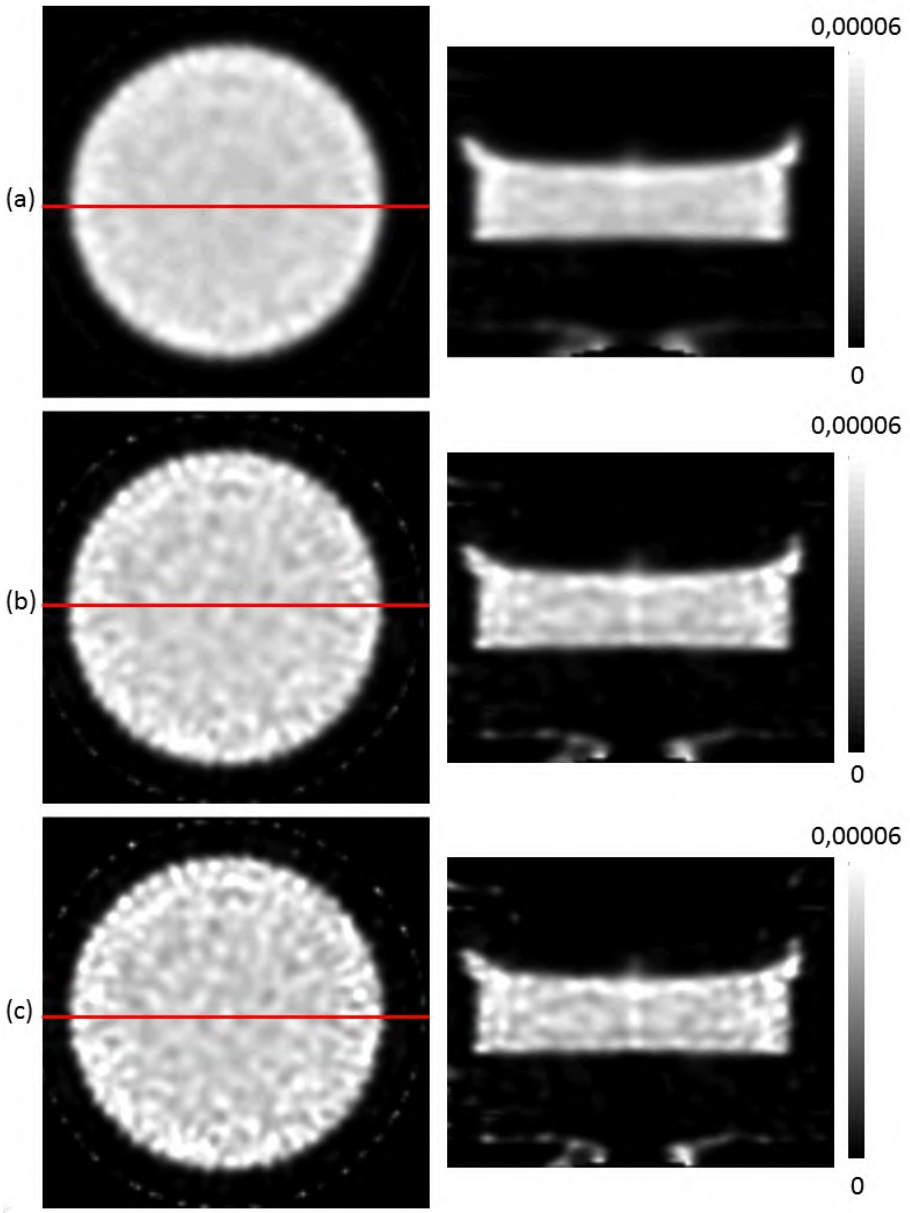

Figure 8.30: The reconstructed uniform phantom (acquisition for 50 angles, 10 bed positions) after (a) 100 iterations, (b) 300 iterations and (c) 500 iterations. The transaxial and coronal view are depicted.

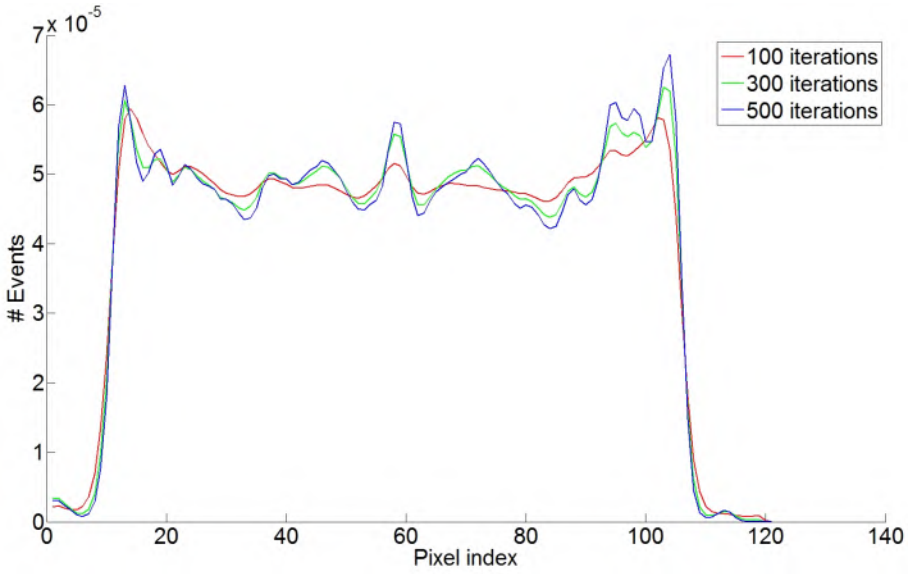

Figure 8.31: Profiles of the reconstructed uniform phantom (acquisition for 50 angles, 10 bed positions) depicted in Fig. 8.28 for 100, 300 and 500 iterations.

This second SPECT system outperforms the previous system (see chapter 5) for resolution; the previous system allows to distinguish the 1.6 mm rods (Fig. 5.13), the new system allows to distinguish the 700 μm rods (Fig. 8.21) of a Derenzo phantom. The obtained resolution is in the same range (0.58 to 0.76 mm) as the three large state-of-the-art systems that were evaluated by Deleye et al. [163].

A sensitivity comparison between our new system, the previous system and other small-animal SPECT systems is more difficult. One can compare the sensitivity for a point source in the center of the FOV but this would be disadvantageous for the new multi-lofthole system because this system has all loftholes focused to different parts of the FOV. Alternatively, one can compare the volume sensitivity but this basically shifts the problem towards the definition of the volume that has to be taken into account.

A approximate comparison can be made if we reconsider the pentagonal system that has all apertures focused on the center of the FOV. The theoretical peak sensitivity of such a system is 0.32% [23], this is larger than the sensitivity of our first system (0.006%). Deleye et al. [163] measured a sensitivity of 0.39% (MILabs U-SPECT-II, 1 mm pinhole apertures), 0.06% (GE X-SPECT) and 0.07% (BioScan NanoSPECT-NSO); our system thus

has a sensitivity which is comparable to the more sensitive small-animal SPECT systems.

8.6 Summary and original contributions

In this chapter we have built a compact SPECT system that consists of an LYSO detector and a multi-lofthole collimator; this system is based on a design by Van Holen et al. [23]. We have described the geometry, the calibration procedure and image reconstruction algorithm. Measurements, using different acquisition protocols, of a Derenzo phantom and a uniform phantom have been presented. The image quality improves when more angles and more bed positions are used. The 700 μm rods of the Derenzo phantom can be resolved when the phantom is scanned using 50 angles.

Chapter 9

General conclusions

An overview of the work presented in this dissertation is given here.

9.1 Summary

The basic concepts of SPECT imaging were introduced in chapter 1. Chapter 1 starts with a brief review of the different possible interaction mechanisms of gamma-rays; photoelectric absorption and Compton scatter are relevant for SPECT imaging. These interaction mechanisms are important to understand the functioning of the collimator and the detector. Thereafter, different types of collimators are discussed. The parallel hole collimator, the workhorse in nuclear medicine was introduced first. The pinhole collimator is thoroughly discussed and, in order to be complete we also introduced the fanbeam and conebeam collimators.

Standard clinical detectors are still based on Anger's first NaI(Tl) gamma-ray detector. There are however interesting alternatives: other scintillator materials might allow a better spatial resolution, PSPMTs or semiconductor based photodetectors allow for more compact detectors and the usage of high-performance event positioning algorithms is important to improve the spatial resolution. Alternatively, one can choose for semiconductor detectors, this can be done for instance to obtain a higher energy resolution. A final section of the introductory chapter handles on image reconstruction. We have introduced the basic concepts of MLEM reconstruction, which is the most frequently used reconstruction algorithm for SPECT imaging.

In chapter 3, a scintillation detector with a high spatial resolution is presented. This detector consists of a NaI(Tl) scintillator, an H8500 PSPMT

and dedicated read-out electronics. These read-out electronics digitize all the PSPMT channels and transmit the values of each channel to a computer using an Ethernet link. A GPU-accelerated MLE-event positioning algorithm is then used to accurately position each detected event. This detector has a spatial resolution of 1.24 mm, which is more than twice as good as traditional detectors used in clinical systems; its energy resolution is 9.3%, which is slightly better than traditional clinical detectors.

The fourth chapter handles on a new pinhole geometry, called the lofthole. The lofthole has a circular aperture and a shaped entrance or exit opening. By shaping the entrance/exit opening one can define the detector area which is irradiated by an aperture. By clearly defining and tiling these areas for a multi-lofthole collimator, we are able to use the valuable detector area more efficiently. Sensitivity formulas for pinholes and loftholes are introduced which take the penumbra/umbra regions into account. Measurements on a prototype lofthole with a square exit opening indicate that the irradiated detector area takes the same square shape as the exit opening and that such a lofthole has less penetrating photons than a pinhole irradiating the same square detector area.

The single lofthole collimator of chapter 4 has been combined with the NaI(Tl) detector to build a simple, flexible and compact demonstrator SPECT system (chapter 5). Two different setups were build: one that fits rat-size objects and one that fits mouse-size objects. The resolution and sensitivity of this demonstrator system are mediocre compared to the state-of-the-art pre-clinical SPECT scanners because only one lofthole is used. To improve on this, a two-stage approach was used. In a first stage, the detector resolution was improved; in a second stage, a new multi-lofthole collimator, that takes advantage of this improved detector resolution, was developed.

The detector resolution can be improved by making use of a thinner scintillator. A thin NaI(Tl) scintillator has a low detection efficiency. In order to compensate for this a more dense scintillator, LYSO, was used. Indeed, a 2 mm thick LYSO scintillator has approximately the same detection efficiency as a 5 mm thick NaI(Tl) detector. The PSPMT and read-out were not modified to build this new LYSO-based detector. The detector was compared with the NaI(Tl) detector. The spatial resolution of the LYSO detector is 780 μm, the energy resolution is 24.4 %. In this chapter we have also introduced a new event-positioning algorithm: mean nearest neighbor (MNN); this algorithm has a slightly worse spatial resolution than MLE-event positioning but is computationally less demanding and as such speeds

up the data processing.

A new multi-lofthole collimator was designed especially for this LYSO detector. The production of this tungsten collimator would have been very expensive or even impossible using traditional machining techniques. We investigated additive manufacturing (a 3D-printing technique) to produce pure tungsten collimators. Two collimators have been made. The first collimator has a density of 17.31 g/cm^3 (89.92% of pure tungsten). The second collimator was produced using updated production techniques and is superior to the first collimator with regards to density (96.4 % of pure tungsten) and production accuracy (max. deviation +0.180 mm, min. deviation -0.137 mm). The major advantage of this new technique is the possibility for novel geometries which could not be produced with conventional techniques. This technique can also be considered to produce high-resolution tungsten parallel hole, conebeam and fanbeam collimators with thin septa and small holes.

Finally, we have merged the multi-lofthole collimator with the LYSO detector to obtain a compact SPECT system with high sensitivity and high resolution. According to simulations, it should be possible to use this setup in a 5-angle mode. Our measurements of a hot rod and uniform phantom indicate that more angles and bed positions are needed. We were able to reconstruct the phantoms with little artifacts using 50 angles and 10 bed positions. The 700 μm rods of the hot rod phantom could be resolved using this scan protocol. Strong artifacts are present when only five angles and one bed position are used. The main reason for this is probably a mismatch between the system matrix and the real system behavior. Further improvements are possible, a more accurate system matrix has the potential to further improve the image quality. To accomplish this one could for example first calibrate the geometry and then generate a system matrix for the calibrated geometry using Monte-Carlo simulations. Additionally, we have now redesigned the collimator. The new collimator has less loftholes and is designed in such a way that overlap on the detector is avoided. We expect that this will make the system matrix calculation more accurate because there are fewer penumbrae and because the flood maps can be acquired simultaneously. A hexagonal system will be built with 6 of these new collimators and 6 detectors, making it suitable for both mouse and rat body imaging. According to simulations it should be possible to use this system stationary (without rotation). By doing so, the COR_{Im} calibration is no longer required.

9.2 Final conclusion

In this dissertation we have developed high resolution SPECT detectors and collimators. The advantage of high-resolution gamma-ray detectors is that they can be employed to build higher sensitivity systems [1, 28, 29]. We have used those components to build two compact pre-clinical SPECT systems. Note that the developed instrumentation and techniques can also be used for clinical SPECT. The high-resolution detectors and the lofthole can be used to improve clinical pinhole-based systems. Additive manufacturing allows for the production of complex tungsten collimators that can also be used for clinical SPECT systems; a tungsten parallel hole collimator might for example allow to use thinner collimator septa and this in turn might lead to an increase in sensitivity.

A new collimator geometry called the lofthole has been developed. The lofthole allows to use a detector more efficiently. Additionally, a lofthole has less penetrating gamma-ray photons than a pinhole that irradiates the same detector area. Sensitivity formulas for the pinhole and for a lofthole with a square exit opening were presented that take the penumbra effect into account.

We have shown that NaI(Tl) and LYSO can be used in combination with a PSPMT to build high-resolution detectors. LYSO provides a higher spatial resolution than NaI(Tl), the drawback is that LYSO has a substantially worse energy resolution than NaI(Tl). The resolution of a scintillation detector could be further improved by making use of photodetectors that have a higher quantum efficiency or a smaller pixel size. The higher quantum efficiency will result in more charge-carriers and the smaller pixel size allows to sample the lightspread more accurately. Additionally, scintillators that have a high light-yield such as $LaBr_3$(Ce) or SrI_2(Eu) can be considered.

Additive manufacturing has been introduced as a new method to produce pure tungsten collimators. This technique allows to design and produce collimators without being hindered by the limitations of traditional subtractive production techniques. We have used this method to build a multi-lofthole collimator. It could also be used to build parallel hole, fanbeam and conebeam collimators with thin septa and small hole diameters.

Finally, we have build two compact pre-clinical SPECT systems. The first system consists of a single lofthole collimator and a compact NaI(Tl) detector, the second system consists of a multi-lofthole collimator and an LYSO detector. The latter system provides the highest sensitivity and resolution but the reconstructed images show artifacts. These artifacts are probably

caused by deviations between the calculated system matrix and the real system behavior. Future work will focus on a compact SPECT system that can be used to perform mouse and rat body imaging. The multi-lofthole collimators for this system have been built in such a way that there should not be overlap on the detector. We expect that this will make system calibration easier and more accurate.

References

[1] Van Holen R, Vandeghinste B, Deprez K, Vandenberghe S. Design and performance of a compact and stationary microSPECT system. *Medical Physics*. 2013;40(11):112501.

[2] Deprez K, Vandenberghe S, Staelens S. Methods and systems for collimating, PCT/EP2010/069303, 2010.

[3] Van Audenhaege K, Deprez K, Vandenberghe S, Van Holen R. Methods and systems for collimating, PCT/EP2012/058589, 2012.

[4] Deprez K, Van Holen R, Vandenberghe S, Staelens S. Design of a high resolution scintillator based SPECT detector (SPECTatress). *Nuclear Instruments and Methods in Physics Research Section A: Accelerators, Spectrometers, Detectors and Associated Equipment*. 2011;648(1):S107 –S110.

[5] Deprez K, Vandenberghe S, Vandeghinste B, Van Holen R. FlexiSPECT: A SPECT System Consisting of a Compact High-Resolution Scintillation Detector (SPECTatress) and a Lofthole Collimator. *IEEE Transactions on Nuclear Science*. 2013;60(1):53–64.

[6] Deprez K, Vandenberghe S, Van Audenhaege K, Van Vaerenbergh J, Van Holen R. Rapid additive manufacturing of MR compatible multipinhole collimators with selective laser melting of tungsten powder. *Medical Physics*. 2012;40(1).

[7] Deprez K, Pato L, Vandenberghe S, Van Holen R. Characterization of a SPECT pinhole collimator for optimal detector usage (the lofthole). *Physics in Medicine in Biology*. 2013;.

[8] Deprez K, Van Holen R, Vandenberghe S. A high resolution SPECT detector based on thin continuous LYSO. *Physics in Medicine and Biology*. 2014;59(1):153–171.

[9] España S, Deprez K, Van Holen R, Vandenberghe S. Fast calibration of SPECT monolithic scintillation detectors using un-collimated sources. *Physics in Medicine and Biology*. 2013;58(14):4807–4825.

[10] Van Audenhaege K, Vandenberghe S, Deprez K, Vandeghinste B, Van Holen R. Design and simulation of a full-ring multi-lofthole collimator for brain SPECT. *Physics in Medicine and Biology*. 2013; 58(18):6317–6336.

[11] Deprez K, Vandenberghe S, Staelens S. Design of a High Resolution Scintillator Based SPECT Detector (SPECTatress). *Imaging 2010, Abstracts*. 2010;.

[12] Deprez K, Van Holen R, Staelens S, Vandenberghe S. A high resolution scintillator based SPECT detector with digital pulse processing (SPECTatress). In: *Nuclear Science Symposium Conference Record (NSS/MIC), 2010 IEEE*. 2010; pp. 3100 –3104.

[13] Deprez K, Van Holen R, Vandenberghe S. The lofthole: A novel shaped pinhole geometry for optimal detector usage without multiplexing and without additional shielding. In: *Nuclear Science Symposium and Medical Imaging Conference (NSS/MIC), 2011 IEEE*. 2011; pp. 3317 –3322.

[14] Van Audenhaege K, Van Holen R, Deprez K, Karp JS, Metzler S, Vandenberghe S. Design of a static full-ring multi-pinhole collimator for brain SPECT. *Nuclear Science Symposium Conference Record (NSS/MIC), 2011 IEEE*. 2011;pp. 4393–4397.

[15] Pato L, Van Holen R, Deprez K, Vandenberghe S. Geometric sensitivity in the Penumbra region of a pinhole: analytic calculation. *Journal of Nuclear Medicine*. 2013;53 Suppl. 1:2395.

[16] Deprez K, Van Holen R, Van Audenhaege K, Vandenberghe S. Additive manufacturing of high density tungsten collimators. *Journal of Nuclear Medicine*. 2013;53 Suppl. 1:2394.

[17] Deprez K, Van Holen R, Vandeginste B, Vandenberghe S. FlexiSPECT: a compact SPECT system with a lofthole collimator and a high-resolution scintillation detector. *Journal of Nuclear Medicine*. 2013;53 Suppl. 1:492.

[18] Van Audenhaege K, Bovijn D, Van Holen R, Deprez K, Vandenberghe S. An MR-compatible shutter mechanism for stationary multi-pinhole

SPECT of large objects. *PET/MR and SPECT/MR : New Paradigms for Combined Modalities in Molecular Imaging Conference, Abstracts*. 2012;.

[19] Van Holen R, Van Audenhaege K, Deprez K, Vandenberghe S. Development of a compact MicroSPECT system for sequential SPECT-MRI. *PET/MR and SPECT/MR : New Paradigms for Combined Modalities in Molecular Imaging Conference, Abstracts*. 2012;.

[20] Van Holen R, Deprez K, Bouckaert C, Vandenberghe S. Design and simulations of a multi-lofthole MicroSPECT imager using minifying projections. *Workshop On Small Animal Imaging, Abstracts*. 2012;.

[21] Van Holen R, Deprez K, Vandeghinste B, Vandenberghe S. Design and simulations of a multi-lofthole MicroSPECT imager using minifying projections. *Journal of Nuclear Medicine*. 2012;53 Suppl. 1:2393.

[22] Bouckaert C, Marcinkowski R, Deprez K, España S, Van Holen R, Vandenberghe S. Optimization of digital silicon photomultipliers for monolithic SPECT scintillators. *Journal of Nuclear Medicine*. 2013; 54 Suppl. 2:2160.

[23] Van Holen R, Deprez K, Vandeghinste B, Vandenberghe S. A compact stationary microSPECT system based on high-resolution detectors and collimator additive manufacturing. *Journal of Nuclear Medicine*. 2013;54 Suppl. 2:2163.

[24] Deprez K, Vandenberghe S, Van Holen R. Performance of continuous LYSO for high resolution SPECT detectors. *Journal of Nuclear Medicine*. 2013;54 Suppl. 2:2159.

[25] Deprez K, Vandenberghe S, Van Holen R. Accuracy and density of pure tungsten collimators produced by additive manufacturing. *Journal of Nuclear Medicine*. 2013;54 Suppl. 2:2165.

[26] Kinahan PE, Townsend DW, Beyer T, Sashin D. Attenuation correction for a combined 3D PET/CT scanner. *Medical Physics*. 1998; 25(10):2046–2053.

[27] Keereman V, Fierens Y, Broux T, De Deene Y, Lonneux M, Vandenberghe S. MRI-Based Attenuation Correction for PET/MRI Using Ultrashort Echo Time Sequences. *Journal of Nuclear Medicine*. 2010; 51(5):812–818.

[28] Rogulski MM, Barber HB, Barrett HH, Shoemaker RL, Woolfenden JM. Ultra-high-resolution brain SPECT imaging: simulation results. *IEEE Transactions on Nuclear Science*. 1993;40(4):1123–1129.

[29] Goorden MC, Rentmeester MCM, Beekman FJ. Theoretical analysis of full-ring multi-pinhole brain SPECT. *Physics in Medicine and Biology*. 2009;54(21):6593–6610.

[30] Müller C, Schibli R. *Molecular Imaging in Oncology*, pp. 65–105. Springer. 2013;.

[31] Guérin B, Tremblay S, Rodrigue S, Rousseau JA, Dumulon-Perreault V, Lecomte R, van Lier JE, Zyuzin A. Cyclotron production of ^{99m}Tc: an approach to the medical isotope crisis. *Journal of Nuclear Medicine*. 2010;51:13N–16N.

[32] Hutton BF, Buvat I, Beekman FJ. Review and current status of SPECT scatter correction. *Physics in Medicine and Biology*. 2011; 56:85–112.

[33] Knoll GF. *Radiation Detection and Measurement (3rd edition)*. Wiley. 1999.

[34] Berger M, Hubbell J, Seltzer S, Chang J, Coursey J, Sukumar R, Zucker D, Olsen K. XCOM: Photon Cross Section Database (version 1.5). *National Institute of Standards and Technology, Gaithersburg*. 2010;.
URL `http://physics.nist.gov/xcom`

[35] Moore S, Kouris K, Cullum I. Collimator design for single photon emission tomography. *European Journal of Nuclear Medicine*. 1992; 19(2):138–150.

[36] Nillius P, Danielsson M. Theoretical Bounds and System Design for Multipinhole SPECT. *IEEE Transactions on Medical Imaging*. 2010; 29(7):1390–1400.

[37] Anger HO. Radioisotope Cameras. In: *Instrumentation in Nuclear Medicine*, pp. 485–552. New York: Academic. 1967;.

[38] Smith MF, Jaszczak RJ. The effect of gamma ray penetration on angle-dependent sensitivity for pinhole collimation in nuclear medicine. *Medical Physics*. 1997;24(11):1701–1709.

[39] Metzler SD, Bowsher JE, Smith MF, Jaszczak RJ. Analytic determination of pinhole collimator sensitivity with penetration. *IEEE Transactions on Medical Imaging*. 2001;20(8):730–741.

[40] Accorsi R, Metzler SD. Analytic determination of the resolution-equivalent effective diameter of a pinhole collimator. *IEEE Transactions on Medical Imaging*. 2004;23(6):750–763.

[41] Smith MF, Jaszczak RJ, Wang H. Pinhole Aperture Design for ^{131}I Tumor Imaging. *IEEE Transactions on Nuclear Science*. 1997; 44(3):1154–1160.

[42] Goorden MC, Beekman FJ. High-resolution tomography of positron emitters with clustered pinhole SPECT. *Physics in Medicine and Biology*. 2010;55(5):1265–1277.

[43] Funk T, Després P, Barber WC. A multipinhole small animal SPECT system with submillimeter spatial resolution. *Medical Physics*. 2006; 33(5):1259–1268.

[44] Zheng Y, Li H, Wang J, Stolin AV, Pole J, Williams MB. Image reconstruction for small animal SPECT with two opposing half cones. *Proc SPIE*. 2007;6498.

[45] Sasov A. Optimization of pinhole cameras for emission tomographic systems. *Proc SPIE*. 2008;7078.

[46] Uribe J, Hugg J, Heukensfeldt Jansen F. Adjustable pinhole collimators method and system. 2008.

[47] Schramm NU, Ebel G, Engeland U, Schurrat T, Behe M, Behr TM. High-Resolution SPECT Using Multipinhole Collimation. *IEEE Transactions on Nuclear Science*. 2003;50(3):315–320.

[48] Wagenaar DJ, Zhang J, Kazules T, Vandehei T, Bolle E, Chowdhury S, Parnham K, Patt BE. In Vivo Dual-Isotope SPECT Imaging with Improved Energy Resolution. In: *Nuclear Science Symposium and Medical Imaging Conference (NSS/MIC), 2006 IEEE*. IEEE. 2006; pp. 3821–3826.

[49] Hesterman JY, Kupinski MA, Furenlid LR, Wilson DW, Barrett HH. The multi-module, multi-resolution system (M3R) - A novel small-animal SPECT system. *Medical Physics*. 2007;34(3):987–993.

[50] Vunckx K, Suetens P, Nuyts J. Effect of Overlapping Projections on Reconstruction Image Quality in Multipinhole SPECT. *IEEE Transactions on Medical Imaging*. 2008;27(7):972–983.

[51] Mok GSP, Wang YWY, Tsui B. Quantification of the Multiplexing Effects in Multi-Pinhole Small Animal SPECT: A Simulation Study. *IEEE Transactions on Nuclear Science*. 2009;56(5):2636–2643.

[52] Mok GSP, Tsui BMW, Beekman FJ. The effects of object activity distribution on multiplexing multi-pinhole SPECT. *Physics in Medicine and Biology*. 2011;56(8):2635–2650.

[53] Lin J. On Artifact-free Projection Overlaps in Multi-pinhole Tomographic Imaging. *Transactions on Medical Imaging*. 2013;accepted for publication.

[54] Van Audenhaege K, Vanhove C, Vandenberghe S, Van Holen R. Data completeness in multiplexing multi-pinhole SPECT. *Nuclear Science Symposium Conference Record (NSS/MIC), 2013 IEEE*. 2013;.

[55] van der Have F, Vastenhouw B, Ramakers RM, Branderhorst W, Krah JO, Ji C, Staelens SG, Beekman FJ. U-SPECT-II: An ultra-high-resolution device for molecular small-animal imaging. *Journal of Nuclear Medicine*. 2009;50(4):599–605.

[56] Tenney C, Smith M, Greer K, Jaszczak R. Uranium pinhole collimators for I-131 SPECT imaging. *Nuclear Science, IEEE Transactions on*. 1999;46(4):1165 –1171.

[57] Bom V, Goorden M, Beekman F. Comparison of pinhole collimator materials based on sensitivity equivalence. *Physics in Medicine and Biology*. 2011;56(11):3199.

[58] Miller BW, Moore JW, Barrett HH, Fryé T, Adler S, Sery J, Furenlid LR. 3D printing in X-ray and Gamma-Ray Imaging: A novel method for fabricating high-density imaging apertures. *Nuclear instruments & methods in physics research Section A, Accelerators, spectrometers, detectors and associated equipment*. 2011;659(1):262–268.

[59] Anger HO. Scintillation camera. *Rev Sci Instrum*. 1958;.

[60] Heemskerk J, Kreuger R, Goorden M, Korevaar M, Salvador S, Seeley Z, Cherepy N, van der Kolk E, Payne S, Dorenbos P, Beekman

F. Experimental comparison of high-density scintillators for EMCCD-based gamma ray imaging. *Physics in medicine and biology*. 2012; 57:4545–4554.

[61] Johnson LC, Desmond LC, Ethan LH, Peterson TE. Characterization of a high-purity germanium detector for small-animal SPECT. *Physics in Medicine and Biology*. 2011;56(18):5877–5888.

[62] Stickel J, Qi J, Cherry SR. Fabrication and characterization of a 0.5-mm lutetium oxyorthosilicate detector array for high-resolution PET applications. *Journal of Nuclear Medicine*. 2007;48(1):115–121.

[63] Hofstadter R. Alkali halide scintillation counters. *Physical Review*. 1948;74:100–101.

[64] Barett HH, Swindell W. *Radiological Imaging: The Theory of Image Formation, Detection, and Processing (Revised Edition)*. Academic Press. 1981.

[65] Grassmann H, Lorenz E, Moser H. Properties of CsI(Tl) - Renaissance of an old scintillation material. *Nuclear Instruments and Methods in Physics Research Section A: Accelerators, Spectrometers, Detectors and Associated Equipment*. 1985;228(2-3):323–326.

[66] Cooke D, McClellan K, Bennett B, Roper J, Whittaker M, Muenchausen R, Sze R. Crystal growth and optical characterization of cerium-doped $Lu_{1.8}Y_{0.2}SiO_5$. *Journal of Applied Physics*. 2000; 88(12):7360–7362.

[67] van Loef E, Dorebos P, van Eijk C. High-energy-resolution scintillator: Ce^{3+} activated $LaBr_3$. *Applied Physics Letters*. 2001;79(10):1573–1575.

[68] Walrand S, Jamar F, de Jong M, Pauwels S. Evaluation of Novel Whole-Body High-Resolution Rodent SPECT (Linoview) Based on Direct Acquisition of Linogram Projections. *Journal of Nuclear Medicine*. 2005;46(11):1872–1880.

[69] Daube-Witherspoon M, Surti S, Perkins A, Kyba C, Wiener R, Werner M, Kulp R, Karp J. The imaging performance of a $LaBr_3$-based PET scanner. *Physics in Medicine and Biology*. 2010;55(1):45–64.

[70] Schaart D, Seifert S, Vinke R, van Dam H, Dendooven P, Löhner H, Beekman F. $LaBr_3$:Ce and SiPMs for time-of-flight PET: achieving

100 ps coincidence resolving time. *Physics in Medicine and Biology*. 2010;55(7):179–189.

[71] Kyushima H, Hasegawa Y, Atsumi A. Photomultiplier tube of new dynode configuration. *IEEE Transactions on Nuclear Science*. 1994; 41:725–729.

[72] Cherry DR, Shao Y, Silverman RW, Meadors K. MicroPET: a high resolution PET scanner for imaging small animals. *IEEE Transactions on Nuclear Science*. 1997;44(3):1161–1166.

[73] Pani R, Cinti MN, Pellegrini R, De Notaristefani F, Bennati P, Betti M, Trotta G, Mattioli M, Garibaldi F, Orsolini Cencelli V, et al. $LaBr_3$ scintillation camera. In: *Nuclear Science Symposium and Medical Imaging Conference (NSS/MIC), 2005 IEEE*. 2005; pp. 2061–2065.

[74] Fabbri A, Cencelli VO, Xu J, Rittenbach A, Galasso M, Tsui B. Sub-millimeter resolution SPECT using a low-cost compact camera based on a continuous NaI(Tl) crystal and PSPMT array. *Journal of Nuclear Medicine*. 2013;54 Suppl. 2:2161.

[75] Sanchez F, Orero A, Soriano A, Correcher C, Conde P, Gonzalez A, Hernandez L, Moliner L, Rodriguez-Alvarez M, Vidal L, Benlloch J, Chapman S, Leevy W. ALBIRA: A small animal PET/SPECT/CT imaging system. *Medical Physics*. 2013;40(5):051906.

[76] Shockley W. Currents to conductors induced by a moving point charge. *Journal of Applied Physics*. 1938;9(10):635–636.

[77] Ramo S. Currents induced by electron motion. *Proceedings of the IRE*. 1939;27(9):584–585.

[78] Moses WW, Derenzo SE, Melcher CL, Manente RA. A room temperature LSO / PIN photodiode PET detector module that measures depth of interaction. *Transactions on Nuclear Science*. 1995; 42(4):1085–1089.

[79] Huber J, Moses W, Derenzo S, Ho H, Andreaco M, Paulus M, Nutt R. Characterization of a 64 channel PET detector using photodiodes for crystal identification. *Transactions on Nuclear Science*. 1997; 44(3):1197–1201.

[80] Gruber GJ, Moses WW, Derenzo SE, Wang NW, Beuville E, Ho M. A discrete scintillation camera module using silicon photodiode readout

of CsI(Tl) crystals for breast cancer imaging. *Transactions on Nuclear Science*. 1998;NS-45:1063–1068.

[81] Shimizu S, Pepin CM, Lecomte R. Assessment of LGSO Scintillators With APD Readout for PET/SPECT/CT Detectors. *Transactions on Nuclear Science*. 2010;57(3):1512–1517.

[82] Maas MC, van der Laan DJ, Schaart DR, Huizenga J, Brouwer JC, Bruyndonckx P, Leonard S, Lemaitre C, van Eijk CWE. Experimental characterization of monolithic-crystal small animal PET detectors read out by APD arrays. *IEEE Transactions on Nuclear Science*. 2006; 53(3):1071–1077.

[83] Bergeron M, Cadorette J, Beausoin JF, Lepage MD, Robert G, Selivanov V, Tétrault MA, Viscogliosi N, Norenberg JP, Fontaine R, Lecomte R. Performance Evaluation of the LabPET APD-Based Digital PET Scanner. *Transactions on Nuclear Science*. 2009;56(1):10–16.

[84] Schlemmer H, Pichler B, Schmand M, Burbar Z, Michel C, Ladebeck R, Jattke K, Townsend D, Nahmias C, Jacob P, Heiss WD, Claussen C. Simultaneous MR/PET Imaging of the Human Brain: Feasibility Study. *Radiology*. 2008;248(3):1028–1035.

[85] Golovin V, Saveliev V. Novel type of avalanche photodetector with Geiger mode operation. *Nuclear Instruments and Methods in Physics Research Section A: Accelerators, Spectrometers, Detectors and Associated Equipment*. 2004;518(1-2):560–564.

[86] Buzhan P, Dolgoshein B, Filatov L, Ilyin A, Kantzerov V, Kaplin V, Karakash A, Kayumov F, Klemin S, Popova E, Smirnov S. Silicon photomultiplier and its possible applications. *Nuclear Instruments and Methods in Physics Research Section A: Accelerators, Spectrometers, Detectors and Associated Equipment*. 2003;504:48–52.

[87] Roncali E, Cherry S. Application of silicon photomultipliers to positron emission tomography. *Annals of Biomedical Engineering*. 2011;39(4):1358–1377.

[88] Schaart D, van Dam H, Seifert S, Vinke R, Dendooven P, Löhner H, Beekman F. A novel, SiPM-array-based, monolithic scintillator detector for PET. *Physics in medicine and biology*. 2009;54:3501–3512.

[89] Yamaya T, Mitsuhashi T, Matsumoto T, Inadama N, Nishikido F, Yoshida E, Murayama H, Kawai H, Sugo M, Watanabe M. A SiPM-based isotropic-3D PET detector X'tal cube with a three-dimensional array of 1 mm^3 crystals. *Physics in medicine and biology*. 2011; 56(21):6793–6807.

[90] Frach T, Prescher G, Degenhardt C, de Gruyter R, Schmitz A, Ballizany R. The digital silicon photomultiplier principle of operation and intrinsic detector performance. In: *Nuclear Science Symposium Conference Record (NSS/MIC), 2009 IEEE*. 2009; .

[91] Seifert S, van der Lei G, van Dam H, Schaart D. First characterization of a digital SiPM based time-of-flight PET detector with 1 mm spatial resolution. *Physics in medicine and biology*. 2013;58(9):3061–3074.

[92] Bouckaert C, Deprez K, España S, Vandenberghe S, Van Holen R. Performance characterization of a compact SPECT detector based on dSiPMs and monolithic LYSO. *Nuclear Science Symposium Conference Record (NSS/MIC), 2013 IEEE*. 2013;.

[93] Fiorini C, Longoni A, Perotti F. New detectors for gamma-ray Spectroscopy and Imaging, based on Scintillators coupled to Silicon Drift Detectors. *Nuclear Instruments and Methods in Physics Research Section A: Accelerators, Spectrometers, Detectors and Associated Equipment*. 2000;454(1):241–246.

[94] Fiorini C, Peloso R, Longoni A, Mennini T, Micotti E. The HICAM Gamma Camera. *IEEE Transactions on Nuclear Science*. 2011; 58(2):559–568.

[95] Fiorini C, Perotti F. Small prototype of Anger camera with submillimeter position resolution. *Review of Scientific Instruments*. 2005; 76(4):044303.

[96] Fiorini C, Busca P, Peloso R, Abba A, Geraci A, Bianchi C, Poli G, Virotta G, Erlandsson K, Hutton B, Lechner P, Soltau H, Strüder L, Pedretti A, Van Mullekom P, Ottobrini L, Lucignani G. The HICAM Gamma Camera. *IEEE Transactions on Nuclear Science*. 2012; 59(3):537–544.

[97] Peterson TE, Furenlid LR. SPECT detectors: the Anger Camera and beyond. *Physics in Medicine and Biology*. 2011;56(17):R145–R182.

[98] Heemskerk JW, Korevaar MA, Huizenga J, Kreuger R, Schaart DR, Goorden MC, Beekman FJ. An enhanced high-resolution EMCCD-based gamma camera using SiPM side detection. *Physics in Medicine and Biology*. 2010;55(22):6773–6784.

[99] de Vree GA, Westra AH, Moody I, van der Have F, Ligtvoet KM, Beekman FJ. Photon-counting gamma camera based on an electron-multiplying CCD. *IEEE Transactions on Nuclear Science*. 2005; 52(3):580–588.

[100] Barrett HH, Hunter WCJ, Miller BW, Moore SK, Chen Y, Furenlid LR. Maximum-Likelihood Methods for Processing Signals From Gamma-Ray Detectors. *IEEE Transactions on Nuclear Science*. 2009; 56(3):725.

[101] Joung J, Miyaoka RS, Lewellen TK. cMiCE:a high resolution animal PET using continuous LSO with a statistics based positioning scheme. *Nuclear Instruments and Methods in Physics Research Section A: Accelerators, Spectrometers, Detectors and Associated Equipment*. 2002;489(1):1137–1141.

[102] Hesterman JY, Caucci L, Kupinski MA, Barrett HH, Furenlid LR. Maximum-Likelihood Estimation With a Contracting-Grid Search Algorithm. *IEEE Transactions on Nuclear Science*. 2010;57(3):1077–1084.

[103] van Dam HT, Seifert S, Vinke R, Dendooven P, Löhner H, Beekman FJ, Schaart DR. Improved Nearest Neighbor Methods for Gamma Photon Interaction Position Determination in Monolithic Scintillator PET Detectors. *IEEE Transactions on Nuclear Science*. 2011;58(5):1–9.

[104] Palms JM, Rao P, Wood R. A Fano factor measurement for silicon using low energy photons. *Nuclear Instruments and Methods*. 1969; 76(1):59–60.

[105] Barber HB, Woolfenden JM. *Nuclear Medicine*, pp. 137–153. Mosby. 2006;.

[106] Takahashi T, Watanabe S. Recent Progress in CdTe and CdZnTe Detectors. *IEEE Transactions on Nuclear Science*. 2001;48(4):950–959.

[107] Tsui BMW, Xu J, Rittenbach A, Chen S, AbdEl-Monem ES, Edelstein WA, Guo X, Liu A, Hugg JW. High performance SPECT system for simultaneous SPECT-MR imaging of small animals. In: *Nuclear Science Symposium Conference Record (NSS/MIC), 2011 IEEE*. 2011; .

[108] Gagnon D, Zeng G, Links J, Griesmer J, Valentino F. Design considerations for a new solid-state gamma-camera: Soltice. *Nuclear Science Symposium Conference Record (NSS/MIC), 2001 IEEE*. 2001; 2:1156–1160.

[109] Buechel R, Herzog B, Husmann L, Burger I, Pazhenkottil A, Treyer V, Valenta I, Schulthess P, Nkoulou R, Wyss C, Kaufmann P. Ultrafast nuclear myocardial perfusion imaging on a new gamma camera with semiconductor detector technique: first clinical validation. *European Journal of Nuclear Medicine*. 2010;37(4):773–778.

[110] Choong WS, Moses WW, Tindall CS, Luke PN. Design for a High-Resolution Small-Animal SPECT System Using Pixellated Si(Li) Detectors for In Vivo ^{125}I Imaging. *IEEE Transactions on Nuclear Science*. 2005;52(1):174–180.

[111] Shokouhi S, Metzler SD, Wilson DW, Peterson TE. Multi-pinhole collimator design for small-object imaging with SiliSPECT: a high-resolution SPECT. *Physics in Medicine and Biology*. 2009;54(2):207–225.

[112] Brzymialkiewicz CN, Tomai MP, McKinley RL, Bowsher JE. Evaluation of fully 3-D emission mammotomography with a compact cadmium zinc telluride detector. *IEEE Transactions on Nuclear Science*. 2005;24(7):868–877.

[113] Guerin L, Verger L, Rebuffel V, Monnet O. A new architecture for pixellated solid state gamma camera used in nuclear medicine. *IEEE Transactions on Nuclear Science*. 2008;55(3):1573–1580.

[114] Meng LJ, Tan J, Spartiotis K, Schulman T. Preliminary evaluation of a novel energy-resolved photon-counting gamma ray detector. *Nuclear Instruments and Methods in Physics Research Section A: Accelerators, Spectrometers, Detectors and Associated Equipment*. 2009; 604(3):548–554.

[115] He Z, Li W, Knoll G, Wehe D, Berry J, Stahle C. 3-D position sensitive CdZnTe gamma-ray spectrometers. *Nuclear instruments methods in*

physics research Section A Accelerators spectrometers detectors and associated equipment. 1999;422(1-3):173–178.

[116] Bruyant P. Analytic and Iterative Reconstruction Algorithms in SPECT. *Journal of Nuclear Medicine*. 2002;43(10):1343–1358.

[117] Shepp LA, Vardi Y. Maximum likelihood reconstruction for emission tomography. *IEEE Transactions on Medical Imaging*. 1982;1(2):113–122.

[118] Vanhove C, Andreyev A, Defrise M, Nuyts J, Bossuyt A. Resolution recovery in pinhole SPECT based on multi-ray projections: a phantom study. *European Journal of Nuclear Medicine and Molecular Imaging*. 2007;34(2):170–180.

[119] van der Have F, Vastenhouw B, Rentmeester M, Beekman FJ. System Calibration and Statistical Image Reconstruction for Ultra-High Resolution Stationary Pinhole SPECT. *IEEE Transactions on Medical Imaging*. 2008;27(7):960–971.

[120] Miller BW, Barrett HH, Furenlid LR, Barber HB, Hunter RJ. Recent advances in BazookaSPECT: Real-time data processing and the development of a gamma-ray microscope. *Nuclear instruments methods in physics research Section A Accelerators spectrometers detectors and associated equipment*. 2008;591(1):272–275.

[121] Pani R, Vittorini F, Pellegrini R, Bennati P, Cinti MN, Mattioli M, Scafe R, Lo Meo S, Navarria F, Moschini G, Boccaccio P, Cencelli VO, De Notaristefani F. High spatial and energy resolution gamma imaging based on $LaBr_3$(Ce) continuous crystals. In: *Nuclear Science Symposium and Medical Imaging Conference (NSS/MIC), 2008 IEEE*. 2008; pp. 1763–1771.

[122] WinPcap packet capture library.
URL `http://www.winpcap.org/`

[123] Ling T, Lee K, Miyaoka RS. Performance Comparisons of Continuous Miniature Crystal Element (cMiCE) Detectors. *IEEE Transactions on Nuclear Science*. 2006;53(5):2513–2518.

[124] Kim J, Choi Y, Joo K, Sihn B, Chong J, Kim S, Lee K, Choe Y, Kim B. Development of a miniature scintillation camera using an NaI(Tl) scintillator and PSPMT for scintimammography. *Physics in Medicine and Biology*. 2000;45(11):3481–3488.

[125] Pani R, Bennati P, Pellegrini R, Cinti M, Scafe R, Stefano R, De Vincentis G, Di Castro E, Lo Meo S, Fabbri A, Cencelli V, de Notaristefani F. LaBr3(Ce) and NaI(Tl) performance comparison for single photon emission imaging. *Nuclear Science Symposium Conference Record (NSS/MIC), 2011 IEEE*. 2011;pp. 4433–4436.

[126] Patton DD, Barrett HH, Chen JC. FASTSPECT: A four-dimensional brain imager. *JNM*. 1994;35(5):P93, Suppl S.

[127] Furenlid LR, Wilson DW, Chen Yc, Kim H, Pietraski PJ, Crawford MJ, Barrett HH. FastSPECT II: a second-generation high-resolution dynamic SPECT imager. *IEEE Transactions on Nuclear Science*. 2004; 51(3):631–635.

[128] Bocher M, Blevis IM, Tsukerman L, Shrem Y, Kovalski G, Volokh L. A fast cardiac gamma camera with dynamic SPECT capabilities: design, system validation and future potential. *European Journal of Nuclear Medicine and Molecular Imaging*. 2010;37(10):1887–1902.

[129] Vanhove C, Defrise M, Lahoutte T, Bossuyt A. Three-pinhole collimator to improve axial spatial resolution and sensitivity in pinhole SPECT. *European Journal of Nuclear Medicine and Molecular Imaging*. 2008;35(2):407–415.

[130] De Smet J, Van Holen R, Staelens S, Vandenberghe S, Lemahieu I. Slat collimated multipinhole human brain SPECT. *Nuclear Science Symposium Conference Record (NSS/MIC), 2008 IEEE*. 2009; pp. 3309 – 3310.

[131] Schramm N, Wirrwar A, Sonnenberg F, Halling H. Compact high-resolution detector for small animal imaging. *IEEE Transactions on Nuclear Science*. 2000;47(3):1163–1167.

[132] McElroy D, MacDonald L, Beekman F, Wang Y, Patt B, Iwanczyk J, Tsui B, Hoffman E. Performance Evaluation of A-SPECT: A High Resolution Desktop Pinhole SPECT System for Imaging Small Animals. *IEEE Transactions on Nuclear Science*. 2002;49(5):2139–2147.

[133] Kastis G, Furenlid L, Wilson D, Peterson T, Barber H, Barrett H. Compact CT/SPECT Small-Animal Imaging System. *IEEE Transactions on Nuclear Science*. 2004;51(1):63–67.

[134] Hong K, Choi Y, Lee S, Lee S, Song T, Min B, Jung J, Choe Y, Lee KH, Kim BT. A Compact SPECT/CT System for Small Animal

Imaging. *IEEE Transactions on Nuclear Science*. 2006;53(5):2601–2604.

[135] Zeniya T, Watabe H, Aoi T, Kim K, Teramoto N, Takeno T, Ohta Y, Hayashi T, Mashino H, Ota T, Yamamoto S, Iida H. Use of a compact pixellated gamma camera for small animal pinhole SPECT imaging. *Annals of Nuclear Medicine*. 2006;20(6):409–416.

[136] Bequé D, Nuyts J, Bormans G, Suetens P, Dupont P. Characterization of pinhole SPECT acquisition geometry. *IEEE Transactions on Medical Imaging*. 2003;22(5):599–612.

[137] Vandeghinste B, Vanhove C, De Beenhouwer J, Van Holen R, Vandenberghe S, Staelens S. Absolute quantification in multi-pinhole micro-SPECT for different isotopes. *Nuclear Science Symposium Conference Record (NSS/MIC), 2011 IEEE*. 2011;pp. 3720 – 3724.

[138] Schramm N, Hoppin J, Lackas C, Gershman B, Norenberg J, de Jong M. Improving resolution, sensitivity and applications for the NanoSPECT/CT: A high-performance SPECT/CT imager for small-animal research. *Journal of Nuclear Medicine meeting abstracts*. 2007; 48:436.

[139] Seidel J, Gandler W, Green M. Characteristics of a pair of small field-of-view LSO scintillation cameras. *IEEE Transactions on Nuclear Science*. 1996;43(3):1968–1973.

[140] Cardi C, Zixiong C, Thakur M, Karp J. Pinhole PET (pPET): a multi-pinhole collimator insert for small animal SPECT imaging on PET cameras. In: *Nuclear Science Symposium Conference Record (NSS/MIC), 2005 IEEE*. 2005; .

[141] Dhanasopon A, Levin C, Foudray A, Olcott P, Habte F. Scintillation Crystal Design Features for a Miniature Gamma Ray Camera. *IEEE Transactions on Nuclear Science*. 2005;52(5):1439–1446.

[142] Lois C, Aguiar P, Couce B, Iglesias A. Characterization of low energy Lu background on continuous LYSO blocks. In: *Nuclear Science Symposium Conference Record (NSS/MIC), 2010 IEEE*. 2010; .

[143] Aguiar P, Iglesias A, Couce B, Lois C. A feasibility study on the use of arrays of discrete SiPMs for MR compatible LYSO readout using Monte Carlo simulation. *Journal of Instrumentation*. 2012;7.

[144] Liang HC, Jan ML, Lin WC, Yu SF, Su JL, Shen LH. Development of an LYSO based gamma camera for positron and scinti-mammography. *Journal of Instrumentation*. 2009;4.

[145] Yao R, Ma T, Shao Y. Lutetium oxyorthosilicate (LSO) intrinsic activity correction and minimal detectable target activity study for SPECT imaging with a LSO-based animal PET scanner. *Physics in Medicine and Biology*. 2008;53(16):4399–4415.

[146] Browne E, Junde H. Nuclear Data Sheets for A = 176. *Nuclear Data Sheets*. 1998;84(2):337–486.

[147] Dorenbos P, de Haas J, van Eijk C. Non-linear response in the scintillation yield of Lu_2SiO_5 : Ce^{3+}. *IEEE Transactions on Nuclear Science*. 1994;41(4):735–737.

[148] Mao R, Zhang L, Zhu RY. Optical and scintillation properties of inorganic scintillators in high energy physics. *IEEE Transactions on Nuclear Science*. 2008;55(4):2425–2431.

[149] Moses W, Payne S, Choong WS, Hull G, Reutter B. Scintillator Non-Proportionality: Present Understanding and Future Challenges. *IEEE Transactions on Nuclear Science*. 2008;55(3):1049 – 1053.

[150] Franc B, Acton P, Mari C, Hasegawa B. Small-Animal SPECT and SPECT/CT: Important Tools for Preclinical Investigation. *Journal of Nuclear Medicine*. 2008;49(10):1651–1663.

[151] Rogers W, Clinthorne N, Stamos J, Koral K, Mayans R, Keyes J, Williams J, Snapp W, Knoll G. SPRINT: A Stationary Detector Single Photon Ring Tomograph for Brain Imaging. *IEEE Transactions on Medical Imaging*. 1982;1(1):63–68.

[152] Park M, Moore S, Kijewski M. Brain SPECT with short focal-length cone-beam collimation. *Medical Physics*. 2005;32(7):2236–2244.

[153] Accorsi R. High-efficiency, high-resolution SPECT techniques for cardiac imaging. In: *Proceedings of Science: Frontiers in Imaging Science: High Performance Nuclear Medicine Imagers for Vascular Disease Imaging (Brain and Heart)*. 2006; .

[154] Chang W, Liang H, Liu J. Design concepts and potential performance of MarC-SPECT - A high-performance cardiac SPECT system. *Journal of Nuclear Medicine*. 2006;47:190– 191P.

[155] Hutton B. New SPECT technology: potential and challenges. *European Journal of Nuclear Medicine and Molecular Imaging*. 2010; 37:1883–1886. 10.1007/s00259-010-1550-x.

[156] Beekman F, van der Have F, Vastenhouw B, van der Linden A, van Rijk P, Burbach J, Smidt M. U-SPECT-I: A novel system for submillimeter-resolution tomography with radiolabeled molecules in mice. *Journal of Nuclear Medicine*. 2005;46(7):1194–1200.

[157] Furenlid L, Wilson D, chun Chen Y, Kim H, Pietraski P, Crawford M, Barrett H. FastSPECT II: a second-generation high-resolution dynamic SPECT imager. *Nuclear Science, IEEE Transactions on*. 2004;51(3):631 – 635.

[158] van der Have F, Vastenhouw B, Ramakers RM, Branderhorst W, Krah JO, Ji C, Staelens SG, Beekman FJ. U-SPECT-II: An Ultra-High-Resolution Device for Molecular Small-Animal Imaging. *Journal of nuclear medicine*. 2009;50(4):599–605.

[159] Hughes S. Archimedes revisited: a faster, better, cheaper method of accurately measuring the volume of small objects. *Physics Education*. 2005;40:468–474.

[160] Zeng GL, Gullberg G, Christian P, Gagnon D, Tung CH. Asymmetric cone-beam transmission tomography. *Transactions on Nuclear Science*. 2001;48:117 – 124.

[161] Van Holen R, , Vandenberghe S. Optimization of a stationary small animal SPECT system for simultaneous SPECT/MRI. *Nuclear Science Symposium Conference Record (NSS/MIC), 2013 IEEE*. 2013; .

[162] Chen YC, Furenlid L, Wilson D, Barrett H. *Small-animal SPECT imaging*, pp. 195–201. Springer. 2005;.

[163] Deleye S, Van Holen R, Verhaeghe J, Vandenberghe S, Stroobants S, Staelens S. Performance evaluation of small-animal multipinhole μSPECT scanners for mouse imaging. *European Journal of Nuclear Medicine and Molecular Imaging*. 2013;40(5):744–758.

List of Publications

Journal papers

[1] Deprez K., Van Holen R., Vandenberghe S., A high resolution SPECT detector based on thin continuous LYSO, *Physics in Medicine and Biology*, 2014, 59(1), 153-171

[2] Deprez K., Vandenberghe S., Van Audenhaege K., Van Vaerenbergh J., Van Holen R., Rapid additive manufacturing of MR compatible multipinhole collimators with selective laser melting of tungsten powder, *Medical Physics*, 2013, 40(1), 012501

[3] Deprez K., Pato L., Vandenberghe S., Van Holen R., Characterization of a SPECT pinhole collimator for optimal detector usage (the lofthole), *Physics in Medicine and Biology*, 2013, 58(4), p.859-885

[4] Deprez K., Vandenberghe S., Vandeghinste B., Van Holen R., FlexiSPECT: A SPECT system consisting of a compact high-resolution scintillation detector (SPECTatress) and a lofthole collimator, *IEEE Transactions on Nuclear Science*, 2013, 60(1), p.53-64

[5] Van Holen R., Vandeghinste B., Deprez K., Vandenberghe S., Design and performance of a compact and stationary microSPECT system, *Medical Physics*, 2013, 40, 112501

[6] España S., Deprez K., Van Holen R., Vandenberghe S., Fast calibration of SPECT monolithic scintillation detectors using un-collimated sources, *Physics in Medicine and Biology*, 2013, 58(14), p.4807-4825

[7] Van Audenhaege K., Vandenberghe S., Deprez K., Vandeghinste B., Van Holen R., Design and simulation of a full-ring multi-lofthole collimator for brain SPECT, *Physics in Medicine and Biology*, 2013, 58(18), p.6317-6336

[8] Deprez K., Van Holen R., Vandenberghe S., Staelens S., Design of a high resolution scintillator based SPECT detector (SPECTatress), *Nuclear Instruments and Methods In Physics Research Section A*, 2011, 648 (Suppl. 1), p.S107-S110

Patent applications

[1] Deprez K., Vandenberghe S., Staelens S., Methods and systems for collimating, filing date Dec 9th 2010, App. nbr. PCT/EP2010/069303

[2] Van Audenhaege K., Deprez K., Vandenberghe S., Van Holen R., Methods and systems for collimating, filing date May 9th 2012, App. nr. PCT/EP2012/058589

Conference proceedings

[1] Deprez K., Van Holen R., Vandenberghe S., The lofthole: a novel shaped pinhole geometry for optimal detector usage without multiplexing and without additional shielding, *IEEE Nuclear Science Symposium Conference Record*, 2011, p.3317-3322

[2] Van Audenhaege K., Van Holen R., Deprez K.; Karp J. S., Metzler S., Vandenberghe S., Design of a static full-ring multi-pinhole collimator for brain SPECT, *IEEE Nuclear Science Symposium Conference Record*, 2011, p.4393-4397

[3] Deprez K., Van Holen R., Staelens S., Vandenberghe S., A high resolution scintillator based SPECT detector with digital pulse processing (SPECTatress), *IEEE Nuclear Science Symposium Conference Record*, 2010, p.3100-3104

Conference abstracts

[1] Deprez K., Vandenberghe S., Van Holen R., Performance of continuous LYSO for high resolution SPECT detectors, *Journal of Nuclear Medicine*, 2013, 54(suppl. 2), p.2159

[2] Deprez K., Vandenberghe S., Van Holen R., Accuracy and density of pure tungsten collimators produced by additive manufacturing, *Journal of Nuclear Medicine*, 2013, 54(suppl. 2), p.2165

[3] Van Holen R., Deprez K., Vandeghinste B., Vandenberghe S., A compact stationary microSPECT system based on high-resolution detectors and collimator additive manufacturing, *Journal of Nuclear Medicine*, 2013, 54(suppl. 2), p.2163

[4] Bouckaert C., Marcinkowski R., Deprez K., España S., Van Holen R., Vandenberghe S., Optimization of digital silicon photomultipliers for monolithic SPECT scintillators, *Journal of Nuclear Medicine*, 2013, 54(suppl. 2), p.2160

[5] Van Holen R., Deprez K., Vandeghinste B., Vandenberghe S., Design and simulations of a multi-lofthole MicroSPECT imager using minifying projections, *Journal of Nuclear Medicine*, 2012, 53(suppl. 1), p.2393

[6] Van Holen R., Deprez K., Bouckaert C., Vandenberghe S., Design and simulations of a multi-lofthole MicroSPECT imager using minifying projections, *Workshop On Small Animal Imaging, Abstracts*, 2012

[7] Van Holen R., Van Audenhaege K., Deprez K., Vandenberghe S., Development of a compact MicroSPECT system for sequential SPECT-MRI, *PET/MR and SPECT/MR : New Paradigms for Combined Modalities in Molecular Imaging Conference*, 2012

[8] Van Audenhaege K., Bovijn D., Van Holen R., Deprez K., Vandenberghe S., An MR-compatible shutter mechanism for stationary multi-pinhole SPECT of large objects, *PET/MR and SPECT/MR : New Paradigms for Combined Modalities in Molecular Imaging Conference, Abstracts*, 2012

[9] Deprez K., Van Holen R., Vandeghinste B., Vandenberghe S., FlexiSPECT: a compact SPECT system with a lofthole collimator and a high-resolution scintillation detector, *Journal of Nuclear Medicine*, 2012, 53(suppl. 1), p.492

[10] Deprez K., Van Holen R., Van Audenhaege K., Vandenberghe S., Additive manufacturing of high density tungsten collimators, *Journal of Nuclear Medicine*, 2012, 53(suppl. 1), p.2394

[11] Pato L., Van Holen R., Deprez K., Vandenberghe S., Geometric sensitivity in the Penumbra region of a pinhole: analytic calculation, *Journal of Nuclear Medicine*, 2012, 53(suppl. 1), p.2395

[12] Deprez K., Vandenberghe S., Staelens S., Design of a High Resolution Scintillator Based SPECT Detector (SPECTatress), *Imaging 2010, Abstracts*, 2010